

Characterization of an electron spin qubit in a Si/SiGe quantum dot

Kawakami, Erika

DOI

[10.4233/uuid:dd0886f0-2f3a-421d-ac92-bdc4da5985b5](https://doi.org/10.4233/uuid:dd0886f0-2f3a-421d-ac92-bdc4da5985b5)

Publication date

2016

Document Version

Final published version

Citation (APA)

Kawakami, E. (2016). *Characterization of an electron spin qubit in a Si/SiGe quantum dot*. [Dissertation (TU Delft), Delft University of Technology]. <https://doi.org/10.4233/uuid:dd0886f0-2f3a-421d-ac92-bdc4da5985b5>

Important note

To cite this publication, please use the final published version (if applicable). Please check the document version above.

Copyright

Other than for strictly personal use, it is not permitted to download, forward or distribute the text or part of it, without the consent of the author(s) and/or copyright holder(s), unless the work is under an open content license such as Creative Commons.

Takedown policy

Please contact us and provide details if you believe this document breaches copyrights. We will remove access to the work immediately and investigate your claim.

**CHARACTERIZATION OF AN ELECTRON SPIN QUBIT
IN A Si/SiGe QUANTUM DOT**

CHARACTERIZATION OF AN ELECTRON SPIN QUBIT IN A Si/SiGe QUANTUM DOT

Proefschrift

ter verkrijging van de graad van doctor
aan de Technische Universiteit Delft,
op gezag van de Rector Magnificus prof. ir. K.C.A.M. Luyben,
voorzitter van het College voor Promoties,
in het openbaar te verdedigen op dinsdag 13 September 2016 om 15:00 uur

door

Erika KAWAKAMI

Master of Engineering,
Graduate School of Science and Technology, Keio University, Yokohama, Japan,
geboren te Osaka, Japan.

Dit proefschrift is goedgekeurd door de
promotor: Prof. dr. ir. L.M.K. Vandersypen

Samenstelling promotiecommissie:

Rector Magnificus,
Prof. dr. ir. L.M.K. Vandersypen,

voorzitter
Technische Universiteit Delft

Onafhankelijke leden:

Prof. dr. Yaroslav Blanter
Prof. dr. Seigo Tarucha
Prof. dr. Edoardo Charbon
Dr. Ferdinand Kuemmeth
Dr. Leonardo Di Carlo

Technische Universiteit Delft
University of Tokyo
Technische Universiteit Delft
University of Copenhagen
Technische Universiteit Delft

The works presented in this thesis were supported in part by Army Research Office (W911NF-12-0607), the Dutch Foundation for Fundamental Research on Matter (FOM) and a European Research Council (ERC) Synergy grant; development and maintenance of the growth facilities used for fabricating samples is supported by DOE (DE-FG02-03ER46028). This research utilized NSF-supported shared facilities at the University of Wisconsin-Madison. Work at the Ames Laboratory was supported by the Department of Energy-Basic Energy Sciences under Contract No. DE-AC02-07CH11358. Erika Kawakami was supported by a fellowship from the Nakajima Foundation.



Printed by: Gildeprint

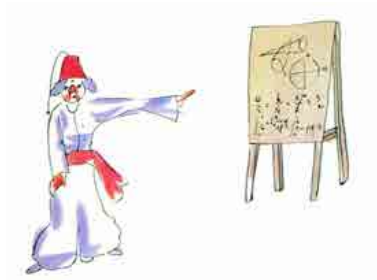
Cover: Schrödinger's cats by Nekoji Aizawa

Copyright © 2016 by E. Kawakami

Casimir PhD series, Delft-Leiden 2016-22

ISBN 978-90-8593-266-6

An electronic version of this dissertation is available at
<http://repository.tudelft.nl/>.



Il avait fait alors une grande démonstration de sa découverte à un Congrès International d'Astronomie. Mais personne ne l'avait cru à cause de son costume.

Antoine de Saint-Exupéry

CONTENTS

Summary	xiii
Samenvatting	xvii
Preface	xxi
1 Introduction	1
1.1 Concept of a quantum computer	1
1.2 Requirements for qubits	2
1.3 Searching for a physical qubit.	4
1.4 How far are we from the realization of a universal quantum computer?	6
1.5 Thesis overview	8
2 Spins in silicon quantum dots	11
2.1 Overview	11
2.2 History of spin qubits in silicon	11
2.2.1 Dopants in silicon	11
2.2.2 Silicon quantum dots	13
2.3 How to realize qubits using quantum dots	14
2.4 How to manipulate and read out the spin state of an electron.	14
2.5 Comparison between GaAs qubits Si spin qubits	16
2.5.1 Nuclear spins in host material	16
2.5.2 Band structure	16
2.5.3 Spin-orbit interaction (SOI)	17
2.5.4 g-factor	17
2.5.5 Effective mass/confinement	19
3 EDSR and decoherence	21
3.1 Electric dipole spin resonance	21
3.1.1 Mixing spin and charge states	22
3.1.2 Microwave excitation	24
3.1.3 Non-conventional electric dipole spin resonance	26
3.2 Stray magnetic field created by micromagnets	28
3.3 Mechanisms of Decoherence	31
3.3.1 Interaction with nuclear spins	31
3.3.2 Decoherence due to the Overhauser field	33
3.3.3 Decoherence due to the electron spin-mediated coupling between the nuclear spins.	35

4	Spin Physics for Si/SiGe Quantum Dots	37
4.1	Introduction	37
4.2	Three-step spin-state measurements	37
4.3	Rabi oscillation	40
4.4	Ramsey fringe.	44
4.5	Dynamical Decoupling	46
4.6	Randomized Benchmarking	53
5	Device and Measurement Setup	61
5.1	Heterostructure growth	61
5.2	Device A	62
5.2.1	Measurement Setup for Device A	62
5.3	Device B and C	62
5.3.1	Sample fabrication for Device B and C	62
5.3.2	Measurement Setup for Device B and C	64
6	Photon-assisted tunneling on a single and a double quantum dot	73
6.1	Charge stability of Device A	74
6.2	Photon-assisted tunneling on a single quantum dot	76
6.3	Heating effect due to d.c. current	76
6.4	Potential for using the antenna to perform single-spin ESR experiments	79
6.5	Charge stability of Device B and Photon-assisted tunneling on a double quantum dot	79
6.6	Potential for using the micromagnet to perform single-spin ESR experiments	82
6.7	Conclusions.	83
7	Electrical control of a long-lived spin qubit in a Si/SiGe quantum dot	85
7.1	Introduction	86
7.2	Device and Quantum dot characterization	86
7.3	Electron spin resonance spectroscopy	87
7.4	Coherent control of electron spin	89
7.5	Spin echo	92
7.6	Electron spin resonance and valley states in Si	92
7.7	Conclusions.	93
7.S1	Heating effects from the microwave bursts	94
7.S2	Finding the spin resonance condition.	94
7.S3	Spin relaxation time T_1	94
7.S4	Rabi oscillation contributed from two valley states	95
7.S5	Population and time dependence of the two resonances	97
7.S6	π pulse fidelity	99
7.S7	Initialization fidelity and read-out fidelity.	99
7.S8	Numerical simulation of Ramsey fringes	102
7.S9	Power dependence of the Rabi frequency	103
7.S10	Difference in g-factors and Rabi frequencies between the two resonances	104
7.S11	Sources of Rabi decay	106
7.S12	Valley phase relaxation length scale	108

7.S13	Valley scattering as a source of spin echo decay	109
8	Second harmonic coherent driving of a single electron spin in Si-Ge single QD	111
8.1	Introduction	112
8.2	Device and measurement technique	113
8.3	Origin of the non linearity.	113
8.4	CW analysis	115
8.5	Coherent spin oscillations	116
8.6	Universal phase control.	118
8.7	Conclusion	120
8.S1	Estimation of the ratio of Rabi frequencies from CW measurements	120
8.S2	Chevron pattern using second harmonic driving	121
8.S3	T_2^* estimation from Ramsey envelope decay and Ramsey simulation	122
8.S4	Echo decay of a qubit driven fundamental harmonic and comparison to results for driving at second harmonic	122
8.S5	Mechanisms mediating second harmonic generation.	124
9	EDSR detection of dressed orbital states in a quantum dot	125
9.1	Introduction	126
9.2	Device and spectroscopic measurements	127
9.3	Model.	128
9.4	Coherence of the inter-valley spin transition	132
9.5	Conclusions.	134
9.S1	Model of the Dynamics	136
	9.S1.1 Adiabatic Effects	137
	9.S1.2 Nonadiabatic Effects	138
	9.S1.3 Simulation Results	139
9.S2	Dressed States	140
	9.S2.1 Orbital-Photon System.	140
	9.S2.2 Spin-Orbital-Photon System	142
	9.S2.3 Hybridization of the Dressed States	148
9.S3	ADDITIONAL MEASUREMENTS AND ANALYSIS	150
	9.S3.1 Variations in time of the spin-valley transition frequency	150
	9.S3.2 Influence of the static and pulsed gate voltages	151
	9.S3.3 Influence of electric field noise.	154
9.S4	Simulation of valley-orbit splitting versus dot position	155
10	Gate fidelity and coherence time of an electron spin in a Si/SiGe quantum dot	157
10.1	Introduction	157
10.2	Device and Measurement Setup	158
10.3	High-quality Rabi Oscillations	158
10.4	Dynamical Decoupling	159
10.5	Randomized benchmarking.	163
10.6	Discussion and Conclusion	166
10.S1	Modeling of decoherence and noise produced by nuclear spins.	167
10.S2	Heating of the electron reservoir as a function of microwave burst time	173

10.S3	Extract the noise spectral density from the echo decays.	175
10.S4	Further analysis of the echo decays	175
10.S5	Generation of noise for the numerical simulations	177
10.S6	Method of the Numerical simulation	177
10.S7	Numerical simulation for Randomized Benchmarking	178
10.S8	Numerical simulation for Dynamical Decoupling.	179
10.S9	additional data for dynamical decoupling.	182
10.S10	Origin of the high-frequency noise spectrum	182
10.S11	Estimation of the valley-orbit splitting	184
11	Conclusions and outlook	187
11.1	Conclusion	187
11.2	DiVincenzo criteria	188
11.3	How good is good enough?	190
11.4	Outlook	191
	Epilogue	197
A	Spin operators	199
A.1	Pauli matrices.	199
A.1.1	Definition	199
A.1.2	Commutation relations	200
A.2	Density operator	200
A.3	Expectation value	201
A.4	Time evolution operator	201
A.4.1	Rotation operator around x , y , and z axes	201
B	Time evolution of a quantum state	203
B.1	Equation of motion of a quantum state	203
B.1.1	Case of pure state: Schrödinger equation	203
B.1.2	General case: Liouville-von Neumann equation	204
B.2	Time evolution operator for time-independent Hamiltonian	204
B.3	Time evolution operator for time-dependent Hamiltonian	204
B.4	Rotating reference frame	204
B.5	Electron Spin Resonance	205
B.5.1	Two level system as qubit	205
B.5.2	Rotating wave approximation	205
C	Multiphoton ESR	207
C.1	Multiphoton electron spin resonance due to a perpendicular oscillating magnetic field.	207
D	Decoherence mechanism	209
D.1	Decoherence due to the Overhauser field	209
D.1.1	Decay due to quasi-static Overhauser field.	209
D.1.2	Relation between quasi-static nuclear spin noise decay and the number of nuclear spins	210

E	Analytic expression for Rabi oscillation and Ramsey fringe	213
E.1	Rabi oscillation	213
E.1.1	Rabi oscillation with on-resonance microwave.	213
E.1.2	Rabi oscillation with off-resonance microwave	214
E.2	Ramsey fringe.	216
F	Physical constants	219
F.1	Physical constants	219
F.2	Energy conversion	220
G	Magnetic field gradient created by micro-magnets	221
G.1	Magnetic field gradients the external magnetic field is applied along the x axis	222
G.2	Magnetic field gradients the external magnetic field is applied along the y axis	223
	Bibliography	225

SUMMARY

Characterization of an Electron Spin Qubit in a Si/SiGe Quantum Dot

In this thesis, we present experiments performed on electrons in quantum dots defined by surface gates on top of a two-dimensional Si/SiGe electron gas towards the realization of a large-scale quantum computer using single electron spin states as single physical quantum bits (qubits). DiVincenzo introduced five criteria which should be met by physical qubits: scalability, initialization, long coherence times, universal set of quantum gates, and read-out. If the number of qubits, the initialization fidelity, the coherence time, the quantum gate fidelity, and the read-out fidelity do not reach certain thresholds, a quantum computer will never outperform a classical computer.

Amongst many candidates of physical systems to realize physical qubits with, we chose spin states of electrons confined in Si/SiGe quantum dots (Loss–DiVincenzo quantum computer). Silicon offers a high potential for scalability as it is the most widely used material for semiconductor devices and integrated circuits.

Experiments using single electron spins as qubits first progressed in GaAs/AlGaAs quantum dots. Making “good” quantum dots in Si/SiGe has been difficult due to the lattice mismatch between Si and SiGe and the higher effective mass of an electron confined in Si. The high-quality heterostructure growth, the high-resolution lithography techniques, and the use of undoped devices make it possible to overcome these problems. The merit of Si compared to GaAs is the lower natural abundance of nuclear spins in the substrate, which leads to longer coherence times. In this thesis, we used natural Si, whose abundance of nuclear spins is 4.67%, while the abundance of nuclear spins in GaAs is 100%. Isotopic purification to Si atoms which have non-zero nuclear spins would reduce this percentage further leading to even longer coherence times as already reported by some other groups.

This thesis focuses on single-spin control and coherence, using an all electrical approach. Since spin-orbit coupling is relatively weak in Si, we need to introduce an artificial spin-orbit interaction, via local currents or micromagnets.

In the first part of this thesis, we performed preliminary measurements towards the manipulation and the read-out of the spin state of an electron confined in a Si/SiGe quantum dot. We prepared two different types of devices: one accommodated with an on-chip antenna to generate a.c. and d.c. magnetic fields for ESR and the other one accommodated with micromagnets to produce a local magnetic field gradient for EDSR. The preliminary measurements showed that the device accommodated with the micromagnets was more promising to achieve single qubit manipulation because it suffers less from heating and has a higher potential to achieve a coherent driving. Thus we decided to perform the EDSR experiments using a similar sample with micromagnets to what we used in the preliminary measurements. Surprisingly we have observed not only one but 5 resonance frequencies for a fixed magnetic field.

The two resonances with the highest resonance frequencies can be attributed to the conventional EDSR transitions, which are sometimes referred to fundamental resonances. Due to the small valley splitting, we initialize electrons to the valley-excited state $\sim 30\%$ of the time. One of the fundamental resonances is attributed to the spin-flip transition of the ground valley state and the other one to the spin-flip transition of the excited valley state. The magnetic field gradients created by the micromagnets renormalize the g -factors of two different valley states differently. Experimentally we measured the g -factor difference between the two valley states to be $\sim 0.026\%$.

Using these fundamental resonances, we demonstrated the universal control of one electron spin and measured the coherence time of an electron spin in a Si/SiGe quantum dot. The highest measured Rabi frequency was ~ 5 MHz. The dephasing time (driving free evolution) was measured to be $\sim 1 \mu\text{s}$ and the coherence time was extended to $\sim 40 \mu\text{s}$ using the Hahn echo technique. These experimental results are the very first promising step towards the realization of a quantum computer using single electron spins in Si/SiGe quantum dots as qubits. We were not able to extend the coherence time by applying higher numbers of π pulses (dynamical decoupling) due to the switching of the electron between the valley-excited state and the valley-ground state.

The resonance frequencies of the other two resonances were exactly half of the two fundamental resonances, respectively, and arise from second harmonic driving. An asymmetric confinement potential of a quantum dot leads to the second-harmonic generation of the a.c. magnetic field felt by the electron in the quantum dot. The highest Rabi frequency measured for the second harmonic driving was ~ 3 MHz, nearly as high as for the fundamental resonances. The measured coherence times are also of the same order as the fundamental resonances. We also observed some features that are typical of second harmonic driving: quadratic dependence of the Rabi frequency on the microwave amplitude and doubling of the qubit phase with respect to the phase of the applied microwave. These experimental results show the feasibility of using second harmonic driving for qubit manipulation. One advantage of using second harmonic driving is that a qubit can be manipulated by microwaves with a frequency that is half the Larmor frequency of the qubit, simplifying microwave engineering. We can also benefit from the quadratic dependence of Rabi frequency for addressability, since it prevents unwanted rotations of spin states more efficiently than with the fundamental resonances.

The resonance frequency of the 5th resonance is ~ 7 GHz lower than that of the fundamental resonances. The linewidth of this resonance is ~ 10 times wider than that of the fundamental resonances and coherent oscillation was not observed for this transition. We attribute this resonance to the transition from the spin-down valley-excited state to the spin-up valley-ground state. Thus we call this an inter-valley spin-flip resonance. The difference of the resonance frequency between the fundamental resonances and this resonance, 7 GHz, corresponds to the valley splitting. Due to the valley-orbit interaction, the valley states have the features of charge states. The wider resonance linewidth can be attributed to the transition between these charge-like states.

Although it allows us to observe very interesting physics, a small valley splitting causes several problems for a quantum computer: low initialization fidelity, low control fidelity and short coherence time. Thus we decided to retune the gate voltages hoping that we will be able to obtain a higher valley splitting so that we only initialize electrons in

the ground-valley state and the switching between the two valley states becomes slow enough to be ignored. We achieved this purpose to some extent but not completely. With a new gate configuration, the population of the excited-valley state was decreased from 30% to 20%. The second-harmonic resonances and the inter-valley spin flip resonance were not able to be observed with this gate configuration. The switching between the ground-valley state and the excited-valley state became slower and we were able to extend the coherence time further using dynamical decoupling. The longest coherence time measured was $400 \mu\text{s}$. We also characterized the single qubit gate fidelity using randomized benchmarking and reached an average gate fidelity of $\sim 99\%$.

Based on the experimental results shown in this thesis, we revisit DiVincenzo's five criteria. All the five criteria are already satisfied to some extent but none of them completely. A single qubit is realized but scalability is yet to be demonstrated. We can initialize the qubit with 95% fidelity, which is still not high enough for quantum error correction. The coherence time of the qubit is much longer than in GaAs quantum dots but can be further improved by isotopic purification of Si. We have demonstrated a universal single qubit gate with a fidelity of $\sim 99\%$ reaching the required threshold for a quantum error correction. We still need to characterize a two-qubit gate fidelity. Finally, we can read out with 95% fidelity, which is still not high enough for quantum error correction.

Just before this thesis went to print, a two-qubit operation was also experimentally demonstrated in Si/SiGe quantum dots by our group. Elementary ingredients for single electron spins being used as qubits have been completed. In order to realize a practical Si quantum computer, we need to increase the number of qubits and improve the fidelities of read-out, initialization, and the quantum gates.

Erika Kawakami
June 2016

SAMENVATTING

Karakterisatie van een Elektron Spin Qubit in een Si/SiGe Quantum Dot

In dit proefschrift demonstreren we experimenten uitgevoerd op elektronen in kwantum dots, die gedefinieerd zijn met behulp van elektrodes boven op een elektronenzee (2DEG) in Si/SiGe. Deze experimenten dragen bij aan het realiseren van een grootschalige kwantum computer met enkele elektronspintoestanden als kwantum bits (qubits).

DiVicenzo introduceerde 5 criteria waaraan praktische qubits moeten voldoen: schaalbaarheid, initialisatie in een qubittoestand, lange levensduur van een toestand, een universele set van kwantum operaties en de betrouwbaarheid van uitlezing van een qubittoestand. Als het aantal qubits, de betrouwbaarheid van initialisatie, de levensduur van een toestand, de precisie van de operaties en van de uitlezing van de toestanden bepaalde minimumeisen niet halen, zal een kwantum computer nooit krachtiger en efficiënter worden dan een klassieke computer.

Hoewel veel fysische systemen mogelijkheden bieden om qubits te realiseren, hebben wij gekozen voor de spin van elektronen gevangen in Si/SiGe kwantum dots (Loss-DiVicenzo kwantum computer). Silicium biedt de potentie om de qubits op te schalen, aangezien Si het vaakst gebruikt wordt in de halfgeleider industrie voor geïntegreerde schakelingen.

Experimenten met een enkele elektronspin als qubit werden van oudsher uitgevoerd in GaAs/AlGaAs kwantum dots. De fabricatie van Si/SiGe kwantum dots van goede kwaliteit was aanvankelijk belemmerd door het verschil in kristalrooster tussen Si en SiGe en door de hogere effectieve massa van elektronen gevangen in Si. Het groeien van hoge kwaliteit heterostructuren, hoge resolutie lithografie technieken en de komst van ongedoteerde heterostructuren hielp deze problemen te overbruggen. Het voordeel van Si ten opzichte van GaAs is een lager aantal kernspins in het substraat, hetgeen leidt tot spins die langer coherent blijven. In dit proefschrift gebruikten we natuurlijk Si, waarvan 4.67% kernspins bevat, terwijl dit in GaAs 100% bedraagt. Si kan verrijkt worden met isotopen die geen kernspin bevatten, zodat dit percentage nog lager wordt en de levensduur van een superpositie toestand langer, zoals gerapporteerd door andere groepen.

Dit proefschrift richt zich op elektrische controle en op coherentie van één enkele spin. Vanwege de zwakke spin-baan koppeling in silicium, moeten we daarvoor een kunstmatige spin-baan wisselwerking creëren, via lokale stromen of micro-magneten.

Eerst zijn metingen uitgevoerd gericht op de manipulatie en de uitlezing van de spin-toestand van een elektron gevangen in een Si/SiGe kwantum dot. De experimenten zijn gedaan met 2 verschillende type samples: 1 sample genereert een a.c. magneetveld met een op de chip geïntegreerde antenne voor ESR en het andere sample produceert een magneetveld met een lokale gradiënt met behulp van micro-magneten. De metingen laten zien dat het apparaat met de geïntegreerde micro-magneten een geschiktere kandidaat is voor qubit manipulatie. We hebben aldus besloten om EDSR experimenten te

doen met micro-magneten. Onverwachts hebben we vijf resonantiefrequenties waargenomen voor het magneetveld.

De twee hoogste frequenties kunnen worden verklaard als de conventionele EDSR transitie en soms refereren we naar deze twee frequenties als de fundamentele resonanties. Vanwege een klein verschil in energie tussen de grond- en geëxciteerde vallei toestand, initialiseren we elektronen in de geëxciteerde toestand voor $\sim 30\%$. Een van de fundamentele resonanties kan worden verklaard als de spin-flip overgang van de vallei grondtoestand en de andere als de spin-flip overgang van de vallei geëxciteerde toestand. De gradiënt in het magneetveld gecreëerd met de micro-magneten resulteert in verschillende g -factoren voor de grond- en geëxciteerde toestand. We hebben een experimenteel verschil in g -factor tussen de 2 toestanden gevonden van $\sim 0.026\%$.

Gebruikmakend van deze fundamentele resonanties, hebben we universele controle over 1 elektronspin aangetoond en de coherentietijd van een elektron spin in een Si/SiGe kwantum dot gemeten. De hoogst gemeten Rabi frequentie is ~ 5 MHz. De gemeten coherentietijd was $\sim 1 \mu\text{s}$ tijdens vrije evolutie en de coherentietijd werd verlengd tot $\sim 40 \mu\text{s}$ met de Hahn echo techniek. Deze experimentele resultaten zijn de eerste veelbelovende stap naar de realisatie van een kwantum computer met enkele elektronspins in Si/SiGe kwantum dots als qubits. We konden de coherentietijd niet verlengen door een hoger aantal pi pulsen toe te passen ('dynamische ontkoppeling) vanwege de overgang van het elektron tussen de vallei geëxciteerde en de vallei grondtoestand.

De resonantiefrequenties van de andere twee resonanties waren precies de helft van de twee fundamentele resonanties en we noemen deze resonanties tweede harmonische resonanties. Een asymmetrische opsluitingspotentiaal voor een kwantum dot leidt tot het genereren van tweede harmonischen in het a.c. magneetveld dat het elektron voelt in de kwantum dot. De hoogste Rabi frequentie gemeten voor de tweede harmonische resonanties is ~ 3 MHz. Dit is bijna even hoog als in het geval van de fundamentele resonanties. De gemeten coherentietijden zijn ook van dezelfde grootte als voor de fundamentele resonanties. We hebben ook een aantal eigenschappen waargenomen die karakteristiek zijn voor tweede harmonische resonanties: kwadratische afhankelijkheid van de Rabi frequentie van de microgolf en de verdubbeling van de qubit fase ten opzichte van de fase van de aangeboden microgolf. Deze experimentele resultaten laten de haalbaarheid zien van het gebruik van tweede harmonische resonanties voor qubit manipulatie. Eén voordeel hiervan is dat een qubit gemanipuleerd kan worden door microgolven met een frequentie gelijk aan de helft van de Larmor frequentie van de qubit. Dit zou microgolf engineering versimpelen. We kunnen ook profijt hebben van de kwadratische afhankelijkheid van de Rabi frequentie wat betreft de adresseerbaarheid, aangezien deze afhankelijkheid ongewenste rotaties van spintoestanden meer voorkomt dan wanneer de fundamentele resonanties gebruikt zouden worden.

De resonantiefrequentie van de vijfde resonantie is ~ 7 GHz lager dan die van de fundamentele resonanties. De breedte van de resonantiepiek is ~ 10 keer breder dan die van de fundamentele resonanties. Eén coherente oscillatie was niet waargenomen voor deze overgang. We verklaren deze resonantie als de overgang van de spin-neer, aangeslagen vallei toestand naar de spin-op grondtoestand. We noemen deze resonantie de inter-vallei spin-flip. Het verschil in resonantiefrequentie tussen de fundamentele resonanties en deze resonantie, zeven GHz, is gelijk aan het verschil in vallei energie.

Vanwege de vallei-orbitaal interactie hebben de vallei toestanden de eigenschappen van ladingstoestanden. De bredere resonantiepiek van worden verklaard als de overgang tussen deze ladingsachtige toestanden.

Hoewel dit ons toestaat om heel interessante fysica waar te nemen, veroorzaakt een klein verschil in vallei energie verschillende problemen voor een kwantum computer: lage initialisatie betrouwbaarheid, lage controle betrouwbaarheid en een korte coherentietijd.

Aldus hebben we besloten om de elektrode voltages weer te tunen in de hoop dat we een groter energieverval tussen de vallei toestanden krijgen, zodat we elektronen alleen initialiseren in de grondtoestand en de overgangen tussen de vallei toestanden traag genoeg worden om te negeren. We hebben dit doel tot op zekere hoogte bereikt, maar niet helemaal. Met een nieuwe elektrode configuratie, was de populatie van de geëxciteerde vallei toestand afgenomen van 30% tot 20% maar niet tot 0%. De tweede harmonische resonanties en de resonantie die correspondeert met de overgang tussen vallei toestanden konden niet worden waargenomen met deze elektrode configuratie. De overgang tussen de grond vallei toestand en de geëxciteerde vallei toestand werd langzamer en we waren in staat om de coherentietijd verder te verlengen met dynamische ont koppeling. De langste coherentietijd gemeten is $400 \mu\text{s}$. We hebben ook de operatie betrouwbaarheid voor een enkele qubit gekarakteriseerd met een techniek die gebaseerd is op het uitvoeren van een aantal gerandomiseerde standaardoperaties. De hieruit volgende gemiddelde operatie betrouwbaarheid bedroeg $\sim 99\%$.

Gebaseerd op de experimentele resultaten uit dit proefschrift, komen we terug op DiVincenzo's vijf criteria. Aan alle vijf criteria is al voldaan tot op zekere hoogte, maar aan geen enkele volledig. Er is maar één qubit gerealiseerd en opschalen moet nog aangetoond worden. De initialisatie van een qubittoestand is gerealiseerd, maar de initialisatie betrouwbaarheid is niet hoog genoeg. De coherentietijd is langer dan wat is aangetoond in GaAs kwantum dots, maar zou nog meer moeten worden verlengd. Een universele set operaties met één qubit is aangetoond en de gemiddelde operatie betrouwbaarheid voldoet aan de vereiste drempelwaarde voor kwantum fouten correctie, maar een 2-qubit operatie is nog niet aangetoond. De uitlezing van een qubittoestand is gerealiseerd maar de uitleesprecisie moet verbeterd worden.

Net voordat dit proefschrift uitgebracht wordt, is een 2-qubit operatie experimenteel aangetoond in Si/SiGe kwantum dots door onze groep. De elementaire ingrediënten voor enkele elektron spins gebruikt als qubits zijn gemaakt. Om een praktische Si kwantum computer te realiseren, moeten we het aantal qubits groter maken en de betrouwbaarheid van uitlezing, initialisatie en operaties verbeteren.

Erika Kawakami
Juni 2016

PREFACE

When I was a master student in Japan, I was working on the electron spin resonance of the ensemble electrons trapped by phosphorus dopants in silicon towards the realization of Kane's quantum computer (Kane, 1998). When I asked a Ph.D. student what was the best current experiment on quantum calculation. He showed me one of Dr. Vandersypen's papers (Vandersypen *et al.*, 2001), telling me that the Shor's factoring algorithm was already experimentally demonstrated.

Thereafter I remembered Dr. Vandersypen as the man who is in the best position for the realization of the quantum computer. I found his Ph.D. thesis on arXiv (Vandersypen, 2001). I learned some basics of the quantum computation from there. I studied Matlab codes in the Appendix of his thesis and adopted them to simulate the decoherence mechanism in my own system.

One year later, even though the coherence time of electron spins is amazing in ^{28}Si (Tyryshkin *et al.*, 2012), I realized that ensemble spins in Si have the problem for scalability. I dreamed of controlling a single electron spin instead of the ensemble spins. I learned that it is possible in GaAs gate-defined quantum dots.

I had been looking for a way to obtain a Ph.D. without paying a tuition fee (in Japan, one should pay a tuition fee for Ph.D.). Luckily, I succeeded in winning a fellowship to obtain a Ph.D. degree abroad from the Japanese research foundation (Nakajima foundation). Based on my 2 years experience in France when I was a bachelor student, I preferred Europe to the other countries. But I didn't know where in Europe I want to obtain a Ph.D. I searched on Google "UK quantum computation", "France quantum information", "Germany quantum computation" etc...

When I typed "Netherlands quantum computer", the Quantum Transport group (QT) at TU Delft came to the first line. Then I found that Prof. Vandersypen is now in Delft and working on the GaAs gate-defined quantum dots. Thanks to the announcement to recruit a master student for Si/SiGe project which was on QT homepage, I understood that he was starting a new project in Si. From that day, it took me 2 weeks to write an email to ask for a Ph.D. position. I was doubtful if a professor would take seriously an email from an unknown student in a far-away country. However, finally, I summoned all my courage to write Prof. Vandersypen.

I visited Delft for the interview one week after the earthquake on the 11th of March 2011 in Japan. I was amazed by the kindness of people in QT, as well as the many dilution refrigerators lined up in the lab (though the number of fridges in QT were less than half or one third now in Qutech).

Through this thesis, I hope I can share my adventure in Delft partly with the readers.

1

INTRODUCTION

1.1. CONCEPT OF A QUANTUM COMPUTER

A quantum computer is able to solve certain problems that cannot be solved by a classical computer within a reasonable computational time. The high speed of a quantum computer relies on quantumness of quantum bits: parallelism and entanglement, which are the characteristics that classical bits do not have. Quantum parallelism uses a superposition of distinct quantum states, simply called a superposition state, and quantum entanglement means inseparability of the state of more than two particles (Nielsen and Chuang, 2011). The concept of a quantum computer was explored in 1980 when Benioff (Benioff, 1980) presented a computation using the time evolution in quantum mechanics. However, this computer does not make use of either parallelism or entanglement and thus can be completely and effectively simulated by a classical computer. Thereafter Feynman introduced his idea using the word "universal quantum simulator" in (Feynman, 1982). Quantum phenomena of more than 3 particles are difficult to simulate with classical computers. Instead, he suggested using a "universal quantum simulator" which employs more easily controllable quantum particles to simulate other quantum systems. The ideas of Benioff and Feynman were combined by Deutsch (Deutsch, 1985), where he presented a universal quantum computer using quantum parallelism. Note that using only the quantum parallelism does not directly speed up the computational time since for one measurement of a quantum state we can just obtain one output. In (Deutsch and Jozsa, 1992), Deutsch and Jozsa presented the first quantum algorithm which surpassed a counterpart classical algorithm and included the use of entanglement. This algorithm is now called Deutsch-Jozsa algorithm and inspired Shor's factoring algorithm (Shor, 1997) and Grover's searching algorithm (Grover, 2001). These two algorithms could have a great impact on daily life. Shor's algorithm could be used to break public-key cryptography and Grover's search algorithm speeds up attacks against symmetric cryptography. Another example of a practical use for Grover's search algorithm is to solve quadratically faster a nondeterministic polynomial time (NP) problem such as the traveling salesman problem.

The above-presented quantum computer is more precisely called a universal digital quantum computer. Alternatively, researchers also work on a counterpart of the conventional analog computer, a so-called quantum simulator (Brumfiel, 2012). Just like an analog computer, a quantum simulator can be tailored to a specific problem. In other words, it is a way to realize Feynman's idea without having a universal quantum computer/simulator. Nowadays one of the difficulties of building a universal quantum computer lies on having a large number of qubits (Di Vincenzo criteria (1), see the following section) and the individual control and individual read-out of each qubit (Di Vincenzo criteria (3) and (4)) at the same time, which is not necessarily required for a quantum simulator. If one finds a good combination of an object to be simulated and a physical system, a quantum simulator will become of practical use much earlier than a universal quantum computer. Analog quantum computing with optical lattices and cold atom traps already made great progress (Bloch, 2005; Bloch, Dalibard, and Nascimbène, 2012).

In this thesis, we worked towards the realization of a universal digital quantum computer. In the following sections, we discuss the physical implementation of qubits for the universal digital quantum computer.

1.2. REQUIREMENTS FOR QUBITS

The building block of a quantum computer is called a quantum bit (qubit), the counterpart of the conventional binary¹ digit (bit). A qubit (or, more precisely, the embodiment of a qubit) can be realized with a two-level quantum system. Two levels out of larger than three-level systems can be used as well as generally done in superconducting qubits (Devoret, Wallraff, and Martinis, 2004). DiVincenzo introduced five requirements which should be met by physical qubits (DiVincenzo, 1997). Experimental research on quantum computers has been a quest for physical qubits which satisfy all the requirements. We will list them here, and review what is meant.

DiVINCENZO CRITERIA

Physical qubits with which quantum computer are realized need to meet the following requirements:

(1) Scalable system with well-characterized qubits

A physical system containing a collection of qubits is needed. A qubit being "well" characterized means that the internal Hamiltonian of the qubit, the presence of and couplings to other states of the qubit, the interactions with other qubits, and the couplings to external fields that might be used to manipulate the state of the qubit are well known. Any lack of knowledge of these parameters leads to the decoherence of the qubit and infidelity in the control gates. The degree of lack of this knowledge, which appears as errors in a calculation, should be so small that it can be corrected by quantum error correction (see Layer 3 of Sec. 1.4 for quantum error correction).

¹There is no fundamental restriction to build up a quantum computer using quantum ternary digits or quantum decimal digits (there is even an advantage of using multiple states for Grover's search algorithm the experimental implementation of which is shown in (Ahn, Weinacht, and Bucksbaum, 2000)). However, the theoretical and experimental studies for a universal digital quantum computer are far behind that of quantum binary bits.

(2) Initialization to a pure state

In the same way as in classical computing, quantum computing requires that registers should be initialized to a known state before the start of computation. For quantum computing, the initialization fidelity (i.e., purity of the initialized state (Nielsen and Chuang, 2011; Sakurai, 1993), see also Sec. 4.2) is important. If the purity of the initialized state is too low, we cannot benefit from the high-speed coming from the quantumness as discussed in the case of bulk nuclear magnetic resonance (NMR) quantum computing in the next section. Besides that there is another initialization requirement: the speed of initialization. For quantum error correction, the measurement qubits should be initialized every time before measuring the state of the data qubits (Fowler *et al.*, 2012; Kelly *et al.*, 2015) in a quantum nondemolition manner (see Layer 3 of Sec. 1.4 for quantum error correction). In order to meet those needs of quantum error correction, we cannot use the natural relaxation to the ground state (T_1 relaxation) for the initialization of measurement qubits since the T_1 time usually does not become longer than the dephasing time (see the next part, T_2^* time) and the initialization for the measurement qubits should be at least faster than the T_2^* time². We should initialize measurement qubits fast enough to make quantum error correction efficient.

(3) Long coherence times

Decoherence (the loss of quantumness) happens due to the dynamics of a physical qubit in contact with its environment (more discussed in Sec. 3.3). Usually, the dephasing time (also known as the intrinsic coherence time) is the time for the quantum state to be lost by $1/e$ without any correction and is denoted by T_2^* . Decoherence degrades the control gate fidelity and memory time of qubits. The control fidelity and memory time define how much a qubit state is preserved/lost when a qubit is subject to an operation and when it is not, respectively. The required T_2^* depends on the feature of the noise causing the decoherence, the operation speed, and the effectiveness of quantum error correction.

(4) Universal set of quantum gates

An operation on a quantum state is implemented by a sequence of quantum gates. Quantum computation requires that any arbitrary unitary operator should be implemented as a quantum gate. A set of universal quantum gates is such a set of gates that any unitary operation can be expressed as a finite sequence of gates from the set. The best known universal set of quantum gates consists of a set of one-qubit quantum gates and a controlled-NOT (CNOT) gate. An example of a set of one-qubit quantum gates consist of Hadamard, and $\pi/8$ gates (also known as a T gate)³.

(5) Read-out of each qubit state

The result of a computation must be read out requiring the ability to measure specific qubits. The read-out fidelity determines, using DiVincenzo's words, quantum

²This may be not the case when the T_1 time can be rapidly changed for instance using so-called hot-spot (Srinivasa *et al.*, 2013; Yang *et al.*, 2013)

³For a universal set of fault-tolerant quantum gates, the phase gate should be added (Nielsen and Chuang, 2011).

efficiency. If the quantum efficiency is 90%, then, in the absence of any other imperfections, a computation with a single-bit output will have 90% reliability. If 97% reliability is needed, this can be achieved by copying the measurement of qubit states three times⁴. Thus there is a trade-off between the error rate permitted and the number of extra qubits required.

As is the case with the initialization, the read-out of measurement qubits is also necessary for quantum error correction. According to some studies, read-out errors for measurement qubits need to be below 10^{-3} (Knill, 2005; Steane, 2004).

For the same reason as the initialization speed, the read-out speed is also required to be as fast as to make quantum error correction efficient.

Together these have become known as the “DiVincenzo criteria. In (DiVincenzo, 2000), two more criteria were added for transmitting qubits from place to place in expectation of the need of quantum communication after the realization of quantum computer. However, they fall outside the scope of this thesis, and will be discussed only in Ch. 11.

- (6) Transfer of a quantum state between stationary and flying qubits
- (7) Transmission of flying qubits between specified locations.

1.3. SEARCHING FOR A PHYSICAL QUBIT

In this section, we would like to present a very brief history of experimental implementation of qubits, selecting only few examples of the various technologies. For more information, we recommend the review (Ladd *et al.*, 2010).

The physical implementation of qubits started with trapped ions and bulk-NMR. In ion-traps, a first controlled-NOT gate was experimentally realized in (Monroe *et al.*, 1995). In bulk-NMR, Deutsch–Jozsa algorithm was experimentally realized in (Chuang *et al.*, 1998), Grover’s search algorithm in (Jones, Mosca, and Hansen, 1998), and Shor’s factoring algorithm in (Vandersypen *et al.*, 2001).

The drawback of bulk NMR quantum computation stems from the low polarization of room temperature nuclear spins. In this system, the difficulty in the initialization of qubit state with high purity (Di Vincenzo criteria (2)) makes it impossible to have an entangled state during the calculation and downgrades the speed of calculation to the same level as a classical computer in most cases (Linden and Popescu, 2001). Another concern of bulk NMR quantum computer is scalability (Di Vincenzo criteria (1)). In bulk NMR quantum computer, nuclear spins of different atoms in a molecule are used as qubits. If you find a suitable molecule, it is straightforward to scale up to a few dozen qubits but it may be difficult to realize hundreds of qubits.

A trapped-ion quantum computer does not have the initialization problem but may also face the scalability problem, since the number of ions which can be stored within a single processing unit (trap) is limited. There are several approaches undertaken to overcome this issue: shuttling ions through space between two units (Kielpinski, Monroe, and Wineland, 2002) or a modular distributed quantum computer, where entanglement

⁴Of course, quantum cloning theorem forbids to copy of a quantum state but we can copy the QND measurement, for example, by adding two more measurement qubits.

of qubits in different modules make possible to perform a quantum gate with distant modules (Brown, Kim, and Monroe, 2016; Kim *et al.*, 2011) in the same way as quantum teleportation.

Clearly, scaling of quantum computing has been a challenging task. If one considers the scalability of semiconductor chips used for a classical computer, it is natural to think of a solid-state quantum computer, using some quantum objects defined on a chip as qubits instead of using natural atoms. However, even if nano-fabrication techniques have been well developed for classical use, it has long remained challenging to see quantum effects on a chip. For superconducting qubits, quantum effects can be observed in a relatively large object and thus fabrication techniques are less demanding than for other systems. A first coherent oscillation on superconducting qubits (charge qubits) was observed in (Nakamura, Pashkin, and Tsai, 1999). Since then, superconducting qubits have been the leading system in solid state quantum computing (Clarke and Wilhelm, 2008) (see also Ch. 1.4).

For quantum dots defined in two-dimensional electron gas (2DEG), even finer nanofabrication techniques are demanded than for superconducting qubits. In 1988, the ability to grow a defect-free interface and fabricate gate electrodes in a fine structure attained such a level that quantized conductance of point contacts was observed (van Wees *et al.*, 1988) in 2DEG. In the late 1990s, it became possible to make a quantum dot as small as it showing atomic-like electronic states (Fujisawa *et al.*, 1998; Tarucha *et al.*, 1996). A first coherent oscillation on quantum dots (charge qubits) was observed in (Hayashi *et al.*, 2003). Although it was an important step towards the implementation of a physical qubit in a semiconductor, using the magnetic moment, called spin, rather than electronic orbitals is more favorable because of its longer coherence time. In 1998, Loss and DiVincenzo (Loss and DiVincenzo, 1998) proposed using single electron spins confined in gate-defined 2DEG quantum dots as qubits. A large magnetic field is used to split the spin states by the Zeeman energy forming a two-level quantum system.

In this thesis, we chose such spin states of electrons confined in gate-defined 2DEG quantum dots to realize qubits with. In the next section, we explore more on spin qubits in quantum dots.

SPIN QUBITS IN QUANTUM DOTS

Experiments using single electron spins as qubits had first progressed greatly in gate-defined quantum dots in GaAs/AlGaAs heterostructure in the middle of 2000s. The initialization and the read-out of a spin state of an electron have been realized by a spin-to-charge conversion, either by spin-selective tunneling between a dot and a reservoir (Elzerman *et al.*, 2004) or by Pauli Spin Blockade (Koppens *et al.*, 2006, 2005). Coherent control of an electron has been achieved by either magnetic control (Koppens *et al.*, 2006) or electrical control (Nowack *et al.*, 2007). The initialization, read-out and coherent control of two-spin states were also demonstrated (Johnson *et al.*, 2005; Petta *et al.*, 2005).

In terms of using electrons spins confined in quantum dots for quantum computation, a Si/SiGe heterostructure is a more preferable material to host quantum dots. A main benefit to move from GaAs to Si is the abundance of non-zero nuclear spins. All the isotopes of Ga or As have non-zero nuclear spins, while in Si only one stable isotope

(^{29}Si), whose natural abundance is 4.67% has non-zero nuclear spin. The isotopic purification to ^{28}Si or ^{30}Si reduces the abundance of non-zero nuclear spins further. Hyperfine coupling between the electron spin and the nuclear spins in the substrate degrades the quality of coherent control and the coherence time of a qubit (de Sousa and Das Sarma, 2003). By reducing the number of nuclear spins in the substrate, the hyperfine coupling is reduced and the coherence time is made considerably longer.

Despite all the favorable conditions, Si/SiGe quantum dots had not been yet the norm because nanofabrication techniques for Si/SiGe quantum dots were less developed and making “good” quantum dots had been more challenging with Si than with GaAs. The advantage of using GaAs/AlGaAs stems from its high mobility due to its low effective electron mass and its lattice-matched heterostructure resulting in a defect-free interface. The in-plane effective mass of electrons in Si is 3 times larger than in GaAs. Thus to compensate the dot size should be smaller for Si than in GaAs. The lattice mismatch between Si and $\text{Si}_{0.7}\text{Ge}_{0.3}$ is $\approx 1.26\%$. In the late 2000s, Eriksson’s group at the University of Wisconsin overcame these problems with high-resolution lithography techniques and high-quality heterostructure growth achieving a Si/SiGe quantum dot that could be tuned to the few electron regime (Simmons *et al.*, 2007).

In this thesis, we chose electron spin states in Si/SiGe quantum dots to realize qubits with and all the experimental results shown in this thesis are done in collaboration with Eriksson group at the University of Wisconsin. Even with the current situation of being behind other systems towards the realization of a quantum computer as a whole as shown in the next section, using Si has a great advantage for the scalability of qubits, as it is the most widely used material semiconductor devices for integrated circuits.

1.4. HOW FAR ARE WE FROM THE REALIZATION OF A UNIVERSAL QUANTUM COMPUTER?

Here we introduce an example of microarchitecture of quantum computer. A layered computer architecture for quantum computing consisting of five layers is presented in (Jones, 2016; Jones *et al.*, 2012) specifically for optically controlled spins in quantum dots as a specific hardware. In this section, we review these five layers in the context of using electron spins in Si/SiGe quantum dots as qubits.

FIVE-LAYERED ARCHITECTURE FOR A UNIVERSAL QUANTUM COMPUTER

- Layer 1: Physical

In the first layer, electron spins in each quantum dot are prepared as physical qubits. All these physical qubits should meet the DiVincenzo criteria. In Ch. 7, we show a first experimental demonstration of an electron spin in a Si/SiGe quantum dot as a physical qubit. This qubit satisfies some of the DiVincenzo criteria and is promising to meet all the DiVincenzo criteria in the near future.

- Layer 2: Virtual

In the second layer, systematic errors on quantum states are reduced before going to Layer 3 (quantum error correction). Contrary to the errors to be corrected by quantum error correction, systematic errors, which have some memories, can

be corrected without measuring the system states. As naively introduced in the section of DiVincenzo criteria (3), the control gate fidelity and the memory time are important indices for quantum computation. Systematic errors affecting the control gate fidelity can be improved by composite pulses (Levitt, 1986; Vandersypen and Chuang, 2005) or dynamically corrected gates (Khodjasteh and Viola, 2009). Systematic errors affecting the memory time can be improved by dynamical decoupling⁵. In Ch. 10, we experimentally demonstrate the improvement in memory time of a SiGe spin qubit using dynamical decoupling. The techniques used in this layer are faster and simpler than quantum error correction.

- Layer 3: Quantum error correction

On the next layer, fault-tolerant logical qubits are provided using quantum error correction. In (Shor, 1995), Shor demonstrated that one logical qubit in 9 physical qubits can be corrected for arbitrary errors in a single qubit. The threshold required for the error rate before starting this type of quantum error correction (error rate of virtual qubits) is extremely low (10^{-4} - 10^{-6}). With recently invented topological quantum codes, the required threshold for the error rate is much improved, as high as 1% per operation (Dennis *et al.*, 2002; Wang, Fowler, and Hollenberg, 2011). Such types of quantum error corrections defined on two-dimensional lattices are known as surface codes (Fowler *et al.*, 2012). Differently from Layer 2, errors of qubits should be measured and corrected in post-processing. The state of qubits should be measured but it should be done in a quantum non-demolition (QND) manner (Dehollain *et al.*, 2015). Besides the data qubits which form logical qubits, we prepared measurement qubits which are used just to read out the state of data qubits in a QND manner.
- Layer 4: Logical

In the logical layer, logical qubits and logical gates needed for the quantum algorithm in the Application layer are provided. If you choose the surface code for a quantum error correction in Layer 3, since the surface code produces high-fidelity logical quantum gates but these are not universal, you should make a universal set of logical quantum gates at this layer. Using "magic states" of an ancillary logical qubit is a way to make logical quantum gates universal (Bravyi and Kitaev, 2005). However using magic states may become an overhead for the quantum calculation and thus more efficient ways to make the logical gates universal after the surface codes are expected to be developed.
- Layer 5: Application

Finally, we can execute a quantum algorithm on logical qubits provided by Layer 4. At the end of the calculations, the state of physical qubits are read out and given to classical users.

In order to achieve a fault-tolerant universal quantum computer, before completing the lower architectures, we cannot start implementing the higher architectures. In early 2016, the community of superconducting qubits and ion traps are working on the layer 3

⁵The improvement of the memory time can be regarded as the improvement of the fidelity of the identity gate.

(quantum error correction) (Devoret and Schoelkopf, 2013; Kelly *et al.*, 2015; Nigg *et al.*, 2014). We, the community of quantum dots, are working on Layers 1 and 2 (Veldhorst *et al.*, 2015b). In this thesis, we show some important achievements in Si/SiGe quantum dots on the layer 1 and 2.

1.5. THESIS OVERVIEW

In this thesis, we present experiments performed on electrons in Si/SiGe quantum dots. In particular, we achieved the experimental demonstration of the coherent control and read-out of the spin-state of an electron spin confined in a Si/SiGe quantum dot. For the manipulation of a spin-state, we employ electric dipole spin resonance (EDSR) using a microwave excitation combined with a magnetic field gradient created by micromagnets. For the read-out of a spin-state, we employed the so-called Elzerman read-out where spin-to-charge conversion is achieved by aligning Fermi level of the reservoir between two different spin states.

In Ch. 2, we review spin qubits in Si/SiGe quantum dots covering two aspects: the history of spins in Si and the history of spins in quantum dots. We also briefly review various methods to manipulate and read out spin states including the EDSR manipulation and Elzerman read-out used in this thesis.

In the first part of Ch. 3, we present the physical implementation of EDSR where we use a microwave excitation and a magnetic field gradient created by micromagnets. In the second part, we explore theoretically the mechanisms that cause decoherence for an electron in a Si quantum dot.

In Ch. 4, we give the mathematical descriptions of typical spin-qubit measurements used for the characterization of the quality of spin-qubits, including Rabi oscillations, Ramsey fringe, dynamical decoupling and randomized benchmarking.

In Ch. 5 we present the details of the three devices used for the experiments shown in this thesis. The three devices are labeled as Device A, Device B, and Device C. We also show the experimental setups, including the implementation of Elzerman read-out, pulsed microwave bursts for EDSR, and signal processing.

In Ch. 6 we present the preliminary measurements towards the spin-state manipulation and read-out using Device A and Device B. The difference between the Device A and Device B is that the former is a doped sample with an on-chip antenna and the latter is an undoped sample with the micromagnets. We measured photon-assisted tunneling on a single quantum dot using Device A and on a double quantum dot using Device B. Based on these experimental results, the potential of using Device A and B for the manipulation and read-out of an electron spin are also discussed, where we conclude that the design of Device B is more promising than Device A for this purpose.

In response to this, we started the measurements on Device C, which is very similar to Device B (an undoped sample with micromagnets). The series of main experimental results using Device C are shown in Ch. 7-10. Fig. 1.1 shows 5 measured resonance frequencies using Device C as a function of the externally applied magnetic field. Fig. 1.2 shows a schematic of energy levels as a function of external magnetic field. The blue lines and the gray lines present two different valley states. The blue dashed line and light blue dashed line in Fig. 1.2 are the EDSR transitions for the ground and the excited valley states and correspond to resonances 1 and 2 (blue open circles and light blue diamonds)

in Fig. 1.1, respectively. The experimental results on *fundamental* resonances 1 and 2 are presented in Ch. 7. Using these resonances, we perform Rabi oscillation, Ramsey fringe and Hahn echo measurements on a single electron spin.

In Ch. 8, we explore resonances 3 and 4, which was exactly half of the resonance frequency of 1 and 2, respectively (second harmonic resonance). The second harmonic resonances also allow us to perform Rabi oscillation, Ramsey fringe and Hahn echo measurements on a single electron spin.

In Ch. 9, we explore resonance 5 (black crosses in Fig. 1.1), which has a different character from the other four resonances. No coherent oscillations were observed for resonance 5. The dashed black line is the EDSR transition corresponding to this resonance. In this transition, both valley states and spin states are flipped (inter-valley spin flip).

The experiment shown in Ch. 10 is also on Device C but with a different gate configuration. With this gate configuration, we did not observe second harmonic resonances or inter-valley spin flip but only two fundamental resonances. Using one of the fundamental resonances, we characterize the quality of an electron spin in a Si/SiGe quantum as a qubit using randomized benchmarking and dynamical decoupling.

Concluding remarks, outlook and possible future directions are presented in Ch. 11.

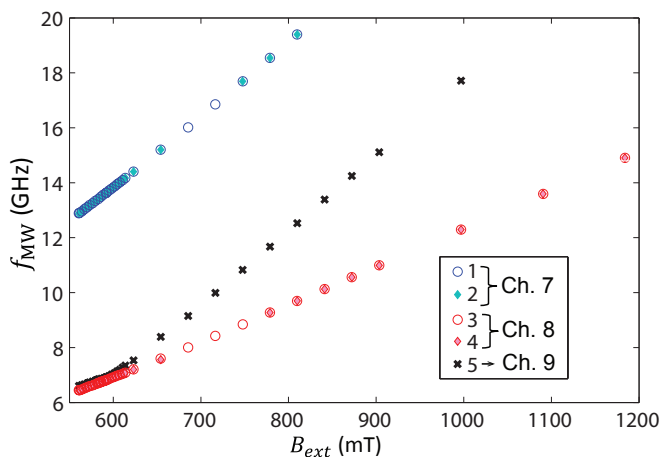


Figure 1.1: Measured 5 resonance frequencies of a single electron spin in Device C as a function of the externally applied magnetic field. These 5 resonances are explored in Ch. 7-9.

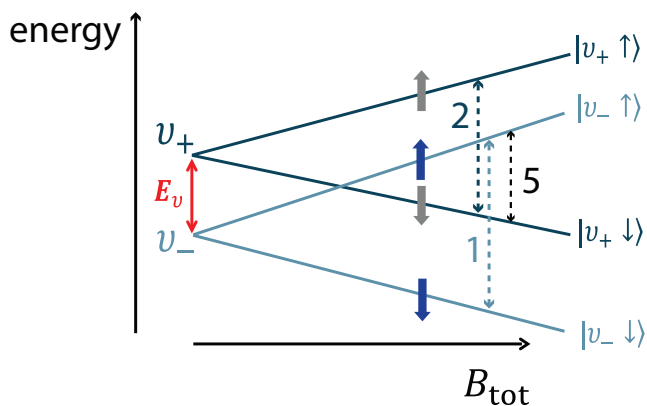


Figure 1.2: Schematic of the energy levels involved in the excitation process as a function of the total magnetic field at the electron location. The dashed arrows correspond to the 3 transitions corresponding to resonances 1, 2 and 5 (blue, light blue and black dashed arrows, respectively). E_v is the valley splitting. Resonances 3 and 4 are also attributed to the transitions represented by the dashed blue and light blue arrows but are driven at half the microwave frequency due to second harmonic process.

2

SPINS IN SILICON QUANTUM DOTS

In this chapter, we discuss the benefits and downsides of Si/SiGe quantum dots compared to similar systems (GaAs/AlGaAs quantum dots, SiMOS quantum dots, and phosphorus donor in Si) both in terms of making qubits and reviewing how we realize a qubit physically.

2.1. OVERVIEW

In this thesis, we chose electrically controlled electron spins in Si/SiGe quantum dots as qubits. Using Si has a great advantage for the scalability of qubits, as it is the most widely used material semiconductor devices for integrated circuits. Nowadays, coherent control of spin qubits in Si is realized in different ways, with single electrons confined in Si/SiGe quantum dots as we show in the later chapters in this thesis, single electrons confined in SiMOS quantum dots (Veldhorst *et al.*, 2014, 2015b), an ensemble of or single electrons bound to phosphorus dopants (Morello *et al.*, 2010; Pla *et al.*, 2012; Tyryshkin *et al.*, 2012), an ensemble of or single phosphorus dopant nuclear spins (Morton *et al.*, 2008; Muhonen *et al.*, 2014; Pla *et al.*, 2013; Simmons *et al.*, 2011b) and an ensemble of electrons trapped by surface defects (Akhtar *et al.*, 2012; Lu *et al.*, 2011).

2.2. HISTORY OF SPIN QUBITS IN SILICON

2.2.1. DOPANTS IN SILICON

Electron spin resonance experiments on electrons bound to donors in bulk Si date back to 1950s. T_2^* and T_2 of electrons bound to phosphorus donors in bulk Si were measured (Gordon and Bowers, 1958) only 8 years after Hahn echo paper was published (Hahn, 1950). Surprisingly T_2^* and T_2 measurements using isotopically enriched silicon 28 samples (^{28}Si) already appear in (Gordon and Bowers, 1958). They found that T_2^* in ^{28}Si is 14 times longer than in natural silicon ($^{\text{nat}}\text{Si}$)¹, while T_2 was extended only twice (the

¹For bulk, T_2^* was calculated from the linewidth of CW measurement: $T_2^* = \frac{\sqrt{2}\hbar}{g\mu_B\sigma_B} = \frac{1}{\sqrt{2}\pi\sigma_f}$ (Eq. 4.41) with $\sigma = \frac{\text{FWHM}}{2\sqrt{2}\ln 2}$.

concentration of ^{29}Si is not reported), claiming that “ ^{29}Si nuclei are at least partly responsible for the loss of phase memory of the spins”. Note that the idea of quantum computing comes into being there only in the 1980s.

Nuclear spin resonance experiments in Si are also explored in the same period. Direct measurements of a nuclear spin state are difficult in Si because its magnetic moment is much smaller than that of the electron (detection by conventional NMR setup can be done only by high concentration of nuclear spins). Feher (Feher, 1956) pioneered a technique to measure the state of nuclear spins via transfer of nuclear spin magnetization to electron spin magnetization and this technique is called ENDOR (electron nuclear double resonance). In (Feher, 1959), he measured the hyperfine coupling constants between an electron bound to a dopant and a Si nuclei at a specified lattice site respect to the electron for the case of phosphorus, arsenic, bismuth, and antimony as a dopant and showed an excellent agreement with a theoretical calculation.

We needed to wait 50 years until the research on electrons bound to dopants in Si started growing again. This time the researchers' interest was the application to a quantum computer. Meanwhile, human beings acquired more sophisticated techniques for isotope purification out of necessity by nuclear development. The end of the cold war made it possible to benefit from these techniques for non military purposes (Banholzer and Anthony, 1992; Itoh *et al.*, 1993). The highest purity of ^{28}Si is realized by the International Avogadro Coordination (IAC) project, which is not only intended for a quantum computer but also to define and realize the SI unit of mass by determining the Avogadro constant with a small uncertainty (Becker *et al.*, 2006; Itoh *et al.*, 2003). Tyryshkin *et al.*, (Tyryshkin *et al.*, 2012) performed the electron spin resonance experiments using one of the samples made by the IAC project (the concentration of ^{29}Si is 50ppm) and measured an extrapolated Hahn echo time of electron spins bound to phosphorus dopants² of $T_2 = 10$ s.

The ideas of Si based quantum computer introduced in late 1990 to early 2000 were based on using nuclear spins (^{29}Si nuclear spins (Itoh, 2005; Ladd *et al.*, 2002) or dopant phosphorus nuclear spins (Kane, 1998)) as qubits. Kane's original idea was using phosphorus nuclear spins as qubits and making interaction between qubits and reading out qubit states via electrons bound to phosphorus. Following this idea, the transfer of a coherent state from an ensemble of electron spins to an ensemble of nuclear spins in bulk ^{28}Si and vice versa was experimentally demonstrated using ENDOR (Morton *et al.*, 2008). An entangled state between an ensemble of electron spins and an ensemble of phosphorus nuclear spins was also demonstrated (Simmons *et al.*, 2011b). The same measurements were repeated using a single electron spin and an phosphorus nuclear spin in (Dehollain *et al.*, 2015; Muhonen *et al.*, 2014), which is an important step towards the realization of a Kane's quantum computer in terms of scalability.

²The extrapolated Hahn echo time of an ensemble of electron spins bound to phosphorus dopants means the Hahn echo time without the effect of dipolar interactions between electron spins, which is equal to the Hahn echo time which would be measured for a single electron spin for the same ^{29}Si concentration under the condition that there is no other additional noise.

2.2.2. SILICON QUANTUM DOTS

As seen in the previous section, spin qubits in Si are first realized using phosphorus dopant nuclei and electrons bound to them. Instead of using atomic confinement, electrons can be also confined at the interface of two different materials using the difference of the level of the conduction band minima of two materials. Such confined electrons are called a two-dimensional electron gas (2DEG) and such combinations of two materials are called semiconductor heterostructures.

As partly discussed in Sec. 1.3, historically the research on 2DEG is enriched using a heterostructure of GaAs and AlGaAs. The band structure of GaAs and AlGaAs is a good combination in order for a quantum well for electrons to form at its interface. Most importantly the lattice constants of the two materials are almost the same (lattice mismatch $\sim 0.1\%$), which is important to realize a smooth interface avoiding having many defects. By applying voltages to the surface gate electrodes, additional confinement potential created along the x and y directions creates a circular isolated area where an electron/electrons can stay, which is called a quantum dot (see (Hanson *et al.*, 2007; van der Wiel *et al.*, 2002) for more details of GaAs quantum dots). In the 2000s, electron spin resonance experiments in GaAs quantum dots are first realized (in several ways see also Sec. 2.4) (Koppens *et al.*, 2006; Nowack *et al.*, 2007; Piore-Ladrière *et al.*, 2008a). The advantage of using electron spins in quantum dots as qubits compared to using electrons bound to dopants is the scalability. In principle, the number of qubits can be increased on demand by changing the design of the surface gates.

The band structure of Si and SiGe is also a good combination to form 2DEG, however making quantum dots using a heterostructure of Si and SiGe has been more challenging due to the larger lattice constant mismatch between Si and SiGe as also discussed in Sec. 1.3. At the same time, it had been expected to measure a longer dephasing time T_2^* in Si quantum dots than in GaAs quantum dots as $T_2^* \sim 1 \mu\text{s}$ of an ensemble of free electron spins in 2DEG was measured (Truitt *et al.*, 2009; Tyryshkin *et al.*, 2005).

One big breakthrough made was moving from doped heterostructure to undoped heterostructure (Maune *et al.*, 2012). Compared with conventional, doped heterostructures, this technology strongly improves charge stability. Maune *et al.*, reported the electron spin $T_2^* = 360 \text{ ns}$ in Si/SiGe quantum dots for the first time, measured via two-spin coherent exchange, ~ 40 times longer in Si/SiGe quantum dots than in GaAs dots (see Table 2.1). In (Kawakami *et al.*, 2014) (Ch. 7), we measured $T_2^* = 1 \mu\text{s}$ of an electron spin state in a Si/SiGe quantum dots using electron spin resonance.

In (Veldhorst *et al.*, 2014), a quantum dot was created at the interface of Si and Si oxides. The main difference between Si/SiGe and SiMOS is the position of 2DEG with respect to the surface. For SiMOS, the 2DEG is very close to the surface and therefore the gates can more directly shape the potential landscape of electric fields. The downside of this structure is that 2DEG is positioned just beneath the silicon oxide, which contains defects and charge traps. Veldhorst *et al.*, used isotopically purified silicon (800ppm ^{29}Si concentration) and measured $T_2^* = 120 \mu\text{s}$. In (Veldhorst *et al.*, 2015b), they also demonstrated a two-qubit operation.

2.3. HOW TO REALIZE QUBITS USING QUANTUM DOTS

In this thesis, we chose and investigated the spin state of one electron confined in one quantum dot to realize a qubit. Compared to the other types of qubits described in the next paragraph, the advantage of using an electron spin as a qubit is a long coherence time and the number of physical qubits per dot. The disadvantage is the requirement of a high magnetic field and direct or indirect coupling to an oscillating magnetic field and a relatively slow manipulation.

In Si or GaAs quantum dot systems, other qubits based on the spin degree of freedom have been realized such as a singlet-triplet qubit with two quantum dots with one electron in each dot (Petta *et al.*, 2005; Shulman *et al.*, 2012), or hybrid-qubit with two quantum dots with two electrons in one dot and one electron in another dot (Kim *et al.*, 2014; Koh *et al.*, 2012). The advantage of these qubits is the non-requirement of high magnetic field and fast manipulation, but the disadvantage is relatively short dephasing time and leakage to other states.

In the following, we restrict ourselves to the discussion of the manipulation and read-out of a single electron spin as a qubit.

2.4. HOW TO MANIPULATE AND READ OUT THE SPIN STATE OF AN ELECTRON

ELECTRON SPIN MANIPULATION

Electron spin states can be manipulated by electron spin resonance (ESR) (Slichter, 1990). The transition between two spin states (spin-up state and spin-down state) can be induced by applying an oscillating magnetic field which has an orthogonal component to the external magnetic field and whose energy is equal to the energy difference between two spin states (Zeeman energy). Such an oscillating magnetic field can be generated directly or indirectly.

The first ESR experiments in GaAs were realized by the direct way (Koppens *et al.*, 2006). The oscillating magnetic field was generated by applying microwave³ to an antenna located next to the quantum dots. ESR experiments on an electron spin bound to a phosphorus dopant in Si (Pla *et al.*, 2012), and on single electron spins in SiMOS quantum dots (Veldhorst *et al.*, 2014, 2015a) were realized in the same way.

In the indirect way, microwave is applied to one of the gate electrodes, which is also used to apply d.c. voltage to make a confinement potential, and a local oscillating electric field is induced at the open end of the transmission, which leads to the modulation of the dot position. When there is some coupling to mix the spin and charge degrees of freedom, an oscillating electric field works like an oscillating magnetic field on the electron in the dot. With the charge state being modulated by a local oscillating electric field, a spin state is flipped. This method, operating electron spins by electric fields, is called electric dipole spin resonance (EDSR; its mechanism is further discussed in Sec. 3.1) and the first experimental realization on electrons in quantum dots was achieved by using spin-orbit coupling in GaAs to mix the spin and charge degrees of freedom (Nowack

³in our research fields, electromagnetic radiation with frequencies between 1 and 100 GHz (300 and 3 mm in wavelength) is called microwave

et al., 2007), and later by using the magnetic field gradient created by the micromagnets (Pioro-Ladrière *et al.*, 2008a).

Exploiting spin-orbit coupling is experimentally the simplest approach as it does not require any additional fabrication of a local micromagnet or an antenna. However, spin-orbit coupling is too weak in Si/SiGe, and thus a local micromagnet or an antenna is required. The downside of using an antenna over a micromagnet is the heating by the current running through the antenna, while when using micromagnet, a spin qubit becomes subject to magnetic field noise converted from charge noise via the magnetic field gradient.

In addition to the ingredients for the manipulation of one electron spin, we should also consider the independent control of each electron spin in multiple quantum dots (addressability), i.e., the Zeeman energy of each electron should differ. In order to separate the Zeeman energies, the g -factor of each electron or the local magnetic field felt by each electron should be different. The g -factor can be modulated by Stark-shift (Veldhorst *et al.*, 2014) but a huge electric field is required to achieve enough change to be sufficient for addressability. The magnetic field gradient can be produced by the micromagnets (thus the magnetic field gradient created by the micromagnets can be used both for the manipulation of one electron spin and the addressability) or d.c. current running through the antenna.

In this thesis, we first chose to apply microwave to the antenna to generate an oscillating magnetic field directly and to apply d.c. current to generate a magnetic field gradient. In the experiments presented in Ch. 6 we showed that the magnetic field gradient created by d.c. current running through the antenna is limited to $1 \mu\text{T}/\text{nm}$ due to Joule heating, which might be a problem for the addressability.

We secondly chose to apply microwave to one of the gate electrodes to generate an oscillating magnetic field indirectly with the help of a magnetic field gradient created by the micromagnet. The magnetic field gradient created by micromagnets can reach $1 \text{ mT}/\text{nm}$ (Appendix G), which is 1000 times larger than what is created with d.c. current through the antenna and this gradient is large enough for addressability (Appendix E.1.2).

ELECTRON SPIN READ-OUT

To read out the electron spin state, two methods can be used. The spin state of an electron confined in a GaAs quantum dot is first detected in a double quantum dot tuned to the so-called Pauli spin blockade (PSB) regime (Brunner *et al.*, 2011; Koppens *et al.*, 2006; Nowack *et al.*, 2007; Ono *et al.*, 2002). In this regime, two-electron spin singlets can be distinguished from spin triplets.

Another way to detect a spin state is using a spin to charge conversion by aligning the Fermi level of the reservoir between the spin-ground state and the spin-excited state (Elzerman *et al.*, 2004). We employed this method and details are further discussed in Sec. 5.3.2.

2.5. COMPARISON BETWEEN GAAS QUBITS SI SPIN QUBITS

In this section, we compare electrons confined in Si/SiGe quantum dots, electrons confined in GaAs/AlGaAs and in SiMOS quantum dots, and an ensemble of or single electrons bound to phosphorus dopant.

2.5.1. NUCLEAR SPINS IN HOST MATERIAL

As discussed in Sec. 3.3, nuclear spins in the substrate induces the decoherence on an electron spin. Thus the nuclear spins of the host material is a nuisance for the realization of a quantum computer. Amongst three stable isotopes of silicon, ^{28}Si , ^{29}Si and ^{30}Si , only ^{29}Si has non-zero nuclear spin and the natural abundance of ^{29}Si is 4.7%, while all the isotopes of Ga or As have non-zero nuclear spins. The isotopic ratio of ^{29}Si in Si substrate can be further decreased. In the first row of Table 2.1, we compared the dephasing time T_2^* of electrons confined in GaAs/AlGaAs quantum dots, in Si/SiGe quantum dots and in SiMOS quantum dots and of an ensemble of or single electrons bound to phosphorus dopants. As a whole, T_2^* in Si is longer than in GaAs and is further extended by isotopic purification.

2.5.2. BAND STRUCTURE

Contrary to GaAs, the conduction band minima of Si are not at a symmetric point. Due to this fact, Si shows rich valley physics but those may turn out to be obstacles for the realization of a quantum computer.

ELECTRONS IN BULK SI

The conduction band minima of Si are along the Δ directions, $\sim 85\%$ of the way to the X point, which results in 2 significant different characteristics in Si compared to GaAs: indirect band gap and valley degeneracy.

Si has an indirect band gap, while GaAs has a direct band gap making it more efficient to transfer spin state to photons for GaAs spin qubits (Fujita *et al.*, 2015).

At the conduction band minima of Si, there are six Δ -directions and therefore six equivalent energy minima (called valleys), while there is no degeneracy state at the conduction band minima of GaAs.

Fig. 2.1(b) shows that the constant energy surfaces at the conduction band minima of Si are ellipsoidal due to a different effective mass along the longitudinal direction from the transverse direction ($m_T \approx 0.98m_0$ and $m_L \approx 0.19m_0$) (Davies, 1998).

2DEG IN SI

By forming 2DEG, the 6-fold degenerate states are lifted as follows (see also Fig. 2.1(b)).

- **strained Si** Due to the lattice mismatch between Si and a SiGe alloy, a Si quantum well is strained in the plane of the Si quantum well. This strain makes four of the six conduction band valleys ($\pm k_x$ and $\pm k_y$) lifting upward and two of them ($\pm k_z$) downward.
- **quantum well (flat interface)** The remaining two-fold degeneracy on the ground valley state is also lifted due to the coupling between two valley states ($\pm k_z$) being caused by the sharp potential difference between the conduction band minima of Si and a SiGe alloy (Scarlino, 2016; Schäffler, 1997). The energy difference between two lowest valley

states is called valley splitting E_V . For the flat interfaces, the valley splitting is predicted to be $E_V \sim 0.1-0.3$ meV.

- **disordered interface** This valley splitting at the previous point can be decreased by defects or heterostructure interface disorder. In reality, the interface between Si and a SiGe alloy is not completely flat as shown in Fig. 2.1(c) (Scarolino, 2016; Zwanenburg *et al.*, 2013). If the electron wave function is spread over more than one atomic step, the different energy levels of the valley states which are defined at each atomic step are averaged out, which results in a smaller valley splitting than without atomic steps. This coupling between the z behavior and x, y behavior is called valley-orbit coupling.
- **perpendicular electric field** Finally perpendicular electric field E_{\perp} also couples two valley states. It is experimentally demonstrated that the valley splitting is controlled (decreased and increased) by the perpendicular electric field E_{\perp} (Takeda, 2015; Yang *et al.*, 2013).

If the resulting valley splitting is small compared to the electron temperature, it leads to the thermal occupation of the excited valley state, or leakage into the excited valley state during qubit manipulation as discussed in Ch. 7.

ELECTRONS BOUND TO PHOSPHORUS DOPANT IN SI

For the electrons bound to phosphorus dopant in Si, the ground state has no valley degeneracy but the 1st excited state has 3-fold degeneracy (Fig. 2.1(d)), which makes the exchange interaction between 2 electrons nontrivial (Tosi *et al.*, 2015; Zwanenburg *et al.*, 2013).

2.5.3. SPIN-ORBIT INTERACTION (SOI)

There are two types of SOI, Rashba-SOI and Dresselhaus-SOI. They change the direction of the spin operator differently depending on the crystallographic direction of the electron momentum and their amplitudes are denoted by α and β , respectively (Hanson *et al.*, 2007; Nowack, 2009; Winkler, 2003). Both types of SOI are much smaller in Si than GaAs. On the one hand this leads to much longer spin relaxation time T_1 in Si than in GaAs. The spin relaxation time of an electron spin in Si/SiGe quantum dot is measured typical timescales upwards of 1 ms (Simmons *et al.*, 2011b). On the other hand, SOI can also be used to control the spin qubit through electric dipole spin resonance as discussed in Sec. 2.4. In GaAs $\beta = 10^3 - 3 * 10^3$ m/s and α can be $\approx \beta$ or bigger depending on the structure (Hanson *et al.*, 2007). α in Si 2DEG is measured to be 6 m/s (Wilamowski *et al.*, 2002). Hao *et al.* (2014); Tahan and Joynt (2014); Yang *et al.* (2013) reported $\beta - \alpha \sim 15-60$ m/s in Si quantum dots.

2.5.4. G-FACTOR

Si has a g-factor that is roughly 5 times larger than GaAs. Thus the magnetic field required to obtain a given Zeeman splitting is 5 times smaller. Small magnetic fields require less magnet engineering. In addition to that, with the same amplitude of an oscillating magnetic field felt by an electron, the Rabi oscillation is 5 times larger in Si. This statement simply turns into a benefit of Si when a local antenna is used to generate an oscillating magnetic field. However, when a micromagnet is employed, it is not that simple. The

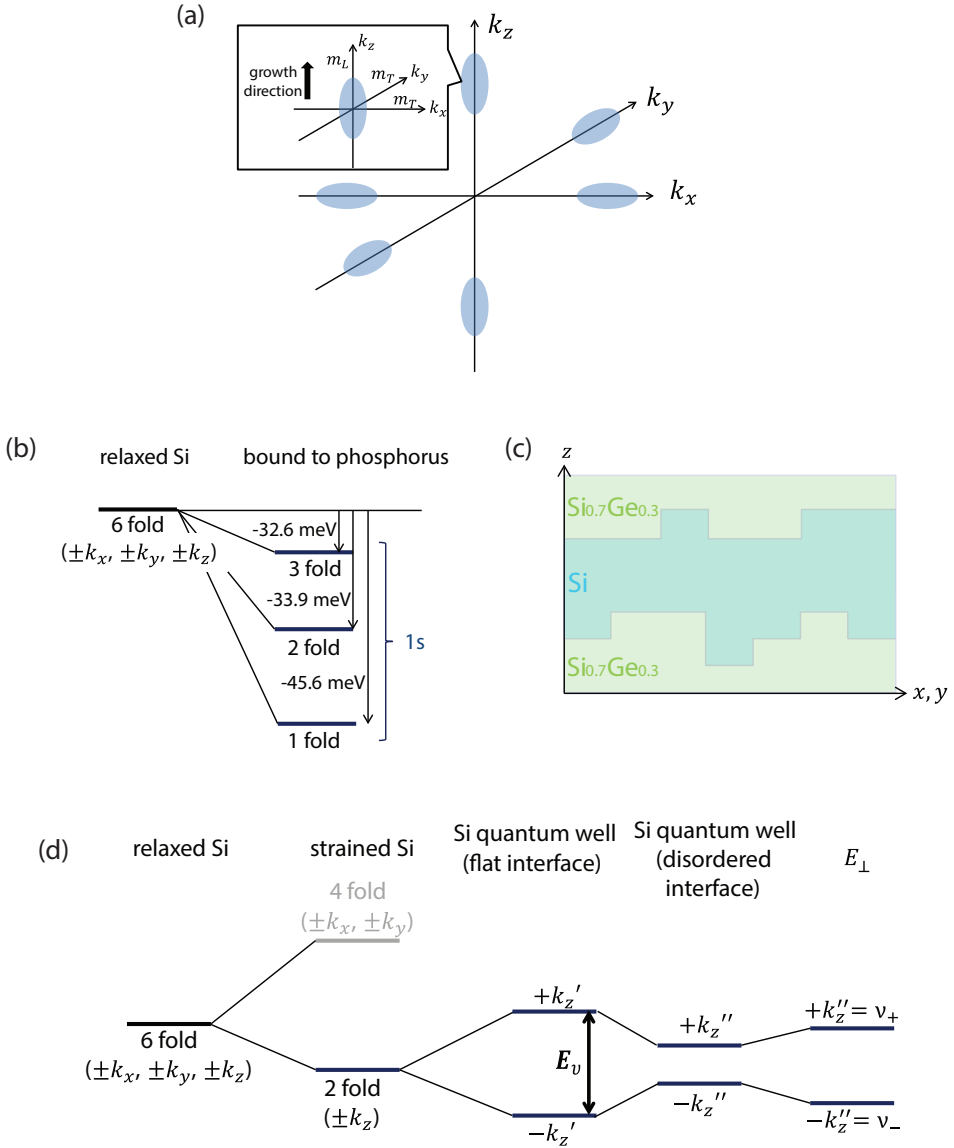


Figure 2.1: (a) Constant energy surfaces for the six equivalent valleys. The bulk dispersion relation around minima can be described by $\epsilon(\mathbf{k}) = E_c + \frac{\hbar^2}{2} \left[\frac{(k_L - k_0)^2}{m_L} + \frac{k_T^2}{m_T} + \frac{k_T^2}{m_T} \right]$ where E_c is a minimum conduction band energy and $k_0 = 0.85 \frac{2\pi}{a_0}$ and thus the constant energy surfaces show ellipsoidal shapes. The electron confined in a quantum dot stays in the ground valley state (k_z direction) and thus the effective mass considered for an electron in a quantum dot is m_L . (b) Lifting of six-fold valley degeneracy electrons in Si 2DEG. See the text for details. (c) Si sandwiched by relaxed $\text{Si}_{0.3}\text{Ge}_{0.7}$ alloys with atomic steps at the interface. The lattice constant of bulk Si is 0.5431 nm and Si quantum well width is typically ~ 10 nm. Here the atomic step size is drawn with exaggeration. One can define each valley splitting for each atomic step. (d) Lifting of six-fold valley degeneracy of electrons bound to phosphorus dopants. Due to the strong confinement by the phosphorus dopant, the degeneracy is broken. The lowest-energy valley state is non-degenerate, which is 11.7 meV lower than the first valley excited states.

amplitude of an oscillating magnetic field is determined by how far one can modulate the position of an electron by applying an oscillating electric field and it is harder to move an electron in Si because of a larger effective mass (discussed below).

2.5.5. EFFECTIVE MASS/CONFINEMENT

The effective mass of electrons in Si is 3 times larger than in GaAs. The tunnel barriers between dots are therefore more sensitive to small changes in the applied gate voltages, which makes it harder to tune the dots to a few-electron regime keeping an appropriate tunnel barrier. This problem may be overcome by making the dot size smaller. The confinement of an electron to a small region also helps to have a large valley splitting for Si based quantum dot. However, it demands more techniques on fabrication. So far GaAs based structures have been able to create the largest number of dots due to its high tunability. Progress in Si-fabrication will probably enable many dots in Si as well in the near future.

property	GaAs quantum dot	Si quantum dot	phosphorus donor in Si
T_2^*	30 ns (1e) (Koppens <i>et al.</i> , 2007) 10 ns (ST) (Petta <i>et al.</i> , 2005) 40 ns (ST) (Bluhm <i>et al.</i> , 2010b)	$\approx 1 \mu\text{s}$ (1e 4.67% Si/SiGe) (Kawakami <i>et al.</i> , 2014) (Ch. 7) 120 μs (1e 800 ppm SiMOS) (Veldhorst <i>et al.</i> , 2014) 360 ns (ST 4.67% Si/SiGe) (Maune <i>et al.</i> , 2012)	55 ns (1e 4.67%) (Pla <i>et al.</i> , 2012) 268 μs (1e 800ppm) (Muhonen <i>et al.</i> , 2014) 75 ns (ensemble 4.67%) (Tyryshkin <i>et al.</i> , 2003) 6 μs (ensemble 50 ppm) (Abe <i>et al.</i> 2010; Tyryshkin <i>et al.</i> 2011)
SOI	$10^3 - 3 \cdot 10^3$ m/s	~ 10 m/s	
T_1	$\approx 1-100$ ms	≈ 1 s (at B=2T)	≈ 1 s (at B=2T)
g	0.2-0.4	≈ 2	≈ 2
m^*	$0.067 m_0$	$0.19 m_0$ (in plane)	
r	≈ 100 nm	≈ 50 nm for Si/SiGe ≈ 20 nm for SiMOS	2.5 nm
bandgap	direct	indirect	indirect
valley degeneracy	no degeneracy	there can be 2-fold valley degeneracy states on the ground states	3-fold valley degeneracy states on the 1st excited states

Table 2.1: Comparison of various properties of electron spins amongst GaAs quantum dots, Si quantum dots, and phosphorus donors in Si. Typical or measured values of the intrinsic dephasing time T_2^* , spin-orbit interaction (SOI), the longitudinal relaxation time T_1 , g -factor and the effective mass m^* for an electron/electrons confined in GaAs quantum dots and Si quantum dots and bound to a phosphorus dopant/phosphorus dopants. The typical diameter of GaAs and Si quantum dots and Bohr radius of phosphorus in silicon r . In the row of T_2^* , ...ppm or ...% indicates the concentration of ^{29}Si . “1e” stands for an electron spin as a qubit. “ST” stands for a singlet-triplet qubit. “ensemble” stands for an ensemble of electron spins as a qubit. r is the diameter of dot or Bohr radius of phosphorus in silicon.

3

EDSR AND DECOHERENCE

In this chapter, we introduce the mechanism of electric dipole spin resonance (EDSR), which we chose as a method to manipulate a quantum state of an electron spin confined in a quantum dot as presented in Sec. 2.4. In order to perform EDSR, we make use of the magnetic field gradient created by the micromagnets. In the second part of this chapter, we present the numerically calculated stray magnetic field created by the micromagnets. From this calculation, we estimate the stray magnetic field at the dot position for the experiments in Ch. 7, Ch. 8 and Ch. 10. In the third part, we discuss the decoherence of the electron spin induced by its coupling with the surrounding nuclear spins.

3.1. ELECTRIC DIPOLE SPIN RESONANCE

As presented in Sec. 2.4, electric dipole spin resonance (EDSR) is a method to manipulate an electron spin state, which is mixed with a charge state due to some coupling between the spin and charge degrees of freedom, by electrically driving the charge property of the electron. The mechanism of EDSR with a micromagnet was first presented by (Tokura *et al.*, 2006) for a 1D quantum dot. The theory for a 2D quantum dot is essentially the same and presented in (Pioro-Ladrière *et al.*, 2008b) together with the experimental reviews on GaAs quantum dots with micromagnets. In the next two sections, by revisiting this mechanism, we derive the familiar Hamiltonian for ESR (Eq. 3.14).

3.1.1. MIXING SPIN AND CHARGE STATES

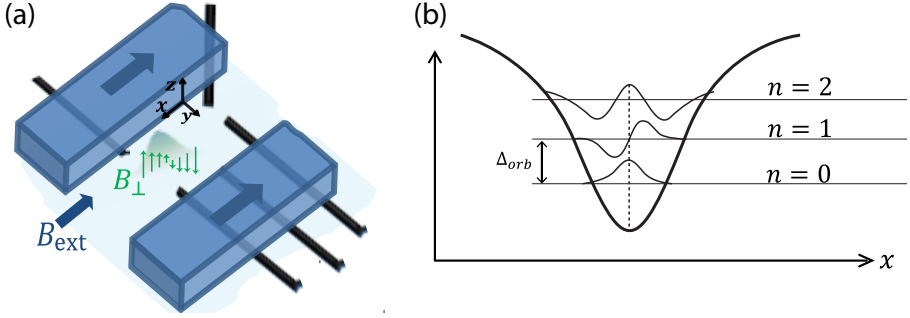


Figure 3.1: (a) Conceptual device image showing two micromagnets (blue rectangles) magnetized along the same direction as the external magnetic field B_0 (along the x axis). The black thick lines represent the gate electrodes to which d.c. voltage and microwave can be applied. More details on the device are found in Sec. 5.3. The green arrows represent the magnetic field gradient created by the micromagnets B_{\perp} along the z axis. The magnetic field gradient is assumed to be created along the z axis and its amplitude varies along the x axis. The green region in the middle of the figure represents the electron wavefunction spread, of which the size is scaled around 100 times larger than the micromagnets and the gate electrodes. (b) A symmetric confinement potential for a 2-dimensional quantum dot is approximated to be a harmonic potential. The electron wavefunctions of the first, second and third orbital states are illustrated along the x axis. Since we assume a symmetric confinement, the expectation value of the position is 0: $\langle n=0|x|n=0\rangle = \langle n=1|x|n=1\rangle = 0$ and the transition dipole moment from the ground state ($n=0$) to the first excited state ($n=1$) is $\langle n=0|x|n=1\rangle = \frac{l_{orb}}{\sqrt{2}}$ where l_{orb} is the typical dimension of the quantum dot and $l_{orb} = \hbar\sqrt{\frac{2}{m\Delta_{orb}}}$ with $\Delta_{orb} = \hbar\omega_h$ the orbital level spacing.

The static Hamiltonian, the Hamiltonian without applying an oscillating electric field for an electron confined in a symmetric potential subjected to a magnetic field gradient created by the micromagnets, is written as

$$H^{\text{stat}} = \frac{1}{2m}(p_x^2 + p_y^2) + \frac{m\omega_h^2}{2}(x^2 + y^2) - \frac{1}{2}g\mu_B B_0 \sigma_x^s - \frac{1}{2}g\mu_B \frac{dB_{\perp}}{dx} x \sigma_z^s, \quad (3.1)$$

where $p_{x,y}$ are the momentum operators, x, y are the position operators, m is the effective electron mass and ω_h is the classical frequency of the harmonic potential. As shown in Fig. 3.1(a), we assumed that an external magnetic field B_0 is applied along the x axis, the stray magnetic field created by the micromagnet has a component only along the z axis of which amplitude is 0 at the dot position ($B_0 \parallel x$, $B_{\perp} \parallel z$, $B_{\perp}(x=0, y=0)=0$, and $B_{\parallel}=0$, where B_{\perp} and B_{\parallel} are the stray magnetic fields perpendicular and parallel to the external magnetic field, respectively), and varies along the x axis for simplicity ($B_{\perp}(x) = \frac{dB_{\perp}}{dx} x \vec{z}$). We also assumed that the position of the electron is modulated along the x axis. σ_i^s are the Pauli spin matrices and $\sigma_x^s = |+\rangle\langle+| - |-\rangle\langle-|$ and $\sigma_z^s = |+\rangle\langle-| + |-\rangle\langle+|$, where $|+\rangle$ is the spin-up state and $|-\rangle$ is the spin-down state. The first and second term of Eq. 3.1 represent the harmonic oscillator potential with ω_h the classical frequency (Fig. 3.1(b)). The third and fourth term are the Zeeman splitting due to the external magnetic field and due to the stray field created by the micromagnets,

respectively. In (Tokura *et al.*, 2006) the approximated eigenstates of Eq. 3.1 are derived with perturbation approach taking the last term of Eq. 3.1 as a small term. Here we take a different path. We restrict ourselves to consider only the lowest two orbital states $|0\rangle$ and $|1\rangle$. In most cases of the experiments on electrons confined in Si quantum dots, the valley splitting is relatively low compared to the orbital level spacing and the valley and orbital degrees of freedom are mixed due to the valley-orbit coupling (and we call these mixed states valley-orbit states). Thus, strictly speaking, we should consider valley, orbital, and spin states. Their Hamiltonian can be written down from first principles but it is too complex to be treated here. For the experiments shown in this thesis, the valley splitting (or the energy difference between the ground valley-orbit state and the first excited valley-orbit state) is lower than the Zeeman splitting and the energy levels of higher valley-orbit states are high enough to make it possible to consider the lowest two valley-orbit states (four lowest states as shown in Fig. 3.2 taking into account of a spin degree of freedom) energetically isolated (see also Ch. 9). A similar approach is used in (Tokura, Kubo, and Munro, 2013) for the case where there are two minima in a confinement potential of a GaAs quantum dot.

Under these assumptions, Eq. 3.1 can be rewritten as

$$H^{\text{stat}} = \frac{1}{2}\Delta_c\sigma_z^c - \frac{1}{2}\epsilon_{z0}\sigma_x^s - \frac{1}{2}\Lambda\sigma_x^c\sigma_z^s, \quad (3.2)$$

with $\sigma_z^c = |1\rangle\langle 1| - |0\rangle\langle 0|$ and $\sigma_x^c = |0\rangle\langle 1| + |1\rangle\langle 0|$, where $|0\rangle$ represents the ground valley-orbit state and $|1\rangle$ represents the first excited valley-orbit state and the splitting between these two states is represented by Δ_c . The index c stands for charge since both valley and orbital states are related to the charge characteristic of an electron. Nevertheless, in this section, we assume that $|c=0\rangle$ and $|c=1\rangle$ are pure orbital states and a symmetric confinement ($\Delta_c = \Delta_{orb}$). In Sec. 3.1.3, an asymmetric confinement and mixing between valley states and orbital states are introduced. $\epsilon_{z0} = g\mu_B B_0$ is the Zeeman splitting due to the external magnetic field and

$$\Lambda = g\mu_B \frac{dB_{\perp}}{dx} \langle c=0|x|c=1\rangle = g\mu_B \frac{dB_{\perp}}{dx} \frac{l_c}{\sqrt{2}}, \quad (3.3)$$

represents the strength of the mixing between a spin state and an orbital state. Here we assume that $|c=0\rangle$ and $|c=1\rangle$ are pure orbital states and thus $\langle c=0|x|c=1\rangle = \langle n=0|x|n=1\rangle$ and $l_c = l_{orb}$. Furthermore, due to the assumption of a symmetric confinement, the diagonal elements are 0:

$$\langle c=0|x|c=0\rangle = \langle n=0|x|n=0\rangle = 0, \quad \langle c=1|x|c=1\rangle = \langle n=1|x|n=1\rangle = 0. \quad (3.4)$$

The eigenstates of the first and second term in Eq. 3.2 are $|cs\rangle = |0-\rangle, |0+\rangle, |1-\rangle, \text{ and } |1+\rangle$. The third term mixes $|0-\rangle$ and $|1+\rangle$, and $|0+\rangle$ and $|1-\rangle$.

Differently from Eq. 3.1, we can obtain the exact eigenstates of Eq. 3.2, which we denote by $|0'-' \rangle, |0'+ \rangle, |1'-' \rangle, \text{ and } |1'+ \rangle$. Eq. 3.2 can be diagonalized by the unitary transformation and the diagonalized Hamiltonian can be written as

$$H^{\text{stat}} = -\frac{1}{4} \left(\sqrt{(\Delta_c + \epsilon_{0z})^2 + \Lambda^2} - \sqrt{(\Delta_c - \epsilon_{0z})^2 + \Lambda^2} \right) \sigma_x^{s'} - \frac{1}{4} \left(\sqrt{(\Delta_c + \epsilon_{0z})^2 + \Lambda^2} + \sqrt{(\Delta_c - \epsilon_{0z})^2 + \Lambda^2} \right) \sigma_z^{c'}, \quad (3.5)$$

where $\sigma_i^{s'}$ is the Pauli matrix of spin-like state, $\sigma_i^{c'}$ is the Pauli matrix of orbit-like state, $\sigma_x^{s'} = |+\rangle\langle +'| - |-\rangle\langle -'|$ and $\sigma_z^{c'} = |1'\rangle\langle 1'| - |0'\rangle\langle 0'|$. The splitting between two spin-like states (renormalized Zeeman energy) is

$$\epsilon_z = \frac{1}{2} \left(\sqrt{(\Delta_c + \epsilon_{0z})^2 + \Lambda^2} - \sqrt{(\Delta_c - \epsilon_{0z})^2 + \Lambda^2} \right). \quad (3.6)$$

Under the assumption¹ that $\Delta_c \gg \epsilon_{0z}, \Lambda$, Eq. 3.6 is approximated to be $\epsilon_z \approx \epsilon_{0z} + \Delta\epsilon_z$ with

$$\Delta\epsilon_z = -\frac{1}{4} \frac{2\Lambda^2}{\Delta_c^2 - \epsilon_{0z}^2} \epsilon_{0z}. \quad (3.7)$$

The renormalization in Zeeman energy presented in Eq. 3.7 is the same as the renormalization in Zeeman energy to the second order being calculated, when taking the last term of Eq. 3.1 as the perturbation term and considering all the orbital levels of harmonic potential as presented in (Tokura *et al.*, 2006).

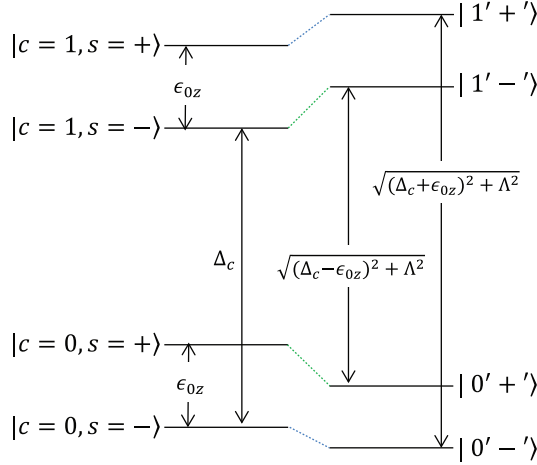


Figure 3.2: Energy diagram of valley-orbit ($c = 0, 1$) and spin ($s = +, -$) states in the case of $\epsilon_{0z} < \Delta_c$ showing the four lowest-energy eigenstates without mixing due to the magnetic field gradient on the left and with mixing on the right. See the text for more details.

3.1.2. MICROWAVE EXCITATION

The microwave excitation generates an a.c. electric field, and we assume that it makes the electron oscillate back and forth along the x axis. The Hamiltonian of the microwave excitation is written as

$$H(t) = eE^{AC} x \cos(\omega_{MW} t + \phi), \quad (3.8)$$

¹ In fact, the assumption $\Delta_c \gg \epsilon_{0z}, \Lambda$ or $\Delta_c \gg \epsilon_z$ is not correct for the experiments shown in this thesis. In Sec. 9.S1-9.S2, we treat the general case including when we cannot take this assumption.

with E^{AC} the amplitude of the electric field for an electron inside the dot, ω_{MW} the microwave carrier frequency and ϕ the microwave phase. As in Eq. 3.2, we restrict ourselves to consider only the lowest orbital states. Eq. 3.8 is rewritten as

$$H(t) = eE^{AC} \frac{l_c}{\sqrt{2}} \sigma_x^c \cos(\omega_{MW}t + \phi). \quad (3.9)$$

Under the assumption¹ that $\Delta_c \gg \epsilon_z$, we can consider the lowest two states $|0'-'\rangle$ and $|0'+'\rangle$ energetically isolated states and we can discard $|1'-'\rangle$ and $|1'+'\rangle$ at this point. Thus Eq. 3.9 can be approximated to be

$$H(t) = \frac{1}{2} \tilde{\epsilon}_1 \cos(\omega_{MW}t + \phi) \sigma_z^{s'}, \quad (3.10)$$

with

$$\tilde{\epsilon}_1 = eE^{AC} \frac{l_c}{\sqrt{2}} \langle 0'+'| \sigma_x^c | 0'-'\rangle \approx eE^{AC} 2\Lambda \frac{l_c}{\sqrt{2}} \frac{\Delta_c}{\Delta_c^2 - \epsilon_{0z}^2}, \quad (3.11)^2$$

and Eq. 3.5 can be approximated to be

$$H^{\text{stat}} = -\frac{1}{2} \epsilon_z \sigma_x^{s'}. \quad (3.12)$$

Then the total Hamiltonian becomes

$$\begin{aligned} H = H^{\text{stat}} + H(t) &= -\frac{1}{2} \epsilon_z \sigma_x^{s'} + \frac{1}{2} \epsilon_1 \cos(\omega_{MW}t) \sigma_z^{s'} \\ &= -\omega_0 S_z + 2\omega_1 \cos(\omega_{MW}t + \phi) S_x, \end{aligned} \quad (3.13)^3$$

with $\omega_0 = \epsilon_z/\hbar$ and $\omega_1 = \tilde{\epsilon}_1/2\hbar$. Here we take $S_z = \hbar \frac{\sigma_z^{s'}}{2}$ and $S_x = \hbar \frac{\sigma_x^{s'}}{2}$ without loss of generality. The x axis and the z axis are swapped because in most literature on magnetic resonance, the quantization axis is taken along the z axis (see also Eq. A.2).

The total Hamiltonian on the rotating frame with microwave frequency ω_{MW} becomes

$$H_R = (\omega_{MW} - \omega_0) S_z + \omega_1 (S_x \cos \phi - S_y \sin \phi), \quad (3.14)$$

with $\omega_1 = \frac{g\mu_B B^{AC}}{\hbar}$, where B^{AC} is the amplitude of an effective oscillating magnetic field:

$$B^{AC} = \frac{1}{2} eE^{AC} \frac{dB_{\perp}}{dx} l_c^2 \frac{\Delta_c^2}{\Delta_c - \epsilon_{0z}^2} \sim \frac{1}{2} eE^{AC} \frac{dB_{\perp}}{dx} \frac{l_c^2}{\Delta_c}. \quad (3.15)$$

We notice that the Rabi frequency ω_1 is proportional to the magnitude of the magnetic field gradient $\frac{dB_{\perp}}{dx}$, to⁴ l_c^2/Δ_c and to the amplitude of the oscillating electric field E^{AC} .

²The diagonal elements are 0: $\langle 0'+'| \sigma_x^c | 0'+'\rangle = \langle 0'-'| \sigma_x^c | 0'-'\rangle = 0$ since $\langle +|- \rangle = 0$ and $\langle 0| \sigma_x^c | 0 \rangle = \langle 1| \sigma_x^c | 1 \rangle = 0$.

³The 2 in the denominator of $\omega_1 = \tilde{\epsilon}_1/2\hbar$ comes from the fact that a linearly polarized field can be considered as a superposition of a right-hand and a left-hand rotating circularly polarized field and only the right-hand polarized field get involved in the resonant interaction with the electron when the rotating wave approximation is valid (Schweiger and Jeschke, 2001). See also Appendix B.4 and Appendix B.5.

⁴Here we assume that $|c=0\rangle$ and $|c=1\rangle$ are pure orbital states and thus $l_c^2/\Delta_c = l_{orb}^2/\Delta_{orb} \propto \frac{1}{\omega^2}$ since $\Delta_{orb} =$

$\hbar\omega_h$ and $l_{orb} = \sqrt{\frac{2\hbar}{m\omega_h}}$.

The effective magnetic field presented in Eq. 3.15 is the same as the effective magnetic field being calculated by taking the last term of Eq. 3.1 as the perturbation term and considering all the orbital levels of harmonic potential as presented in (Tokura *et al.*, 2006).

3.1.3. NON-CONVENTIONAL ELECTRIC DIPOLE SPIN RESONANCE

In the previous section, we assume that the confinement potential is symmetric ($|c=0\rangle$ and $|c=1\rangle$ are pure orbital states, and the magnetic field gradient which is parallel to the external magnetic field is 0. In this case, according to Eq. 3.2 and Eq. 3.9, the full Hamiltonian becomes

$$H^{\text{stat}} + H(t) = \frac{1}{2}\Delta_c\sigma_z^c - \frac{1}{2}\epsilon_{z0}\sigma_x^s - \frac{1}{2}\Lambda\sigma_x^c\sigma_z^s + eE^{AC}\frac{l_c}{\sqrt{2}}\sigma_x^c\cos(\omega_{\text{MW}}t + \phi). \quad (3.16)$$

In this section, we introduce an asymmetric confinement, valley states, finite parallel field gradients to Eq. 3.16, which allows non-conventional electric dipole spin resonance such as a second harmonic electric dipole spin resonance (Ch. 8) and an inter-valley spin-flip resonance (Ch. 9).

ASYMMETRIC CONFINEMENT

First, we assume that $|c=0\rangle$ and $|c=1\rangle$ are pure orbital states and the confinement potential is asymmetric as shown in Fig. 3.3(a). In this case, the diagonal elements are non-zero:

$$\langle c=1|x|c=1\rangle = \langle n=1|x|n=1\rangle = -\langle c=0|x|c=0\rangle = -\langle n=0|x|n=0\rangle = \frac{\delta x}{\sqrt{2}}, \quad (3.17)$$

and $\Lambda\sigma_x^c\sigma_z^s$ in the third term and $\frac{l_c}{\sqrt{2}}\sigma_x^c$ in the fourth term in Eq. 3.16 should be replaced as

$$\Lambda\sigma_x^c\sigma_z^s \rightarrow \left(\Lambda\sigma_x^c + \Lambda\frac{\delta x}{l_c}\sigma_z^c\right)\sigma_z^s \equiv \Lambda\frac{\sqrt{l_c^2 + \delta x^2}}{l_c}\widetilde{\sigma}_x^c\sigma_z^s, \quad (3.18)$$

$$\frac{l_c}{\sqrt{2}}\sigma_x^c \rightarrow \frac{l_c}{\sqrt{2}}\sigma_x^c + \frac{\delta x}{\sqrt{2}}\sigma_z^c \equiv \frac{\sqrt{l_c^2 + \delta x^2}}{\sqrt{2}}\widetilde{\sigma}_x^c. \quad (3.19)$$

Without loss of generality, we can rewrite Eq. 3.16 using new Pauli matrix basis in the charge subspace: $\widetilde{\sigma}_x^c$ and $\widetilde{\sigma}_z^c$, as

$$H^{\text{stat}} + H(t) = \frac{1}{2}\Delta\widetilde{\sigma}_z^c + \frac{1}{2}\epsilon_0\widetilde{\sigma}_x^c - \frac{1}{2}\epsilon_{z0}\sigma_x^s - \frac{1}{2}\Lambda\frac{\sqrt{l_c^2 + \delta x^2}}{l_c}\widetilde{\sigma}_x^c\sigma_z^s + eE^{AC}\frac{\sqrt{l_c^2 + \delta x^2}}{\sqrt{2}}\widetilde{\sigma}_x^c\cos(\omega_{\text{MW}}t + \phi), \quad (3.20)$$

with $\Delta = \Delta_c\frac{l_c}{\sqrt{l_c^2 + \delta x^2}}$ and $\epsilon_0 = \Delta_c\frac{\delta x}{\sqrt{l_c^2 + \delta x^2}}$.

MIXING ORBITAL STATES AND VALLEY STATES

Secondly, we introduce valley states. As discussed in Sec. 2.5.2, the coupling between the z degree of freedom and the x - y degree of freedom is called valley-orbit coupling

(Friesen and Coppersmith, 2010; Zwanenburg *et al.*, 2013) and causes non-zero dipole matrix elements between two valley states (Yang *et al.*, 2013):

$$\langle v_+ | x | v_+ \rangle - \langle v_- | x | v_- \rangle \neq 0, \quad (3.21)$$

where we denote the ground valley-orbit state ($|c = 0\rangle$) and excited valley-orbit state ($|c = 1\rangle$) by $|v_- \rangle$ and $|v_+ \rangle$, respectively. Thus we can deduce the same Hamiltonian as in the case of the asymmetric confinement (Eq. 3.20). The difference is that Δ can be larger than ϵ_0 in the case of mixing orbital states and valley states, while, in order to have a good confinement for an electron, δx cannot be so large (thus $\Delta \ll \epsilon_0$) in the case of the asymmetric confinement. When this simple model (Eq. 3.20) is applied to explain the experimental results shown in Ch. 9, we extract $\Delta < \epsilon_0$ and we interpret Δ as the coupling between the ground and the excited valley-orbit states and ϵ_0 as the valley splitting that can be modulated by the microwave excitation.

GENERATION OF HIGHER HARMONIC ELECTRIC DIPOLE SPIN RESONANCE AND INTER-VALLEY SPIN-FLIP RESONANCE

Inside Eq. 3.20, one can find a well-known Hamiltonian for Landau-Zener-Stückelberg (LZS) interferometry (Shevchenko, Ashhab, and Nori, 2010) :

$$\frac{1}{2} \Delta \widetilde{\sigma}_z^c + \frac{1}{2} \epsilon_0 \widetilde{\sigma}_x^c + eE^{AC} \frac{\sqrt{l_c^2 + \delta x^2}}{\sqrt{2}} \widetilde{\sigma}_x^c \cos(\omega_{\text{MW}} t + \phi). \quad (3.22)$$

The two curves in Fig. 3.3(b) represent the adiabatic energy levels of the above equation. For pure charge states, these processes are known as photon-assisted tunneling in quantum dots. The LZS process is responsible for the generation of the following experimentally observed two resonances: a second harmonic electric dipole spin resonance (Ch. 8) and an inter-valley spin-flip resonance (Ch. 9). The mechanisms of these two resonances are introduced in Sec. 9.S1-9.S2 in detail. In short, the second harmonic electric dipole spin resonance is attributed to the charge-two photon transition induced by the LZS process accompanied by the charge flip and the spin flip induced by the $\sigma_x^c \sigma_z^s$ term (see Eq. 3.20; called $f_{x,x}$ process in Sec. 9.S2; note that σ_z^s in this section corresponds to τ_x in Ch. 9). The inter-valley spin-flip resonance is attributed to the charge-one photon transition by the LZS process accompanied by the spin-flip induced by the $\sigma_z^c \sigma_z^s$ term (see the next paragraph for the generation for this term; called $f_{z,x}$ process in Sec. 9.S2).

$\sigma_z^c \sigma_z^s$, $\sigma_z^c \sigma_x^s$ and $\sigma_x^c \sigma_x^s$ terms appear if the field gradient of the stray magnetic field parallel to the external magnetic field along the modulation direction (dB_{\parallel}/dx here) is nonzero. In Sec. 3.1.1, we assumed that the stray magnetic field parallel to the external magnetic field is 0 everywhere ($dB_{\parallel} = 0$) for simplicity. However, in reality, it can be nonzero and can vary along the x axis ($dB_{\parallel}/dx \neq 0$) as seen in Appendix G. In this case, $\Lambda \sigma_x^c \sigma_z^s$ in the third term in Eq. 3.16 is replaced by $\Lambda \sigma_x^c \sigma_z^s + \Lambda' \sigma_x^c \sigma_x^s$. Together with the asymmetric confinement or mixing between valley states and orbital states (Eq. 3.18), $\sigma_z^c \sigma_z^s$ and $\sigma_z^c \sigma_x^s$ also appear.

The second or higher harmonic electron spin resonance can also be generated by a magnetic field oscillating along the parallel axis to the spin quantization axis (x axis here) as demonstrated in (Gromov and Schweiger, 2000) and in Appendix C.1. In our system,

this component can arise due to the $\sigma_x^c \sigma_x^s$ term. The amplitude of the magnetic field oscillating along the parallel axis is expected to be smaller or the same order of magnitude as the magnetic field oscillating along the perpendicular axis ($\bar{\epsilon}_1' \sim \bar{\epsilon}_1$). The ratio in Rabi frequency between the second harmonic resonance and fundamental resonance is

$$\frac{\omega_2}{\omega_1} \sim \frac{\bar{\epsilon}_1'}{\hbar\omega_0} \sim \frac{\bar{\epsilon}_1}{\hbar\omega_0} \quad (3.23)$$

(Eq. C.7). Since $\bar{\epsilon}_1 \ll \hbar\omega_0$, ω_2 is very small and we expect that the second or higher harmonic electron spin resonance should be difficult to observe.

In the case of the electric dipole spin resonance via the LZS process accompanied by the charge flip and the spin flip, the ratio in Rabi frequency between the second harmonic resonance and fundamental resonance becomes

$$\frac{\omega_2}{\omega_1} \sim \frac{\epsilon_1}{\hbar\omega_0}, \quad (3.24)$$

(Eq. 9.S36), where $\frac{\epsilon_1}{e} = E^{AC} \frac{l_c}{\sqrt{2}}$ is the voltage amplitude for the electron inside the dot induced by the microwave. Differently from $\bar{\epsilon}_1$, ϵ_1 can be the same order of magnitude as $\hbar\omega_0$ (according to Eq. 3.11, there is a relation: $\bar{\epsilon}_1/\epsilon_1 = 2\Lambda\Delta_c/(\Delta_c^2 - \epsilon_{0z}^2)$). Thus we conclude that the measured second harmonic resonance (Ch. 8) is induced by this process.

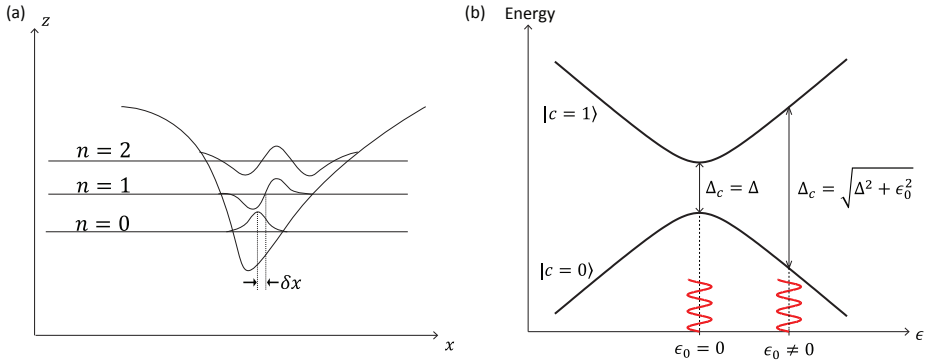


Figure 3.3: (a) An asymmetric confinement potential for a 2-dimensional quantum dot. Contrary to the symmetric case, the expectation value of position is different between the ground state ($n = 0$) and the excited state ($n = 1$) and we denote this difference by δx : $\langle n = 1 | x | n = 1 \rangle = -\langle n = 0 | x | n = 0 \rangle = \frac{\delta x}{\sqrt{2}}$. (b) Energy diagram of the valley-orbit ($c = 0, 1$) states of Eq. 3.22 as a function of ϵ_0 . In our model, the electron is modulated along $\tilde{\sigma}_x^c$. When $\epsilon_0 \ll \Delta$ ($\epsilon_0 \gg \Delta$), the electron is modulated along the orthogonal (parallel) direction to the energy axis of the valley-orbit states.

3.2. STRAY MAGNETIC FIELD CREATED BY MICROMAGNETS

Next, we would like to estimate the magnetic field gradient created by micromagnets $\frac{dB_{\perp}}{dx}$ for the experiments in Ch. 7, Ch. 8 and Ch. 9. The stray magnetic field created by the micromagnets at the position of a quantum dot depends on the direction and the amplitude of the external magnetic field, the shape of the micromagnets, and the relative

location of the dot with respect to the micromagnets. We chose cobalt as a ferromagnetic material for the convenience of the fabrication and its high enough maximum permeability to form micromagnets following (Pioro-Ladrière *et al.*, 2008b, 2007; Takakura *et al.*, 2010; Yoneda *et al.*, 2014, 2015).

NUMERICAL SIMULATION OF THE MAGNETIC FIELD CREATED BY THE MICROMAGNETS

We calculated the local magnetic field created by the micromagnets for Device C, assuming that the micromagnets are fully magnetized. The shape of the micromagnets is presented in Sec. 5.3.1 and are shown in Fig. 5.1(a) and its SEM image is in Fig. 5.1(b). As shown in Fig. 5.1(c) the bottom of the micromagnets and the 2DEG is separated by 147 nm. For the experiments in Ch. 7 and Ch. 8 and most of the experiments in Ch. 9, the external magnetic field is applied along the x axis as shown in Fig. 3.1(a).

We used Matlab codes which were initially written by (Keizer, 2007) based on (Goldman *et al.*, 2000)⁵, where an analytic expression for the magnetic field created by a rectangular shape of the magnet is presented. The analytic expression was obtained by solving the integral of magnetic fields created by infinitely small magnets using the fact that an infinitely small magnet can be regarded as a magnetic dipole.

In Fig. G.2, we show the result of a numerical calculation of the x , y , z components of the magnetic field created by the micromagnets, and the magnetic field gradient of the x , y and z components along the x and y directions in the cases where the external magnetic field is applied along the x axis. The z axis is perpendicular to the quantum well and the x and y axes are indicated in Fig. 3.1(a) or in Fig. 5.1(a). The estimated dot position is indicated by the black rectangle in Fig. G.2. The calculated magnitudes of the stray magnetic field at the estimated position of the dot are $B_{\parallel} = B_x = -120$ mT and $|B_{\perp}| = \sqrt{B_y^2 + B_z^2} = 50$ mT. The total magnetic field is calculated as $B_{\text{tot}} = \sqrt{(B_{\text{ext}} + B_{\parallel})^2 + B_{\perp}^2}$. The top figures in Fig. 3.4 show the results of the numerical calculation of the total magnetic field gradient when the external magnetic field $B_{\text{ext}} = 800$ mT is applied along the x axis.

The bottom figures in Fig. 3.4 show the gradient of the magnetic field component perpendicular to the external magnetic field when the external magnetic field is applied along the x axis. The gradient of the magnetic field component perpendicular to the external magnetic field is calculated as $\left| \frac{dB_{\perp}}{dx, dy} \right| = \sqrt{\left(\frac{dB_y}{dx, dy} \right)^2 + \left(\frac{dB_z}{dx, dy} \right)^2}$, when the external magnetic field is applied along the x axis. The position of the electron is modulated along the x axis by the microwave excitation⁶. Thus $\left| \frac{dB_{\perp}}{dx} \right| \sim 0.3$ mT/nm is the amplitude of the

⁵The Mathematica package Radia based on a finite element method, available at <http://www.esrf.fr>, can be also used (Pioro-Ladrière *et al.*, 2008b). Further information on the micromagnet numerical simulation is found in (Pioro-Ladrière *et al.*, 2008b, 2007; Takakura *et al.*, 2010; Walvoort, 2014; Yoneda *et al.*, 2014, 2015).

⁶Using the same charge configuration as Ch. 10, we found that the Rabi frequency is almost the same when we applied the magnetic field along the x axis or the y axis (data not reported here) and when microwave is sent to gate 3 or 8. Together with the calculated field gradients shown in Appendix G, we concluded that the dot modulation direction is closer to the x axis than the y axis when microwave is sent to either gate 3 or 8.

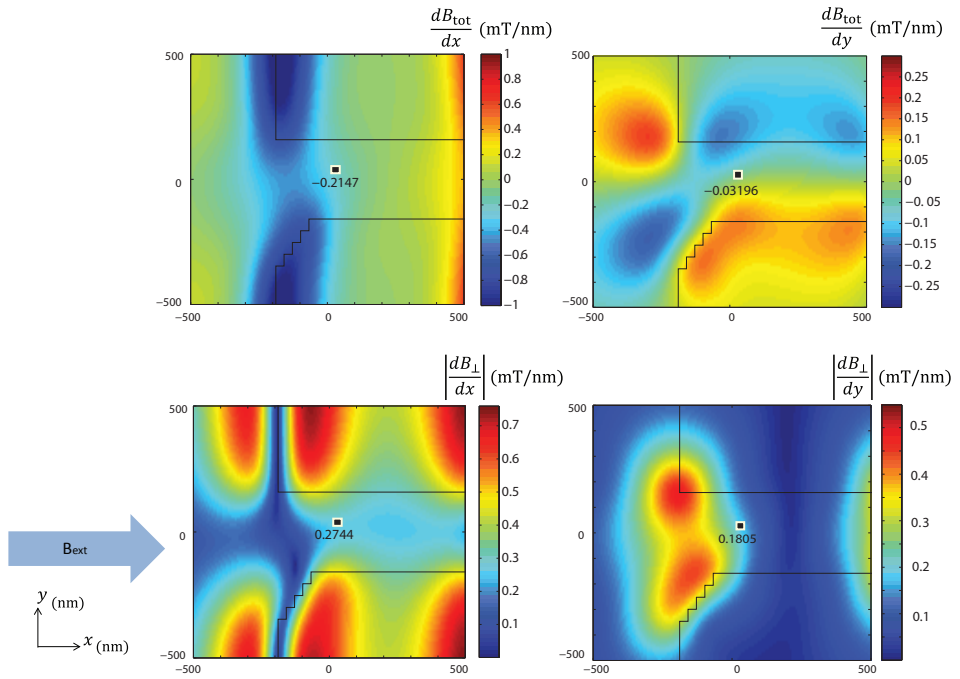


Figure 3.4: Numerically computed magnetic field gradient induced by the micromagnets in the plane of the Si quantum well, for fully magnetized micromagnets when the external magnetic field is applied along the x axis. The top left and the top right figures show the gradient of the total magnetic field along the x axis and along the y axis, respectively, with the external magnetic field at 800 mT. The bottom left and the bottom right figures show the gradient of the magnetic field component perpendicular to the external field along the x axis and along the y axis, respectively. The black rectangle shows the estimated position of the dot in the experiments shown in Ch. 7, Ch. 8 and Ch. 9. The black solid lines indicate the edges of the micromagnets simulated. The region shown is outlined with dotted lines in Fig. 5.1(a).

magnetic field gradient which contributes to the Rabi frequency⁷. The Rabi frequency is linear for the fundamental driving (Eq. 3.15, Ch. 7) or quadratic for the second-harmonic driving (Ch. 8) to the amplitude of the microwave. In fact, the magnetic field gradient would have been 4 times larger if the external magnetic field had been applied along the y axis instead of the x axis and the dot position is in the middle of the edge of the two micromagnets instead of the position of the black rectangle in Fig. 3.4 and thus the Rabi frequency would have been 4 times higher for the fundamental driving and 16 times higher for the second-harmonic driving. More discussions on the optimized condition for the magnetic field gradient are found in Appendix G.

3.3. MECHANISMS OF DECOHERENCE

Any physically realized qubit unavoidably interacts with its environment, leading to the eventual loss of the superposition state of a quantum state. This phenomenon is called decoherence and in our system the environment is ^{29}Si nuclear spins in the substrate. The magnetic moment of ^{29}Si nuclear spins creates local magnetic fields at the position of electron and, contrary to the externally applied magnetic field or the stray magnetic field introduced in the previous section, this magnetic field is changed when the direction of the magnetic moment (the spin state) of ^{29}Si nucleus changes. Thus interaction with nuclear spins induces the effective magnetic field on the electron and it fluctuates over time as derived in Eq. 3.36 later and this fluctuation in the magnetic field induces the decoherence.

3.3.1. INTERACTION WITH NUCLEAR SPINS

The full Hamiltonian for a single electron interacting with N_n ^{29}Si nuclear spins is given by (Schweiger and Jeschke, 2001; Slichter, 1990; de Sousa, 2009)

$$H = H_{eZ} + H_{nZ} + H_{en} + H_{nn}. \quad (3.25)$$

These four terms are:

- H_{eZ} is the Zeeman energy for the electron spin

$$H_{eZ} = H^{\text{stat}} = -\omega_0 S_z = \gamma_e B S_z, \quad (3.26)$$

where $S_z = \frac{\hbar}{2} \sigma_z$ is an electron spin operator and σ_z is a Pauli matrix as introduced in Eq. A.1. $\gamma_e = -g\mu_B/\hbar$ is the gyromagnetic ratio of the electron and B is the total magnetic field of the external magnetic field and the stray magnetic field created by the micromagnets at the center position of the electron.

- H_{nZ} is the Zeeman energy for the nuclear spins

$$H_{nZ} = \sum_i^{N_n} \gamma_n B_i \hbar I_{iz}, \quad (3.27)$$

⁷In (Kawakami *et al.*, 2014), we used $\frac{d|B_{\perp}|}{dx, dy}$. Later we realized that we should have considered $\left| \frac{dB_{\perp}}{dx, dy} \right|$ instead of $\frac{d|B_{\perp}|}{dx, dy}$. At the estimated dot position, $\frac{d|B_{\perp}|}{dx} \sim \left| \frac{dB_{\perp}}{dx} \right| \sim 0.3$ mT/nm, $\frac{d|B_{\perp}|}{dy} \sim 0.04$ mT/nm and $\left| \frac{dB_{\perp}}{dy} \right| \sim 0.2$ mT/nm (see also Fig. 3.4). However, It does not alter any discussion in (Kawakami *et al.*, 2014).

where $I_{iz} = \frac{1}{2}\sigma_{iz}$ is a nuclear spin operator for a nucleus located at position R_i and B_i is the magnetic field at position R_i . γ_n is the gyromagnetic ratio of the ^{29}Si nucleus. We assume that the quantization axis of all the nuclear spins can be approximated to be the same as the electron spin.

- H_{en} is the isotropic hyperfine interaction between the electron spin and the nuclear spins

$$H_{en} = \left(\sum_i^{N_n} \frac{\mu_0}{4\pi} \frac{8\pi}{3} \hbar \gamma_e \gamma_n |\Psi(\mathbf{R}_i)|^2 \mathbf{I}_i \right) \cdot \mathbf{S} = \left(\sum_i^{N_n} A_i \mathbf{I}_i \right) \cdot \mathbf{S}, \quad (3.28)$$

where $\mathbf{I}_i = \frac{1}{2}\boldsymbol{\sigma}_i$ and $\mathbf{S} = \frac{\hbar}{2}\boldsymbol{\sigma}$, with the hyperfine coupling constant

$$A_i = \frac{\mu_0}{4\pi} \frac{8\pi}{3} \hbar \gamma_e \gamma_n |\Psi(\mathbf{R}_i)|^2 [\text{rad} \cdot \text{Hz}]. \quad (3.29)$$

$\Psi(\mathbf{R}_i)$ is the electron wave function of the electron spin at position R_i . μ_0 is the magnetic permeability of free space (i.e. vacuum) of $4\pi \times 10^{-7}$ Wb/(A·m) in the MKS-SI system and of 1 in the CGS.

We can further rewrite Eq. 3.28 as $H_{en} = H_O + H_{ff}$, the sum of the secular term

$$H_O = \sum_i^{N_n} A_i I_{iz} S_z, \quad (3.30)$$

and the non-secular term

$$H_{ff} = \frac{1}{2} \left(\sum_i^{N_n} A_i (I_{i-} S_+ + I_{i+} S_-) \right), \quad (3.31)$$

for the later discussions.

- H_{nn} is the dipolar interaction between the nuclear spins

$$H_{nn} = \frac{\mu_0}{4\pi} \hbar^2 \gamma_n^2 \sum_{i < j} \left[\frac{\mathbf{I}_i \cdot \mathbf{I}_j}{R_{ij}^3} - \frac{3(\mathbf{I}_i \cdot \mathbf{R}_{ij})(\mathbf{I}_j \cdot \mathbf{R}_{ij})}{R_{ij}^5} \right], \quad (3.32)$$

where $\mathbf{R}_{ij} = \mathbf{R}_i - \mathbf{R}_j$ is the distance between two nuclei. In the presence of an external magnetic field, we can neglect the terms in Eq. 3.32 which do not conserve nuclear spin Zeeman energy, and thus Eq. 3.32 is approximated to be (Slichter, 1990)

$$H_{nn} \approx \sum_{i < j} b_{ij} (1 - 3 \cos^2 \theta_{ij}) \left(I_{iz} I_{jz} - \frac{I_{i+} I_{j-} + I_{i-} I_{j+}}{4} \right), \quad (3.33)$$

with

$$\frac{b_{ij}}{\hbar} = \frac{\mu_0}{4\pi} \frac{\hbar \gamma_n^2}{R_{ij}^3} [\text{rad} \cdot \text{Hz}]. \quad (3.34)$$

θ_{ij} is the angle formed by the applied magnetic field and the vector R_{ij} linking the two nuclear spins i, j . This approximation is called secular approximation and it is valid under the condition $\frac{b_{ij}}{\hbar} \gg \gamma_n B_i, \gamma_n B_j$.

When the coupling between the spin qubit and the environment is weak, we may rewrite Eq. 3.25 in a linearized effective Hamiltonian of the form (de Sousa, 2009):

$$H = H^{\text{stat}} + \eta_x(t)S_x + \eta_y(t)S_y + \eta_z(t)S_z, \quad (3.35)$$

where $\eta_x(t)$, $\eta_y(t)$ and $\eta_z(t)$ are the noise amplitude of the effective magnetic field as a function of time along the x , y and z axes, respectively. Since the spin states precess about the z axis with the Larmor frequency $\gamma_e B$, and the energy along the z axis is much larger than the noise amplitudes ($\gamma_e B \gg \eta_x(t), \eta_y(t), \eta_z(t)$), the noise terms $\eta_x(t)$ and $\eta_y(t)$ around the frequency $\gamma_e B$ affect the z component of the spin state, while the quasi-static noise term $\eta_z(t)$ affects the x and y components of the spin state. The effect of $\eta_x(t)$ and $\eta_y(t)$ on the z component of the spin state is called a longitudinal relaxation or T_1 relaxation and the effect of $\eta_z(t)$ on the x and y components of the spin state is called a transverse relaxation or decoherence. As the nature of the noise, the low-frequency noise is larger than the high-frequency noise and thus the z component of the spin state survives longer than the x and y components of the spin state, i.e., T_1 relaxation is slower than the decoherence. See (Clerk *et al.*, 2010; Nowack, 2009; de Sousa, 2009) for more rigorous arguments. The mechanism of T_1 relaxation of an electron or an ensemble of electrons in Si are reported in (Tyryshkin *et al.*, 2012; Yang *et al.*, 2013; Zwanenburg *et al.*, 2013) and the decay time is typically \sim seconds. In addition to that, from our measurements (Sec. 7.S3), we concluded that the effect of T_1 relaxation can be ignored and thus Eq. 3.35 can be rewritten as

$$H = H^{\text{stat}} + \eta(t)S_z, \quad (3.36)$$

without loss of generality.

In the following subsections, we explore how H_{nZ} , H_{en} and H_{nn} induce the fluctuation of magnetic field $\eta(t)$, i.e., the decoherence.

3.3.2. DECOHERENCE DUE TO THE OVERHAUSER FIELD

The secular term of the isotropic hyperfine interaction, H_O (Eq. 3.30), induces Overhauser field. This coupling between the electron spin and a nuclear spin at position R_i , $A_i I_{iz} S_z$, shifts the Larmor frequency of the electron spin by $\xi_i A_i$, where $\xi_i = \frac{1}{2}$ when the nuclear spin is in a spin-up state and $\xi_i = -\frac{1}{2}$ when the nuclear spin is in a spin-down state. This shift is called Overhauser shift (Abe, Isoya, and Itoh, 2006; Slichter, 1990) and the corresponding magnetic field is called Overhauser field. Thus the Larmor frequency of the electron spin coupled with N_n nuclear spins is shifted by $\sum_i^{N_n} \xi_i A_i$ in total.

If the nuclear spin states are unchanged over time, Overhauser field is fixed and does not lead the decoherence. However, the time evolution of Overhauser field is induced by the dipolar interaction between the nuclear spins, H_{nn} (Eq. 3.33). The nuclear spin states are flipped from spin-up state to spin-down state or vice versa due to the $I_{i+} I_{i-} + I_{i-} I_{i+}$ term in H_{nn} (Eq. 3.33). The frequency of a flip-flop between two nuclear spins is determined by the strength of the dipolar interaction and the energy cost for the flip-flop. The strength of the dipolar interaction decreases cubically with the distance between two nuclear spins and thus flip-flops happen mostly between neighbor nuclear spins (see Fig. 3.5(a)). The energy cost for this process is the difference between two nuclear

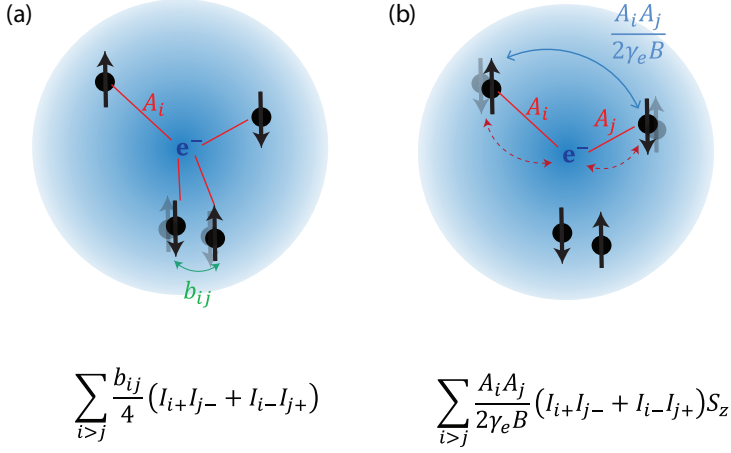


Figure 3.5: Conceptual figures of flip-flops induced by the dipolar coupling between nuclear spins (indicated by a green arrow) in (a) and induced by the electron spin-mediated coupling between nuclear spins (indicated by a blue arrow) in (b). Blue shadowed circles represent the wavefunction of an electron spin. Black arrows represent the ^{29}Si nuclear spins. Gray arrows represent the flip-flop between nuclear spins. The hyperfine coupling between an electron and nuclear spins are indicated by red lines. While the flip-flops mostly happen between neighbored nuclear spins in (a), they can happen between distant nuclear spins in (b).

spins in the hyperfine constant and in the Zeeman energy, which is almost 0 ($|A_i - A_j| \sim 0$, $|B(x_i) - B(x_j)| \sim 0$) for nuclear spins which are located at a short distance.

Due to the flip-flop process, the Overhauser field evolves over time and so the shift of the electron Larmor frequency does, which leads to the decoherence. In Sec. 10.S1, the time evolution of the Overhauser field is numerically calculated using the coupled cluster expansion (CCE) (Yang and Liu, 2009).

In the rest of this subsection, we analytically calculate the quasi-static Overhauser field, which determines the intrinsic coherence time T_2^* (Hanson *et al.*, 2007). The quasi-static treatment is done by assuming that the nuclear spins do not evolve but by considering all the possible combination of spin states (quasi-static bath approximation).

The decay of a quantum superposition state $\rho_0 = \frac{1}{2} \mathbb{1} + S_x$ over time t due to H_O

(Eq. 3.30) is denoted by $P(t)$, which is introduced in Eq. 4.58:

$$P(t) = \text{Tr}(\sigma_x \exp(iH_0 t) \rho_0 \exp(-iH_0 t)) = \text{Tr}\left(\sigma_x S_x \cos\left(\sum_i A_i I_{iz} t\right)\right) \quad (3.37)$$

$$= \prod_i^{N_n} \cos\left(\frac{A_i}{2} t\right) = \prod_i^{N_n} \frac{1}{2} \left(e^{\frac{i}{2} A_i t} + e^{-\frac{i}{2} A_i t}\right) \quad (3.38)$$

$$= \sum_{\xi_1=\pm 1, \xi_2=\pm 1, \dots, \xi_{N_n}=\pm 1} \frac{1}{2} \exp\left(\frac{i}{2} t(\xi_1 A_1 + \xi_2 A_2 + \dots + \xi_{N_n} A_{N_n})\right) \quad (3.39)$$

$$= e^{-\frac{1}{8} z^2 t^2}. \quad (3.40)$$

(de Sousa, 2009) with

$$\sigma_z = \sqrt{\sum_i^{N_n} A_i^2}, \quad (3.41)$$

(see Appendix. D.1.1 for more detail). Here we assumed that the nuclear spins are unpolarized (finite temperature approximation) and thus all the combinations of $(\xi_i, \xi_i, \dots, \xi_{N_n})$ happen with the same probability. From Eq. 3.39 to Eq. 3.40, the central limit theorem is employed assuming that $N_n \rightarrow \infty$. We denote the time constant of the Gaussian decay in Eq. 3.40 as the intrinsic decoherence time and use the notation T_2^* :

$$T_2^* = \frac{2\sqrt{2}}{\sigma_z}. \quad (3.42)$$

From this, we can further infer that the quasi-static noise of $\eta(t)$ has a Gaussian distribution with the standard deviation $\frac{\sigma_z}{2}$ ($=\sigma_\omega$ in Eq. 4.40). Next, we are interested in evaluating $T_2^* \cdot \sigma_z$ in Eq. 3.41 can be written as (see Appendix. D.1.2 for more detail)

$$\sigma_z = \sqrt{\sum_i^{N_n} A_i^2} = \sqrt{c \sum_i^N A_i^2} = \sqrt{c} \frac{A_{\text{sum}}}{\sqrt{N}} = \frac{A}{\sqrt{N_n}}. \quad (3.43)$$

c is the nuclear spin concentration and thus $A = c A_{\text{sum}}$ and $N_n = cN$ where N is the number of overlapped Si atoms with the electron wavefunction and is proportional to the size of the dot. A_{sum} is the sum of hyperfine coupling constant between the electron and each Si atom overlapped with the electron wavefunction: $A_{\text{sum}} = \sum_i^N A_i$, and depends on the material. The way to make T_2^* longer is to make the dot size larger, change the material for smaller A_{sum} or do the isotope purification for smaller c (Abe *et al.*, 2010).

3.3.3. DECOHERENCE DUE TO THE ELECTRON SPIN-MEDIATED COUPLING BETWEEN THE NUCLEAR SPINS

The non-secular term of the isotropic hyperfine interaction, H_{ff} (Eq. 3.31), induces decoherence due to the electron spin-mediated coupling between the nuclear spins (Cywinski, 2011; Cywinski, Witzel, and Das Sarma, 2009; de Sousa, 2009). At finite magnetic field ($|\gamma_e B + \gamma_n B_i| \gg A_i$), due to the Zeeman energy mismatch between an electron spin and a nuclear spin, a direct electron-nuclear flip-flop is forbidden. Thus we can ignore

H_{ff} to the first order. However, remembering that one electron spin couples to many nuclear spins, the second-order process in which the electron spin flip-flops with the i -th nuclear spin and then flip-flops back with the j -th nuclear can happen once a virtual state which requires an energy difference ($|\gamma_e B + \gamma_n B_i| \sim |\gamma_e B|$) is accessed. The Hamiltonian for this indirect coupling between nuclear spins mediated by the electron spin is written as

$$H_{ff}^{(2)} = \sum_{i < j} \frac{A_i A_j}{2\gamma_e B} (I_i^+ I_j^- + I_i^- I_j^+) S_z. \quad (3.44)$$

Since this coupling term contains both S_z and $I_i^+ I_j^- + I_i^- I_j^+$, it contributes both to the Larmor frequency shift and to its time evolution.

Now we consider the frequency of the flip-flops happening due to this coupling. The coupling strength $\frac{A_i A_j}{2\gamma_e B}$ does not contain any distance dependence. The energy cost of the whole process is proportional to $|A_i - A_j|$ and thus the flip-flops due to the electron spin-mediated coupling happen between nuclear spins which are located at the same distance from the electron spin. Contrary to the flip-flops induced by the dipolar coupling between nuclear spins, this process can happen between distant nuclear spins (see Fig. 3.5(b)).

In GaAs quantum dots (Bluhm *et al.*, 2010b), the decoherence due to the electron spin-mediated coupling between the nuclear spins was significantly observed. However, under our experimental conditions, $\sum_{i < j} \frac{A_i A_j}{2\gamma_e B}$ in $H_{ff}^{(2)}$ (Eq. 3.44) is much smaller than $\sum_i^{N_n} A_i$ in H_O (Eq. 3.30) or $\sum_{i > j} \frac{b_{ij}}{4\hbar}$ in H_{nn} (Eq. 3.33). Thus the decoherence due to the electron spin-mediated coupling between the nuclear spins is much smaller than the decoherence due to the Overhauser field (see Sec. 10.S1 for more discussions).

4

SPIN PHYSICS FOR SI/SIGE QUANTUM DOTS

In this chapter, we introduce analytic expressions for typical measurements used to characterize the performance of the qubits presented in Ch. 7, Ch. 8 and Ch. 10: Rabi oscillation, Ramsey fringe, dynamical decoupling, and randomized benchmarking, in the Schrödinger picture.

4.1. INTRODUCTION

If a Si-based quantum computer using single electron spins as physical qubits is realized, then the operations on each of the physical qubits in the processor unit can be simplified to the following 3 steps: (1) First a qubit is initialized to a known state. (2) Second the qubit is subject to a calculation. The state of the qubit is changed by quantum gates depending on the given calculations. (3) Finally, the result of the calculation is read out with projective measurements. For all the spin-state measurements shown in the later chapters of this thesis, we also used these 3 steps.

4.2. THREE-STEP SPIN-STATE MEASUREMENTS

Here we present how the 3 steps are described in quantum mechanics.

(1) Initialization of a quantum state

In all the spin-state measurements shown in the later chapters of this thesis, an electron is always initialized to a spin-down state with an error represented by γ . This initial quantum state can be written with

$$\rho_0 = (1 - \gamma) |\downarrow\rangle\langle\downarrow| + \gamma |\uparrow\rangle\langle\uparrow|, \quad (4.1)$$

where $|\downarrow\rangle$ and $|\uparrow\rangle$ represent a spin-down state and a spin-up state, respectively, and γ is the probability that an electron is prepared to a spin-up state instead of a spin-down

state. Eq. 4.1 can be rewritten as

$$\rho_0 = (1 - 2\gamma)|\downarrow\rangle\langle\downarrow| + 2\gamma\frac{\mathbb{1}}{2}, \quad (4.2)$$

where the first term is a pure state and the second term is a maximally mixed state and $\mathbb{1}$ is the identity operator. The second term stays unchanged under any quantum operation during the second step.

(2) **Evolution of a quantum state over time** In the Schrödinger picture, a quantum state evolves over time according to the Hamiltonian H . The quantum state after time t is described as

$$\mathcal{U}(\rho_0) = U\rho_0U^\dagger, \quad (4.3)^1$$

where U is a unitary propagator

$$U = T \left[\exp \left(i \int H(t) dt \right) \right]. \quad (4.4)$$

Here T is the Wick-Dyson operator, which denotes temporal ordering (see Eq. B.10) and can be omitted when the Hamiltonian at a time commute with the Hamiltonian at any different time. That is Eq. 4.4 can be rewritten as

$$U = \exp \left(i \int H(t) dt \right), \quad (4.5)$$

when $[H(t), H(t')] = 0$ for any combination of t and t' .

Coherent manipulation

In order to manipulate the quantum state we engineer a certain Hamiltonian of the system. In the experiments shown in this thesis, the engineering of the Hamiltonian is done by Electron Dipole Spin Resonance (EDSR) using microwave excitation (see Sec. 3.1 for more details).

In the rotating reference frame at the microwave carrier frequency ω_{MW} , the Hamiltonian of the microwave excitation is written with Eq. 3.14. In this section we denote Eq. 3.14 by $H_{\text{EDSR}}(t)$:

$$H_{\text{EDSR}}(t) = (\omega_{\text{MW}} - \omega_0)S_z + \omega_1(t)(S_x \cos \phi(t) - S_y \sin \phi(t)), \quad (4.6)$$

where ω_0 is the center Larmor frequency, $\omega_1(t)$ is the Rabi frequency and $\phi_1(t)$ is the phase of microwave. We take the Rabi frequency and the phase of the microwave to be a function of time since we turn on and turn off the microwave excitation and change the microwave phase differently depending on the measurements.

Decoherence

If the qubit-environment interaction is sufficiently weak, we can describe decoherence

¹We denote $U_\bullet \rho U_\bullet^\dagger$ by $\mathcal{U}_\bullet(\rho)$ for any suffix \bullet . Later in this chapter, we also denote a calligraphic style of unitary operator in the same way: $\mathcal{K}(\rho) = K\rho K^\dagger$, $\mathcal{C}(\rho) = C\rho C^\dagger$.

using classical environmental noise ($\eta(t)$) as in the second term of Eq. 3.36. This term stays the same in the rotating reference frame at the microwave carrier frequency ω_{MW} and is denoted by $H_\eta(t)$:

$$H_\eta(t) = \eta(t)S_z. \quad (4.7)$$

Total Hamiltonian

We denote $H(t)$ as the sum of the microwave excitation Hamiltonian and the decoherence Hamiltonian in the rotating reference frame at the microwave carrier frequency ω_{MW} :

$$H(t) = H_{\text{EDSR}}(t) + H_\eta(t) \quad (4.8)$$

$$= \omega_1(t)(S_x \cos \phi(t) - S_y \sin \phi(t)) + \Delta\omega S_z, \quad (4.9)$$

with $\Delta\omega = \eta(t) + (\omega_{\text{MW}} - \omega_0)$. Unless otherwise stated, in the rest of this thesis, any Hamiltonian is described in the rotating reference frame at the microwave carrier frequency ω_{MW} .

(3) Measurement of a quantum state.

Finally, we measure a quantum state by projecting it onto a quantization axis. In our experiments, the measurement is done by spin to charge conversion and the measurement axis is parallel to the quantization axis. The measurement outcome is 1 (current running through a charge sensor exceeds a threshold value, i.e., spin-up state (Elzerman *et al.*, 2004)) or 0 (the current does not exceed a threshold value, i.e., spin-down state).

The projection of a quantum state to the quantization axis with read-out errors is described by a positive operator valued measure (POVM) which represents a generalized quantum observable (Takahashi, Bartlett, and Doherty, 2013). The operator,

$$E = (1 - \beta) |\uparrow\rangle\langle\uparrow| + \alpha |\downarrow\rangle\langle\downarrow|, \quad (4.10)$$

describes the measurement outcome 1 (the operator $\mathbb{1} - E$ describes the measurement outcome 0). Here, α is the probability that the measurement gives outcome 1 when an electron was in the spin-down state and β is the probability that the measurement gives outcome 0 when an electron was in the spin-up state (Elzerman *et al.*, 2004). The probability that the outcome is 1 (0) is given by $\text{Tr}[E\mathcal{U}(\rho_0)]$ ($\text{Tr}[(\mathbb{1} - E)\mathcal{U}(\rho_0)]$).

Repeating (1), (2) and (3) and averaging the outcomes.

We are interested in the spin-up probability $\text{Tr}[E\mathcal{U}(\rho_0)]$ to obtain the information on the final quantum state $\mathcal{U}(\rho_0)$. In order to measure the spin-up probability, we repeat the sequence of 3 steps and average the outcomes. The average of the outcomes is

$$1 \times \text{Tr}[E\mathcal{U}(\rho_0)] + 0 \times \text{Tr}[(\mathbb{1} - E)\mathcal{U}(\rho_0)] = \text{Tr}[E\mathcal{U}(\rho_0)] \equiv p_1. \quad (4.11)$$

Thus the average of the measurement outcomes is equal to the spin-up probability if there is no read-out error, i.e., $\alpha = \beta = 0$. We denote p_{10} as the average of the measurement outcomes in the case of a perfect initialization and a read-out, i.e., $\alpha = \beta = \gamma = 0$, $E = |\uparrow\rangle\langle\uparrow| = \frac{1+\sigma_z}{2}$ and $\rho_0 = |\downarrow\rangle\langle\downarrow| = \frac{1-\sigma_z}{2}$,

$$p_{10} = \text{Tr}[|\uparrow\rangle\langle\uparrow|\mathcal{U}(|\downarrow\rangle\langle\downarrow|)]. \quad (4.12)$$

Since the repetition of the sequence of 3 steps takes non-negligible time, by averaging the final outcomes we need to consider the time evolution of the noise $\eta(t)$. We name the average of the measurement outcomes including this effect as the measured spin-up probability and denote it by $P_{\uparrow} = \langle p_{\uparrow} \rangle$, where $\langle \bullet \rangle$ is the average over all possible realization² of $\eta(t)$. We denote the measured spin-up probability for a perfect initialization and a read-out to be $P_{\uparrow 0} = \langle p_{\uparrow 0} \rangle$.

There is a simple relation between $P_{\uparrow 0}$ and P_{\uparrow} :

$$P_{\uparrow} = A \left(P_{\uparrow 0} - \frac{1}{2} \right) + B, \quad (4.13)$$

with $A = (1 - 2\gamma)(1 - \beta - \alpha)$ and $B = \frac{1 - \beta + \alpha}{2}$. This equation is easily derived if one focuses attention on the fact that the initial state is written as Eq. 4.2 and the POVM operator Eq. 4.10 can be rewritten as $E = (1 - \beta - \alpha) |\uparrow\rangle\langle\uparrow| + 2\alpha \frac{\mathbb{1}}{2}$. As seen in Eq. 4.13, the visibility loss is caused by both the read-out and initialization infidelities.

4

4.3. RABI OSCILLATION

INTRODUCTION

Rabi oscillations are the oscillations in probability that a quantum state is found between two levels (spin-up state and spin-down state). In order to observe a Rabi oscillation, we apply microwave of high-enough power and vary its burst time (We may observe a Rabi oscillation by applying a fixed burst time of microwave and varying its output power. We vary microwave burst time here as we have done experimentally.)

HAMILTONIAN AND GENERAL EXPRESSION

For the measurement of a Rabi oscillation, the microwave with fixed phase and fixed amplitude is applied for a time t_p . By setting $\omega_1(t) = \omega_1$ and $\phi(t) = 0$ for $0 < t < t_p$ in Eq. 4.9, the Hamiltonian for a Rabi oscillation for the time $0 < t < t_p$ can be written as

$$H_{\text{Rabi}} = \omega_1 S_x + \Delta\omega S_z, \quad (4.14)$$

with $\Delta\omega = \eta(t) + (\omega_{\text{MW}} - \omega_0)$. In Fig. 4.1, the microwave burst used for the measurement of Rabi oscillations is described with a blue rectangle. We do not need to consider the Hamiltonian before and after the microwave burst for a Rabi measurement (before the first microwave burst and after the microwave burst for Ramsey, dynamical decoupling and randomized benchmarking measurements) since it does not influence the measured spin-up probability. We note that T_1 relaxation, which might affect the measured spin-up probability, is ignored since T_1 is much longer than the measurement time (the time for one repetition of the 3 steps) in our system (Sec. 7.S3). In the Bloch sphere in Fig. 4.2, this Hamiltonian is shown by using the red arrow for the term $\Delta\omega S_z$ and the orange arrow for $\omega_1 S_x$. The combination of these two terms is described by the blue arrow, which is the vector sum of the red and orange arrows and its length is $\omega_{\text{eff}} = \sqrt{\omega_1^2 + \Delta\omega^2}$.

²In quantum mechanics, the expectation value of an observable A in the state ρ is denoted as $\langle A \rangle_{\rho}$ as shown in Appendix A.3 but in the main texts we use $\langle \bullet \rangle$ for statistical average but not for quantum mechanical average.

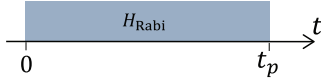


Figure 4.1: Microwave pulse sequence for a Rabi measurement. The microwave pulse is approximated to be perfect square pulse and is represented by the blue rectangle. The Hamiltonian during the microwave burst is expressed by H_{Rabi} (Eq. 4.14).

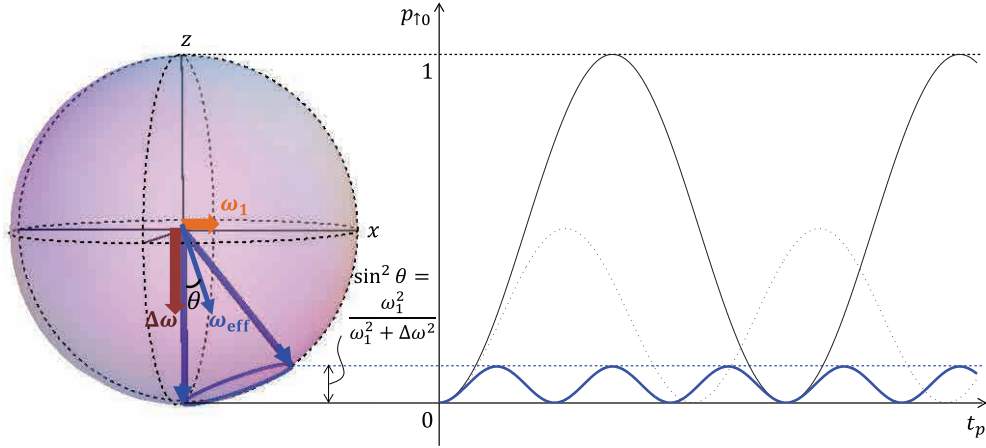


Figure 4.2: Rabi oscillations. Bloch sphere on the right and spin-up probability p_1 on the left for $\frac{\Delta\omega}{\omega_1} = 0$ (black line), $\frac{\Delta\omega}{\omega_1} = 1$ (black dashed line) $\frac{\Delta\omega}{\omega_1} = 2.93$ (blue line). The red arrow and orange arrow in the Bloch sphere represent $\Delta\omega S_z$ and $\omega_1 S_x$ in Eq. 4.14, respectively, and the blue arrow represents the combination of two terms. The blue arrow is tilted by $\theta (= \arctan(\omega_1 / \Delta\omega))$. The blue ellipsoidal curve in the Bloch sphere is the trajectory of the spin state in the case of $\frac{\Delta\omega}{\omega_1} = 2.93$. The highest spin-up probability p_1 for a given $\Delta\omega$ and ω_1 is $\sin^2 \theta = \frac{\omega_1^2}{\omega_1^2 + \Delta\omega^2}$.

For Rabi oscillations, we only consider the quasi-static noise of $\eta(t)$, i.e., $\eta(t)$ can be regarded as constant during one run of the measurement but varies between different measurement runs since the evolution of the noise is slow compared to the microwave burst time for the measurement of Rabi oscillations t_p . In most cases, this is a good approximation³. We model the distribution of η over different measurement runs with a

³If we consider the time evolution of $\eta(t)$ during the microwave burst time of a Rabi oscillation measurement, the Hamiltonian for $\omega_{\text{MW}} = \omega_0$ is approximated as

$$H_{\text{Rabi}}(t) = \omega_1 S_x + \eta(t) S_z. \quad (4.15)$$

$$\approx \omega'_1 S_x. \quad (4.16)$$

with $\omega'_1 = \omega_1 + \frac{\eta(t)^2}{2\omega_1}$, which is valid for $\omega_1 \gg \eta(t)$ (Dobrovitski et al., 2009). The average of the measurement outcome is

$$p_{10} = \text{Tr} \left[\frac{\mathbb{1}}{4} - \cos \omega'_1 \frac{\mathbb{1}}{4} \right] = \frac{1 - \cos \omega'_1}{2}, \quad (4.17)$$

Gaussian,

$$G(\eta) = \frac{1}{\sqrt{2\pi}\sigma_\omega} \exp\left(-\frac{\eta^2}{2\sigma_\omega^2}\right), \quad (4.19)$$

where σ_ω is the standard deviation of η , which corresponds to the standard deviation of the Larmor frequency and can be written as $\sigma_\omega = \sqrt{\sum_i N_n \left(\frac{A_i}{2}\right)^2}$ using the hyperfine coupling constant A_i (Eq. 3.29) and the total number of nuclear spins overlapped with the electron wave function N_n (Abe, Isoya, and Itoh, 2006; Abe *et al.*, 2010)⁴.

Following Eq. 4.12, the spin-up probability for a specific noise η is written as

$$p_{\uparrow 0} = \text{Tr}[\uparrow\uparrow] \langle \uparrow | \mathcal{U}_{\text{Rabi}}(|\downarrow\rangle\langle\downarrow|) | \uparrow \rangle. \quad (4.20)$$

$$= \sin^2 \theta \sin^2 \left(\frac{t_p}{2} \sqrt{\omega_1^2 + \Delta\omega^2} \right), \quad (4.21)$$

where $U_{\text{Rabi}} = \exp(-H_{\text{Rabi}}t)$ ⁵ and $\sin \theta = \omega_1 / \sqrt{\omega_1^2 + \Delta\omega^2}$, and it is shown in Fig. 4.2 for different ratio of ω_1 and $\Delta\omega$. The average of spin-up probability over different measurement runs is calculated by averaging $p_{\uparrow 0}$ (Eq. 4.21) over the Gaussian distribution of η (Eq. 4.19):

$$P_{\uparrow 0} = \langle p_{\uparrow 0} \rangle_\eta = \int_{-\infty}^{\infty} G(\eta) p_{\uparrow 0} d\eta \quad (4.23)$$

$$= (G * LT)(\omega_{\text{MW}} - \omega_0) \quad (4.24)$$

$$= \int_{-\infty}^{\infty} \frac{1}{\sqrt{2\pi}\sigma_\omega} \exp\left(-\frac{(\eta + (\omega_{\text{MW}} - \omega_0))^2}{2\sigma_\omega^2}\right) \frac{\omega_1^2}{\omega_1^2 + \eta^2} \sin^2\left(\frac{t_p}{2} \sqrt{\omega_1^2 + \eta^2}\right) d\eta, \quad (4.25)$$

with $L(\eta) = \frac{\omega_1^2}{\omega_1^2 + \eta^2}$ and $T(\eta) = \sin^2\left(\frac{t_p}{2} \sqrt{\omega_1^2 + \eta^2}\right)$. There is no general analytic solution to the integral of Eq. 4.25. In the following sections, we investigate analytic solutions to this integral in two extreme cases where the Rabi frequency is much larger than the broadening of the Larmor frequency ($\omega_1 \gg \sigma_\omega$) and where the Rabi frequency is much smaller than the broadening of the Larmor frequency ($\omega_1 \ll \sigma_\omega$).

and thus the measurement outcome considering the time evolution of $\eta(t)$ can be written as

$$P_{\uparrow 0} = \langle p_{\uparrow 0} \rangle = \frac{1 - \langle \cos \omega_1' \rangle}{2} = \frac{1 - \text{Re} \langle \exp i \omega_1' \rangle}{2}. \quad (4.18)$$

The analytic expression of Eq. 4.18 under the assumption that the time evolution of $\eta(t)$ is Ornstein-Uhlenbeck process is derived in (Dobrovitski *et al.*, 2009).

⁴ $\sigma_\omega = \frac{\sigma_z}{2}$ and $T_2^* = \frac{2\sqrt{2}}{\sigma_z} = \frac{\sqrt{2}}{\sigma_\omega}$ according to Eq. 3.41 and Eq. 3.42.

⁵ Following Eq. A.19, U_{Rabi} is found to be

$$U_{\text{Rabi}} = \exp(-iH_{\text{Rabi}}t_p) = \cos\left(\frac{\omega_{\text{eff}}t_p}{2}\right) \mathbb{1} - i \sin\left(\frac{\omega_{\text{eff}}t_p}{2}\right) \left(\frac{\Delta\omega}{\omega_{\text{eff}}}\sigma_z + \frac{\omega_1}{\omega_{\text{eff}}}\sigma_x\right), \quad (4.22)$$

with $\omega_{\text{eff}} = \sqrt{\omega_1^2 + \Delta\omega^2}$.

ANALYTIC EXPRESSION FOR STRONG DRIVING $\omega_1 \gg \sigma_\omega$

First, we consider the case where the Rabi frequency is much larger than the broadening of the Larmor frequency.

Under the assumption $\omega_1 \gg \sigma_\omega$ and restricting ourselves to $|\omega_{\text{MW}} - \omega_0| \ll \omega_1$, we can take $T(\omega_{\text{MW}} - \omega_0)L(\omega_{\text{MW}} - \omega_0)$ out of the integral (see Appendix E for more detail). Thus Eq. 4.25 can be rewritten as

$$P_{10} \approx T(\omega_{\text{MW}} - \omega_0)L(\omega_{\text{MW}} - \omega_0) \int_{-\infty}^{\infty} G(\eta)\eta \quad (4.26)$$

$$= \sin^2 \left(\frac{t_p}{2} \sqrt{\omega_1^2 + (\omega_{\text{MW}} - \omega_0)^2} \right) \frac{\omega_1^2}{\omega_1^2 + (\omega_{\text{MW}} - \omega_0)^2}. \quad (4.27)$$

This equation shows that the spin-up probability along the microwave frequency exhibits a Lorentzian shape and the linewidth is determined by the Rabi frequency ω_1 , not by the broadening of the Larmor frequency σ_ω . The spin state oscillates over the microwave burst time t_p at the effective Rabi frequency $\omega_{\text{eff}} = \sqrt{\omega_1^2 + (\omega_{\text{MW}} - \omega_0)^2}$.

ANALYTIC EXPRESSION FOR WEAK DRIVING $\omega_1 \ll \sigma_\omega$

Secondly, we consider the case where the Rabi frequency is much smaller than the broadening of the Larmor frequency. Under the assumption $\omega_1 \ll \sigma_\omega$, we can take $G(\omega_{\text{MW}} - \omega_0)$ out of the integral. Thus Eq. 4.25 can be rewritten as (see Appendix E for more detail)

$$P_{10} \approx G(\omega_{\text{MW}} - \omega_0) \int_{-\infty}^{\infty} L(\eta)T(\eta)d\eta \quad (4.28)$$

$$\approx \frac{1}{\sqrt{2\pi}\sigma_\omega} \exp\left(-\frac{(\omega_{\text{MW}} - \omega_0)^2}{2\sigma_\omega^2}\right) \frac{\pi\omega_1}{2} (1 - \exp(-\omega_1 t_p)) \quad (4.29)$$

$$= \frac{1}{\sqrt{2\pi}\sigma_\omega} \exp\left(-\frac{(\omega_{\text{MW}} - \omega_0)^2}{2\sigma_\omega^2}\right) \frac{\pi\omega_1}{2} \left(\omega_1 t_p - \frac{(\omega_1 t_p)^2}{2} + \dots \right). \quad (4.30)$$

This equation shows that the spin-up probability along the microwave frequency exhibits a Gaussian shape and the linewidth is determined by the broadening of the Larmor frequency σ_ω . The spin states do not oscillate coherently over the microwave burst time t . When $\omega_1 t \ll 1$ the spin-up probability at $\omega_{\text{MW}} = \omega_0$ is proportional to the square of the Rabi frequency $P_{10} \propto \omega_1^2$. This relation is used to determine the population ratio of two valley states in Ch. 7.

ANALYTIC EXPRESSION FOR THE INTERMEDIATE CASES

In (Koppens *et al.*, 2007), the analytic solution at $\omega_{\text{MW}} = \omega_0$ in the case where $\omega_1 < \sigma_\omega$ is shown as

$$P_{10} \approx \frac{1}{2} - \frac{1}{2} \cos \left[\omega_1 t_p + \frac{\arctan(t_p/\gamma)}{2} \right] \sqrt[4]{1 + (t_p/\tau)^2}, \quad (4.31)$$

where $\gamma = \omega_1/\sigma_\omega^2$. This approximation holds for⁶ $t_p \gg \max\left(\frac{1}{\sigma_\omega}, \frac{1}{\omega_1}, \gamma\right)$. This equations shows a damped oscillation with a phase shift ($\pi/4$ in the limit $t_p/\tau \rightarrow \infty$). The envelope

⁶Eq. 4.31 holds for all the time t in the limit $\omega_1 \gg \sigma_\omega$.

decay is a quadratic (Gaussian) decay for a short time t_p and a $1/\sqrt{t_p}$ decay for a long time t_p .

In the case of $\omega_1 \geq \sigma_\omega$ (, which is the case for most of the experiments presented in the thesis), we cannot write a Rabi oscillation with any simple analytic formula as described above. Thus we fitted the numerical integration of Eq. 4.25 to the experimental data in Ch. 7, Ch. 8 and Ch. 10.

4.4. RAMSEY FRINGE

INTRODUCTION

A Ramsey fringe experiment is a way to measure decoherence since its envelope decay shows the decoherence during the free evolution. Terminologically it is called Ramsey "fringe" since the fringe appears along the detuning of microwave frequency as shown in Fig. 8.4(c-e). This experiment corresponds to the Free Induction Decay (FID) in NMR and it is also called Ramsey interferometry in atomic physics. The experiment consists of applying two microwave pulses and varying the time interval between two pulses τ .

HAMILTONIAN AND GENERAL EXPRESSION

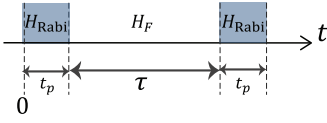


Figure 4.3: Microwave pulse sequence for a Ramsey fringe measurement. Microwave pulses are approximated to be perfect square pulses and are represented by blue rectangles. Two pulses are separated by the interval time τ and the Hamiltonian during the microwave burst is expressed with H_{Rabi} and the Hamiltonian during the free evolution time with H_F .

The Hamiltonian during the microwave burst ($0 < t < t_p$, $t_p + \tau < t < 2t_p + \tau$) is the same as H_{Rabi} (Eq. 4.14) and the Hamiltonian during the free evolution ($t_p < t < t_p + \tau$) is written as

$$H_F = \Delta\omega S_z, \quad (4.32)$$

with $\Delta\omega = \eta(t) + (\omega_{\text{MW}} - \omega_0)$. The microwave pulse sequence for Ramsey fringe measurements and the corresponding Hamiltonians are shown in Fig. 4.3. The spin-up probability for a specific noise η is

$$\begin{aligned} p_{\uparrow 0} &= \text{Tr} [|\uparrow\rangle\langle\uparrow| \mathcal{U}_{\text{Rabi}} \mathcal{U}_F \mathcal{U}_{\text{Rabi}} (|\downarrow\rangle\langle\downarrow|)] \\ &= 4 \sin^2 \theta \sin^2 \left(\frac{t_p}{2} \sqrt{\omega_1^2 + \Delta\omega^2} \right) \\ &\quad \times \left[\cos \left(\frac{\tau}{2} \Delta\omega \right) \cos \left(\frac{t_p}{2} \sqrt{\omega_1^2 + \Delta\omega^2} \right) - \cos \theta \sin \left(\frac{\tau}{2} \Delta\omega \right) \sin \left(\frac{t_p}{2} \sqrt{\omega_1^2 + \Delta\omega^2} \right) \right]^2, \end{aligned} \quad (4.34)$$

where $U_{\text{Rabi}} = \exp(-H_{\text{Rabi}}t)$, $U_F = \exp(-H_Ft)$, and $\sin\theta = \omega_1/\sqrt{\omega_1^2 + \Delta\omega^2}$. In the same way as for the Rabi oscillation, we only consider the quasi-static noise, i.e., $\eta(t)$ and we

model the distribution of η as a Gaussian (Eq. 4.19). This is a good approximation when the evolution of the noise is dominated by quasi-static noise during the free evolution time τ and the microwave burst time $2t_p$, which is usually the case. The average of spin-up probability over different measurement runs is calculated by averaging p_{10} over the Gaussian distribution of η ,

$$P_{10} = \langle p_{10} \rangle_\eta = \int_{-\infty}^{\infty} G(\eta) p_{10} d\eta, \quad (4.35)$$

where p_{10} is given by Eq. 4.34. There is no general analytic solution to this integral. In the following sections, we investigate the analytic solution in the case of strong driving ($\omega_1 \gg \sigma_\omega$) and moderate driving ($\omega_1 \sim \sigma_\omega$) during the two pulses.

ANALYTIC EXPRESSION FOR STRONG DRIVING $\omega_1 \gg \sigma_\omega$

First, we consider the case where the Rabi frequency is much larger than the broadening of Larmor frequency: $\omega_1 \gg \sigma_\omega$. By restricting ourselves to the case where $|\omega_{\text{MW}} - \omega_0| \ll \omega_1$ in the same way as done in the Rabi oscillation section, we can take the second term of Eq. 4.34 as 0. The spin-up probability for a specific noise η becomes

$$p_{10} = \frac{\omega_1^2}{\omega_1^2 + \Delta\omega^2} \sin^2 \left(t_p \sqrt{\omega_1^2 + \Delta\omega^2} \right) \cos^2 \left(\frac{\tau}{2} \Delta\omega \right), \quad (4.36)$$

and Eq. 4.35 becomes

$$P_{10} = (G * LT'R)(\omega_{\text{MW}} - \omega_0), \quad (4.37)$$

with $T'(\eta) = \sin^2 \left(t_p \sqrt{\omega_1^2 + \eta^2} \right)$ and $R(\eta) = \cos^2 \left(\frac{\tau}{2} \eta \right)$. As done in the Rabi section, we can take $T(\omega_{\text{MW}} - \omega_0)L'(\omega_{\text{MW}} - \omega_0)$ out of the integral (see Appendix E for more detail):

$$P_{10} = T'(\omega_{\text{MW}} - \omega_0)L(\omega_{\text{MW}} - \omega_0) \int_{-\infty}^{\infty} G(\eta)R(\eta) d\eta \quad (4.38)$$

$$= \frac{\omega_1^2}{\omega_1^2 + (\omega_{\text{MW}} - \omega_0)^2} \sin^2 \left(t_p \sqrt{\omega_1^2 + (\omega_{\text{MW}} - \omega_0)^2} \right) \frac{1 + e^{-\frac{\sigma_\omega^2 \tau^2}{2}}}{2}. \quad (4.39)$$

The time constant of the Gaussian decay is

$$T_2^* = \frac{\sqrt{2}}{\sigma_\omega}. \quad (4.40)^7$$

⁷Under the assumption that T_2^* is determined by static noise, there is the following relation between T_2^* and the linewidth of the resonance line:

$$T_2^* = \frac{\sqrt{2}}{\sigma_\omega} = \frac{\sqrt{2}\hbar}{g\mu_B\sigma_B} = \frac{1}{\sqrt{2}\pi\sigma_f} = \frac{2\sqrt{\ln(2)}}{\pi\delta f_{\text{FWHM}}}, \quad (4.41)^8$$

(Hanson *et al.*, 2007).

ANALYTIC EXPRESSION FOR $\omega_1 \sim \sigma_\omega$

Secondly, we consider the case where the Rabi frequency is comparable to the broadening of Larmor frequency: $\omega_1 \sim \sigma_\omega$ and we further restrict ourselves to the case where $\omega_{\text{MW}} \sim \omega_0$ and $\omega_1 t_p = \frac{\pi}{2}$. Usually, t_p is chosen so that the two microwave pulses are $\pi/2$ pulses to obtain the highest visibility. We can take $\eta \ll \omega_1$ again and the spin-up probability for a specific noise η can be written with Eq. 4.36 as in the case for $\omega_1 \gg \sigma_\omega$. Eq. 4.35 becomes (see Appendix E for more detail)

$$P_{10} = (G * LT'R)(\omega_{\text{MW}} - \omega_0) \quad (4.42)$$

$$\approx \int_{-\infty}^{\infty} \frac{1}{\sqrt{2\pi}\sigma_\omega} \exp\left(-\frac{(\eta + (\omega_{\text{MW}} - \omega_0))^2}{2\sigma_\omega^2}\right) \exp\left(-\frac{\eta^2}{\omega_1^2}\right) \cos^2\left(\frac{\tau}{2}\eta\right) d\eta \quad (4.43)$$

$$= \frac{1}{2} \frac{e^{-\left(\frac{(\omega_{\text{MW}} - \omega_0)^2}{2\sigma_\omega^2} + \frac{(\omega_{\text{MW}} - \omega_0)^2}{2(\sigma_\omega^2 + \omega_1^2)}\right)}}{\sqrt{1 + \left(\frac{\sigma_\omega^2}{\omega_1^2}\right)}} \left[1 + \exp\left(-\frac{1}{2} \frac{\sigma_\omega^2 \tilde{\omega}_1^2}{\sigma_\omega^2 + \tilde{\omega}_1^2} \tau^2\right) \cos\left(\frac{\tilde{\omega}_1^2}{\sigma_\omega^2 + \tilde{\omega}_1^2} (\omega_{\text{MW}} - \omega_0) \tau\right) \right], \quad (4.44)$$

with $\tilde{\omega}_1 = \omega_1 / \sqrt{2}$. The time constant of the Gaussian decay is

$$T_2^* = \frac{\sqrt{2}}{\sigma_\omega} \sqrt{1 + \frac{\sigma_\omega^2}{\tilde{\omega}_1^2}}. \quad (4.45)$$

This equation shows that a small Rabi frequency induces an artificial extension on the decay time. As the driving of the spin by microwave excitation becomes slower, the off-resonant spins (large η) contribute less to the signal. This effect was observed in the Ramsey decay measurement of a single spin in a GaAs quantum dot (Koppens, Nowack, and Vandersypen, 2008).

In order to determine T_2^* , we fitted Eq. 4.44 to the experimental data in Ch. 7, Ch. 8 and Ch. 10. For the numerical simulation shown in Fig. 7.S5, we used the numerical integration of Eq. 4.35 for Sec. 7.S8 because Fig. 7.S5 also covers the region $|\omega_{\text{MW}} - \omega_0| > \omega_1$.

4.5. DYNAMICAL DECOUPLING

INTRODUCTION

Decoherence is one of the most fundamental obstacles to be overcome for the realization of a quantum computer. In most of the cases, how the quantum coherence of a qubit is lost depends on the strength and the type of the interaction between the qubit and the environment (Sec. 3.3). Dynamical decoupling is a simple and widely used strategy to decouple the qubit-environment interaction and thus to extend the coherence time.

If the qubit-environment interaction is weak enough, decoherence can be approximated by classical environmental noise as $H_F = \eta(t)S_z$ (Eq. 4.7). Assuming that the statistic of the fluctuation of the noise $\eta(t)$ is Gaussian, the noise affecting the decoherence is completely defined by the two-point correlation function of $\eta(t)$

$$C(t - t') = \langle \eta(t)\eta(t') \rangle. \quad (4.46)$$

as demonstrated below (Eq. 4.60) and in several papers (Cywinski *et al.*, 2008; de Sousa, 2009)⁹. This fact enables us to use dynamical decoupling pulse schemes as filter functions on the noise $\eta(t)$ as demonstrated below. Thus dynamical decoupling can be used to characterize the nature of the noise.

The most simple form of dynamical decoupling is Hahn echo (Hahn, 1950). A variety of spin echo sequences was first developed in the field of nuclear magnetic resonance (NMR) spectroscopy (and electron paramagnetic resonance spectroscopy) used for the structural determination of molecules. The sequences were developed to decouple the ensemble of spins of a targeted nuclear spin species from the environment or the interaction between the targeted nuclear spins in order to resolve its signal better (Slichter, 1990). Dynamical decoupling is the term introduced later for such pulse sequences when used for the purpose of extending the coherence time in terms of quantum information. The direct use of an NMR echo sequence as a dynamical decoupling pulse sequence is not always appropriate. One should be careful not to overestimate the coherence time just looking at one component of the quantum state without considering the possibility that other components are not protected as well as the observed component. In (de Lange *et al.*, 2010), the extension of the coherence time using the dynamical decoupling is demonstrated in the most proper way, i.e., for any initial quantum state using quantum process tomography. If one only wants to demonstrate that the extension of the coherence time is possible with dynamical decoupling, choosing an initial quantum state which gives the worst coherence time also suffices. In most of the cases, the quantum state is the most preserved when it points along the quantization axes and is the most vulnerable when it points along an orthogonal direction to the quantization axis. Thus it is wise to think of the pulse sequences to preserve the quantum state when it points along orthogonal directions to the quantization axis. By doing so, at the same time, it is important to preserve the quantum state along all the orthogonal directions to the quantization axis.

HAMILTONIAN AND GENERAL EXPRESSION

We only consider the case where the microwave carrier frequency matches the Larmor frequency: $\omega_{\text{MW}} = \omega_0$ for simplicity. For dynamical decoupling, differently from for Rabi oscillation and Ramsey fringe, we do not approximate $\eta(t)$ as the quasi-static noise, since the free evolution time for the dynamical decoupling is usually long enough to see the time evolution of the noise $\eta(t)$. The first and last pulses are set so that these act as $\pi/2$ pulses and the others are set as π pulses.

The first line of Fig. 4.4 shows how the microwave pulses are applied for the dynamical decoupling pulse sequence. As with the Ramsey fringe, Hamiltonian during the microwave burst is H_{Rabi} (Eq. 4.14) and Hamiltonian during the free evolution is H_{F} (Eq. 4.32).

If we focus only on how the dynamical decoupling works on the noise and when the free evolution time is much longer than the microwave burst, we can approximate that the pulses are realized instantly and thus are not affected by the noise ($\eta \rightarrow 0$) as shown

⁹Even if the noise is non-Gaussian, for example, a random telegraph noise, the noise affecting the decoherence can be still defined by Eq. 4.46 in the motional narrowing regime (Bergli, Galperin, and Altshuler, 2009; Cywinski *et al.*, 2008).

in the second line of Fig. 4.4. The unitary operator for π pulses can be written as

$$U_{\text{Rabi}} = -i(\cos\phi\sigma_x + \sin\phi\sigma_y), \quad (4.47)$$

by setting $\Delta\omega = 0$ and $\omega_1 t_p = \pi$ in Eq. A.19. The unitary operator for $\pi/2$ pulses can be written as

$$U_{\text{Rabi}} = \frac{1}{\sqrt{2}}\mathbb{1} - \frac{i}{\sqrt{2}}(\cos\phi\sigma_x + \sin\phi\sigma_y), \quad (4.48)$$

by setting $\Delta\omega = 0$ and $\omega_1 t_p = \pi/2$ in Eq. A.19.

For dynamical decoupling, we apply the microwave pulses along \hat{x} , $-\hat{x}$, \hat{y} , and $-\hat{y}$, which correspond to $\phi = 0, \frac{\pi}{2}, \pi$, and $\frac{3\pi}{2}$, respectively. Using the rotation operators presented in Eq. A.21 and Eq. A.22, the π pulses are rewritten as

$$R_{x,y}(\pm\pi) \approx \mp i\sigma_{x,y} \equiv P_k, \quad (4.49)$$

and the $\pi/2$ pulses are rewritten as $R_{x,y}(\pm\pi/2)$. We denote the unitary operator for k -th pulses ($k = 1, 2, \dots, n$) by P_k .

As a result of the above discussions, the unitary operator for the dynamical decoupling becomes

$$U_{\text{DD}} = R_{x,y}(\pi/2) \exp\left(\int_{t_n}^{t_{n+1}} -i\eta(t)S_z dt\right) \left[\prod_{k=1}^n P_k \exp\left(\int_{t_{k-1}}^{t_k} -i\eta(t)S_z dt\right) \right] R_{x,y}(\pi/2) \quad (4.50)$$

$$= R_{x,y}(\pi/2) \exp\left(\int_{-\infty}^{\infty} -if(t)\eta(t)S_z dt\right) \left[\prod_{k=1}^n P_k \right] R_{x,y}(\pi/2), \quad (4.51)$$

with

$$f(t) = \sum_{k=0}^n (-1)^k \Theta(t_{k+1} - t) \Theta(t - t_k), \quad (4.52)$$

where $\Theta(t)$ is the Heaviside step function. This function switches between 1 and -1 at the times t_k ($k = 1, 2, \dots, n$), when the k th π pulse is applied, and 0 for $t < t_0$ and $t_{n+1} < t$ ($t_{n+1} - t_0 = t_{\text{wait}}$). Examples of $f(t)$ are plotted with gray lines in Fig. 4.5(a). From Eq. 4.50 to Eq. 4.51, the relation

$$R_{x,y}(\pm\pi)R_z(\theta) = R_z(-\theta)R_{x,y}(\pm\pi), \quad (4.53)$$

where R_z is given by Eq. A.23, is used (see also the caption of Fig. 4.4).

The spin-up probability for a specific noise η is

$$p_{\uparrow 0} = \text{Tr}[E\mathcal{U}_{\text{DD}}(\rho_0)] \quad (4.54)$$

$$= \text{Tr}\left[\frac{\mathbb{1} + \sigma_z}{2} \mathcal{P}_{n+1} \circ \mathcal{U}_{\text{dephasing}} \circ O_{i=1}^n \mathcal{P}_i \circ \mathcal{P}_0 \left(\frac{\mathbb{1} - \sigma_z}{2}\right)\right] \quad (4.55)$$

$$= \text{Tr}\left[\frac{\mathbb{1} + \sigma_{x,y}}{2} \mathcal{U}_{\text{dephasing}} \left(\frac{\mathbb{1} \pm \sigma_{x,y}}{2}\right)\right] \quad (4.56)$$

$$= \frac{1 \pm \cos\left(\int_{-\infty}^{\infty} -if(t)\eta(t)dt\right)}{2} = \frac{1 \pm \text{Re}[\exp\left(\int_{-\infty}^{\infty} -if(t)\eta(t)dt\right)]}{2}, \quad (4.57)$$

with $\mathcal{U}_{\text{dephasing}} = \exp\left(\int_{-\infty}^{\infty} -if(t)\eta(t)dtS_z\right)$.

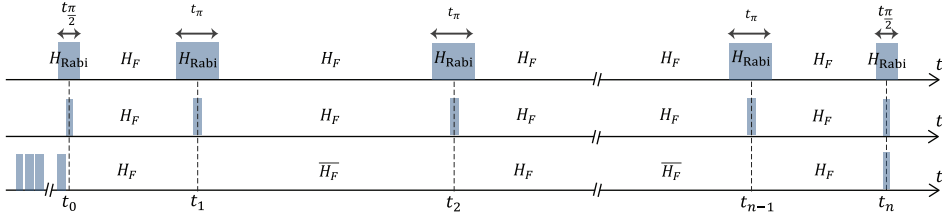


Figure 4.4: The first line shows how we experimentally apply a dynamical decoupling pulse sequence. Microwave pulses are approximated to be a perfect square pulses and shown by blue rectangles. The first and last pulses are applied during the time $t_{\frac{\pi}{2}}$ and the other pulses during the time t_{π} . The timings when the k -th pulse is applied are denoted by t_k . The Hamiltonian during the microwave burst is expressed with H_{Rabi} and the Hamiltonian during the free evolution time with $H_F = \eta(t)S_z$. In the second line, the thin pulse widths represent that the pulse length can be ignored i.e., $\pi/2$ and π pulses are considered to be perfect and they are applied instantly. The second line represents Eq. 4.50. In the third line, all the π pulses are shifted to $t < t_0$ and the signs of H_F are changed depending on the number of π pulses applied later. The third line represents Eq. 4.51. By moving the π pulses forward in time, using the relation Eq. 4.53, the sign of the Hamiltonian during the free evolution time for $t_k < t < t_{k+1}$ (k : even) is flipped and is denoted by $\bar{H}_F = -\eta(t)S_z$.

By introducing $P_{f,\eta}(t_{\text{wait}}) = \text{Re} \left[\left\langle \exp \left(- \int_{-\infty}^{\infty} -i f(t) \eta(t) dt \right) \right\rangle \right]$, the spin-up probability considering the time evolution of $\eta(t)$ can be written as

$$P_{\uparrow 0} = \frac{1 \pm P_{f,\eta}(t_{\text{wait}})}{2}, \quad (4.58)$$

where $P_{f,\eta}(t_{\text{wait}})$ represents the decay of a quantum state over waiting time t_{wait} and is sometimes idiomatically called echo decay.

FILTER FUNCTION REPRESENTATION

The indexes f and η of $P_{f,\eta}(t_{\text{wait}})$ indicate that the echo decay is as a function of the π pulse timings and the feature of the noise, respectively. $P_{f,\eta}(t_{\text{wait}})$ is analytically calculated using Gaussian functional integral as shown in the following. The average over all possible $\eta(t)$ of $\exp \left(\int -i f(t) \eta(t) dt \right)$ can be rewritten as

$$P_{f,\eta}(t_{\text{wait}}) = \text{Re} \left[\left\langle \exp \left(- \int_{-\infty}^{\infty} -i f(t) \eta(t) dt \right) \right\rangle \right] \quad (4.59)$$

$$= \text{Re} \left[\int \mathcal{D}[\eta] \exp \left(- \frac{1}{2} \int dt \int dt' \eta(t) C^{-1}(t-t') \eta(t') + \int dt (-i f(t)) \eta(t) \right) \right] \quad (4.60)$$

$$= \exp \left(- \frac{1}{2} \int dt \int dt' f(t) C(t-t') f(t') \right), \quad (4.61)$$

where \mathcal{D} represents the functional integral measure and $C^{-1}(t-t')$ is defined by

$$\int dt C^{-1}(t'-t) C(t-t'') = \delta(t'-t''). \quad (4.62)$$

Eq. 4.46 shows that $C(t)$ is the auto-correlation function of $\eta(t)$. From Eq. 4.61 $P_{f,\eta}(t_{\text{wait}})$ can be written as

$$P_{f,\eta}(t_{\text{wait}}) = \exp(-W_{f,\eta}(t_{\text{wait}})). \quad (4.63)$$

with

$$W_{f,\eta}(t_{\text{wait}}) = \frac{1}{2} \int dt \int dt' f(t) C(t-t') f(t') \quad (4.64)$$

$$= \frac{1}{2} \int dt \int dt' f(t) f(t') \int \frac{S_\eta(\omega)}{2\pi} e^{-i\omega(t-t')} d\omega \quad (4.65)$$

$$= \int \left[\frac{1}{2} \int dt \int dt' f(t) f(t') e^{-i\omega(t-t')} \right] \frac{S_\eta(\omega)}{2\pi} d\omega \quad (4.66)$$

$$= \int \frac{1}{2} \frac{F_f(\omega)}{\omega^2} \frac{S_\eta(\omega)}{2\pi} d\omega. \quad (4.67)$$

The noise spectral density $S_\eta(\omega)$ is the Fourier transform of the auto-correlation function:

$$S_\eta(\omega) = \int_{-\infty}^{\infty} C(t) e^{i\omega t} dt. \quad (4.68)^{10}$$

The filter functions that depends on the π pulse timings of the dynamical decoupling sequences are defined as

$$\begin{aligned} F_f(\omega) &= \omega^2 \int dt \int dt' f(t) f(t') e^{i\omega(t-t')} = \omega^2 \left| \int dt f(t) e^{i\omega t} \right|^2 \\ &= \left| \sum_{k=0}^{N_\pi} (-1)^k (\exp(i\omega t_{k+1}) - \exp(i\omega t_k)) \right|^2. \end{aligned} \quad (4.70)^{11}$$

ANALYTIC EXPRESSION OF THE FILTER FUNCTIONS FOR SYMMETRIC AND FIXED TIMING PULSE SEQUENCES

In this section, we introduce a dynamical decoupling pulse sequence where the time separation between π pulses is fixed and symmetric i.e., the timing of k -th π pulse is $t_k = \frac{t_{\text{wait}}}{N_\pi} (k - \frac{1}{2})$. The filter function for this pulse sequence is shown in Fig. 4.5 for $N_\pi = 0, 1, 4$ and 8. Such π pulse timings are used for the first developed multiple pulse sequence, Carr-Purcell (CP) sequence (Carr and Purcell, 1954). Later new pulse sequences which have the same π pulse timings but with different phases of π pulses such as CPMG (Carr-Purcell-Meiboom-Gill) (Meiboom and Gill, 1958), XY4, XY8, XY16 (Gullion, Baker, and Conradi, 1990) and (XY4)^{*n*} (vCDD) (Álvarez, Souza, and Suter, 2012) were discovered. The XY4, XY8 and (XY4)^{*n*} (vCDD) sequences are described further in Ch. 10. For a descriptive purpose, we label the dynamical decoupling pulse sequences which have such

¹⁰The auto-correlation function is the inverse Fourier transform of the spectral density,

$$C(t) = \frac{1}{2\pi} \int_{-\infty}^{\infty} S_\eta(\omega) e^{-i\omega t} d\omega. \quad (4.69)$$

¹¹ The filter function with finite π pulse length t_π , in general, can be written as

$$F_f(\omega) = \left| -1 + (-1)^{N_\pi} \exp(i\omega t) - 2 \sum_{k=1}^{N_\pi} (-1)^k \exp(i\omega t_k) \cos\left(\frac{\omega t_\pi}{2}\right) \right|^2, \quad (4.71)$$

(Biercuk *et al.*, 2009). We did not see a significant difference on the extracted power spectrum using Eq. 4.70 or Eq. 4.71 in Ch. 10. Therefore in this thesis, we assumed that t_π can be regarded as 0 for the filter function.

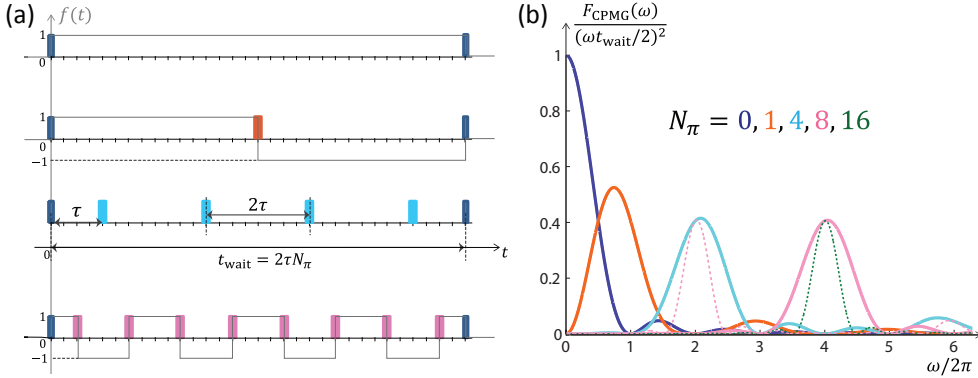


Figure 4.5: (a) CPMG-timing dynamical decoupling pulse sequences for $N_\pi = 0, 1, 4, 8$ and (b) their filter functions for $N_\pi = 0$ (blue), 1 (orange), 4 (light blue), 8 (pink), 16 (green) with $t_{\text{wait}} = 1$ (solid line) and $t_{\text{wait}} = 2$ (dashed line). In (a) the switching function $f(t)$ (Eq. 4.52) is shown with gray solid lines.

π pulse timings as CPMG (In certain papers (Cywinski *et al.*, 2008; Wang *et al.*, 2012), these π pulse timings are called CPMG timing.). For such π pulse timings, the filter function Eq. 4.70 is simplified to

$$F_{\text{CPMG}}(\omega) = 4 \sin^4 \left(\frac{\omega t_{\text{wait}}}{4N_\pi} \right) \frac{\sin^2 \left(\frac{\omega t_{\text{wait}}}{2} \right)}{\cos^2 \left(\frac{\omega t_{\text{wait}}}{2N_\pi} \right)}. \quad (4.72)$$

for an even number of π pulses N_π ,

$$F_{\text{Hahn}}(\omega) = 4 \sin^4 \left(\frac{\omega t_{\text{wait}}}{4} \right). \quad (4.73)$$

for $N_\pi = 1$ (Hahn echo), and

$$F_{\text{Ramsey}}(\omega) = \sin^2 \left(\frac{\omega t_{\text{wait}}}{2} \right). \quad (4.74)$$

for $N_\pi = 0$ (Ramsey decay or free induction decay).

The dynamical decoupling pulse sequences which have different π pulse timings such as UDD (Uhrig, 2007), CDD (Khodjasteh and Lidar, 2005) and PDD (Viola, Lloyd, and Knill, 1999) (in analogy with these sequences, the symmetric and fixed timing pulse sequences are sometimes called SDD) have different filter functions. Depending on the characteristic of the noise, different pulse sequences work the best. In (Soare *et al.*, 2014), they show a way to determine the best pulse sequence for a system suffering from an unknown characteristic noise experimentally.

EXTRACTION OF THE NOISE SPECTRAL DENSITY

It is important to understand and quantify the noise which qubits suffer from and one way to describe the noise $\eta(t)$ is the noise spectral density $S(\omega)$. In this section, we demonstrate how the noise spectral density $S(\omega)$ is extracted from the echo decay $P(t_{\text{wait}})$

using dynamical decoupling as a filter on the noise $\eta(t)$. The key point is that the filter function $F_{\text{CPMG}}(\omega)$ peaks at $\omega_0 = \frac{2\pi}{4\tau}$ with $\tau = \frac{t_{\text{wait}}}{2N_\pi}$ as shown in Fig. 4.5(b) and the peaked point moves to higher frequency with a higher number of π pulses for a fixed t_{wait} . For a large enough number of N_π (The large enough number depends on the characteristic of the noise, i.e., the shape of $S_\eta(\omega)$. If $S_\eta(\omega)$ changes abruptly inside the bandwidth of the filter function, we cannot capture the characteristic of $S_\eta(\omega)$.), the filter function $F_{\text{CPMG}}(\omega)$ is sufficiently narrow around ω_0 . We can treat the noise as constant within the bandwidth of the filter function and then Eq. 4.67 is reduced to

$$W_{\text{large}N,\eta}(t_{\text{wait}}) \approx S_\eta(\omega_0) \int_{-\infty}^{\infty} \frac{1}{2\pi} \frac{F_{\text{any}}(\omega)}{\omega^2} d\omega = \frac{S_\eta(\omega_0)}{2} t_{\text{wait}}, \quad (4.75)$$

(Bylander *et al.*, 2011)¹². From the Eq. 4.75 and Eq. 4.63, $S_f(\omega_0)$ is determined by the echo decay as

$$S_\eta\left(\omega_0 = \frac{N_\pi\pi}{t_{\text{wait}}}\right) \approx \frac{-2\log P_{f,\eta}(t_{\text{wait}})}{t_{\text{wait}}}. \quad (4.77)$$

ANALYTIC EXPRESSION FOR THE ECHO DECAYS

In the previous section, we demonstrate how to extract the noise spectrum from the echo decay. In this section, we present the shape of the echo decay for some specific noise. If such characteristic shapes of the echo decay as shown below are measured, we already have a good guess on the noise spectrum.

- White noise

First, we consider the echo decay in the case of a white noise. The spectrum of the white noise has equal power at any frequency and thus can be written as $S(\omega) = A$. By inserting this relation to Eq. 4.67, we obtain¹²

$$W_{\text{any,white}}(t_{\text{wait}}) = \frac{A}{2} \int dt |f(t)|^2 = \frac{A}{2} \int_0^{t_{\text{wait}}} 1 dt = \frac{A}{2} t_{\text{wait}}. \quad (4.78)$$

Eq. 4.78 is true for any $F_f(\omega)$, i.e., the echo decay is exponential with the same decay time constant $T_2 = T_2^* = \frac{A}{2}$.

In conclusion, the dynamical decoupling is ineffective against the white noise. Due to the absence of the correlation over time, a dephased state cannot be refocused by a π pulse or any sequence of π pulses. In the end, the echo decay always shows an exponential curve with the same time constant $T_2 = T_2^*$ for any type of dynamical decoupling pulse sequence.

- Quasi-static noise

Second, we consider the case of a quasi-static noise. The quasi-static noise here

¹² The integral definition of a delta function $\delta(t) = \int_{-\infty}^{\infty} \frac{e^{i\omega t}}{2\pi} d\omega$ is used. We also note that Parseval's theorem can be applied to the filter functions as

$$\int_{-\infty}^{\infty} \frac{1}{2\pi} \frac{F(\omega)}{\omega^2} d\omega = \int_{-\infty}^{\infty} f^2(t) dt = \int_0^{t_{\text{wait}}} 1 dt = t_{\text{wait}}, \quad (4.76)$$

(Cywinski *et al.*, 2008).

means that the noise can be considered as constant during one cycle of the step (2) but it changes over the repetitions of all the 3 steps. Its spectrum can be written as $S(\omega) = A\delta(\omega)$ and by inserting it into Eq. 4.67, we obtain

$$W_{f,\text{quasi-static}}(t_{\text{wait}}) = \int \frac{1}{2} \int dt \int dt' f(t) f(t') e^{i\omega(t-t')} \frac{A\delta(\omega)}{2\pi} d\omega = \frac{A}{2\pi} \frac{F_f(\omega)}{\omega^2} \Big|_{\omega=0}. \quad (4.79)$$

For Ramsey fringe, the decay shape is Gaussian

$$W_{\text{Ramsey,quasi-static}}(t_{\text{wait}}) = \frac{At_{\text{wait}}^2}{2 \cdot 2\pi}, \quad (4.80)$$

with a decay time constant $T_2^* = \frac{2\sqrt{\pi}}{\sqrt{A}}$. When a Gaussian distribution of the quasi-static noise is written with Eq. 4.19, its noise spectrum is $S(\omega) = A\delta(\omega)$ with $A = 2\pi\sigma_\omega^2$ and thus $T_2^* = \frac{\sqrt{2}}{\sigma_\omega}$. This result is consistent with Eq. 4.40. For the cases where $N_\pi \geq 1$, the decay shape becomes

$$W_{N_\pi \geq 1, \text{quasi-static}}(t_{\text{wait}}) = 0, \quad (4.81)$$

which shows the dephasing due to the quasi-static noise can be refocused completely by one π pulse.

- Monotone noise

Third, we consider the case of a colored noise especially when the noise power decreases monotonically. The noise spectrum can be written as

$$S_{\text{monotone}}(\omega) = \frac{A}{\omega^{\alpha-1}}. \quad (4.82)$$

By inserting this relation to Eq. 4.75,

$$W_{\text{largeN,monotone}}(t_{\text{wait}}) = \frac{S_{\text{monotone}}(\omega_0)}{2} t_{\text{wait}} \quad (4.83)$$

$$= \frac{A}{2\omega_0^{\alpha-1}} t_{\text{wait}} \quad (4.84)$$

$$= \frac{A}{2 \left(\frac{\pi N_\pi}{t_{\text{wait}}} \right)^{\alpha-1}} t_{\text{wait}} \quad (4.85)$$

$$= \left(\frac{t_{\text{wait}}}{T_2} \right)^\alpha, \quad (4.86)$$

with $T_2 = \left(\frac{2}{A} \right)^{\frac{1}{\alpha}} \pi^{\frac{\alpha-1}{\alpha}} N_\pi^{\frac{\alpha-1}{\alpha}}$. Eq. 4.86 is valid only when N is large enough to take the approximation in Eq. 4.75.

4.6. RANDOMIZED BENCHMARKING

While dynamical decoupling is a way to characterize the quality of a quantum bit as a quantum memory, randomized benchmarking is a way to characterize it as a quantum

processor. In the previous sections, we assumed that the system's Hamiltonian can be approximated to be Eq. 4.9. By using dynamical decoupling, the spectrum of the noise $\eta(t)$ can be determined under the assumption that the noise can be described as simply as by only one parameter and the statistics of its fluctuation is Gaussian. In this section, we present a way to characterize how the noise affects the gate control without any assumption of the system's Hamiltonian. In Ch. 10, we compare the noise spectrum extracted by the dynamical decoupling measurement with how the noise affects the gate control by the randomized benchmarking, and we find that these two results are consistent.

Quantum process tomography allows us to completely characterize an experimental implementation of a unitary operation (Chuang and Nielsen, 1997). However, there are two drawbacks to using quantum process tomography. First, complete process tomography is infeasible for a large number of qubit systems due to a huge number of experiments required. Second, the process error (control-gate infidelity) and the state preparation and measurement (SPAM) errors (initialization infidelities and read-out infidelities) cannot be completely separated, which leads to the underestimation of the process fidelity. Randomized benchmarking is a way to partially characterize the noise affecting a quantum system overcoming these drawbacks. The number of experiments required for randomized benchmarking scales efficiently with the number of qubits and this method is insensitive to SPAM errors. Another advantage of randomized benchmarking is that it can estimate the process error (control-gate infidelity) influenced by all the error sources which qubits suffer from in the course a real quantum calculation (decoherence, imperfect pulse shapes, and unknown error sources) since the measurement of randomized benchmarking uses long microwave pulse sequences, which is similar to the case for a real quantum calculation.

The concept of randomized benchmarking was first introduced in (Emerson, Alicki, and Zyczkowski, 2005). By applying a motion reversal sequence, the error on the control gate fidelity can be transformed into the state fidelity between the initial state and the final state. By measuring the residual population of the initial state, the fidelity of the motion reversal sequence is interpreted as shown in Fig. 4.6. In (Emerson, Alicki, and Zyczkowski, 2005), it is also shown that by varying the length of the motion reversal sequence, the SPAM errors are separated from the error on the control gate. In (Knill *et al.*, 2008), the protocol is given the name "randomized benchmarking". In this paper, the sequence of the motion reversals is replaced by a sequence of random gates (π pulse and $\pi/2$ pulse along two axes). In (Emerson, 2008; Emerson *et al.*, 2007; Magesan, Gambetta, and Emerson, 2011, 2012), it is demonstrated that choosing a set of random gates out of the Clifford group (In short, the n -qubit Clifford group is the normalizer of the n -qubit Pauli group. See also Eq. 4.101.) is an efficient way to realize randomized gates. In (Magesan *et al.*, 2012), the fidelity of a specific gate can be also measured by interleaving it between randomized gates.

DEFINITION OF GATE FIDELITY

To measure how well a quantum operation \mathcal{E} approximates a quantum gate \mathcal{U} (a unitary operation) acting on a specific pure state ρ , the state fidelity for comparing $\mathcal{E}(\rho)$ and

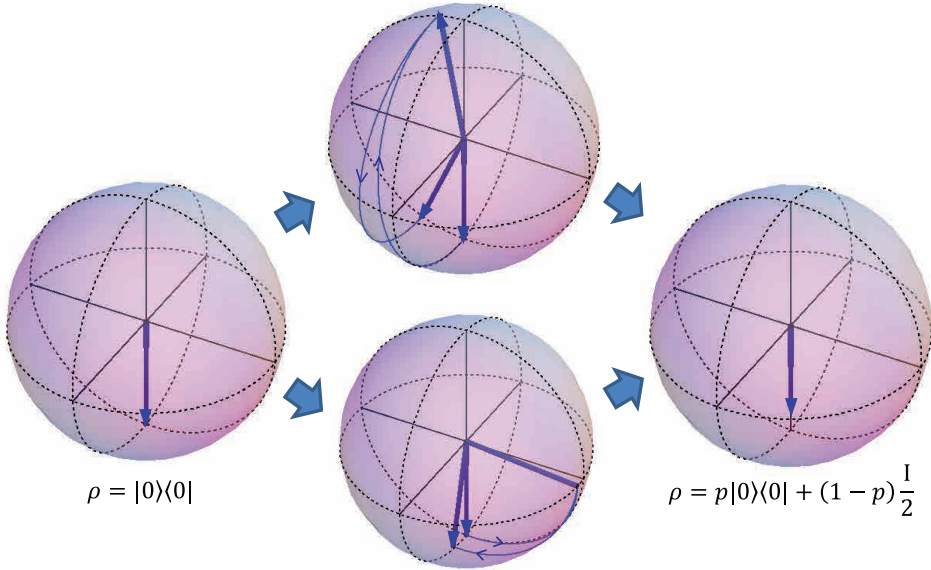


Figure 4.6: Principle of randomized benchmarking describing the spin state on the Bloch sphere. On the left, it is shown that the quantum state is prepared to be $|0\rangle$. In the middle, two examples of motion reversal are shown. Due to the errors in the motion, the quantum state does not come back to the initial state. The average of the final states after applying randomized motion reversals is shown on the right. Averaging over randomized motion reversals acts as a depolarizing channel (see Eq. 4.98 and Eq. 4.108). The residual population of the initial state p is relevant to the average fidelity of the motion reversals.

$\mathcal{U}(\rho)$ is commonly used:

$$F(\mathcal{E}(\rho), \mathcal{U}(\rho)) = \text{Tr}[\mathcal{E}(\rho)\mathcal{U}(\rho)]. \quad (4.87)^{13}$$

We define a noisy quantum channel Λ_U associated with a unitary operation U and represents how much \mathcal{E} deviates from \mathcal{U} . The state fidelity becomes

$$F(\mathcal{E}(\rho), \mathcal{U}(\rho)) = \text{Tr}[\Lambda_U(\rho)\rho] = F(\Lambda_U(\rho), I(\rho)). \quad (4.89)$$

Λ_U is a noisy quantum channel associated with a unitary operation U and represents how much \mathcal{E} deviates from \mathcal{U} . The state fidelity between the actual and ideal gate outputs for an aimed quantum gate U in Eq. 4.89 is an initial-state-dependent value, i.e., the gate fidelity for a specific initial state. Thus we define the gate fidelity¹⁴ as that averaged

¹³The state fidelity for comparing $\mathcal{E}_1(\rho)$ and $\mathcal{E}_2(\rho)$ is

$$F(\mathcal{E}_1(\rho), \mathcal{E}_2(\rho)) = \left(\text{Tr} \left[\sqrt{\sqrt{\mathcal{E}_1(\rho)}\mathcal{E}_2(\rho)\sqrt{\mathcal{E}_1(\rho)}} \right] \right)^2, \quad (4.88)$$

for any quantum operation \mathcal{E}_1 and \mathcal{E}_2 and for any quantum state ρ . Although Jozsa's original convention of the state fidelity (Jozsa, 1994) is as described here, \sqrt{F} is more commonly used as a state fidelity in recent literatures. Eq. 4.88 can be rewritten as Eq. 4.89 when ρ is a pure state and one of the quantum operations is a unitary operator.

¹⁴In most of the literature, it is called "average gate fidelity" but here we call it simply "gate fidelity" in order to avoid confusion with "average gate fidelity over all the Clifford gates", which is introduced later.

over all input pure states

$$\mathcal{F}_{\mathcal{E},\mathcal{U}} = \mathcal{F}_{\Lambda_U, I} = \int d\rho F(\Lambda_U(\rho), \mathcal{I}(\rho)) = \int d\rho \text{Tr}[\Lambda_U(\rho)\rho]. \quad (4.90)^{15}$$

Here the integral uses the uniform unitary invariant measure ρ on the pure state space, normalized as $\int d\rho = 1$. Hence the gate fidelity provides an indicator that is independent of the choice of initial state. Since $d\rho$ is the unitary invariant measure, $\int d\rho \text{Tr}[\Lambda_U(\rho)\rho] = \int d\rho \text{Tr}[\Lambda_U(\mathcal{U}'(\rho))\mathcal{U}'(\rho)]$ (Emerson, Alicki, and Zyczkowski, 2005; Horodecki, Horodecki, and Horodecki, 1999; Nielsen, 2002).

TWIRLED OPERATION OF A QUANTUM CHANNEL = DEPOLARIZING CHANNEL
Furthermore, we average the gate fidelity $\mathcal{F}_{\mathcal{E},\mathcal{U}}$ over all unitaries uniformly with a normalized unitary invariant Haar measure dU' . Since $\mathcal{F}_{\mathcal{E},\mathcal{U}}$ is not a function of U' and $\int dU' = 1$. We can write

$$\mathcal{F}_{\mathcal{E},\mathcal{U}} = \mathcal{F}_{\Lambda_U, I} \quad (4.94)$$

$$= \int dU' \int d\rho \text{Tr}[\Lambda_U(\rho)\rho] \quad (4.95)$$

$$= \int d\rho \text{Tr} \left[\int dU' \mathcal{U}'^\dagger (\Lambda_U(\mathcal{U}'(\rho))) \right] \quad (4.96)$$

$$= \int d\rho \text{Tr}[\Lambda_U^T(\rho)\rho] = \mathcal{F}_{\Lambda_U^T, I}, \quad (4.97)$$

where

$$\Lambda_U^T(\rho) = \int dU' \mathcal{U}'^\dagger (\Lambda_U(\mathcal{U}'(\rho))), \quad (4.98)$$

is a twirled operation of a quantum channel Λ , which is the uniform average of a quantum channel sandwiched by a unitary operation and its inverse over all unitaries. The

¹⁵ There is a simple relationship between the process fidelity and the average fidelity for any process:

$$\mathcal{F}_{\mathcal{E},\mathcal{U}} = \mathcal{F}_{\Lambda_U, I} = \frac{dF_p + 1}{d + 1}, \quad (4.91)$$

(Bowdrey *et al.*, 2002; Chow *et al.*, 2009). A quantum channel Λ can be represented as

$$\Lambda(\rho) = \sum_k A_k \rho A_k^\dagger = \sum_{i,j} \chi_{i,j} \sigma_i \rho \sigma_j. \quad (4.92)$$

The process fidelity is defined as $F_p = \text{Tr}(\chi_{\text{real}} \chi_{\text{idea}})$ (Chow *et al.*, 2009) and $F_p = \text{Tr}(\chi_I \chi_\Lambda) = \chi_{\Lambda 00}$ when the ideal process is an identity. From Eq. 4.92, $\text{Tr}(\hat{\Lambda}) = \sum_k (\text{Tr}(A_k))^2 = \chi_{\Lambda 00} d^2$. From Eq. 4.98, $\text{Tr}(\hat{\Lambda}^T) = \text{Tr}(\hat{\Lambda})$.

From Eq. 4.99, $p_U = \frac{\text{Tr}(\hat{\Lambda}^T) - 1}{d^2 - 1}$.

By substituting this relation into Eq. 4.105,

$$\mathcal{F}_{\mathcal{E},\mathcal{U}} = \mathcal{F}_{\Lambda_U, I} = \mathcal{F}_{\Lambda_U^T, I} = \frac{\sum_k (\text{Tr}(A_k))^2 / d + 1}{d + 1}. \quad (4.93)$$

twirled operation of any quantum channel is a depolarizing channel:

$$\Lambda_U^T(\rho) = p_U \rho + (1 - p_U) \frac{\mathbb{1}}{d}, \quad (4.99)$$

where $d = 2^n$ is the dimension of Hilbert space with the number of qubits n , as intuitively understood since Eq. 4.98 gives the same value for any input pure state ρ as rigorously demonstrated in (Nielsen, 2002). By substituting Eq. 4.99 into Eq. 4.97, the gate fidelity is obtained as

$$\mathcal{F}_{\mathcal{E}, \mathcal{U}} = \mathcal{F}_{\Lambda_U, I} = \mathcal{F}_{\Lambda_U^T, I} = F(\Lambda_U^T(\rho), \rho) = p_U + \frac{1 - p_U}{d}. \quad (4.100)$$

APPROXIMATION OF THE AVERAGE OVER ALL UNITARIES TO THE AVERAGE OVER ALL THE CLIFFORD GATES

According to (Dankert *et al.*, 2009), Eq. 4.98 can be approximated to

$$\int dU' \mathcal{U}'^\dagger (\Lambda_U(\mathcal{U}'(\rho))) \sim \frac{1}{K} \sum_{j=1}^K \mathcal{C}_j^\dagger (\Lambda_U(\mathcal{C}_j(\rho))). \quad (4.101)$$

where \mathcal{C}_j is an element of the Clifford group, which is the subgroup of the unitary group for which the relation $C_j P_k C_j^\dagger = P_i$ holds for any $P_k, P_i \in \{\mathbf{P} \setminus \{\mathbb{1} \times \{\pm 1, \pm i\}\}\}$, where $\mathbf{P} = \{\sigma_0, \sigma_x, \sigma_y, \sigma_z\}^{\otimes n} \times \{\pm 1, \pm i\}$ is the Pauli group. K is the number of gates in the Clifford group. The number of gates in the 1-qubit ($n = 1$) Clifford group is 24 ($K = 24$). From Eq. 4.99 and Eq. 4.101, twirling a quantum operation over the Clifford group produces a depolarizing channel:

$$\frac{1}{K} \sum_{j=1}^K \mathcal{C}_j^\dagger (\Lambda_U(\mathcal{C}_j(\rho))) \approx \Lambda_U^T(\rho) = p_U \rho + (1 - p_U) \frac{\mathbb{1}}{d}. \quad (4.102)$$

We define the average error operator affecting different Clifford gates as

$$\Lambda_{\bar{C}} = \frac{1}{K} \sum_{j=1}^K \Lambda_j, \quad (4.103)$$

where Λ_j is the error associated with a specific Clifford gate C_j . By substituting Λ_U by $\Lambda_{\bar{C}}$, Eq. 4.102 becomes

$$\frac{1}{K} \sum_{j=1}^K \mathcal{C}_j^\dagger (\Lambda_{\bar{C}}(\mathcal{C}_j(\rho))) \approx \Lambda_{\bar{C}}^T(\rho) = p_{\bar{C}} \rho + (1 - p_{\bar{C}}) \frac{\mathbb{1}}{d}. \quad (4.104)$$

According to Eq. 4.105, the average gate fidelity over all the Clifford gates is given by

$$\mathcal{F}_{\Lambda_{\bar{C}}, I} = p_{\bar{C}} + \frac{1 - p_{\bar{C}}}{d}. \quad (4.105)$$

EXPERIMENTAL IMPLEMENTATION

We now consider the experimental implementation for the measurement of the average gate fidelity over all the Clifford gates. We denote an experimentally realized Clifford gate by $\mathcal{C}_j^{\text{real}} (= \Lambda_j \circ \mathcal{C}_j)$. By applying the motion reversals of all the Clifford gates to an initial quantum state ρ_0 , the averaged final state is

$$\rho = \frac{1}{K} \sum_{j=1}^K \mathcal{C}_j^{\text{real}\dagger} \circ \mathcal{C}_j^{\text{real}}(\rho_0) = \frac{1}{K} \sum_{j=1}^K \mathcal{C}_j^\dagger \circ \Lambda'_j \circ \mathcal{C}_j(\rho_0) \quad (4.106)$$

$$\sim \frac{1}{K} \sum_{j=1}^K \mathcal{C}_j^\dagger \left(\Lambda'_C(\mathcal{C}_j(\rho_0)) \right) \quad (4.107)$$

$$\approx \Lambda'^T_C(\rho) = p'_C(\rho_0) + (1 - p'_C) \frac{\mathbb{1}}{d}, \quad (4.108)$$

where Λ'_j denotes the cumulative noise from the motion reversal of \mathcal{C}_j and $\Lambda'_C = \frac{1}{K} \sum_{j=1}^K \Lambda'_j$. The approximation in Eq. 4.107 is valid when the gate-dependent error $\delta \Lambda'_j = \Lambda'_C - \Lambda'_j$ is small.

By taking the initial quantum state as ρ_0 and the POVM operator as E , the measured spin-up probability of the final state is

$$P_\uparrow = \text{Tr}[E\rho] = \text{Tr} \left[E \left(\rho_0 - \frac{\mathbb{1}}{d} \right) \right] p'_C + \text{Tr} \left[E \left(\frac{\mathbb{1}}{d} \right) \right]. \quad (4.109)$$

Eq. 4.109 shows that the initialization and read-out error also affect the measured spin-up probability of the final state. We overcome this problem by repeating the motion reversals. The key point is that by doing so the gate error is accumulated as the number of repetitions is increased while the initialization error and read-out error stay the same.

If we repeat the motion reversals m times, there are K^m different Clifford gates sequences over all the possible combinations of (j_1, \dots, j_m) . The averaged final state becomes

$$\rho = \frac{1}{K^m} \sum_{(j_1, \dots, j_m)} O_{i=1}^m \mathcal{C}_{j_i}^{\text{real}\dagger} \circ \mathcal{C}_{j_i}^{\text{real}}(\rho_0) \quad (4.110)$$

$$= p'^m_C \rho_0 + (1 - p'^m_C) \frac{\mathbb{1}}{d}, \quad (4.111)$$

and the measured spin-up probability becomes

$$P_\uparrow = \text{Tr}[E\rho] = \text{Tr} \left[E \left(\rho_0 - \frac{\mathbb{1}}{d} \right) \right] p'^m_C + \text{Tr} \left[E \left(\frac{\mathbb{1}}{d} \right) \right]. \quad (4.112)$$

By measuring the decay curve of P_\uparrow as function of m , we can determine p'_C allowing us to calculate for the average gate fidelity over all the motion reversals of Clifford gates using Eq. 4.105. This method to measure the gate fidelity by repeating the motion reversals is similar to the method presented in the original paper (Emerson, Alicki, and Zyczkowski, 2005). Later it is presented that the sequence of the motion reversals can be replaced by a sequence of gates which acts as an identity gate (or a known gate) as a whole (Emerson,

2008; Emerson *et al.*, 2007; Knill *et al.*, 2008; Magesan, Gambetta, and Emerson, 2011, 2012). We denote such a sequence by

$$S_{j_m} = \mathcal{C}_{j_{m+1}}^{\text{real}} \circ \mathcal{C}_{j_m}^{\text{real}} \circ \dots \circ \mathcal{C}_{j_1}^{\text{real}} \quad (4.113)$$

$$= \Lambda_{j_{m+1}} \circ \mathcal{C}_{j_{m+1}} \circ \Lambda_{j_m} \circ \mathcal{C}_{j_m} \circ \dots \circ \Lambda_{j_1} \circ \mathcal{C}_{j_1} \quad (4.114)$$

$$\sim \Lambda_{\bar{C}} \circ \mathcal{C}_{j_{m+1}} \circ \Lambda_{\bar{C}} \circ \mathcal{C}_{j_m} \circ \dots \circ \Lambda_{\bar{C}} \circ \mathcal{C}_{j_1}. \quad (4.115)$$

We choose $C_{j_{m+1}}$ so that

$$C_{j_{m+1}} C_{j_n} \dots C_{j_1} = K, \quad (4.116)$$

where K is $\mathbb{1}$ (or another known gate).

We define a new Clifford gates sequence by $(D_{j_1}, \dots, D_{j_m})$ and D_{j_i} is uniquely created from $(C_{j_1}, \dots, C_{j_m})$ by the equation $C_{j_{i+1}} = D_{j_{i+1}} \circ D_{j_i}$, i.e.,

$$D_{j_{i+1}} = C_{j_{i+1}} C_{j_i} \dots C_{j_1}. \quad (4.117)$$

From Eq. (4.116) and Eq. (4.117), $D_{j_{m+1}} = K$ and so $D_{j_{m+1}}$ is independent of j .

By replacing \mathcal{C}_{j_i} with $\mathcal{D}_{j_i} \circ \mathcal{D}_{j_{i-1}}$, Eq. (4.115) is rewritten as

$$S_{j_m} \approx \Lambda_{\bar{C}} \circ \mathcal{K} \circ \mathcal{D}_{j_m}^\dagger \circ \Lambda_{\bar{C}} \circ \mathcal{D}_{j_m} \circ \dots \circ \mathcal{D}_{j_1}^\dagger \circ \Lambda_{\bar{C}} \circ \mathcal{D}_{j_1} \quad (4.118)$$

$$= \Lambda_{\bar{C}} \circ \mathcal{K} \circ (O_{i=1}^m (\mathcal{D}_{j_i}^\dagger \circ \Lambda_{\bar{C}} \circ \mathcal{D}_{j_i})), \quad (4.119)$$

where \mathbf{j}_m is defined as the m -tuple (j_1, \dots, j_m) .

After applying this sequence, the averaged final state becomes

$$\rho = \frac{1}{K^m} \sum_{(j_1, \dots, j_m)} S_{j_m}(\rho_0) \quad (4.120)$$

$$= \Lambda_{\bar{C}} \circ \mathcal{K} \left(p_{\bar{C}}^m \rho_0 - p_{\bar{C}}^m \frac{\mathbb{1}}{d} \right), \quad (4.121)$$

and the measured spin-up probability becomes

$$P_{\uparrow} = \text{Tr}[E\rho] = \text{Tr} \left[E \left(\Lambda_{\bar{C}} \circ \mathcal{K} \left(\rho_0 - \frac{\mathbb{1}}{d} \right) \right) \right] p_{\bar{C}}^m + \text{Tr} \left[E \Lambda_{\bar{C}} \left(\frac{\mathbb{1}}{d} \right) \right]. \quad (4.122)^{16}$$

In the same way as for the motion reversals, we can determine $p_{\bar{C}}$ by varying m experimentally allowing us to calculate the average gate fidelity over all the Clifford gates.

We can further remove the term $\text{Tr} \left[E \Lambda_{\bar{C}} \left(\frac{\mathbb{1}}{d} \right) \right]$ in Eq. 4.122 by looking at the difference in the measured spin-up probability between different choices of K . Following (Muhonen *et al.*, 2015; Veldhorst *et al.*, 2014), for the experiments in Ch. 10, we take the difference of the measured spin-up probability between $|\uparrow\rangle$ as the target state and $|\downarrow\rangle$ as the target state. The difference of the measured spin-up probability can be written as

$$P_{\uparrow}^{|\uparrow\rangle} - P_{\uparrow}^{|\downarrow\rangle} = \text{Tr} [E\Lambda \circ \mathcal{K}_{|\uparrow\rangle}(\rho_0)] p_{\bar{C}}^m - \text{Tr} [E\Lambda \circ \mathcal{K}_{|\downarrow\rangle}(\rho_0)] p_{\bar{C}}^m, \quad (4.123)$$

where $|\cdot\rangle$ in the suffix of \mathcal{K} is the target state. $K_{|\downarrow\rangle} = \mathbb{1}$ and $K_{|\uparrow\rangle}$ is randomly chosen out of X, \bar{X}, Y or \bar{Y} . Eq. 4.123 is reduced to

$$P_{\uparrow}^{|\uparrow\rangle} - P_{\uparrow}^{|\downarrow\rangle} = a p_{\bar{C}}^m, \quad (4.124)$$

where $a = \text{Tr} [(1 - 2\gamma)E\Lambda (|\uparrow\rangle\langle\uparrow| - |\downarrow\rangle\langle\downarrow|)]$ does not depend on either $p_{\bar{C}}^m$ or m .

¹⁶ $\mathcal{K}(\mathbb{1}) = \mathbb{1}$ because \mathcal{K} is a perfect quantum gate and thus unitary operator.

5

DEVICE AND MEASUREMENT SETUP

In this chapter, we first introduce 3 different devices used in the experiments presented in this thesis: Device A, Device B and Device C. Device A is based on a doped Si/SiGe heterostructure accommodated with a microwave stripline. Device B and Device C are based on an accumulation mode undoped Si/SiGe heterostructure accommodated with one and two micromagnet(s), respectively. The experiments using Device A and Device B are presented in Ch. 6 and the experiments using Device C are presented in Ch. 7, Ch. 8, Ch. 9 and Ch. 10. Secondly, we present the measurement setup used in the electrical measurements of these devices including the DC wirings, high frequency coaxial lines, and the spin-state detection scheme.

As discussed in Sec. 2.4, a local micromagnet or a microwave antenna is required for the manipulation of a spin state of a single electron spin in Si. For Device A, we choose an on-chip antenna, adjacent to a Si/SiGe quantum dot, to produce microwave excitation and static magnetic field gradients, by driving with both DC and AC currents. For Device B and Device C, micromagnets are fabricated on top of the devices to form a local magnetic field gradient.

5.1. HETEROSTRUCTURE GROWTH

As presented in Sec. 2.2.2, a quantum well for electrons is formed at the interface of Si and SiGe. In order to obtain a heterojunction, a layer control with an atomic precision is required. Generally molecular beam epitaxy (MBE) or chemical vapor deposition (CVD) technologies are used. In MBE, the atoms or molecules for the new layer are injected into a ultrahigh vacuum chamber until they reach the substrate. Depending on the temperature of the substrate, layers of different material can be grown on top of each other. CVD is based on chemical reactions that transform gaseous molecules into a thin film on the surface of a substrate. Si/SiGe heterostructures used for all the 3 devices: Device A, Device B and Device C were grown by Don Savage in Prof. Max Laggaly group at Wisconsin

University with CVD (Schäffler, 1997).

5.2. DEVICE A

Device A was fabricated by Jonathan Prance in Prof. Mark Eriksson's group at Wisconsin University. The device is fabricated on a phosphorus-doped Si/Si_{0.7}Ge_{0.3} heterostructure with a strained Si quantum well approximately 75 nm below the surface. The phosphorus-doping layer is covered by a Si_{0.7}Ge_{0.3} upper spacer of 45 nm and a Si cap of 7 nm to minimize leakage from the gates to the quantum well. Palladium surface gates are fabricated to form a single dot or a double dot and an on-chip antenna (Ti/Au, 5 nm/305 nm) is fabricated close to these dot gates. (SEM picture shown in Fig. 6.1(a))

5.2.1. MEASUREMENT SETUP FOR DEVICE A

The sample was glued on a printed circuit board (PCB) and the PCB was attached to the mixing chamber (MC) of a dilution refrigerator (Oxford Kelvinox 300) with base temperature ~ 25 mK. DC and AC currents through the antenna (stripline) were combined via a bias-T (Anritsu K251 (Hendrichs, 2011)) placed at the 1 K stage of the refrigerator as shown in Fig. 5.4. Both ends of the antenna are connected to high-frequency lines. Another high-frequency line was connected to gate 2 labeled in Fig. 6.1(a). The high-frequency signal was combined on the PCB with a DC voltage line by a homemade resistive bias tee ($R=10$ M Ω , $C=47$ nF; $1/RC\sim 2$ Hz) to allow fast pulsing of the gate voltages or microwave excitation while also maintaining a DC bias on the gates. The details of the materials used for the DC lines and high-frequency coaxial cables for the measurements of Device A are found in (Hendrichs, 2011). Electronics used for transport measurements and filtering used for DC voltage lines are similar to what are shown in Sec. 5.3.2.

5.3. DEVICE B AND C

Device B and C are based on an undoped Si/SiGe heterostructure with two layers of electrostatic gates (Fig. 5.1(a,c)). Compared to conventional, doped heterostructures, this technology strongly improves charge stability (Maune *et al.*, 2012). First, accumulation gates are used to induce a two-dimensional electron gas (2DEG) in a 12 nm wide Si quantum well 37 nm below the surface. Second, a set of depletion gates, shown with gray regions in Fig. 5.1(a), is used to form a single or double quantum dot in the 2DEG, flanked by a quantum point contact and another dot intended as charge sensors. Two 1 μm -wide, 200 nm-thick, and 1.5 μm -long Co magnets are placed on top of the accumulation gates (Fig. 5.1(a)), providing a stray magnetic field with components B_{\parallel} and B_{\perp} , parallel and perpendicular to the external magnetic field, respectively (Sec. 3.1.1).

5.3.1. SAMPLE FABRICATION FOR DEVICE B AND C

Device B and Device C were fabricated by Dan Ward in Prof. Mark Eriksson's group at Wisconsin University. A SEM image of Device C is shown in Fig. 5.1(b). Device B is the same as Device C, except for the absence of the top micromagnet due to incomplete lift-off during fabrication. The epitaxial structure, shown in (Fig. 5.1(c)), is grown by CVD. An 800 nm Si_{0.7}Ge_{0.3} buffer is deposited on a substrate, followed by a 12 nm thick strained Si well. A 32 nm Si_{0.7}Ge_{0.3} layer is then deposited, followed by a 1 nm thick Si

cap layer. The sample is undoped; charge carriers are induced in the Si quantum well by application of positive voltages to the accumulation gates, forming a 2DEG (Borselli *et al.*, 2011; Ward *et al.*, 2013). To minimize unwanted accumulation and charge leakage, most of the substrate is etched to below the Si quantum well using reactive ion etching, leaving active material for the dot structures only in small $100\ \mu\text{m} \times 100\ \mu\text{m}$ mesas. All exposed surfaces are then uniformly coated with 10 nm of Al_2O_3 via atomic layer deposition (ALD). Ohmic contacts to the 2DEG are created by 20 kV phosphorus implantation activated with a 15 s, $700\ ^\circ\text{C}$ anneal. Two layers of gates, separated by an isolating layer of 80 nm of Al_2O_3 deposited by ALD, are defined by a combination of photo- and electron-beam lithography and deposited by electron-beam evaporation of 1.7 nm Ti/40 nm Au. Two Co micromagnets are defined on top of the upper layer of gates by electron-beam lithography and deposited by electron-beam evaporation of 5 nm Ti/ 200 nm Co / 20 nm Au. The top Au layer minimizes oxidation of the Co material.

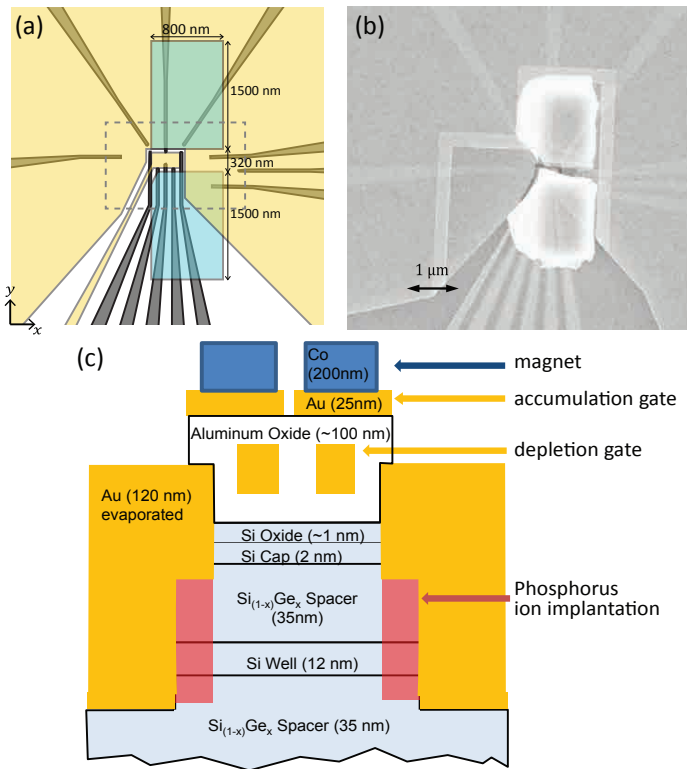


Figure 5.1: Device C (a) False color device image showing a fabricated pattern of split gates (gray regions). The blue semitransparent rectangles show the position of two Co 200 nm thick micromagnets. The top edge of the bottom micromagnet is partially cut in order to avoid the electrical short between two accumulation gates. The yellow shaded pieces show the location of two accumulation gates, one for the reservoirs and another for the double quantum dot region. (b) Scanning electron micrograph of the sample. The white regions around the area of the micromagnets are thin pieces of metal that were bent upwards during lift-off. (c) Schematic cross-section of the device.

5.3.2. MEASUREMENT SETUP FOR DEVICE B AND C

The sample is attached to the MC stage in the same way as for Device A in the same dilution refrigerator.

EXTERNAL MAGNETIC FIELD

The strength and the direction of the external magnetic field is set by the currents running through two-vector (7 T along the horizontal axis (denoted as the y axis in this thesis) and 3 T along one of the vertical axes (denoted as the x axis)) superconducting magnets which are equipped on the Helium Dewar. The sample is mounted so that the external magnetic field is applied in the plane of 2DEG. The out-of-plane component of the magnetic field due to the misalignment between the surface of the sample board and the vertical axis of the superconducting magnet was found to be less than 5 degrees and using Shubnikov–de Haas effect on a GaAs sample (Scarlino *et al.*, 2014). This should have a negligible effect on the spin-qubit measurements because the cyclotron frequency due to this out-of-plane magnetic field is small compared to other energy scales for the spin-qubit measurement.

5

LOW-FREQUENCY LINES

We have 4 times 12 twisted pairs of wires running from room temperature down to the plate at MC of the dilution refrigerator. We use manganese as the material of wires which go to the ohmics or gates on the sample from room temperature to MC plate. We chose manganese, which has a small enough resistance in order to reduce the Johnson noise in the wires and a high enough thermal conductivity for thermal anchoring. Below MC plate to the sample, copper wires, which have very high thermal conductivity, are chosen in order to suppress the temperature gradient between the MC plate and the sample as much as possible. All the wires are thermally anchored to the fridge by wrapping them around copper posts at several temperature stages. This anchoring causes a parasitic capacitance to the ground of about 0.5 nF (Fig. 5.2). All gates are connected to room temperature voltage sources via RC and copper powder filters (parasitic capacitance to ground ~ 0.4 nF) mounted below the MC as depicted in Fig. 5.2 and some of them have room temperature pi filters. We have such 3 different filters (RC, copper, and pi filters) in order to have a good filtering over broad frequency ranges. More discussions are found in Sec. 3.3.1 of (Shafiei, 2013). RC-filters have different cut-off frequencies of 20 Hz (second order filter)¹, 150 kHz (second order filter), and 1.5MHz (first order filter) for wires connecting to the gates, slow ohmics and fast ohmics, respectively. Slow ohmics are meant to be for the average current measurement and fast ohmics are meant to be for single-shot read out measurements.

¹We realized that the distortion of the voltage pulses (Scarlino *et al.*, 2014) is caused not only by the bias-tee on the PCB but also by the RC filters on the DC wires for the gates. A cut of frequency of 20Hz is lower than what is required. By increasing the cut-off frequency, we can reduce the pulse distortion caused by RC filters. Alternatively we also started working on room-temperature analog circuits which compensate pulse distortion caused by bias-tee or RC filters.

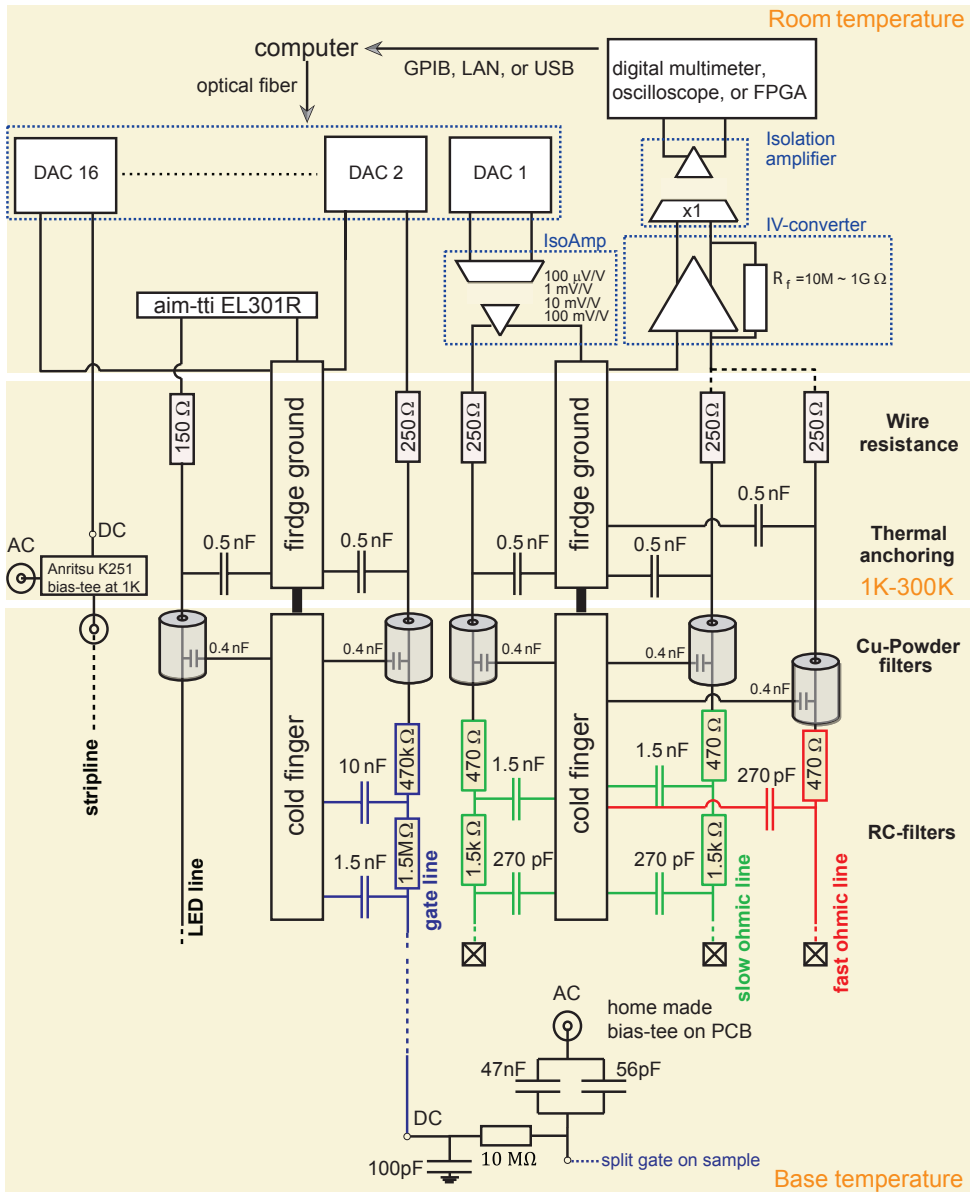


Figure 5.2: Schematic overview of DC wirings to apply voltages to the gates and the ohmics. A commercial bias-tee (Anritsu K251) is placed at 1K plate for the measurement of Device A and it is removed for the measurement of Device B and Device C. 780 nm wavelength LED is placed at the same level as the sample for the measurement of Device B and Device C.

LED

For the measurements of Device B and C, which are undoped Si/SiGe heterostructures, we implement a laser diode in the face of the sample (Scarlino, 2016). By shining light with an energy larger than the energy gap of Si before tuning the gate voltages of the device, charges, which otherwise make unwanted electrical potential in 2DEG, are released from traps. We used copper wires to connect a commercial current source (aimtti EL301R) at room temperature to the LED at the base temperature. These lines are filtered by copper powder but not by RC filters. We do not use RC filters in order to avoid heating the dilution fridge while sending high current. The laser diode used in this experiment has a wavelength of 780 nm, a maximum optical output of 5 mW (US-lasers, D780-5). More information for the use of this LED at cryogenic temperature is found in (Hendrichs, 2011). The current through the LED was limited to ~ 10 mA so that the heating due to LED does not exceed the cooling power of the dilution fridge. The LED does not reach the lasing regime but still works to release the charges from traps.

5

HIGH-FREQUENCY LINES

We have four coax lines, Line 1, 2, 3, and 4; two with 2.4 mm connectors (V-connectors) and two with 2.9 mm connectors (K-connectors or SMA connectors). The coax lines with V connectors are specified up to 50 GHz, the lines with K connectors are up to 40 GHz and the lines with SMA are up to 18 GHz. Line 1 and 2 are connected via a V-connector feedthrough and line 3 and 4 via SMA at room temperature. Each line consists of three segments all of which are produced by Keycom: (i) From room temperature to 1 Kelvin we use Keycom ULT-05 cables (outer diameter 2.2 mm; inner conductor: silver-plated brass; outer conductor: stainless steel (SUS304) with a $5 \mu\text{m}$ layer of copper). (ii) From 1 K to the mixing chamber, we use Keycom 085 semi-rigid coax lines with both inner and the outer conductor made of NbTi. (iii) From the mixing chamber to the sample holder, we use tin plated Cu coaxial cables which are flexible and therefore convenient to use. The outer conductors of the coaxial lines are thermally anchored to the dilution unit at 4 K, 1 K, ~ 800 mK and ~ 40 mK (Pictures are shown in Fig. 2.7 of (Scarlino, 2016)). In order to anchor the inner conductor of the coaxial lines as well, we use cryogenic attenuators which are anchored at 1 K (all -20 dB; INMET V-connector attenuators for the 2.4 mm lines; unknown brands, presumably XMA corporation, SMA attenuators for the 2.9 mm lines) and at the MC (-6dB Weinschel V-connector attenuators for the 2.4 mm lines; -10dB unknown brands, presumably XMA corporation, SMA attenuators for the 2.9 mm lines). The material for the coaxes is chosen according to the discussion in Sec. 3.6 of (Shafiei, 2013). The summary of coaxes and attenuators is shown in Fig. 5.3. We tested the transmission of the whole microwave line with a spectrum analyzer at room temperature and we found that the attenuation is $\sim 5\text{dB} + 0.8\text{dB} \times (\text{carrier frequency in GHz})$ in addition to the attenuation from the attenuators. Below the MC, the easily formable cables of lines 1, 2, and 3 are connected to K connectors on the PCB which are connected to the gates 11, 9 and 8, respectively and that of line 4 is connected to SMA connector on the PCB which is connected to the gate 3. On the PCB, the 4 lines are fitted with homemade resistive bias tees ($R=10 \text{ M}\Omega$, $C=47 \text{ nF}$; $1/RC \sim 2 \text{ Hz}$).

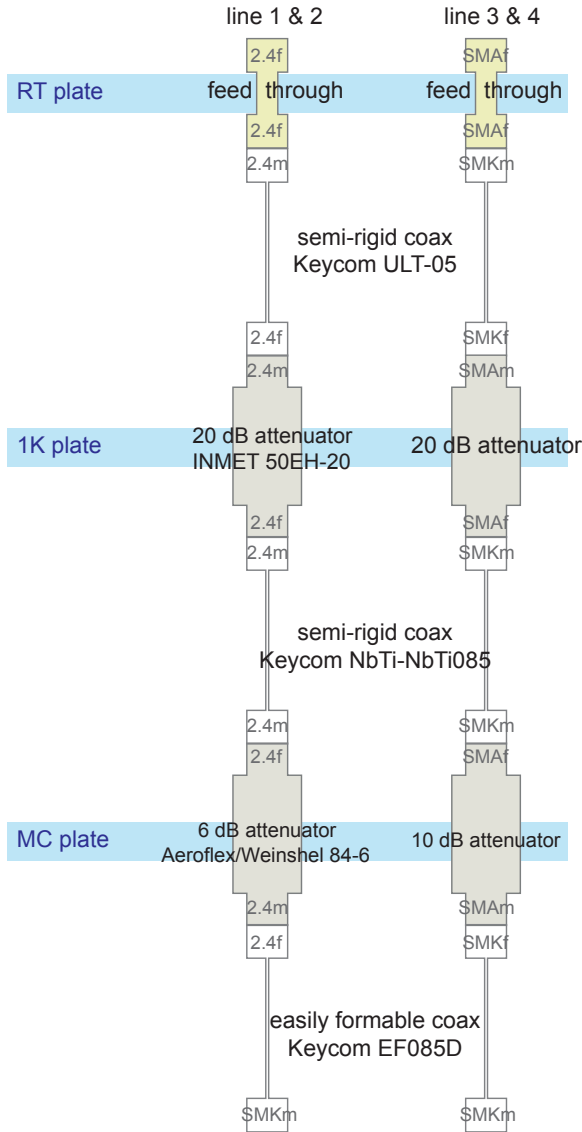


Figure 5.3: Cryogenic high-frequency coaxial lines: The lines 1 and 2 are not used in the experiments shown in this thesis. 2.4f (2.4m) stands for female (male) V-connectors, SMAf (SMAm) stands for female (male) SMA-connectors and SMKf (SMKm) stands for female (male) K-connectors.

VOLTAGE PULSE AND PHASE-CONTROLLED MICROWAVE

A voltage pulse is generated by an arbitrary waveform generator (Tektronix AWG 5014C). Phase-controlled microwave bursts are generated by an Agilent microwave vector source E8267D with the I (in-phase) and Q (out-of-phase, quadrature) components controlled by two channels of the AWG. More explicitly, ϕ in Eq. 4.6 is set by $\exp(i\phi) = V_I + iV_Q$. The on/off ratio of the I/Q modulation is 40 dB. If the microwave power arriving at the sample is not sufficiently suppressed in the “off” state, the control fidelity is reduced and the effective electron temperature increases, which in turn will result in a lower read-out and initialization fidelities. Reduced fidelities were indeed observed when applying high power microwave excitation (> 15 dBm at the source) using I/Q modulation only. As a solution, we use digital pulse modulation (PM) in series with the I/Q modulation, which gives a total on/off ratio of ≈ 120 dB. A drawback of PM is that the switching rate is lower. Therefore, the PM is turned on 200 ns before the I/Q modulation is turned on (see Fig. 5.5(b)). Light blue lines in Fig. 5.5(b) show input voltages to I/Q modulation for $\pi/2$ rotation about \hat{x} followed by $\pi/2$ rotation about \hat{y} and $\pi/2$ rotation about $-\hat{y}$ for Rabi frequency $f_1 = 1$ MHz with the time interval between gates 5 ns, where \hat{x} and \hat{y} are two axes which are orthogonal to the quantization axis on the rotating reference frame, as an example. We also observe that the total microwave burst time applied to the sample per cycle affects the read-out and initialization fidelities (Sec. 10.S2). For the experiments shown in Ch. 10, in order to keep the read-out and initialization fidelities constant we apply an off-resonance microwave burst (with microwave frequency detuned by 30 MHz from the resonance frequency) $2 \mu\text{s}$ after the on-resonance microwave burst, so that the combined duration of the two bursts is fixed. To achieve this rapid shift of the microwave frequency, we used Frequency Modulation (FM) controlled by another channel of the AWG. FM is turned on $1 \mu\text{s}$ after the on-resonance burst is turned off. The MW burst of duration ends about 100 ns – 500 ns before the detection stage.

For the measurements shown in Ch. 7, Ch. 8 and Ch. 9, we apply a voltage pulse to gate 3 and microwave excitation to gate 8. For the measurements shown in Ch. 10, we apply a voltage pulse to gate 8 and microwave excitation to gate 3.

MEASUREMENT SCHEME

We use 4-stage voltage pulses: (1) initialization to spin-down [4 -5 ms], (2) spin manipulation through microwave excitation of gate 8 or 3 [1-1.5 ms], (3) detection/single-shot spin read-out [4-5 ms] and (4) a compensation/empty stage [1 - 1.5 ms]. In Fig. 5.5(a), a voltage pulse and recorded current traces for the initialization and detection time 5 ms and the manipulation and empty time 1 ms. Due to the very long spin relaxation time, we cannot initialize by equilibration, as was commonly done in previous work (Elzerman *et al.*, 2004; Nowack *et al.*, 2011), since this would take 100 ms or more. Therefore we pulse so that only the lowest energy spin level (spin down) is below the Fermi level of the reservoir during the initialization stage. The presence of the bias tee is the reason why we use four stage pulses (Scarlinio *et al.*, 2014) while we could have used two stage pulses (Pla *et al.*, 2012). The extra two stages make the voltage level during the initialization and detection stages much less variable. At the read-out stage, an electron can leave the dot when it is projected to a spin-down state. The dot-reservoir tunnel events can be monitored in real time by collecting the charge sensor current (current running next

to the dot, depicted as a white arrow and I in the inset of Fig. 5.4), read through a room temperature I-V converter, after a low-pass-filter with a corner frequency of 30 kHz. The charge sensor current level is changed by typically 400 pA depending on the number of electrons in the dot. Thus an electron spin state is converted to a charge sensor current level and the current level is monitored on a single-shot mode (Elzerman *et al.*, 2004). By taking the measurement outcome as 1 when the sensor current surpasses the threshold and the measurement outcome as 0 when the sensor current does not surpass the threshold, the average measurement outcomes (typically we average over 150-1000 measurements) gives a measurement of the spin-up probability with some errors. The analysis of the real-time traces and the statistical analysis of the read-out events are done on-the-fly using a field-programmable gate array (FPGA) as depicted in Fig. 5.4. This allows us to measure faster without waiting for the transfer of real-time traces to a computer. For the experiments shown in Ch. 10, data points were taken by cycling through the various burst times, spin echo waiting times, or randomized gate sequences, and repeating these entire cycles 150 - 1000 times. This order of the measurements helps to suppress artifacts in the data caused by slow drift in the set-up or sample.

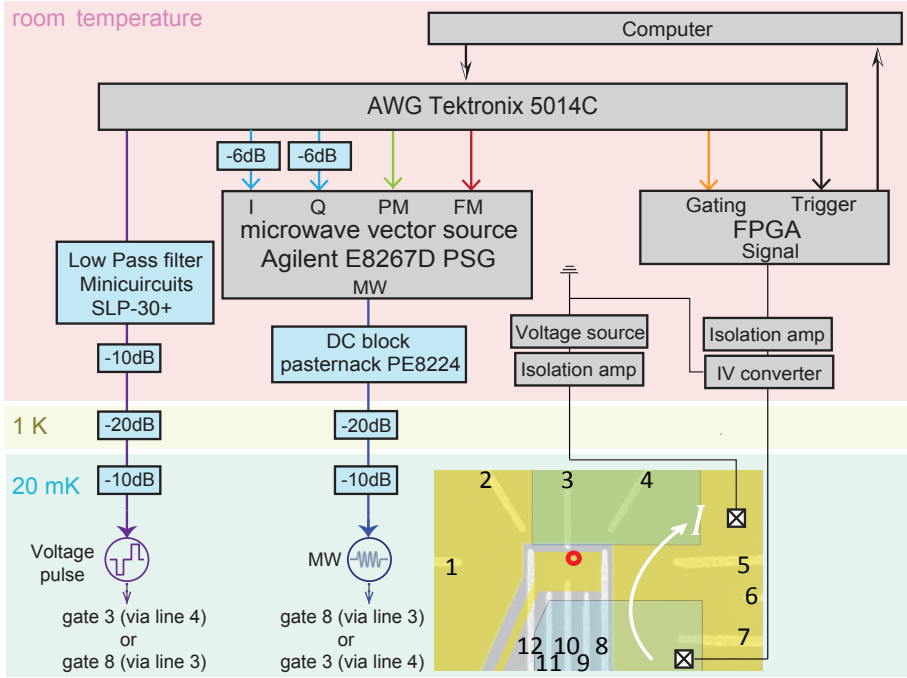


Figure 5.4: Device schematic and block diagram depicting the generation of gate voltage pulses and phase-controlled microwave bursts, and read-out trace analysis and post-analysis using an FPGA. The main components are described in the text. For the I/Q inputs, 6 dB attenuators are added to reduce the noise from the AWG. In order to reduce the noise going to the sample from the AWG, a Minicircuit low pass filter SLP-30+ and a 10 dB attenuator are added at room temperature. A Pasternack DC block PE8224 is added at room temperature behind the microwave source to reduce low frequency noise. The 30 dB attenuation at low temperature is divided over a 20 dB attenuator at the 1 K plate and a 10 dB attenuator at the MC stage for each of two high frequency lines, connected to gate 3 and gate 8. One of the two ohmic contacts of the sensing dot is connected to a room-temperature voltage source and the other is connected to the input of a homemade JFET current-to-voltage (IV) converter via RC and copper powder filters mounted at the MC stage and pi-filters at room temperature (not shown in the figure). The output voltage signal of the IV converter is digitized and processed by an FPGA. A gating pulse sent to the FPGA defines the segment of the signal that is to be analyzed. An additional trigger pulse is applied to the FPGA before the entire sequence starts for the measurements in Ch. 10. The bottom right inset shows false color device schematics of the dotted region of Fig. 5.1(a). We create a single quantum dot (QD) on Device C, its estimated location for the measurements presented in Ch. 7, Ch. 8, and Ch. 9 is presented by the red circle.

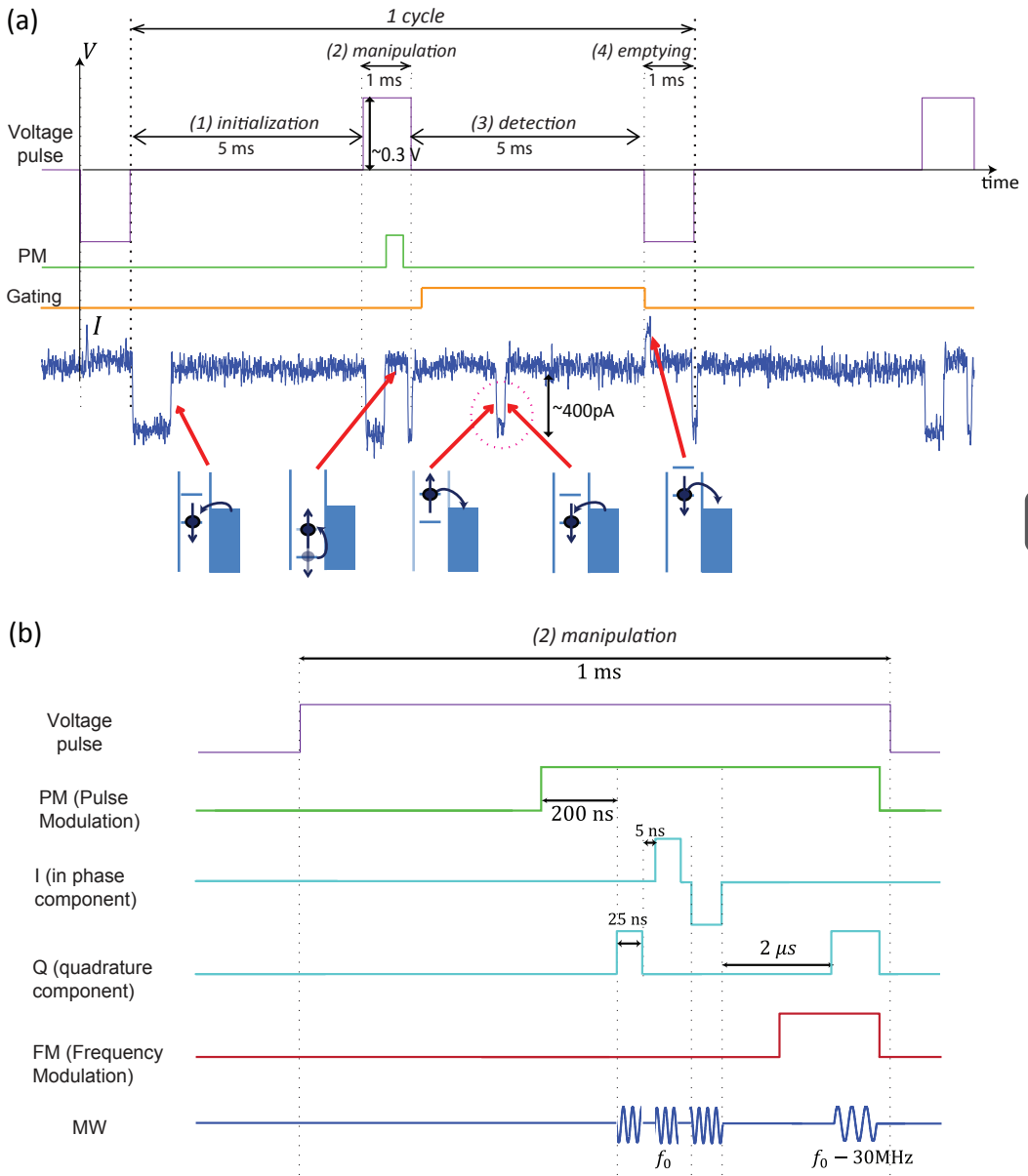


Figure 5.5: (a) Measurement scheme consisting of 4 stages (see main text) along with an example trace of recorded during the pulse cycle (blue line) and cartoons illustrating the dot alignment and tunnel events, voltage pulse (purple line), the pulse used for PM (green line), and gating the FPGA (orange line). During stages (1) and (3), the Fermi level in the reservoir is set in between the spin-down and spin-up energy levels so that only a spin-down electron can tunnel into the dot and only a spin up electron can tunnel out. During stage (2), the dot is pulsed deep into Coulomb blockade, in order to minimize photon-assisted tunneling. When a step is observed during stage (3), see the spike inside the dotted circle, we count the electron as spin-up. Stage (4) serves to keep the DC component of the pulse zero and to symmetrize pulse distortions from the bias tee. In the process, the QD is emptied. The spike during the manipulation stage is due to the influence of the microwave burst (here 700 μs) on the detector. The gating of the FPGA opens 50 μs after the voltage pulse is set for the stage (3) considering the time needed for the voltage pulse reaching the sample and the signal from the sample reaching the detector. (b) Voltage pulse (purple line), the pulses used for PM (green line, the same as in (a)), for I/Q modulation (light blue lines), and FM (red line) during the stage (2). See the text for details.

6

PHOTON-ASSISTED TUNNELING ON A SINGLE AND A DOUBLE QUANTUM DOT

In this chapter, we show preliminary measurements towards electron spin resonance in Si/SiGe quantum dots. Contrary to GaAs, spin-orbit interaction is weak in Si and so an antenna or micromagnets is required for the qubit manipulation as discussed in Sec. 2.4.

For Device A, we choose an on-chip antenna, adjacent to a Si/SiGe quantum dot, to produce microwave excitation and static magnetic field gradients, by driving with both d.c. and a.c. currents. For Device B, we use a local magnetic field gradient from a micromagnet for spin manipulation.

In the first part of this chapter (Sec. 6.1-6.4), we perform transport measurements on a single quantum dot using Device A. The response with a microwave excitation via an on-chip antenna shows signatures of photon-assisted tunneling on a single quantum dot while only having a small effect on charge stability. We also study the heating effects by sending d.c. current to the antenna on the transport characteristics of a single quantum dot and evaluate the potential of using such an antenna to perform single-spin ESR experiments in Si/SiGe devices.

In the second part of this chapter (Sec. 6.5-6.6), we performed charge sensing measurements on a double quantum dot using Device B. The response with a microwave excitation via one of the gate electrodes shows signatures of photon-assisted tunneling on a double quantum dot. We also discuss the potential of using a micromagnet field gradient for ESR experiments.

The part of work shown in this chapter has been published as: E. Kawakami, P. Scarlino, L. R. Schreiber, J. R. Prance, D. E. Savage, M. G. Lagally, M. A. Eriksson, and L. M. K. Vandersypen, *App. Phys. Lett.* **103**, 132410 (2013).

6.1. CHARGE STABILITY OF DEVICE A

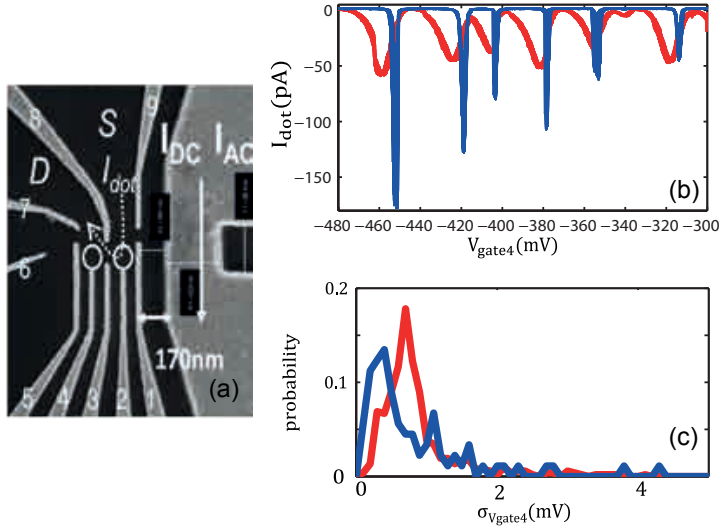


Figure 6.1: (a) Scanning electron micrograph of a device with identical design to the one we used. The quantum dot is formed at the locations of the left or right circle, depending on the measurement. Transport measurements are performed by applying a voltage between the source and drain reservoirs (S and D) and monitoring the current I_{dot} through the dot. The microwave antenna, on the right of the image, consists of a short wire connecting the two arms of a coplanar stripline. (b) Measured current through the left dot as a function of the voltage on gate 4, under microwave irradiation via the on-chip antenna at $f = 20$ GHz (red lines); the microwave source emits +10 dBm, there is a -10 dB attenuator at room temperature, and a -20 dB attenuator at 1 K) and in the absence of the microwave radiation (blue lines). $V_{SD} = -50 \mu\text{eV}$ in both cases (all V_{SD} include thermal voltages). (c) Histogram of the charge noise expressed in units of gate voltage with microwave excitation (red) and without microwave excitation (blue).

Device A is based on a phosphorus-doped Si/SiGe heterostructure with a strained Si quantum well approximately 75 nm below the surface. A thick rf antenna (Ti=Au, 5 nm=305 nm) was fabricated near the dot gates aiming for producing AC magnetic field to achieve ESR and field gradient to mix the $m = 0$ triplet T_0 with the singlet S for the detection. Palladium surface gates labeled 1-9 in Fig. 6.1(a) can be used to form a single dot or a double dot. The experiments shown here use a single dot. An on-chip antenna (Ti/Au, 5 nm/305 nm) is fabricated close to the dot gates, as shown in Fig. 6.1(a).

First, we test whether the charge stability of the Si/SiGe quantum dot in the few-electron regime is affected by microwave excitation of the antenna. The electric field component of the excitation may perturb and rearrange charges trapped in the substrate, thereby generating electrical noise. An AC excitation of $f = 20$ GHz is applied to both ends of the antenna. The ratio of the microwave electric versus magnetic field strength at the dot depends on the relative phase of the excitation at the two ends of the antenna. (See Fig. 6.S1(a) in the supplementary section of this chapter.) In the measurements reported here, the relative phase is arbitrary. To probe charge stability, we repeatedly measure the current through the left quantum dot, by sweeping the voltage

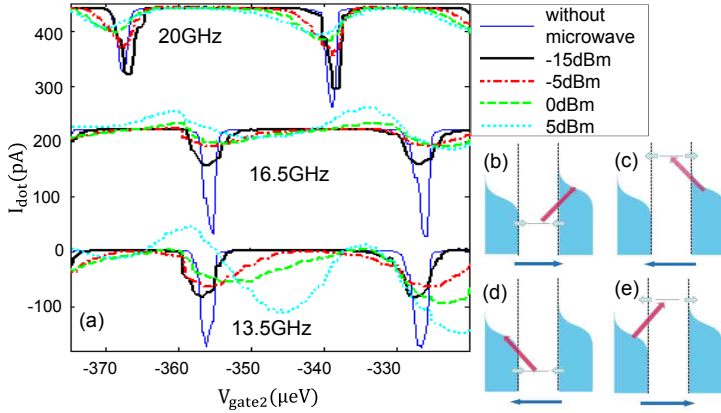


Figure 6.2: (a) Measured current through the right dot as a function of the voltage on gate 2 for different microwave powers and frequencies applied to the antenna. $V_{SD} = -58 \mu\text{V}$ (the lines are offset for clarity). The 10 mV shift in the Coulomb peak position between 16.5 GHz and 20 GHz is due to a background charge switch, which occasionally occurs in this sample, both with and without microwave excitation. (b–e) Schematics of the energy diagram of the quantum dot for $V_{SD} < 0$. (b) and (c) show PAT through the right barrier at two different gate voltages. (d) and (e) show PAT through the left barrier at two different gate voltages. The net electron flow is from the drain to the source in (b, e) and from the source to the drain in (c, d).

on gate 4 with and without microwave radiation applied to the antenna. The measured Coulomb peaks from 29 repetitions are plotted on the top of each other in Fig. 6.1(b). The microwave excitation broadens the Coulomb peaks to the point where they begin to overlap. The broadening is due to heating and photon-assisted tunneling, which is discussed further below. We evaluate charge stability in units of gate voltage $\sigma_{V_{\text{gate}4}}$ ($\sigma_{V_{\text{gate}4}} = \sigma_{I_{\text{dot}}} / (dI_{\text{dot}}/dV_{\text{gate}4})$), as charge noise in the substrate affects the dot in a similar way as gate voltage noise. We calculate $\sigma_{V_{\text{gate}4}}$ over $-483 \text{ mV} < V_{\text{gate}4} < -300 \text{ mV}$, restricting ourselves to current levels $I_{\text{dot}} < -2 \text{ pA}$, where $\sigma_{V_{\text{gate}4}}$ is $\sigma_{I_{\text{dot}}}$, the standard deviation of the current level over 29 repetitions, divided by $dI_{\text{dot}}/dV_{\text{gate}4}$, the numerical derivative of the current with respect to the gate voltage. The histogram of $\sigma_{V_{\text{gate}4}}$ is shown in Fig. 6.1(c).

We see that microwave excitation produces only a small shift in the distribution of $\sigma_{V_{\text{gate}4}}$, i.e., there is only a small increase in charge noise, even with a high power applied to the antenna. We measured the GaAs sample in the same setup and the charge stability was better than the SiGe sample used in this work, telling us that the observed noise results from the sample and not from the set-up. The two traces in Fig. 6.1(b) are recorded under identical conditions. Dot currents were measured using a low bandwidth (200 Hz) I-V converter with a noise floor of $5 \text{ fA}/\sqrt{\text{Hz}}$.

6.2. PHOTON-ASSISTED TUNNELING ON A SINGLE QUANTUM DOT

We now analyze the Coulomb peak shape in the presence of microwave excitation. We show the response for different excitation frequencies and microwave powers in Fig. 6.2(a). We interpret the microwave response in terms of photon-assisted tunneling (PAT) in a single quantum dot, which gives a net contribution to current when the microwave field couples asymmetrically to the device (Braun and Burkard, 2008; Dovinos and Williams, 2005; Oosterkamp *et al.*, 1997; Prati, Latempa, and Fanciulli, 2009). Specifically, the microwaves can couple differently to the dot, to the source, and to the drain, as discussed in (Oosterkamp *et al.*, 1997). This results in unequal voltage drops at the left and right tunnel barriers due to the a.c. excitation. Figs. 6.2(b-e) depict the extreme cases, where there is an a.c. voltage drop only across the right and left barrier, respectively. When the dot level is above the Fermi level of a reservoir by exactly the microwave energy, tunneling from the reservoir into the dot across this barrier is made possible through PAT, as depicted by the long red arrows in Figs. 6.2(c,e). Similarly, the dot can be depopulated by PAT if it is below the Fermi level of a reservoir by exactly the microwave energy, as shown in Figs. 6.2(b,d). Once the dot is populated (depopulated) through PAT, it can depopulate (populate) by tunneling through either barrier, as represented by the short gray arrows in Figs. 6.2(b-e). The sequence of population and depopulation induces a non-zero net electron flow as indicated by the blue arrows at the bottom of Figs. 6.2(b-e), which would be present even without a voltage bias across the dot (Kouwenhoven *et al.*, 1994a,b). The pumping contribution, which is asymmetric, adds to the gate-voltage symmetric contribution from the bias. A further asymmetric contribution to net current can arise from tunnel-barrier modulation as discussed in (Braun and Burkard, 2008; Bruder and Schoeller, 1994; Kouwenhoven *et al.*, 1991).

The asymmetry of the Coulomb peaks for $f = 13.5$ GHz and 16.5 GHz in Fig. 6.2(a) indicates that the left barrier has the larger a.c. voltage drop, corresponding to the situation of Figs. 6.2(d,e). On the right side of the peaks (shown in Fig. 6.2(d)), PAT leads to extra negative current and on the left side (the case of Fig. 6.2(e)) to extra positive current. Thus, the single dot operates as an electron pump under microwave irradiation. As expected, the pumping current becomes more pronounced with stronger microwave power (Braun and Burkard, 2008; Oosterkamp *et al.*, 1997), and eventually it can dominate transport through the dot. The asymmetry of the peaks is reversed for $f = 20$ GHz, indicating that here the right barrier has the larger a.c. voltage drop, corresponding to the situation of Figs. 6.2(b,c). A qualitatively similar frequency and power dependence of the Coulomb peak shape was observed when applying microwave excitation to gate 2, indicating that these observations are not specific to excitation of the antenna. (See Fig. 6.S1(b) in the supplementary section of this chapter.)

6.3. HEATING EFFECT DUE TO D.C. CURRENT

Next, we turn to applying a d.c. current to the antenna, creating a local static magnetic field gradient at the position of the dots. To detect ESR using transport measurements in the spin blockade regime (often the method of choice (Brunner *et al.*, 2011; Koppens *et al.*, 2006; Ono *et al.*, 2002)), S - T_0 mixing, which lifts spin blockade, should be faster

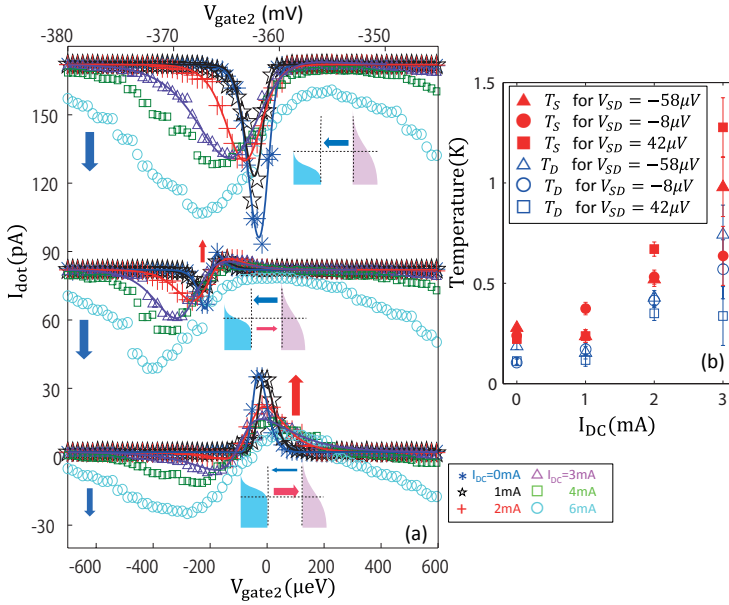


Figure 6.3: (a) Measured current through the right dot as a function of the voltage on gate 2 with different d.c. currents through the antenna (see symbols in the legend). The voltage difference between the source and drain is $V_{SD} = -58 \mu\text{V}$, $-8 \mu\text{V}$ and $42 \mu\text{V}$ (the lines are offset for clarity). The solid lines are fits to Eq. 6.4 with the temperatures in the source T_S and in the drain T_D as fitting parameters. Insets show schematics of the energy levels for the corresponding V_{SD} , and for the case where the temperature is higher in the source reservoir than in the drain. (b) Temperatures in the source and drain reservoir as a function of d.c. current through the antenna extracted from the fits in panels (a). The error bars indicate 95% confidence intervals for the fitting parameters T_S and T_D .

than 1 MHz. This gives current levels $\sim 160 \text{ fA}$, which is a good target value to give an observable contrast between parallel and anti-parallel spins (Koppens *et al.*, 2006). Based on numerical simulations of the magnetic field profile generated by the antenna, we estimate that a 4 mA d.c. current produces a $\sim 40 \mu\text{T}$ field difference between two dots that are 30 nm apart and separated from the antenna by 200 nm (the lateral distance between the center of the two dots and the end of the on-chip antenna). A $\sim 40 \mu\text{T}$ field difference is ~ 3 times higher than the intrinsic nuclear field difference in Si/SiGe (Maune *et al.*, 2012), and would give a 1.1 MHz S - T_0 mixing rate for a g -factor of 2. A further contribution to singlet-triplet mixing arises when the microwave field amplitude is different in the two dots (with this sample, we expect 10% of amplitude difference), causing the spins to rotate at different Rabi frequencies (Koppens *et al.*, 2006).

The d.c. current that can be applied is ultimately limited by Joule heating. This increases the temperature of the reservoirs and broadens the Coulomb blockade peaks. We have determined the heating of the electron reservoirs by the d.c. biased antenna. Fig. 6.3(a) show a Coulomb peak measured while applying d.c. currents up to 6 mA for three different source-drain voltages $V_{SD} = -58 \mu\text{V}$, $-8 \mu\text{V}$, and $+42 \mu\text{V}$. The horizontal

axis of Fig. 6.3(a) is the electrochemical potential of the dot, converted from V_{gate2} using the conversion factor $50 \mu\text{eV}/\text{mV}$ (extracted from Coulomb diamonds). According to the Landauer formula (Datta, 1997; Hoffmann and Linke, 2009; Mani *et al.*, 2011), the current through a single quantum dot as a function of energy ϵ_0 is given by

$$I(\epsilon_0) = -2eh \int_{-\infty}^{\infty} (f_{S(\epsilon)} - f_{D(\epsilon)}) \tau(\epsilon - \epsilon_0) d\epsilon, \quad (6.1)$$

where $\tau(\epsilon)$ is the transmission coefficient of the quantum dot as a function of energy ϵ ,

$$\tau(\epsilon) = \frac{(\Gamma/2)\pi}{(\Gamma/2)^2 + \epsilon^2}, \quad (6.2)$$

and $f_S(\epsilon)$ ($f_D(\epsilon)$) is the Fermi distribution of the source (drain),

$$f_i(\epsilon) = \exp\left(\frac{\epsilon - \mu_i}{kT_i}\right) + 1, \quad (6.3)$$

with $i = S, D$, $\mu_S - \mu_D = V_{SD}$, k Boltzmann's constant and T the temperature. If the tunnel coupling Γ between the dot and the reservoir is much less than kT , the transmission coefficient is well approximated by a delta function: (Foxman *et al.*, 1993) $\tau(\epsilon - \epsilon_0) \approx \delta(\epsilon - \epsilon_0)$. Fitting the Coulomb peak for $V_{SD} = -8 \mu\text{V}$, without any d.c. current or a.c. excitation, (* symbols in Fig. 6.3(a)) with Eq. 6.1 gives $\Gamma \sim 0.9 \mu\text{eV}$ ($\sim 10 \text{ mK}$). Therefore, we can apply the delta function approximation and the current can be rewritten as

$$I(\epsilon_0) = -2eh (f_S(\epsilon_0) - f_D(\epsilon_0)). \quad (6.4)$$

The Coulomb peaks of the right dot with $I_{DC} = 0 \text{ mA}$, 1 mA , 2 mA , and 3 mA and for $V_{SD} = -58 \mu\text{V}$, $-8 \mu\text{V}$ and $42 \mu\text{V}$ are fitted to Eq. 6.4 (solid lines in Fig. 6.3(a)). This expression applies as long as transport occurs via a single quantum dot level only, i.e., when the energy level spacing is larger than the temperature of the reservoirs. The smallest energy splitting in Si/SiGe quantum dots is usually the valley-orbit splitting, which is typically of the order of $100 \mu\text{eV}$ (Borselli *et al.*, 2011; Simmons *et al.*, 2010). Thus, we assume that Eq. 6.4 is a good fitting model below 1.2 K ($\sim 100 \mu\text{eV}$). Fig. 6.3(b) shows the temperatures in the source and drain reservoirs (T_S and T_D) obtained from the fits. As expected, both temperatures increase with the applied d.c. current, and the temperature in the source reservoir, which is closest to the on-chip antenna, is higher in all cases. The arrows in Fig. 6.3(a) show the direction of the electron flow at different gate voltages. At certain points, the difference of the temperatures in the two reservoirs can induce electron flow in the opposite direction of the applied bias. This looks superficially similar to the pumping currents due to PAT. We can directly compare the Coulomb peaks in Fig. 6.3(a) with the Coulomb peak at $V_{\text{gate2}} = -355 \text{ mV}$ in Fig. 6.2(a), since they are measured at the same gate voltage settings and for the same charge configuration. We see that at high microwave power, the Coulomb peak shape in Fig. 6.2(a) for the case of 13.5 GHz and 16.5 GHz has an opposite asymmetry to the Coulomb peak seen in Fig. 6.3(a), which is caused by heating below the antenna. We take this as evidence that at high power, photon-assisted tunneling effects are dominant over heating via phonons. On the other hand, the Coulomb peak shape in Fig. 6.2(a) for the case of 20 GHz is similar to the Coulomb peak seen in Fig. 6.3(a). However, we can conclude that the pumping

current observed in Fig. 6.2(a) cannot be explained by heating because of the following reasoning. There is a -10 dB attenuator at room temperature, and a -20 dB attenuator at 1 K. The additional frequency dependent attenuation in the high-frequency lines is measured to be about 0.75 dB/GHz, bringing the total attenuation at 20 GHz to -45 dB. The largest power emitted by the source in Fig. 6.2(a) is 5dBm, so the power arriving at the sample is about -40 dBm. Going into 50Ω , this power would result in 2.25 mV and 45 μ A rms amplitudes. This is 20–100 times smaller than the DC currents applied in Fig. 6.3(a), dissipating 400–10000 times less power. Since the microwave antenna has an impedance different from 50Ω , some of the incident power is reflected and the power dissipated locally is even smaller. We note that an asymmetric Coulomb peak is observed for $V_{SD} = 0$ V even without d.c. or a.c. current (see Fig. 6.3(a)). From fits to Eq. 6.4, we find that the temperature difference between the two reservoirs is around 100 mK even for $I_{DC} = 0$ as shown in Fig. 6.3(b). The d.c. line connected to the on-chip antenna goes to the room temperature current source without filtering. Thus Johnson–Nyquist noise coming from the room temperature may cause heating beneath the antenna, giving a temperature difference between two reservoirs. Similar asymmetric heating of the reservoirs was found when measuring the left dot, and when the constriction between gates 1 and 9 was pinched off.

6.4. POTENTIAL FOR USING THE ANTENNA TO PERFORM SINGLE-SPIN ESR EXPERIMENTS

In spin qubit measurements, the temperature should be smaller than the energy scale that is important for initialization and single-shot read-out: (Elzerman *et al.*, 2004; Nowack *et al.*, 2011) the Zeeman energy, which is $\sim 100 \mu\text{eV}/T$ in silicon. Another relevant energy scale is the lowest orbital splitting, or the valley-orbit splitting, typically at least 100 μeV for PSB read-out. Other energy scales such as the charging energy are significantly larger. The temperature should therefore remain well below ~ 1 K, and from the results shown in Fig. 6.3(b), this implies that we should limit the d.c. current to 2 mA. This is about two times less than the 4 mA needed for efficient detection of ESR-induced Rabi oscillations, as discussed above (We note that an oscillation can be detected even without a gradient if the magnetic excitation differs in strength between the two dots, but with a frequency given by the difference between the respective Rabi frequencies, or a much lower frequency than with field gradient.). Alternative approaches that could be used to produce a local static magnetic field gradient without Joule heating are a micromagnet (Brunner *et al.*, 2011; Pioro-Ladrière *et al.*, 2008b) or a superconducting on-chip antenna.

6.5. CHARGE STABILITY OF DEVICE B AND PHOTON-ASSISTED TUNNELING ON A DOUBLE QUANTUM DOT

In the previous sections, we presented the photon-assisted-tunneling of an electron between a dot and a reservoir. In this section, we demonstrate photon-assisted-tunneling of an electron from one dot to another dot (Oosterkamp *et al.*, 1998; Shevchenko, Ashhab, and Nori, 2010; Stehlik *et al.*, 2012) using Device B (Sec. 5.3).

The device schematic around the position of the double dot is presented with false

color in Fig. 6.4(a). A double quantum dot is formed around the position indicated by a green circle and a blue circle. Fig. 6.4(b) shows the differential conductance $\frac{dI}{dV_{\text{gate11}}}$ as a function of the voltage on gate 11 and gate 9. Tentative absolute electron numbers of the left dot and the right dot are shown in Fig. 6.4(b). The inter-dot charge transition has a negative slope because both gate 11 and 9 are more strongly coupled to the left dot than to the right dot.

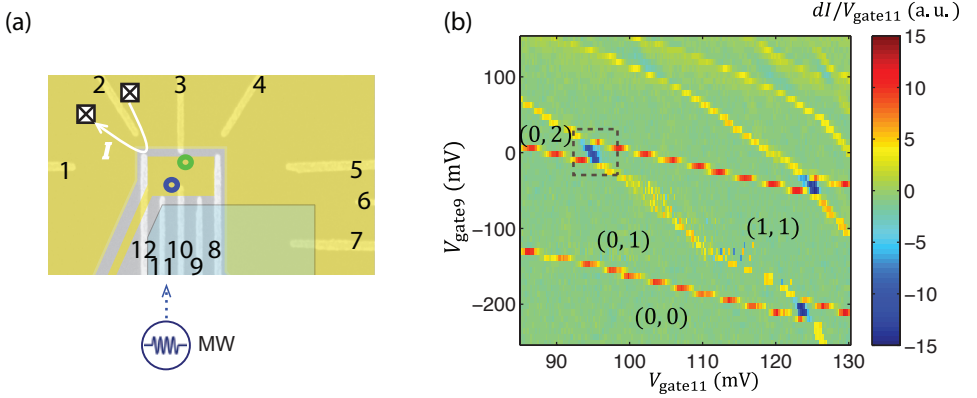


Figure 6.4: Device schematic and charge stability diagram (a) False color device image showing the fabricated pattern of split gates, labeled 1-12. For this experiment, we created a double quantum dot, with the estimated location shown by the blue and green circles. A QPC charge sensor is created between the gate 2 and gate 12. The blue semi-transparent rectangle shows the position of a 200 nm thick Co micromagnet. Microwaves are applied to gate 11 for the measurements shown in Fig. 6.5(b) and Fig. 6.6. (b) Charge stability diagram of the double dot system, measured via the differential transconductance of the QPC created between the gate 2 and gate 12. The tentative absolute electron numbers for the left dot (L) and the right dot (R) are shown by (L, R) . The dotted rectangle shows the region of the stability diagram measured in Fig. 6.5(a,b).

Fig. 6.5(a,b) show the measured charge stability diagram around the $(0,2) - (1,1)$ charge transition without microwave excitation for (a) and with microwave excitation for (b). Microwaves can induce an electron to tunnel from the right to left dot or from the left to the right dot when the microwave photon frequency is equal to the energy separation between the $(0,2)$ and $(1,1)$ charge state (Brune, Bruder, and Schoeller, 1997; Petta *et al.*, 2004; Stafford and Wingreen, 1996; Stoof and Nazarov, 1996). This photon-assisted tunneling event can be measured by charge sensing shown in Fig. 6.5(b). Four satellite peaks appear in the presence of microwave excitation. The first (second) satellite peaks on both sides of the inter-dot transition are attributed to one-photon (two-photon) process and these are $\sim \hbar\omega$ ($\sim 2\hbar\omega$) further away from the inter-dot charge transition.

Although we did not study the charge stability of Device B systematically, comparing Fig. 6.5(a) and Fig. 6.5(b), we suggest that we did not observe any significant effect on the charge stability diagram by microwave excitation to gate 11.

In Fig. 6.6(a), we plot the derivative of the QPC current measured through a lock-in amplifier as a function of detuning and applied microwave power at a fixed microwave frequency of 35 GHz. The derivative of the QPC current represents the probability of the

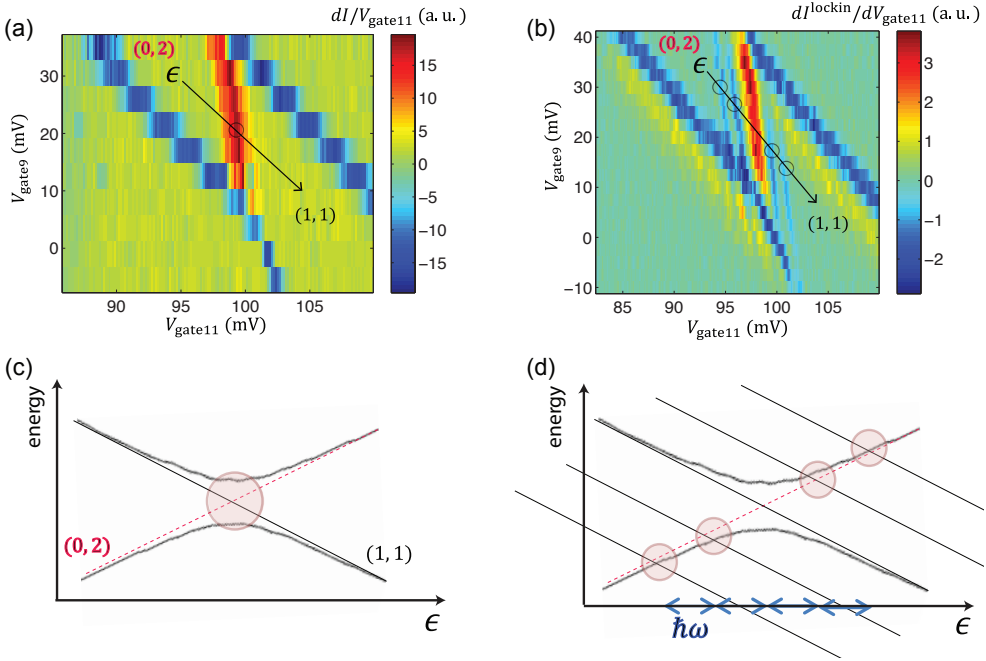


Figure 6.5: (a) Derivative of the QPC current without microwave excitation. (b) Derivative of the QPC current measured through a lock-in amplifier with 14dBm, 35 GHz microwave excitation. The microwaves were chopped at the reference frequency of the lock-in amplifier (2.015 kHz). 2 parallel lines (single and two-photon process) appear on each side of the inter-dot transition. (c,d) Energy level diagram as a function of detuning between (0,2) and (1,1) without microwave excitation for (c) and with microwave excitation for (d). The black curves represent the adiabatic energy levels with an avoided crossing. The black (dotted red) line shows the diabatic energy level of (0,2) state ((1,1) state). The red circles indicate the detuning position where the tunneling of an electron between (0,2) and (1,1) states occurs. In (d), when microwaves are applied, virtual (1,1) states whose energy levels are lower or higher by the integer multiple of $\hbar\omega$ with microwave frequency ω appear. It leads to the inter-dot tunneling at the detuning position $n\hbar\omega$, where n is an integer, further away from the inter-dot charge transition as indicated by red circles.

electron tunneling from the left to the right dot or vice versa. The probability oscillates as a function of the detuning due to multi-photon processes and as a function of the microwave power due to the Stückelberg phase (Oosterkamp *et al.*, 1998, 1997; Shevchenko, Ashhab, and Nori, 2010; Stehlik *et al.*, 2012; van der Wiel *et al.*, 1999).

As discussed above, the satellite peaks appear $n\hbar\omega$ further away from the inter-dot charge transition. However, when the microwave frequency is comparable to the tunnel coupling, the distance between the satellite peaks and the inter-dot charge transition is corrected to $\sqrt{(n\hbar\omega)^2 - (2t)^2}$. When the microwave frequency is lower than the tunnel coupling, the first satellite peaks cannot be observed. Fig. 6.6(b) shows the experimental data for the distance between the first (second) satellite peaks and the inter-dot charge transition as a function of the microwave frequency with blue (red) points. The experi-

mental data have been fit using (Shang *et al.*, 2013; van der Wiel *et al.*, 1999)

$$\alpha \delta V_{\text{gate}11} = \sqrt{(n\hbar\omega)^2 - (2t)^2}, \quad (6.5)$$

for the n -th photon process, where n is an integer, f is the microwave frequency, and t is the inter-dot tunnel coupling. From this fit, we obtained a tunnel coupling of $t \sim 7.5$ GHz.

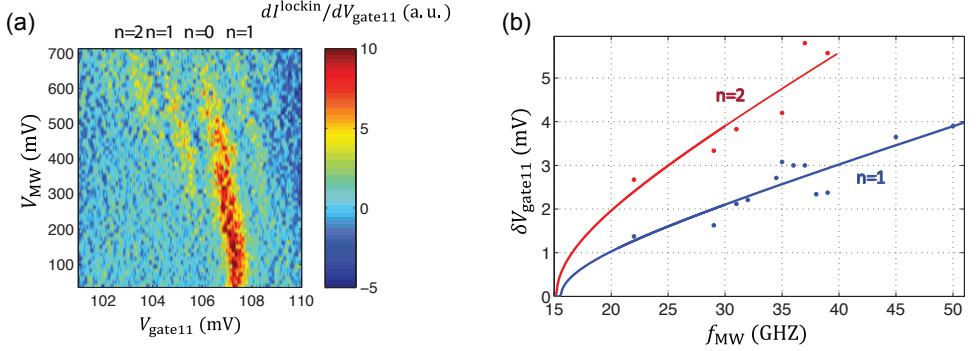


Figure 6.6: (a) Derivative of the QPC current measured through a lock-in amplifier with 35 GHz microwave excitation as a function of the microwave power on the microwave source and detuning (ϵ in Fig. 6.5, represented by the voltage on gate 11). The reference frequency of the lock-in amplifier is 3.832 kHz. (b) Distance between the main resonance and the first two satellites as a function of the applied microwave frequency f_{MW} from 22 to 50 GHz. Solid lines are best fit theory curves. The inter-dot tunnel coupling t results in a splitting of $2t$ at 0 detuning ($\delta V_{\text{gate}11} = 0$).

6.6. POTENTIAL FOR USING THE MICROMAGNET TO PERFORM SINGLE-SPIN ESR EXPERIMENTS

In Sec. 6.4, we discussed the potential for using an antenna for ESR experiments, where we concluded that we cannot run a high enough d.c. current through the antenna to perform the spin state detection in PSB regime due to the Joule heating. As implicitly already discussed in Sec. 2.4, we do not have such a concern for Device B. With the micromagnets fabricated on top of Device B, we can reach the magnetic field gradient required for the addressability (1 mT/nm, see also Appendix E.1.2), which is higher than that required for the spin state detection in the PSB regime. In this section, we discuss whether the amplitude of the electric field created on the device with microwave excitation is high enough to achieve electron spin resonance in future experiments, following (Nowack, 2009; Nowack *et al.*, 2007).

The inter-dot tunnel barrier with microwave excitation is proportional to the square of the n -th order Bessel function $J_n^2(\alpha)$ with $\alpha = \frac{eV_{\text{interdot}}^{AC}}{\hbar f_{\text{MW}}}$, where \hbar is Planck constant, e is the elementary charge, and V_{interdot}^{AC} is the voltage amplitude across the left dot and the

right dot created by a microwave excitation. As shown in Fig. 6.6, we observed the first and second photon process of the photon-assisted tunneling. Thus the maximum voltage amplitude created at the dot position in this experiment is estimated to be $V_{\text{interdot}}^{AC} \sim \alpha h f_{\text{MW}} / e \sim 0.33$ mV with $f_{\text{MW}} = 40$ GHz and $\alpha = 2$. Assuming that the voltage drops linearly over the left dot and the right dot, the amplitude of the oscillating electric field at the double dot position is calculated to be $E^{AC} = V_{\text{interdot}}^{AC} / l_{\text{interdot}}$, where l_{interdot} is the distance between the two dot centers. In order to estimate the Rabi frequency which we can obtain with this amplitude of the electric field E^{AC} , we rewrite Eq. 3.15 as

$$B^{AC} \sim \frac{1}{2} e V_{\text{interdot}}^{AC} \frac{dB_{\perp}}{dx} \frac{l_{orb}^2}{l_{\text{interdot}} \Delta_{orb}}. \quad (6.6)$$

For a rough estimation, by taking $l_{\text{interdot}} = 200$ nm, the dot diameter $l_{orb} = 50$ nm, the field gradient created by the micromagnets $\frac{dB_{\perp}}{dx} = 1$ mT/nm (Appendix G) and the orbital splitting $\Delta_{orb} = 1$ meV, the amplitude of an effective oscillating magnetic field is calculated to be $B^{AC} = 2$ mT. This magnetic field amplitude corresponds to 54 MHz Rabi frequency for an electron spin in Si and is high enough to achieve coherent driving of an electron spin considering the expected dephasing time for electron spins in Si quantum dots (Assali *et al.*, 2011).

6.7. CONCLUSIONS

In conclusion, we have demonstrated photon-assisted tunneling in a single Si/SiGe quantum dot on Device A and a double Si/SiGe quantum dot on Device B using a microwave excitation. In Device A, microwaves were applied to an antenna, which had a small effect on charge stability. In Device B, microwaves were applied to one of the surface gates, which did not have any observable effect on charge stability. On Device A, we explore the use of a d.c. current applied to the antenna for generating local, tunable magnetic field gradients. A field gradient around $1 \mu\text{T}/\text{nm}$ is achievable with a 2 mA d.c. current through the antenna, limited by Joule heating. On Device B, we measured that the maximum voltage amplitude across two dots that we created is 0.33 mV, which is high enough to perform ESR experiments when combined with the magnetic field gradient (1 mT/nm) created by the micromagnets.

SUPPLEMENTARY SECTION

In this supplementary section, we present the supplementary information for the photon-assisted tunneling measurement for one dot using Device A.

The pumping direction is determined by both the settings of the voltages on the gates and the applied microwave frequency (Braun and Burkard, 2008; Oosterkamp *et al.*, 1997). In Fig. 6.2(a), we show that the pumping direction is changed depending on the microwave frequency keeping the same gate voltage settings. The comparison between Fig. 6.2(a) and Fig. 6.S1(a) shows that the pumping direction can also be reversed by changing the gate voltages, keeping the same microwave frequency. (Note that Fig. 6.2(a) shows the measurement on the right dot while Fig. 6.S1(a) is taken on the left dot.). The reversal of the pumping current occurs when the change in gate voltages reverses

the asymmetry in the coupling of the microwaves to the corresponding barriers, as explained in (Oosterkamp *et al.*, 1997). For the case of Joule heating induced by a DC current through the antenna, in contrast, we did not observe any change in the pumping direction when changing the gate voltages, as expected.

Fig. 6.S1(a) also shows the effect of changing the relative phase of the excitation at the two ends of the antenna. In the experiment, the relative phase was varied via an uncalibrated phase shifter in the line between one end of the antenna and the microwave source. The figure clearly shows that the relative phase strongly affects the strength of the microwave response, without changing the pumping direction. This strong dependence is expected, since the relative phase of the microwaves applied to the two ends of the antenna sets the voltage amplitude at the antenna, and hence the electric field amplitude at the dot (the AC voltage is at a maximum when the AC current is at a minimum and vice versa). Also as expected, the change in the phase shifter setting required to return to the same response is approximately 1/3 smaller for 30 GHz than for 20 GHz (the phase shifter works by effectively increasing the length of the coax line). Finally, we note that asymmetric pumping was also observed when applying microwave excitation to gate 2, indicating that these observations are not specific to excitation of the antenna. (Fig. 6.S1(b))

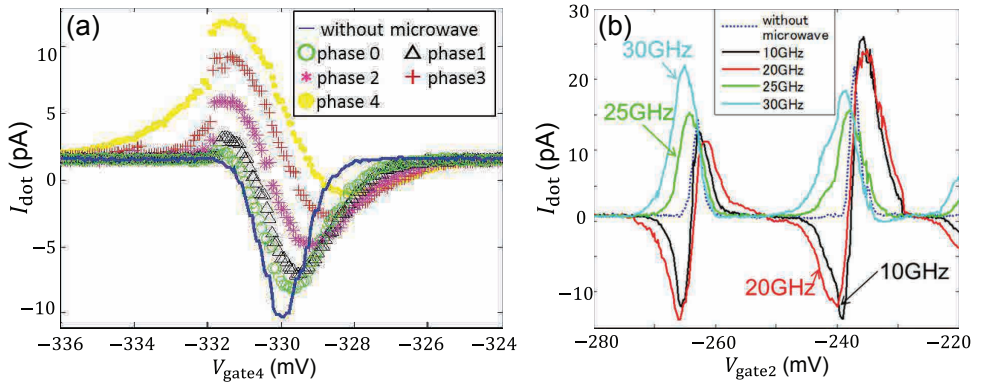


Figure 6.S1: (a) Measured current through the left dot as a function of the voltage on gate 4 with the excitation of 20 GHz 0 dBm microwave applied to the antenna by changing the relative phase of the excitation at the two ends of the antenna. The phase (uncalibrated) is incremented from phase0 (green open circles) to phase1 (black triangles), phase2 (pink asterisks), phase3 (red crosses), and phase4 (yellow filled circles). $V_{SD} = -35 \mu\text{V}$ (b) Measured current through the right dot as a function of the voltage on gate 2 for different microwave frequencies (here the microwaves are applied to gate 2 instead of the antenna). The current in the absence of microwaves (blue dotted line) is shown for comparison. $V_{SD} = 25 \mu\text{V}$

7

ELECTRICAL CONTROL OF A LONG-LIVED SPIN QUBIT IN A SI/SiGE QUANTUM DOT

Nanofabricated quantum bits permit large-scale integration but usually suffer from short coherence times due to interactions with their solid-state environment (Eckstein and Levy, 2013). The outstanding challenge is to engineer the environment so that it minimally affects the qubit, but still allows qubit control and scalability. Here we demonstrate a long-lived single-electron spin qubit in a Si/SiGe quantum dot with all-electrical two-axis control. The spin is driven by resonant microwave electric fields in a transverse magnetic field gradient from a local micromagnet (Tokura *et al.*, 2006), and the spin state is read out in single-shot mode (Elzerman *et al.*, 2004). Electron spin resonance occurs at two closely spaced frequencies, which we attribute to two valley states. Thanks to the weak hyperfine coupling in silicon, a Ramsey decay timescale of 900 ns is observed, almost two orders of magnitude longer than the intrinsic timescales in GaAs quantum dots (Chekhovich *et al.*, 2013; Petta *et al.*, 2005), while gate operation times are comparable to those reported in GaAs (Hanson *et al.*, 2007; Koppens *et al.*, 2006; Obata *et al.*, 2010). The spin echo decay time is around 40 μ s both with one and with four echo pulses, possibly limited by inter-valley scattering. These advances strongly improve the prospects for quantum information processing based on quantum dots.

The work in this chapter has been published as: E. Kawakami*, P. Scarlino*, D. R. Ward, F. R. Braakman, D. E. Savage, M. G. Lagally, Mark Friesen, S. N. Coppersmith, M. A. Eriksson and L. M. K. Vandersypen, *Nature Nanotech.* **9**, 666 (2014).

7.1. INTRODUCTION

The proposal by Loss and DiVincenzo (Loss and DiVincenzo, 1998) to define quantum bits by the state of a single electron spin in a gate-defined semiconductor quantum dot has guided research for the past 15 years (Hanson *et al.*, 2007). Most progress was made in well-controlled III-V quantum dots, where spin manipulation with two (Nowack *et al.*, 2011; Petta *et al.*, 2005), three (Medford *et al.*, 2013) and four (Shulman *et al.*, 2012) dots has been realized, but gate fidelities and spin coherence times are limited by the unavoidable interaction with the fluctuating nuclear spins in the host substrate (Chekhovich *et al.*, 2013; Petta *et al.*, 2005). While the randomness of the nuclear spin bath could be mitigated to some extent by feedback techniques (Bluhm *et al.*, 2010a), eliminating the nuclear spins by using group IV host materials offers the potential for extremely long electron spin coherence times. For instance, a dynamical decoupling decay time of half a second was observed for an electron bound to a P impurity in 28Si (Muhonen *et al.*, 2014).

Much effort has been made to develop stable spin qubits in quantum dots defined in carbon nanotubes (Churchill *et al.*, 2009; Laird, Pei, and Kouwenhoven, 2013), Ge/Si core/shell nanowires (Higginbotham *et al.*, 2014), Si MOSFETs (Hao *et al.*, 2014; Yang *et al.*, 2013) and Si/SiGe 2D electron gases (Maune *et al.*, 2012; Prance *et al.*, 2012; Zwanenburg *et al.*, 2013). However, coherent control in these group IV quantum dots is so far limited to a Si/SiGe singlet-triplet qubit with a spin dephasing time of 360 ns but single-axis control only (Maune *et al.*, 2012) and a carbon nanotube single-electron spin qubit, with two-axis control but a Hahn echo decay time of only 65 ns (Laird, Pei, and Kouwenhoven, 2013).

7

7.2. DEVICE AND QUANTUM DOT CHARACTERIZATION

The device schematic around the position of the dot is presented with false color in Fig. 7.1(a). This device is based on an undoped Si/SiGe heterostructure with two layers of electrostatic gates: a set of accumulation gates and a set of depletion gates, accommodated with two Co micromagnets. Compared to conventional, doped heterostructures, this technology strongly improves charge stability (Maune *et al.*, 2012). The design of the fine gates is meant to be used for the creation of a double quantum dot but in the experiments shown here we created only one dot.

By applying $\sim +150$ mV on two accumulation gates, we induce a two-dimensional electron gas (2DEG) in a Si quantum well. The right dot is tuned to the few-electron regime by adjusting the voltages on depletion gates 3, 4, 5, 8, 9 and 10. Fig. 7.1(b) shows the differential transconductance $\frac{dI}{dV_{gate3}}$ as a function of the voltages on gates 3 and 5. No other charge transitions are observed when pushing the voltage of gate 3 down to -375 mV with the other gate voltages kept at the same values as used in Fig. 7.1(b), which permits us to assign tentative absolute electron numbers as shown in Fig. 7.1(b). The experiment is done at the 0-1 charge transition. This quantum dot presents an addition energy of 9 meV and an orbital level spacing of $450 \mu\text{eV}$, estimated by pulse spectroscopy measurements. From the addition energies we extract a dot radius $r \sim 21$ nm (in the approximation of a circular QD); from the orbital level spacing we deduce $r \sim 28$ nm assuming a harmonic confining potential and again a circular dot. Pulse spectroscopy

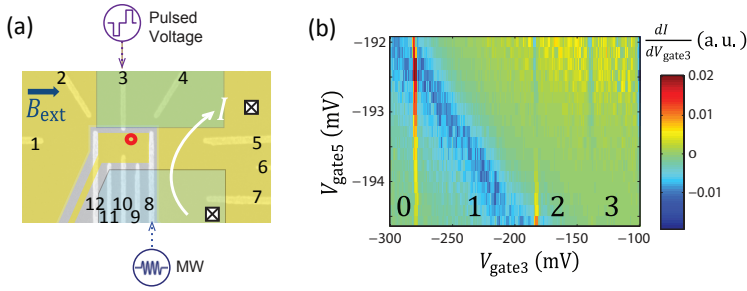


Figure 7.1: Device schematic and charge stability diagram (a) False color device image showing a fabricated pattern of split gates, labeled 1-12. The region shown is outlined with dotted lines in Fig. 5.1. For the experiments in Ch. 7-9, we create a single quantum dot (QD), estimated location at the red circle, and a sensing dot (SD). The current I is measured as a function of time for a fixed voltage bias of $-600 \mu\text{eV}$. The voltage pulses are applied to gate 3 and the microwaves are applied to gate 8. The blue semi-transparent rectangles show the position of two Co 200 nm thick micromagnets. The yellow shaded pieces show the location of two accumulation gates, one for the reservoirs and another for the double quantum dot region. (b) Charge stability diagram of the single dot system, measured via the sensing quantum dot differential transconductance as a function of $V_{\text{gate}3}$ and $V_{\text{gate}5}$. The sharp nearly vertical lines correspond to changes in the dot occupation. The broad diagonal blue line corresponds to a Coulomb peak in the sensing dot. The tentative absolute electron numbers 0-3 are shown.

measurements (not reported here) also show the linear dependence of the Zeeman splitting of the lowest orbital state as a function of external magnetic field, allowing us to calibrate the conversion factor between pulse amplitude and energy. The left dot is not used in the experiment and the constrictions between gates 4 and 8 and between 3 and 10 are pinched off. The tunnel rate between the dot and the reservoir is adjusted to ~ 1 kHz, so that dot-reservoir tunnel events can be monitored in real time using the sensing dot (Fig. 7.1(b)). The electron temperature estimated from transport measurements is ~ 150 mK (not applying microwaves).

Thanks to the capacitive coupling between the dot and the sensing QD, the current level of the sensing QD is decreased (increased) by ~ 400 pA when an electron jumps from the dot to the reservoir (from the reservoir to the dot). We use a room temperature IV converter to record the sensing dot current, I , using a low-pass filter with ~ 20 kHz cut-off to obtain a sufficient signal-to-noise ratio.

7.3. ELECTRON SPIN RESONANCE SPECTROSCOPY

For all measurements shown here, we use 4-stage voltage pulses applied to gate 3 and microwave excitation to gate 8 (Fig. 7.1(b)). The initialization and read-out stages take 4 ms and the manipulation and emptying stages take 1 ms. Both the initialization fidelity and the read-out fidelities were measured to be ~ 0.95 (Sec. 7.S7). The cycle was typically repeated 150-1000 times, unless otherwise stated, to measure the spin-up probability P_{\uparrow} . The external magnetic field was applied along the x axis in Fig. 5.1(a). As discussed in Sec. 3.1.1, we applied the magnetic field along this direction to maximize the field gradient for EDSR at the position of the dot.

The measured spin resonance frequency as a function of applied magnetic field is

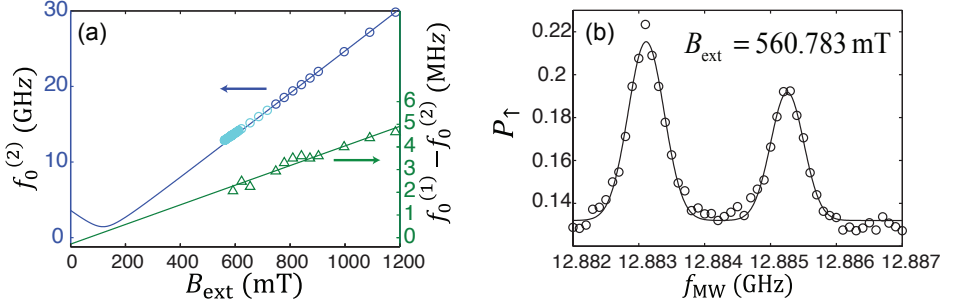


Figure 7.2: : Qubit spectroscopy a, Measured microwave frequency that matches the electric dipole spin resonance (EDSR) condition $f_0^{(2)}$ (dark blue and light blue circles) and the difference between the two resonance frequencies $f_0^{(1)} - f_0^{(2)}$ (green triangles) as a function of externally applied magnetic field. The 6 points where $f_{\text{MW}} > 6$ GHz are measured by two-photon transitions (Ch. 8). The microwave burst time $t_p = 700 \mu\text{s} \gg T_2^*$, effectively corresponding to continuous wave (CW) excitation (here we used low power excitation, $P = -33$ dBm to -10 dBm at the source, decreasing with lower microwave frequency). The upper of the two resonances in panel (b) is shown. The blue solid curve is a fit to the dark blue circles using equation (1). The light blue circles are excluded from the fit; presumably the micromagnet begins to demagnetize here. The green line is a linear fit to the green triangles. b, Measured spin-up probability P_{\uparrow} as a function of applied microwave frequency f_{MW} for $B_{\text{ext}} = 560.782$ mT ($P = -33$ dBm), averaged over 200 minutes, i.e. 1200000 single-shot measurements.

shown in Fig. 7.2(a). We can extract the electron g -factor using the relation:

$$hf_0 = g\mu_B B_{\text{local}}, \quad (7.1)$$

where $B_{\text{local}} = \sqrt{(B_{\text{ext}} + B_{\parallel})^2 + B_{\perp}^2}$, h is Planck constant and μ_B is the Bohr magnetron. From fits to Eq. 7.1 (blue curve in Fig. 7.2(a)), we find $g = 1.998 \pm 0.002$, where we used $B_{\parallel} = -120$ mT and $B_{\perp} + 50$ mT, based on numerical simulation of the stray magnetic field from the micromagnet at the estimated dot location (Sec. 3.2).

Surprisingly, when measuring the EDSR peak at a sufficiently low power to avoid power broadening, we resolve two lines, separated by 2-4 MHz in the range $B_{\text{ext}} = 0.55$ -1.2 T (Fig. 7.2(b)). We return to the origin of this splitting in Sec. 7.6.

Fitting each resonance peak with a Gaussian function (Eq. 4.30) yields $\delta f_{\text{FWHM}}^{(1)} = 0.63 \pm 0.06$ MHz for the higher-energy transition at frequency $f_0^{(1)}$ and $\delta f_{\text{FWHM}}^{(2)} = 0.59 \pm 0.56$ for the lower-energy transition at frequency $f_0^{(2)}$. From this line width, we extract a dephasing time $T_2^* = \frac{2\sqrt{\ln(2)}}{\pi\delta f_{\text{FWHM}}} = 840 \pm 70$ ns (Eq. 4.41), 30-100 times longer than T_2^* in III-V dots (Chekhovich *et al.*, 2013; Hanson *et al.*, 2007; Koppens *et al.*, 2006; Petta *et al.*, 2005). This dephasing timescale can be attributed to the random nuclear field from the 0.05% ^{29}Si atoms in the substrate with standard deviation $\sigma_B = 9.6 \mu\text{T}$, consistent with theory (Assali *et al.*, 2011). Previous T_2^* measurements in Si/SiGe dots (Maune *et al.*, 2012; Wu *et al.*, 2014) gave somewhat shorter values of 220 ns to 360 ns. T_2^* is expected to scale with the square root of the number of nuclear spins the electron wavefunction overlaps with (Eq. 3.43). Considering these other measurements were done on double dots, this would imply variations in the volume per dot up to a factor of 7, if nuclear spins were dominating the decay. Given the presence of a magnetic field gradient $dB_{\parallel}/dx \sim 0.2$ mT/nm

(Sec. 3.2), the line width also gives an upper bound on the electron micromotion induced by low-frequency charge noise of ~ 50 pm (rms).

7.4. COHERENT CONTROL OF ELECTRON SPIN

Coherent control of the electron spin is achieved by applying short high-power microwave bursts of duration t_p . Fig. 7.3(a) shows the measured spin-up probability, P_1 , as a function of f_{MW} and burst time t_p , which exhibits the chevron pattern that is characteristic of high-quality oscillations (here two partly overlapping patterns). On resonance, the spin rotates at the bare Rabi frequency, f_1 . When detuned away from resonance by $\Delta f = f_{\text{MW}} - f_0$, the spin rotates about a tilted axis, the oscillation frequency increases as $\sqrt{\Delta f^2 + f_1^2}$, and the visibility is reduced. The fast Fourier transform over the microwave burst time of the data in Fig. 7.3(a) is shown in Fig. 7.3(c) and exhibits the expected hyperbolic dependence as a function of Δf for both transitions, $f_0^{(1)}$ and $f_0^{(2)}$. We fit both hyperbola with one free parameter f_1 each (black rectangles and red circles), giving $f_1^{(2)} = 5.0 \pm 0.6$ MHz ($B_1 \sim 0.18$ mT) and $f_1^{(1)} = 3.1 \pm 0.6$ MHz (errors arise from the finite number of points in the FFT) for the respective transitions. These single-spin Rabi frequencies are comparable to those observed in GaAs (Koppens *et al.*, 2006; Obata *et al.*, 2010). The relative amplitude of the oscillations at $f_0^{(2)}$ and $f_0^{(1)}$ is about 30/70; note that despite its lower weight, the peak at $f_0^{(2)}$ is tallest in Fig. 7.2(b), since its Rabi frequency is a factor of 1.5 ± 0.2 higher than that of the other peak (Sec. 7.S5). The extracted Rabi frequencies of both transitions are proportional to the microwave amplitude, as expected (Sec. 7.S9).

The observed decay of the Rabi oscillations cannot be explained only by the spread in the Larmor frequency, σ_B . Numerical simulations of the Rabi oscillations give good agreement with the measurements of Fig. 7.3(a) when including a variation in the Rabi frequency, $\sigma_{f_1} \sim 0.25$ MHz (Sec. 7.S4). The fluctuations in the transverse nuclear field (Laird *et al.*, 2009) are too small to explain this spread. Instead, instrumentation noise could be responsible. Modeling the gate operation taking into account f_1 , σ_B , and σ_{f_1} , we estimate that the fidelity for flipping a spin from down to up is 0.99 (0.97) for an electron spin resonant at $f_1^{(2)}$ ($f_1^{(1)}$). For an electron in a 30/70 statistical mixture of the two resonance conditions, the fidelity is ~ 0.80 (Sec. 7.S6).

Two-axis control of the spin is demonstrated by varying the relative phase ϕ of two $\pi/2$ microwave bursts resonant with $f_1^{(1)}$ separated by a fixed waiting time $\tau = 40$ ns $\ll T_2^*$ (Fig. 7.3(f), black trace). As expected, the signal oscillates sinusoidally in ϕ with period 2π . For $\tau = 2$ μ s $\gg T_2^*$, the contrast has vanished, indicating that all phase information is lost during the waiting time (Fig. 7.3(f), red trace). Similar measurements with the pulses applied off-resonance by an amount Δf with $\phi = 0$, are expected to show an oscillation with frequency Δf and an envelope that decays on the timescale T_2^* . Because of the presence of two resonance lines just 2.1 MHz apart, the measurement of P_1 versus f_{MW} and τ (Fig. 7.3(b)) shows a superposition of two such patterns. This becomes clear from taking the Fourier transform over the waiting time τ (Fig. 7.3(d)) which shows 2 linear patterns superimposed, with vertices at $f_0^{(1)}$ and $f_0^{(2)}$. The stability of the measurement can be appreciated from Fig. 3e, which shows P_1 versus f_{MW} and the relative phase between the two bursts at $\tau = 400$ ns.

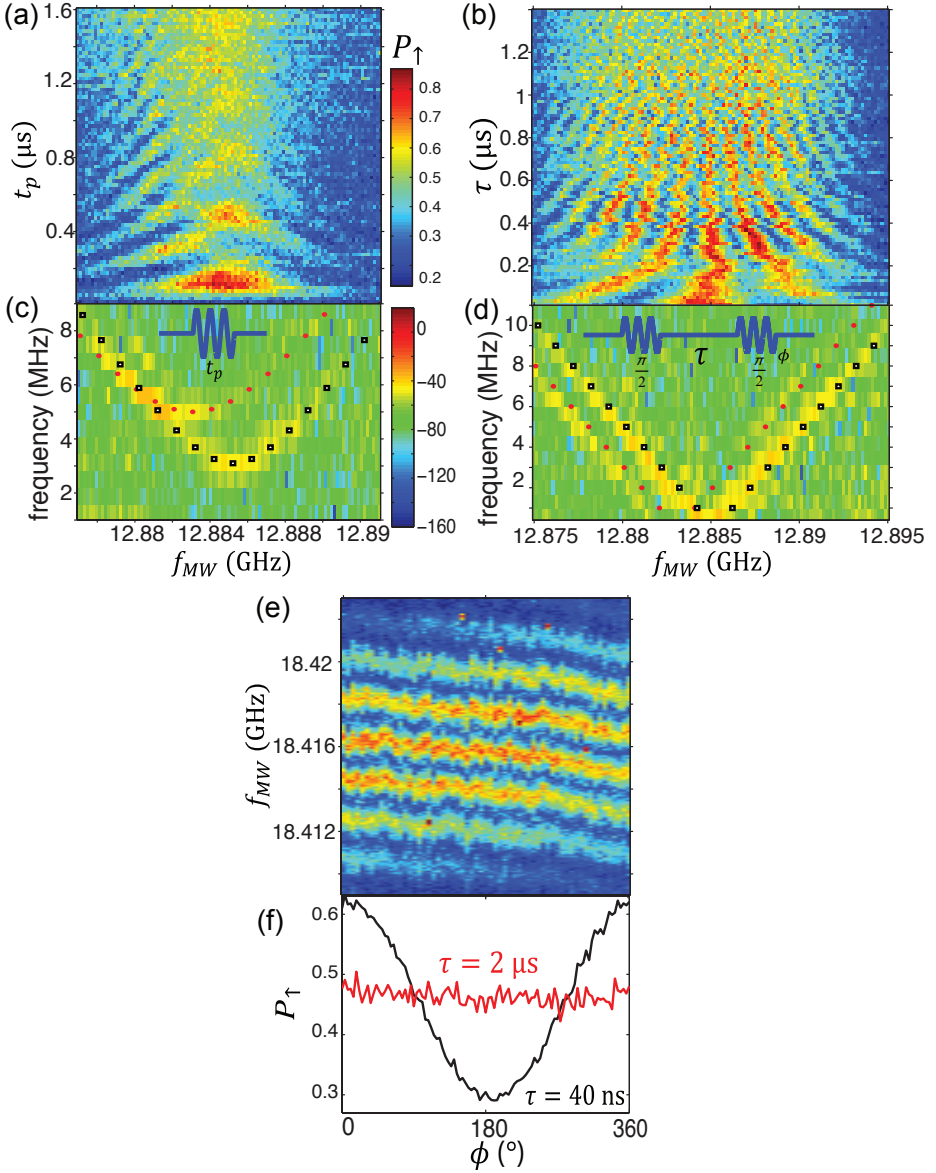


Figure 7.3: : Universal qubit control (a) Measured spin-up probability, P_{\uparrow} , as a function of f_{MW} and burst time t_p ($B_{\text{ext}} = 560.782$ mT, $P=16.4$ dBm). (b) Measured spin-up probability, P_{\uparrow} , as a function of f_{MW} and waiting time τ ($B_{\text{ext}} = 560.782$ mT, $P=16.4$ dBm) between two $\pi/2$ (75 ns) pulses with equal phase, showing Ramsey interference (Color map as in (a)). (c) Fourier transform over the microwave burst time t_p of Fig. 3A showing a hyperbolic dependence (black rectangles and red circles) as a function of f_{MW} for each transition, $f_0^{(1)}$ and $f_0^{(2)}$. Inset: microwave pulse scheme used in (a). (d) Fourier transform over the waiting time τ of Fig. 3b showing two linear patterns superimposed, with vertices at $f_0^{(1)}$ and $f_0^{(2)}$. Inset: microwave pulse scheme used in (b,d,e,f). (Color map as in (c)) (e) Measured spin-up probability, P_{\uparrow} , as a function of f_{MW} and the relative phase ϕ between two microwave pulses for $\tau = 400$ ns ($B_{\text{ext}} = 763.287$ mT, $P=18.8$ dBm). (Color map as in (a)) (f) Ramsey signal as a function of the relative phase ϕ between the two microwave pulses for $\tau = 400$ ns (black curves) and $\tau = 2 \mu\text{s}$ (red curves) ($B_{\text{ext}} = 763.287$ mT, $P=18.8$ dBm, $f_{MW} = f_0^{(1)} = 18.41608$ GHz).

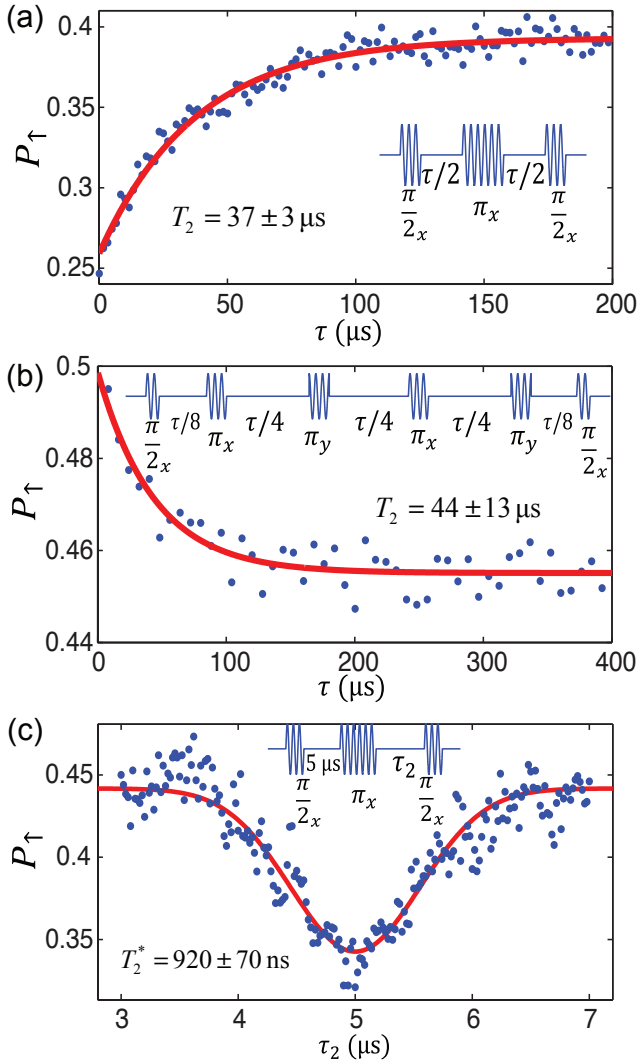


Figure 7.4: : Qubit coherence (Here, $B_{ext} = 747.710 \text{ mT}$, $P = 18.4 \text{ dBm}$, $f_{MW} = f_0^{(1)} = 17.695 \text{ GHz}$, $f_1^{(1)} = 2.7 \text{ MHz}$.) (a) Measured spin-up probability, P_{\uparrow} , as a function of the total free evolution time τ in a Hahn echo experiment (pulse scheme in inset). We did not see a significant difference in the decay when changing the relative phase between the first pulse (77 ns) and the π pulse (150 ns) from $\phi = 0$ to $\phi = 90$. The decay curve is fit well to a single exponential decay. (b) Measured spin-up probability, P_{\uparrow} , as a function of the total free evolution time τ when using four decoupling pulses. (c) Measured spin-up probability, P_{\uparrow} , as a function of the position of the third pulse in the Hahn echo experiment. The free evolution time between the first and second pulse is fixed at $5 \mu\text{s}$ and that between the second and third pulse is varied from 3 to $7 \mu\text{s}$.

7.5. SPIN ECHO

Spin coherence can be extended by spin echo techniques, provided the source of dephasing fluctuates slowly on the timescale of the electron spin dynamics. We perform a Hahn echo experiment, consisting of $\pi/2$, π and $\pi/2$ pulses separated by waiting times $\tau/2$ (Hanson *et al.*, 2007; Zwanenburg *et al.*, 2013), and record P_{\uparrow} as a function of the total free evolution time τ (Fig. 7.4(a)). A fit to a single exponential yields a time constant $T_2 = 37 \pm 3 \mu\text{s}$, almost 50 times longer than T_2^* . While this is encouraging, we had expected an even longer T_2 based on the 200 μs Hahn echo decay observed for an electron spin bound to a P-impurity in natural Si (Pla *et al.*, 2012). Furthermore, contrary to our expectations for an echo decay dominated by slowly fluctuating nuclear spins, the decay is well-described by a single exponential, with no signatures of a flat top. One possible explanation is that the fluctuations that dominate the echo decay are fast compared to the few μs timescale of the first few data points (Cywinski *et al.*, 2008). Another possible explanation is that the observed decoherence rate reflects the valley switching rate; as soon as the valley switches, the spin resonance frequency jumps by about 2 MHz, and the phase of the spin is randomized (cannot be recovered anymore). Both explanations are consistent with the fact that a four-pulse decoupling pulse sequence does not further extend the decay time (Fig. 7.4(b)). Either way, this implies that the slowly fluctuating nuclear field does not yet limit T_2 (Witzel and Das Sarma, 2006). Finally, when we shift the position of the third pulse, the time intervals before and after the echo pulse are no longer equal and coherence is lost, as expected (Fig. 7.4(c)). A fit of this decay with a Gaussian function, gives measured in the time domain, consistent with T_2^* extracted from the line width.

7

7.6. ELECTRON SPIN RESONANCE AND VALLEY STATES IN SI

We now return to the origin of the two resonance lines that are visible in all the measurements. From the individual measurements, we deduce that the higher (lower) frequency resonance contributes to the signal 0.7 (0.3) of the time, indicating that the system does not simply exhibit two resonances but instead switches between two conditions (Sec. 7.S13). The splitting between the two lines varies linearly with B_{ext} , corresponding to a difference in g-factors of about 0.015 percent, and an offset in B_{local} between the two resonances of $65 \pm 138 \text{ mT}$ (Fig. 7.2(a), green triangles). Finally, as mentioned before, the higher-frequency resonance exhibits ~ 1.5 times slower Rabi oscillations than the lower-frequency resonance.

We propose that the two lines correspond to EDSR with the electron in one or the other of the two lowest valley states, with a 30/70 occupation ratio. This ratio is set either by the injection probabilities into the respective valley states, or by thermal equilibration, depending on whether the valley lifetime is shorter than the few ms delay between injection and manipulation. We note that either way, initialization to a single valley can be achieved when the valley splitting is several times larger than the electron temperature. Initial reports of electric-field controlled valley splittings in Si dots may point to a way of achieving such control (Yang *et al.*, 2013). A valley-dependent spin splitting can arise from several sources. Intrinsic spin-orbit coupling is weak in silicon, but the field gradient from the micromagnet admixes spin and orbitals, leading to a renormal-

ization of the g -factor by an amount that depends on the orbital level spacing (Tokura *et al.*, 2006). Due to valley-orbit coupling, the orbital level spacing in turn depends on the valley. We estimate that this can result in observed valley-dependent g -factor shifts of $\sim 0.015\%$ (Sec. 7.S10). The difference in Rabi frequencies can be understood from a valley-dependent orbital level spacing as well. Another mechanism that can account for the observed g -factor shifts is valley-dependent penetration of the Bloch wave function into the SiGe barrier region (Sec. 7.S12). Other explanations we considered include switching between two separate dot locations, a double dot, and transitions in a two-electron manifold, but these are not consistent with the above observations; see also the supplementary information.

7.7. CONCLUSIONS

The demonstration of all-electrical single-spin control with coherence times orders of magnitude longer than intrinsic coherence timescales in III-V hosts greatly enhances the promise of quantum dot based quantum computation. The presence of two closely spaced resonances that we attribute to occupation of two different valleys shows the necessity for valley splitting control (Yang *et al.*, 2013) not only for exchange-based quantum gates (Zwanenburg *et al.*, 2013) but also for single-spin manipulation. The use of a micromagnet facilitates selective addressing of neighbouring spins and provides a coupling mechanism of quantum dot spins to stripline resonators that can form the basis for two-qubit gates and a scalable architecture (Xiang *et al.*, 2013).

SUPPLEMENTARY SECTIONS

7.S1. HEATING EFFECTS FROM THE MICROWAVE BURSTS

The application of high power microwave bursts affects the response of the sensing dot, presumably due to heating, and this effect increases with burst time. In order to keep the response constant and get better uniformity in the visibility of the spin oscillations as we vary the burst time during the manipulation stage, we include a second microwave burst at the end of the read-out stage such that the total microwave burst duration over a full cycle is kept constant at $2 \mu\text{s}$.

7.S2. FINDING THE SPIN RESONANCE CONDITION

Before performing the experiment, the electron spin g -factor is not precisely known. The presence of the micromagnet creates further uncertainty in the spin resonance condition. The continuous wave low power EDSR response exhibits very narrow lines, making it easy to miss the resonance when scanning the magnetic field or frequency for the first time. At higher power, the line is power broadened, so larger steps in field or frequency can be taken, accelerating the scan. We used an even more efficient technique, adiabatic rapid passage. This technique was successfully used in quantum dots before ([Shafiei et al., 2013](#)) and allows one to step the frequency in increments corresponding to the frequency chirp range used for the adiabatic inversion (40-60 MHz in our experiments).

7.S3. SPIN RELAXATION TIME T_1

We did not observe any change in the measured spin-up probability when changing the timing of the microwave burst during the manipulation stage by up to 2 ms. Thus we conclude that the spin relaxation time T_1 is much longer than the ms timescale of our pulse cycle and that the measurements shown here are not affected by T_1 decay, consistent with the long T_1 times seen in earlier measurements on Si or Si/SiGe dots and donor ([Morello et al., 2010](#); [Simmons et al., 2011b](#); [Yang et al., 2013](#)).

7.S4. RABI OSCILLATION CONTRIBUTED FROM TWO VALLEY STATES

We calculate the measured spin up probability of the Rabi oscillation considering the contribution from both two valley states. As discussed in Sec. 4.3, we cannot use any analytical expression in the case of $f_1 \sim \sigma_f$ and thus we perform a numerical integral of Eq. 4.25 with $\sigma_\omega = 2\pi\sigma_f$. The standard deviation of the Larmor frequency is extracted from the line width in Fig. 7.2 $\sigma_f = \frac{\delta f_{\text{FWHM}}}{2\sqrt{2\ln(2)}} = 0.268$ MHz. Here we rewrite the average of the measurement outcome (Eq. 4.25) for the valley state (n) ($n = 1$ or 2) as $\langle p_{\uparrow 0}^{(n)} \rangle(\omega_{\text{MW}}, \omega_0^{(n)}, \omega_1^{(n)}, t)$ in order to explicitly show that it is a function of the applied microwave frequency ω_{MW} , the center Larmor frequency for each valley state $\omega_0^{(n)}$, and the Rabi frequency for each valley state $\omega_1^{(n)}$ for each valley state and the microwave burst time t . Here we assume that the populations in resonances (1) and (2) are $\varepsilon^{(1)}$, and $\varepsilon^{(2)}$, respectively. If in addition we assume that not only the Larmor frequency but the Rabi frequency also follows a Gaussian distribution, the measured spin-up probability for perfect initialization and read-out is given by

$$P_{\uparrow 0}(f_{\text{MW}}, t_p) = \sum_{n=1,2} \varepsilon^{(n)} P_{\uparrow 0}^{(n)}(f_{\text{MW}}, t_p), \quad (7.S1)$$

where $P_{\uparrow 0}^{(n)}(f_{\text{MW}}, t_p) = \int d\omega_1 g^{(n)}(\omega_1) \langle p_{\uparrow 0}^{(n)} \rangle(2\pi f_{\text{MW}}, 2\pi f_0^{(n)}, \omega_1, t_p)$,

with $g^{(n)}(\omega_1) = \frac{1}{\sqrt{2\pi}\sigma_{\omega_1}} \exp\left(-\frac{(\omega_1 - \omega_1^{(n)})^2}{2\sigma_{2\pi\sigma_{f_1}}^2}\right)$, and $\omega_1^{(n)} = 2\pi f_1^{(n)}$. The standard deviation of the Larmor frequency $\sigma_f = 0.268$ MHz is extracted directly from the line width (Fig. 7.2(b)). In order to estimate the standard deviation of the Rabi frequency, σ_{f_1} , and the ratio of the two populations $\varepsilon^{(2)}/\varepsilon^{(1)}$ that applies in the experiment, we compare the measurement results of Fig. 7.3(a) with results from numerical simulations for $P_{\uparrow 0}(f_{\text{MW}}, t_p)$ shown in Fig. 7.S1(a) for a range of values for both the ratio $\varepsilon^{(2)}/\varepsilon^{(1)}$ and σ_{f_1} . Based on this rough comparison, we consider the agreement the best for $\varepsilon^{(2)}/\varepsilon^{(1)} \sim 0.3 \pm 0.1/0.7 \pm 0.1$ and $\sigma_{f_1} \sim 0.25 \pm 0.05$ MHz. As a further consistency check, we plot the same simulation results again in Fig. 7.S1(b), but now re-scaled according to Eq. 4.13

$$P_{\uparrow}(f_{\text{MW}}, t_p) = A \left(P_{\uparrow 0}(f_{\text{MW}}, t_p) - \frac{1}{2} \right) + B, \quad (7.S2)$$

for the read-out and initialization fidelities estimated in Sec. 7.S7. The same values $\varepsilon^{(2)}/\varepsilon^{(1)} \sim 0.3 \pm 0.1/0.7 \pm 0.1$ and $\sigma_{f_1} \sim 0.25 \pm 0.05$ MHz give good agreement with the data of Fig. 7.3(a).

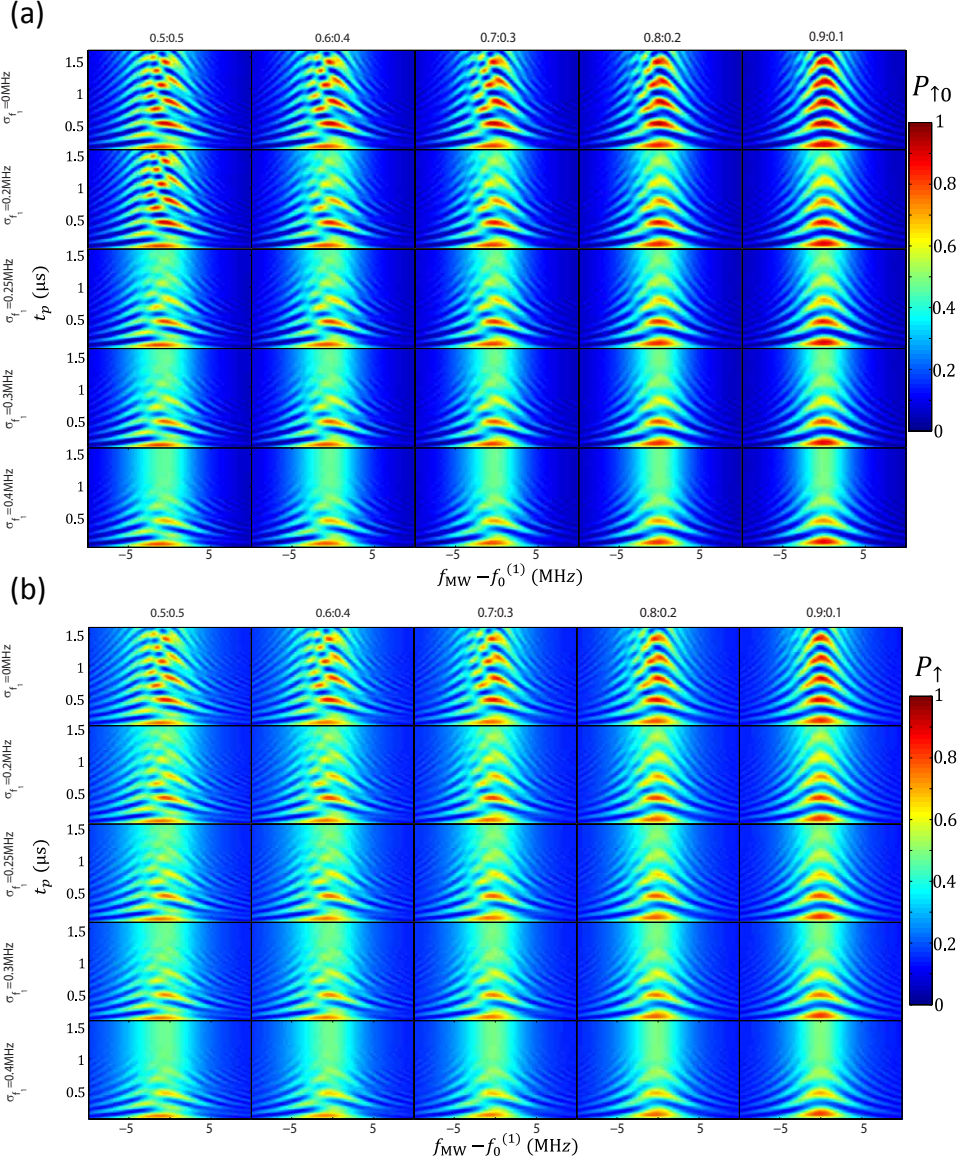


Figure 7.S1: Simulation for Rabi oscillations (a) Numerically simulated spin flip probability for perfect initialization and read-out $P_{10}(f_{MW}, t_p)$ for population ratios $\epsilon^{(2)}/\epsilon^{(1)} = 0.5:0.5, 0.4:0.6, 0.3:0.7, 0.2:0.8, 0.1:0.9$ and spread in Rabi frequencies $\sigma_{f_1} = 0, 0.2$ MHz, 0.25 MHz, 0.3 MHz, 0.4 MHz, as a function of driving duration t_p and frequency detuning $f_{MW} - f_0^{(1)}$. From comparison with the data of Fig. 3a, we conclude that $\epsilon^{(2)}/\epsilon^{(1)} \sim 0.3 \pm 0.1/0.7 \pm 0.1$ and $\sigma_{f_1} \sim 0.25 \pm 0.05$ MHz are reasonable. (b) The same simulation results as in panel (a), but taking into account the initialization and read-out fidelities estimated in Sec. 7.S7. Again $\epsilon^{(2)}/\epsilon^{(1)} \sim 0.3 \pm 0.1/0.7 \pm 0.1$ and $\sigma_{f_1} \sim 0.25 \pm 0.05$ MHz match well to the data.

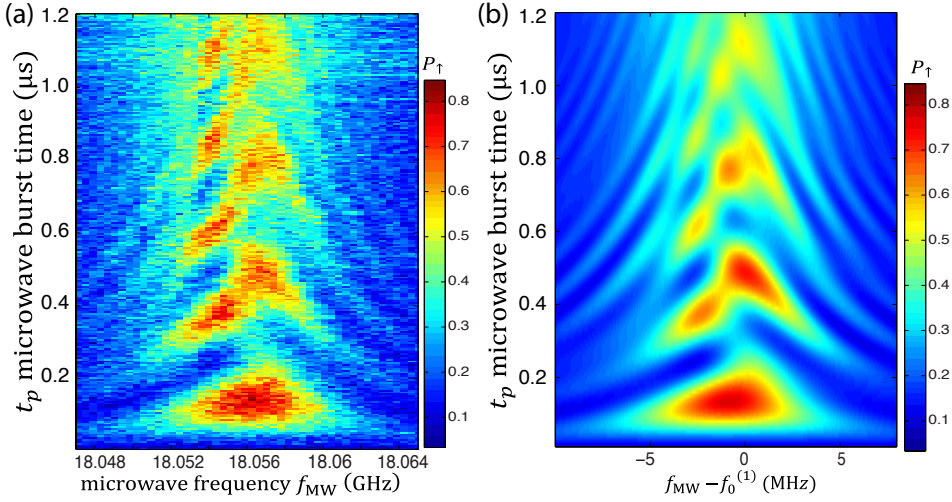


Figure 7.S2: Comparison of the data to a simulation for Rabi oscillations at $B_{\text{ext}} = 763.287$ mT. (a) The measured spin-up probability P_1 for a Rabi experiment. (b) The simulated spin-up probability P_1 using population fractions $\epsilon^{(2)}/\epsilon^{(1)} = 0.3 : 0.7$, spread in Rabi frequencies $\sigma_{f_1} \sim 0.25$ MHz, read-out fidelity parameters $\alpha = 0.06$, $\beta = 0.05$, $\gamma = 0.04$, and the two Rabi frequencies $f_1^{(1)} = 3.1$ MHz and $f_1^{(2)} = 4.1$ MHz.

Fig. 7.S2(a) shows the measured spin-up probability, P_1 , as a function of f_{MW} and burst time t_p , for $B_{\text{ext}} = 763.287$ mT. At this magnetic field, the two resonances are separated by $f_0^{(1)} - f_0^{(2)} = 2.838$ MHz. Thus the individual chevron patterns produced by two resonances are more easily distinguished than in Fig. 7.3(a). The numerical simulations for $P_1(f_{\text{MW}}, t_p)$ for $f_0^{(1)} - f_0^{(2)} = 2.838$ MHz, taking into account the read-out and initialization fidelities estimated in Sec. 7.S7, are shown in Fig. 7.S2(b).

7.S5. POPULATION AND TIME DEPENDENCE OF THE TWO RESONANCES

Fig. 7.2(b) shows the average of the 86 traces shown in Fig. 7.S3. We see from Fig. 7.S3 that the center of the resonance frequency f_0 fluctuates over time and the fluctuation behaviour is the same for the two resonances.

For the measurement of Fig. 7.2(b), the applied microwave power is very low ($\sigma_f \gg f_1$). Thus Eq. 4.30 is applied. If we can assume that the microwave burst time is short compared to the Rabi frequency ($t_p \gg \frac{1}{\omega_1}$), $P_{10} \propto \omega_1^2$. Assuming further that we can neglect the unknown spread in f_1 for low microwave power, the ratio of the spin up probability of two valley states at the respective center Larmor frequencies is

$$\frac{P_{10}^{(1)}}{P_{10}^{(2)}} = \left(\frac{\omega_1^{(1)}}{\omega_1^{(2)}} \right)^2. \quad (7.S3)$$

If we assume that the ratio of the Rabi frequencies between two resonances at low MW

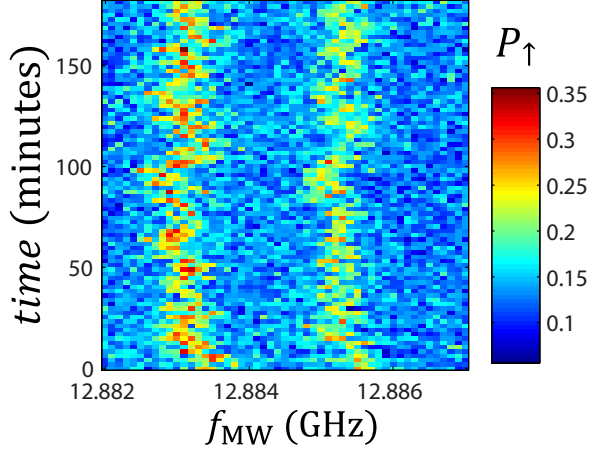


Figure 7.S3: Measured spin-up probability P_{\uparrow} as a function of applied microwave drive frequency f_{MW} and time (external field, power $P = -33$ dBm, microwave pulse duration $t_p = 700 \mu\text{s}$). The raw data on which Fig. 2(b) is based are shown in Fig. S5. Each horizontal scan in the figure takes ~ 2 minutes (200 cycles, which takes 2 s, per datapoint), and the scan is repeated 86 times. Fig. 2(b) shows the average of the 86 horizontal scans.

power is the same as the ratio at high MW power determined in Sec. 7.S9 then $\frac{\omega_1^{(2)}}{\omega_1^{(1)}} = 1.53 \pm 0.19$. The ratio of the measured peak amplitudes in Fig. 7.2(b) is 1.4 ± 0.3 and it is the product of the ratio of the spin-up probabilities and the ratio of the populations:

$$\frac{P_{10}^{(2)}}{P_{10}^{(1)}} \frac{\varepsilon^{(2)}}{\varepsilon^{(1)}} = 1.4 \pm 0.3. \quad (7.S4)$$

From Eq. 7.S3 and Eq. 8.S1, we get

$$\frac{\varepsilon^{(2)}}{\varepsilon^{(1)}} = 1.4 \pm 0.3 \left(\frac{\omega_1^{(1)}}{\omega_1^{(2)}} \right)^2 = \frac{1.4 \pm 0.3}{2.34 \pm 0.58} = 0.60 \pm 0.28. \quad (7.S5)$$

From this relation, we get $\varepsilon^{(2)}/\varepsilon^{(1)} \sim 0.37/0.63$, consistent with the rough estimate of $0.3/0.7$ based on the Rabi oscillations in Sec. 7.S4.

7.S6. π PULSE FIDELITY

According to Eq. 4.89, the π pulse fidelity for a spin-down state as an initial state is given by

$$F(\mathcal{E}(|\downarrow\rangle\langle\downarrow|)|\uparrow\rangle\langle\uparrow|) = \text{Tr}(\mathcal{E}(|\downarrow\rangle\langle\downarrow|)|\uparrow\rangle\langle\uparrow|) = P_{\uparrow 0} \left(f_{\text{MW}} = f_0, t_p = \frac{1}{2f_1} \right). \quad (7.S6)$$

The spin-up probability corresponds to the state fidelity of the output state relative to the ideally expected spin up state. This fidelity is here estimated based on a numerical model with input from the experiment. Quantum process tomography or randomized benchmarking can be used to estimate the gate fidelity directly from the experiment. For the lower transition, using the values $f_1^{(2)} = 5$ MHz, $\sigma_f = 0.268$ MHz and $\sigma_{f_1} = 0.25$ MHz, we find a spin-up probability

$$P_{\uparrow 0}^{(2)} \left(f_{\text{MW}} = f_0^{(2)}, t_p = \frac{1}{2f_1^{(2)}} = 100\text{ns} \right) = 0.99. \quad (7.S7)$$

For the higher transition, using $f_1^{(1)} = 3.1$ MHz, $\sigma_f = 0.268$ MHz and $\sigma_{f_1} = 0.25$ MHz, we find

$$P_{\uparrow 0}^{(1)} \left(f_{\text{MW}} = f_0^{(1)}, t_p = \frac{1}{2f_1^{(1)}} = 160\text{ns} \right) = 0.97. \quad (7.S8)$$

When we have a $\varepsilon^{(2)}/\varepsilon^{(1)} = 0.3/0.7$ contribution of the two resonances, $P_{\uparrow 0} (= 0.3 \times P_{\uparrow 0}^{(2)} + 0.7P_{\uparrow 0}^{(1)})$ reaches its maximum 0.79 when $P_{\uparrow 0}^{(2)} = 0.53$ and $P_{\uparrow 0}^{(1)} = 0.90$ at $t_p = 130$ ns and for $f_{\text{MW}} = f_0^{(1)}$.

7.S7. INITIALIZATION FIDELITY AND READ-OUT FIDELITY

For applications in quantum information processing it is important to know the read-out and initialization fidelities. These fidelities are usually characterized by three parameters α , β and γ (Sec. 4.1).

Experimentally, the parameter α corresponds to the probability that the sensing dot current exceeds the threshold even though the electron was actually spin-down, for instance due to thermally activated tunneling or electrical noise. The parameter β corresponds to the probability that the sensing dot current does not cross the threshold even though the electron was actually spin-up at the end of the microwave burst time. The measurement time (< 4 ms) we used is much shorter than T_1 and so β is not affected by T_1 decay (Sec. 7.S3). It is limited by the bandwidth of the sensing dot current measurement (~ 20 kHz). $(1 - \beta)$ can be directly measured as the probability that the step from the charge sensor in correspondence of the electron jumping in during the initialization stage is missed using the same threshold value as is used for detection of the electron jumping out during the read-out stage. We find $\beta \sim 0.05$ (Fig. 7.S4). The parameter γ corresponds to the probability that the electron is in spin-up instead of spin-down at the end of the initialization stage. Here we assumed that initialization and read-out fidelities are the same for the two valley states, i.e., α , β and γ are the same for the both two valley states. The measured spin-up probability P_{\uparrow} can be written as follows using the parameters α , β

and γ and $P_{\uparrow 0}$:

$$P_{\uparrow} = AP_{\uparrow 0} + \left(B - \frac{A}{2} \right) \quad (7.S9)$$

$$= (1 - 2\gamma)(1 - \beta - \alpha)P_{\uparrow 0} + \gamma(1 - \beta) + (1 - \gamma)\alpha \quad (7.S10)$$

$$= P_{\uparrow 0}(1 - \gamma)(1 - \beta) + (1 - P_{\uparrow 0})\gamma(1 - \beta) + (1 - P_{\uparrow 0})(1 - \gamma)\alpha + P_{\uparrow 0}\gamma\alpha. \quad (7.S11)$$

When $P_{\uparrow 0} = 0$ (i.e. the microwaves are applied far off-resonance or not at all), the measured spin-up probability can be expressed as follows:

$$P_{\uparrow}(P_{\uparrow 0} = 0) = (1 - \gamma)\alpha + \gamma(1 - \beta) \quad (7.S12)$$

$$= \alpha + \gamma(1 - (\alpha + \beta)). \quad (7.S13)$$

$P_{\uparrow}(P_{\uparrow 0} = 0) \sim 0.1$ is measured. From this and Eq. 7.S13, we get an upper bound on α .

$$P_{\uparrow}(P_{\uparrow 0} = 0) > \alpha, \quad 0.1 > \alpha. \quad (7.S14)$$

As discussed above, $(1 - \beta) \sim 0.95$ is measured (Fig. 7.S4). From this and Eq. 7.S13, we get an upper bound on γ .

$$P_{\uparrow}(P_{\uparrow 0} = 0) > \gamma(1 - \beta) \Rightarrow \frac{P_{\uparrow}(P_{\uparrow 0} = 0)}{(1 - \beta)} > \gamma \Rightarrow 0.11 > \gamma. \quad (7.S15)$$

By looking at Fig. 7.3(a), $P_{\uparrow}(f_{\text{MW}} = f_0^{(1)})$ reaches its maximum ~ 0.72 when $t_p \sim 130$ ns. Here, since $P_{\uparrow 0}$ is expected to be large, the 2nd, 3rd and 4th terms of Eq. 7.S11 are much smaller than the 1st t term (each of them contains two factors much smaller than 1, whereas the 1st term contains no such small factors). So P_{\uparrow} can be well approximated as follows:

$$P_{\uparrow} \sim P_{\uparrow 0}(1 - \gamma)(1 - \beta) = 0.72 \Rightarrow P_{\uparrow 0}(1 - \gamma) = 0.72/(1 - \beta) = 0.76. \quad (7.S16)$$

Using the upper bound of γ (Eq. 7.S15), we can put bounds on $P_{\uparrow 0}(f_{\text{MW}} = f_0^{(1)}, t_p \sim 130$ ns):

$$0.76 < P_{\uparrow 0}(f_{\text{MW}} = f_0^{(1)}, t_p \sim 130 \text{ ns}) < 0.85. \quad (7.S17)$$

Numerical simulation for $\sigma_{f_1} = 0.25$ MHz gives $P_{\uparrow 0}^{(1)}(f_{\text{MW}} = f_0^{(1)}, t_p = 130 \text{ ns}) = 0.9$ and $P_{\uparrow 0}^{(2)}(f_{\text{MW}} = f_0^{(1)}, t_p = 130 \text{ ns}) = 0.53$, where we note that the 130 ns burst time is longer respectively shorter than the burst time for a π pulse for the lower and higher energy resonance. Then, using $\varepsilon^{(2)}/\varepsilon^{(1)} = 0.3/0.7$, we obtain $P_{\uparrow 0}(f_{\text{MW}} = f_0^{(1)}, t_p = 130 \text{ ns}) = 0.53 \times 0.3 + 0.9 \times 0.7 = 0.79$, which is consistent with Eq. 7.S17. Now, using $P_{\uparrow 0}(f_{\text{MW}} = f_0^{(1)}, t_p = 130 \text{ ns}) = 0.79$ and Eq. 7.S16, we can estimate $\gamma = 0.04$.

Then, from Eq. 7.S13, we can also extract α :

$$P_{\uparrow}(P_{\uparrow 0} = 0) = (1 - \gamma)\alpha + \gamma(1 - \beta) = 0.10 \Rightarrow 0.96\alpha + 0.04 \times 0.95 = 0.10 \Rightarrow \alpha = 0.06. \quad (7.S18)$$

We use $\alpha = 0.06$, $\beta = 0.05$ and $\gamma = 0.04$ in Eq. 7.S11 to compute the spin-up probability P_{\uparrow} that can be expected in the measurement, which is shown in Fig. 7.S1(b), Fig. 7.S2(b) and Fig. 7.S5(b).

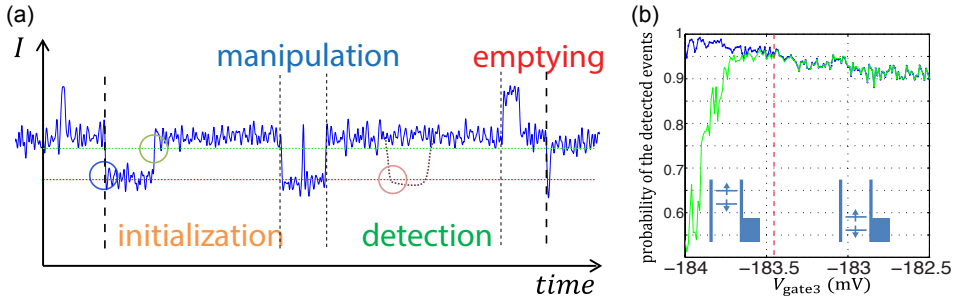


Figure 7.S4: Measurement of fidelity parameter $(1 - \beta)$ (a) An example real time trace of the sensing dot current. The black dashed lines indicate the start and end of one cycle. When the recorded current dips below the threshold level indicated by the dotted red line during the detection stage, we conclude an electron tunneled out from the dot to the reservoir. In this case, we infer the electron was spin up. When the signal remains above the threshold, we conclude the electron was spin down (the lowest energy spin state). (b) Blue trace: Measured probability that the sensing dot current passes below the threshold indicated by the red dotted line in panel (A) during the initialization stage, as a function of V_{gate3} (averaged over 1000 cycles). Since the dot is always emptied during the previous stage, ideally we would always see the signal dip below the red threshold at the start of the initialization stage (blue circle in (A)). However, because of the finite bandwidth of the measurement, the dip will be missed if it is too fast. This occurs with the same probability as the probability of missing dips in the detection stage, and is thus a good measure of $(1 - \beta)$. Green trace: Measured probability that the current subsequently passes the green threshold from below during the initialization stage, as a function of V_{gate3} (green circle in (A)). When the green and blue traces coincide, the dot is filled during the initialization stage. When the dot level is high (V_{gate3} is low, see also the schematic in the inset), the time it takes for an electron to tunnel in is long, and so $(1 - \beta)$ is high, but the dot is not always filled (the green line is low here). As the dot level is lowered ($(1 - \beta)$ is raised, see also inset), the tunneling rate increases, and the dot is always initialized, at the cost of a slightly lower value of $(1 - \beta)$, due to the finite measurement bandwidth. The vertical red dashed line indicates the operating point used in the experiments.

7.S8. NUMERICAL SIMULATION OF RAMSEY FRINGES

Here we give results of numerical simulations corresponding to the two-pulse Ramsey interference measurements of Fig. 7.3(c). The overall procedure is analogous to that used for the simulations of the Rabi oscillations. Instead of a single microwave burst, we now have two bursts of duration $t_p = 1/(4f_1^{(1)})$ separated by a wait time τ . Here we can neglect the spread in f_1 because t_p is short and its effect is small. Then the spin flip probability averaged over the Larmor frequency distribution is expressed as

$$P_{\uparrow 0}(f_{\text{MW}}, t_p) = \sum_{n=1,2} \varepsilon^{(n)} P_{\uparrow 0}^{(n)}(f_{\text{MW}}, t_p), \quad (7.S19)$$

where $P_{\uparrow 0}^{(n)}(f_{\text{MW}}, t_p) = \langle p_{\uparrow 0}^{(n)} \rangle(2\pi f_{\text{MW}}, 2\pi f_0^{(n)}, 2\pi f_1^{(n)}, \tau)$ and $\langle p_{\uparrow 0}^{(n)} \rangle$ is given by Eq. 4.35. Using $\alpha = 0.06$, $\beta = 0.05$, and $\gamma = 0.04$ in Eq. 4.13, we compute the expected spin-up probability P_{\uparrow} at the end of the Ramsey sequence, see Fig. 7.S5(b). The corresponding data is shown in Fig. 7.S5(a).

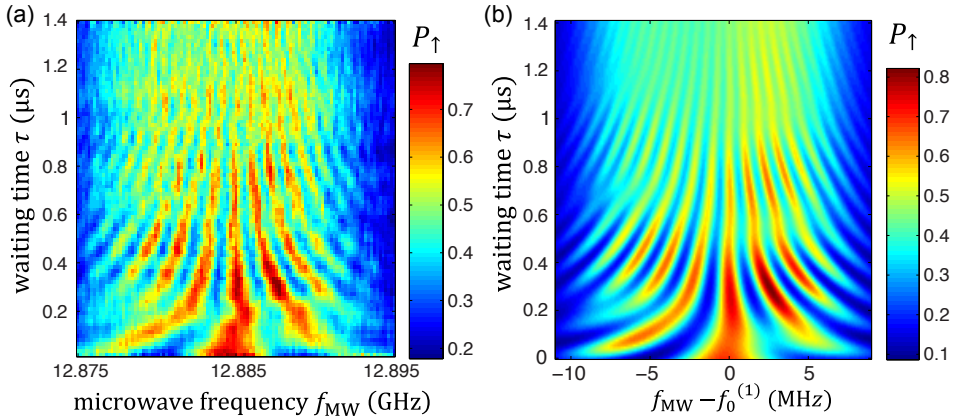


Figure 7.S5: Comparison of the data to a simulation for Ramsey fringes. (a) The measured spin-up probability P_{\uparrow} for a two-pulse Ramsey style experiment. The data are those shown in Fig. 3c but taking a moving average along t_p over 5 points (79 ns). (b) The simulated spin-up probability P_{\uparrow} using $\varepsilon^{(2)} : \varepsilon^{(1)} = 0.3 : 0.7$, $\sigma_f = 0.268$ MHz, $\alpha = 0.06$, $\beta = 0.05$, and $\gamma = 0.04$ as a function of τ and $f_{\text{MW}} - f_0^{(1)}$, also taking a moving average over 79 ns. There is good agreement between the data and simulation.

7.S9. POWER DEPENDENCE OF THE RABI FREQUENCY

Fig. 7.S6(a) shows the measured Rabi frequencies for the two resonance conditions, $f_1^{(1)}$ and $f_1^{(2)}$, as a function of the microwave amplitude emitted from the source. $f_1^{(1)}$ and $f_1^{(2)}$ are determined by the fast Fourier transform (FFT) of Rabi oscillations, as in Fig. 7.3(b). The error bars arise from the finite number of points in the FFT. The linear fits show that the ratio of the Rabi frequencies of two resonance transitions is $f_1^{(2)}/f_1^{(1)} = 1.53 \pm 0.19$.

Fig. 7.S6(b) shows Rabi oscillations for a range of microwave amplitudes emitted from the source. The scattering and the low spin-up probability around microwave amplitude 500 mV \sim 800 mV may be due to a background charge switch that caused the dot to move away from the electrochemical potential alignment that is best for read-out. The measurement of Fig. 7.S6(b) took 20 hours.

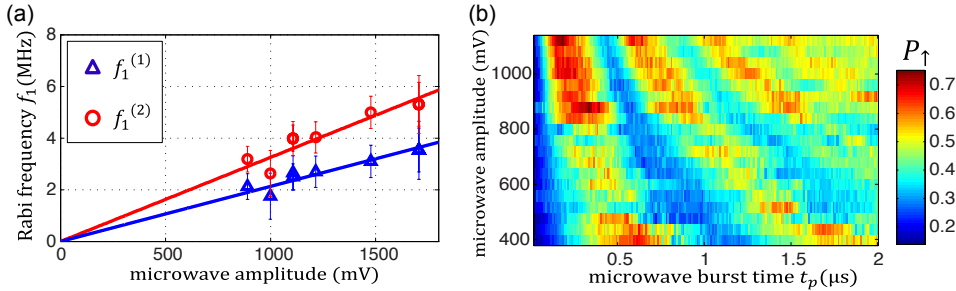


Figure 7.S6: Rabi oscillations versus microwave amplitude (a) Rabi frequencies $f_1^{(2)}$ (red circles) and $f_1^{(1)}$ (blue triangles) at $B_{\text{ext}} = 763.287$ mT as a function of the microwave amplitude emitted from the source, as verified with a spectrum analyzer. The solid lines are linear fits to the data. As expected, the Rabi frequency is linear in the driving amplitude. (b) The measured spin-up probability P_\uparrow as a function of the microwave burst time t_p and the microwave amplitude emitted from the source by applying microwave excitation at $f_{\text{MW}} = f_0^{(1)} = 12.885$ GHz. ($B_{\text{ext}} = 763.287$ mT) We see the pattern expected for Rabi oscillations.

7.S10. DIFFERENCE IN G-FACTORS AND RABI FREQUENCIES BETWEEN THE TWO RESONANCES

Here we discuss several possible explanations for the existence of two closely spaced electron spin resonance conditions, characterized by g -factors that differ by 0.015% and Rabi frequencies that differ by 50%.

As stated in the main text, we attribute the presence of two spin resonance signals to a partial occupation of the two lowest valley states. We can estimate the valley splitting E_V from the 30/70 relative contributions of the two resonances, assuming it results from thermal equilibration between the two valley states. This gives $E_V \sim 0.85 k_B T_e$, which for $T_e = 150$ mK yields $E_V = 11 \mu\text{eV}$. We note that the electron temperature may be somewhat larger since we apply microwave excitation to the sample, so the valley splitting may be larger as well.

We have identified two mechanisms that can explain a 0.015% relative difference in the electron g factors between the two valleys, defined as $2(g^{(1)} - g^{(2)})/(g^{(1)} + g^{(2)})$. The first is valley-dependent g factor renormalization due to the transverse gradient magnetic field; the other is valley-dependent penetration of the electron wavefunction into the SiGe barrier region. We first discuss these two mechanisms. We then mention other potential mechanisms that cannot explain the observed g factor shift.

(1) The unperturbed Zeeman splitting ϵ_{0z} is renormalized in the presence of a magnetic field gradient by $\Delta\epsilon_z = -\frac{1}{4} \frac{(g\mu_B \max(b_{sl}) l_{orb})^2}{(\Delta_{orb})^2 - \epsilon_{0z}^2} \epsilon_{0z}$ (Tokura *et al.*, 2006) where l_{orb} represents the electron wavefunction spread, Δ_{orb} is the energy splitting between the ground orbital state and the first excited orbital state and $\max(b_{sl}) \sim \frac{dB_{\perp}}{dx}$. We see that $\epsilon_z (= \epsilon_{0z} + \Delta\epsilon_z)$ depends on the orbital energy splitting Δ (energy level spacing to the first excited state). At lowest order in the valley-orbit coupling, Δ_{orb} depends only on the orbital energy splitting, which can differ for the two valley states due to valley-orbit coupling (Friesen and Coppersmith, 2010). Contributions to the renormalization of the g -factor from differences in the lateral positions of the different valley states can also occur, but are higher order in the valley-orbit coupling.

The difference in g -factors between the two valleys could then be explained if the two valley states exhibit sufficiently different orbital splittings Δ_{orb} . Valley-dependent orbital splitting arises from the valley-orbit interaction due to disorder at the interface, and can have important effects. In (Gamble *et al.*, 2013), it is estimated that the centers of the charge distributions of the two valley states can be separated by as much as the dot diameter, and differences in orbital splitting between the two valleys can be 20% or more. Taking $dB_{\perp}/dx = 1$ mT/nm, $E_{0z} \sim 60 \mu\text{eV}$, $\Delta_{orb}^{(1)} \sim 400 \mu\text{eV}$ and $\Delta_{orb}^{(2)} \sim 320 \mu\text{eV}$ (where the superscripts refer to the two resonances as in the main text), we obtain $\Delta\epsilon_z/\epsilon_{0z} = 0.013\%$ and 0.010%. The difference between the two corresponds to a difference in g -factors of 0.003%, within a factor of 5 of the observed value.

A valley-dependent orbital splitting can also account for the observed difference in Rabi frequencies for the two resonances. From (Pioro-Ladrière *et al.*, 2008a; Tokura *et al.*, 2006), neglecting the contribution from spin-orbit interaction as it is small in Si/SiGe, we roughly have $f_1 = \frac{g\mu_B}{2h} eE^{AC} \left| \frac{dB_{\perp}}{dx} \right| \frac{l_{orb}^2}{\Delta_{orb}}$, where the approximation is valid under the condition $\epsilon_{0z} \ll \Delta_{orb}$ (Tokura *et al.*, 2006). Given that $l_{orb} \propto 1/\sqrt{\Delta_{orb}}$, it follows that $f_1 \propto$

$1/\Delta_{orb}^2$. Then, we have that $f_1^{(2)}/f_1^{(1)} = (\Delta_{orb}^{(1)}/\Delta_{orb}^{(2)})^2$. Assuming that E^{AC} is equal for the two valley states, the factor 1.5 between the Rabi frequencies of the two resonances can be explained by a $\sim 20\%$ difference in orbital level spacing, $2(\Delta_{orb}^{(2)} - \Delta_{orb}^{(1)}) / (\Delta_{orb}^{(2)} + \Delta_{orb}^{(1)})$. This is consistent with the difference in orbital splitting needed to explain the g -factor shifts.

(2) A second explanation for the g -factor shifts could be that the two valley states penetrate differently into the SiGe barrier. This effect also gives rise to valley splitting. For g -factors, the state with the largest probability in the barrier should have the g -factor closest to SiGe. It is difficult to estimate the resulting g -factor shift because the g -factors in SiGe alloys are not well known. Our rough estimate yields a g -factor shift of 0.0025%, which is 6 times smaller than the experiment, but is still comparable. We view this mechanism as less likely than mechanism (1) above because observing the difference in Rabi frequencies would require that the different valley states have significantly different direction of wavefunction motion. In principle, further experiments have the potential to distinguish these two mechanisms for g -factor shifts. Valley-dependent penetration should be similar in similar devices, and its dependence on extrinsic parameters (e.g., accumulation gate voltages) should be systematic. On the other hand, valley-orbit renormalization should vary significantly from device to device.

We now briefly consider explanations for the g -factor shifts that yield less successful agreement with experiment.

(3) In principle, the combination of valley-orbit coupling and spin-orbit coupling could give rise to valley-dependent g -factor shifts. The renormalization in the g -factor from this mechanism is proportional to the inverse square of the spin-orbit length (Borhani and Hu, 2012). According to (Wilamowski *et al.*, 2002) the spin-orbit coupling strength in quantum well structures is three orders of magnitude smaller in Si than in III-V semiconductors. Since such g -factor renormalization effects are small already in GaAs, we can conclude that the change in g -factor mediated by this mechanism in Si will be much smaller than the 0.015% that is observed experimentally.

(4) As mentioned above, valley-orbit coupling may cause a lateral separation of the centers of the charge distributions for the two valley states (Gamble *et al.*, 2013). When this effect is combined with local fluctuations of the Ge concentration in the SiGe alloy, it yields slightly different g -factor shifts for the two states. In general, the g -factor shift described in (2) (above) would be expected to dominate over such a disorder effect. However, because valley-orbit coupling depends on the interference between valley state (Friesen and Coppersmith, 2010), destructive interference could suppress the dominant g -factor shift in (2). Our simulations (not reported here) indicate that it is possible for the disorder-induced effect to dominate, though still smaller than the estimate given in (2) above.

(5) Finally, we consider explanations for the two closely spaced spin resonance conditions that do not invoke valley physics. A natural thought is that we may be driving spin transitions in a two- or three-electron manifold, either in a single dot or in a double dot. Under appropriate conditions, this could give rise to closely spaced spin resonance frequencies with g -factors around 2. However, in this scenario, whenever microwave excitation is applied at either one of the two resonance frequencies, spin transitions would be induced 100% of the time. In the experiment, in contrast, when applying microwave

excitations resonant with the lower (upper) resonance frequency, there is a contribution to the signal only $\sim 30\%$ (70%) of the time. If the dot location jumped between two positions, for instance due to a background charge that is hopping back and forth, a 30/70 occupation would be possible. Due to the magnetic field gradient, we can also expect different spin splittings for different dot locations. However, the difference in spin splittings would be a fixed value set by the stray field from the micromagnet (as soon as it is fully polarized). In contrast, in the measurements, the difference between the resonance frequencies varies linearly with magnetic field (Fig. 7.2(a)).

We have not been able to come up with other plausible explanations except those related to valley physics presented above.

7.S11. SOURCES OF RABI DECAY

Here we estimate how much random nuclear fields, instrumentation and charge noise can contribute to the spread in the Rabi frequency. The Rabi frequency in the present EDSR measurements can be expressed as $f_1 \sim \frac{g\mu_B}{2\hbar} eE^{AC} \left| \frac{dB_{\perp}}{dx} \right| \frac{l_{orb}^2}{\Delta_{orb}}$. We consider here only fluctuations in the electric field E^{AC} and in the transverse gradient dB_{\perp}/dx , as we expect fluctuations in l_{orb} and Δ_{orb} to give smaller contributions. For each noise source, we estimate whether it can account for the 5% spread in the Rabi frequency (rms) observed in the experiment.

First, the transverse component of the nuclear field exhibits a gradient that adds to the gradient from the micromagnet by a random amount that slowly fluctuates in time over the course of the measurement. The lateral displacement of the electron induced by the microwave excitation is estimated to be $\Delta x_{\text{rms}} = 0.707 \frac{B_1}{dB_{\perp}/dx} = 0.707 \frac{0.18\text{mT}}{0.27\text{mT/nm}} = 0.47\text{ nm}$. An approximate upper bound on the transverse nuclear field gradient is $\Delta B_{\text{nuc}}/2r = 7.6\text{ kHz/nm}$. To estimate this bound, we assume that the nuclear field is uncorrelated between two positions that are separated by the dot diameter, $2r \sim l_{orb} \sim 50\text{ nm}$. The measured spread in Larmor frequency is $\sigma_f = 0.268\text{ MHz}$ so the rms difference in nuclear fields ΔB_{nuc} between these two positions becomes $\Delta B_{\text{nuc}} = \sqrt{2}\sigma_f = 0.38\text{ MHz}$. Then the spread in the nuclear field gradient is $\Delta x_{\text{rms}}(\Delta B_{\text{nuc}}/2r) = 3.6\text{ kHz}$, which is about 70 times smaller than σ_{f_1} we measured.

An additional contribution of the random transverse nuclear field arises from a modulation in the phase ϕ of the atomic scale oscillations of the electron wave function that is present in Si/SiGe quantum dots (Zwanenburg *et al.*, 2013). If an electric field changes ϕ by 90 degrees, the electron wave function is in contact with a different ensemble of nuclei. An AC electric field excitation at frequency f_0 then leads to a (random) contribution to the Rabi frequency. The effect of an out-of-plane electric field is small as ϕ does not depend on this component to leading order in the ratio of the valley coupling to the quantum well depth (for example, see Eqs. 10, 13 and 14 in (Friesen *et al.*, 2007)). The effect of an in-plane electric field is mediated by disorder at the quantum well interface. We have found (see section S12 below) that ϕ varies over length scales of order $d = 10 \sim 100\text{ nm}$, which implies that the nuclear field would be uncorrelated for two positions $10 \sim 100\text{ nm}$. Taking $d = 10\text{ nm}$ and following an analogous reasoning as above, the estimated dot displacement $\Delta x_{\text{rms}} = 0.47\text{ nm}$ produces a random contribution to the

Rabi frequency of order $\frac{\Delta x_{\text{rms}}}{d} \Delta B_{\text{nucl}} \sim 0.02$ MHz, 13 times smaller than σ_{f_i} we measured.

Second, low-frequency charge noise or gate voltage noise can cause random shifts in the average dot position. If the transverse field gradient from the micromagnet itself changes with position, low-frequency charge noise leads to a low-frequency fluctuation in the gradient strength, and thus to a spread in the Rabi frequency. As discussed in the main text, the EDSR linewidth puts an upper bound on the electron micromotion induced by low-frequency charge or voltage noise of $\delta x = 50$ pm (rms). Based on simulations, the variation of the transverse gradient from the micromagnet with position is $\frac{d}{dx} \left(\frac{dB_{\perp}}{dx} \right) \sim 2 \mu\text{T}/(\text{nm})^2$ and so the spread in transverse field gradient due to low-frequency noise is $\frac{d}{dx} \left(\frac{dB_{\perp}}{dx} \right) \delta x = 0.1 \mu\text{T}/(\text{nm})$. This spread is 3000 times smaller than the average transverse gradient of 0.3 mT/nm, and can thus not explain the 5% spread in the Rabi frequency we observe.

Third, charge noise/instrumental noise that is resonant with the Larmor frequency adds to E^{AC} and can thus cause a spread in the Rabi frequency. The output amplitude of the microwave source (Agilent Vector Signal Generator E8267D) could fluctuate, either rapidly or in the form of a slow drift. We measured the drift in the output amplitude of the vector source operating in vector modulation mode over twenty hours. We found a variation in output amplitude, which correlates with the temperature in the room, of about 0.2%. Thermal noise (and other broadband noise sources) also has some spectral content at the resonance frequency, which is independent of the microwave power. However, if this spectral content amounted to 5% in amplitude of the driving from the vector source during Rabi experiments, it would overwhelm the driving amplitude of the source during the CW measurements, where we applied about 50 dB less power than during the Rabi experiments, corresponding to 300 times smaller amplitudes. In this case, spin transitions would have been observed also when the applied microwave frequency is applied off-resonance, which is clearly not the case. Fourth, fluctuations in E^{AC} are also introduced by the vector modulation whereby the microwave signal is multiplied by a 250 mV rectangular pulse generated by a Tektronix Arbitrary Wave function Generator (AWG 5014C) and applied to the I and Q inputs of the vector source. Fluctuations in the AWG pulse amplitude then translate to fluctuations in E^{AC} . The twenty hour measurement of the output amplitude of the vector source was done with the same 250 mV pulse amplitude from the AWG applied to the I and Q inputs, so this contribution is already included in the 0.2% variation in output amplitude discussed above.

Finally, high frequency phase noise of the microwave source causes fluctuations in the applied frequency. The specifications for the frequency stability of the source are many orders of magnitude below the measured line width of 0.6 MHz. Finally, noise in the amplitude of the AWG channels going into the I and Q inputs causes not only amplitude fluctuations (discussed above) but also phase fluctuations. The noise of the AWG is dominated by low-frequency noise, which thus translates to low-frequency phase noise of the vector source output. When measuring Rabi oscillations, low-frequency phase noise does not contribute to damping.

7.S12. VALLEY PHASE RELAXATION LENGTH SCALE

Here we estimate the length scale over which the valley phase relaxes by considering a quantum well interface that is not perfectly flat, but contains a single-atom step. Far enough away from the step, a single-electron wavefunction does not feel the presence of the step, and we wish to estimate the width d of the region near the step over which the wavefunction is perturbed. We will estimate the perturbation to the energy of the electron ground state due to this step, taking d as a variational parameter. Minimizing this energy then provides an expression for the valley relaxation length scale d . A characteristic length scale emerges because of the competition between the energy cost of deforming the phase and the possible energy gain that deformation yields because of the decrease of the valley splitting in the vicinity of the step.

The shift in the kinetic energy of the electron ground state is of order $\frac{\hbar^2}{2m_t} \left(\frac{d\phi}{dx} \right)^2 \frac{d}{L}$. Here, $m_t = 0.19m_e$ is the transverse electronic effective mass in silicon, d is the lateral extent of the disturbance, and L is a normalization constant that is essentially the lateral extent of the wavefunction. (Note that L plays no role in our calculation if it is much larger than the other length scales in the problem.) The quantity $\frac{d\phi}{dx}$ is the spatial rate of change of the valley phase, which is given approximately by $\frac{\Delta\phi}{d}$, where $\Delta\phi = k_0 a_0/4$ is the change in the asymptotic values of the valley phase arising from a single step, $k_0 = 0.85 \frac{2\pi}{a_0}$ is the position of the center of the valley in the Brillouin zone, and $a_0 = 0.54$ nm is the length of the Si cubic unit cell. If E_V is the valley splitting for a flat quantum well, then the presence of a step suppresses the total valley splitting by an amount $E_V(d/L)$, and therefore increases the ground state energy by $E_V(d/L)$. Minimizing the total energy shift of the ground state with respect to d yields $d = \sqrt{\frac{\hbar^2}{m_t E_V} \frac{0.85\pi}{2}}$. For typical valley splittings in the range 0.1-1 meV (Boykin *et al.*, 2004; Goswami *et al.*, 2007) this yields valley relaxation lengths on the order of tens of nm. A 2D tight binding calculation using the model described in (Saraiva, Koiller, and Friesen, 2010) corroborates these results.

7.S13. VALLEY SCATTERING AS A SOURCE OF SPIN ECHO DECAY

We assume that the switching between valley (1) and valley (2) happens in a Poisson process and the switching rate from valley (1) to valley (2) is Γ . When the first MW pulse is applied (in the beginning of the manipulation stage), the electron is in valley (1) with probability 70% and in valley (2) with probability 30%.

We consider the following 4 cases.

(I) The electron is in valley (1) when the first pulse is applied. It stays in valley (1) until the third pulse is applied.

(II) The electron is in valley (1) when the first pulse is applied. It switches to valley (2) before the third pulse is applied.

(III) The electron is in valley (2) when the first pulse is applied. It stays in valley (2) until the third pulse is applied.

(IV) The electron is in valley (2) when the first pulse is applied. It switches to valley (1) before the third pulse is applied.

The point is that Hahn echo works only for the case (I).

In the cases (II) and (IV), the phase information is lost as soon (~ 500 ns knowing that the difference in resonance frequency of two valleys is ~ 2 MHz) as the valley switches. The Hahn echo cannot recover the phase information, even if the valley switches back again to the original valley later.

In case (III), the Hahn echo does not work because the second pulse acts as $\sim 2\pi$ pulse instead of π pulse. We set the microwave burst time so that the second pulse acts as π pulse for valley (1). The Rabi frequency of valleys (1) and (2) are $f_1^{(1)} = 2.7$ MHz and $f_1^{(2)} = 4.3$ MHz respectively. Since the microwave excitation is applied here $\Delta f = 2.9$ MHz away from the resonance frequency for valley (2), the effective Rabi frequency for valley (2) is $f_{1\text{ eff}}^{(2)} = \sqrt{\Delta f^2 + f_1^{(2)2}} = 5.2$ MHz. Then the second pulse acts as a $\frac{f_1^{(2)}}{f_1^{(1)}} \times \pi = 96\% \times 2\pi$ pulse for valley (2). Thus we expect that the echo signal is very small in this case.

In case (I), the Hahn echo works. The probability that the electron stays in valley (1) until the third pulse is applied is $\exp(-\Gamma\tau)$. Thus if Γ is faster than the other decoherence mechanisms, we observe $\exp(-\Gamma\tau)$ as the spin echo decay.

The same reasoning applies to the four-pulse decoupling sequence (CPMG). As soon as the valley switches, spin coherence is irreversibly lost. The probability that the valley has not yet switched (and spin coherence is not yet lost) after a time τ goes as $\exp(-\Gamma\tau)$.

Finally, we note that valley switching on a $40 \mu\text{s}$ timescale cannot explain the decay of the Rabi oscillations which occurs on a few μs timescale.

8

SECOND HARMONIC COHERENT DRIVING OF A SINGLE ELECTRON SPIN IN SI-GE SINGLE QD

We demonstrate coherent driving of a single electron spin using second harmonic excitation in a Si/SiGe quantum dot. Our estimates suggest that the anharmonic dot confining potential combined with a gradient in the transverse magnetic field dominates the second harmonic response. As expected, the Rabi frequency depends quadratically on the driving amplitude and the periodicity with respect to the phase of the drive is twice that of the fundamental harmonic. The maximum Rabi frequency observed for the second harmonic is just a factor of two lower than that achieved for the first harmonic when driving at the same power. Combined with the lower demands on microwave circuitry when operating at half the qubit frequency, these observations indicate that second harmonic driving can be a useful technique for future quantum computation architectures.

The work in this chapter has been published as: P. Scarlino, E. Kawakami, D. R. Ward, D. E. Savage, M. G. Lagally, Mark Friesen, S. N. Coppersmith, M. A. Eriksson, and L. M. K. Vandersypen, *Phys. Rev. Lett.* **115**, 106802 (2015).

8.1. INTRODUCTION

Controlled two-level quantum systems are essential elements for quantum information processing. A natural and archetypical controlled two-level system is the electron spin doublet in the presence of an external static magnetic field (Hanson *et al.*, 2007; Loss and DiVincenzo, 1998). The common method for driving transitions between the two spin states is magnetic resonance, whereby an a.c. magnetic field (B^{AC}) is applied transverse to the static magnetic field (B_{ext}), with a frequency, f_{MW} , matching the spin Larmor precession frequency $f_0 = g\mu_B B_{\text{tot}}/h$ (h is Planck's constant, μ_B is the Bohr magneton and B_{tot} the total magnetic field acting on the spin). When the driving rate is sufficiently strong compared to the dephasing rates, coherent Rabi oscillations between the ground and excited state are observed.

Both spin transitions and Rabi oscillations can be driven not just at the fundamental harmonic but also at higher harmonics; i.e., where the frequency of the transverse a.c. field is an integer fraction of the Larmor frequency, $f_{\text{MW}} = f_0/n$, with n an integer. Second or higher harmonic generation involves non-linear phenomena. Such processes are well known and explored in quantum optics using non-linear crystals (Franken *et al.*, 1961) and their selectivity for specific transitions is exploited in spectroscopy and microscopy (Denk, Strickler, and Webb, 1990; Heinz *et al.*, 1982; König, 2000; Shen, 1989; Xu *et al.*, 1996). Two-photon coherent transitions have been extensively explored also for biexcitons in (In,Ga)As quantum dots (Stufler *et al.*, 2006) and in superconducting qubit systems (Nakamura, Pashkin, and Tsai, 2001; Oliver *et al.*, 2005; Shevchenko, Omelyanchouk, and Il'ichev, 2012; Wallraff *et al.*, 2003). In cavity QED systems, a two-photon process has the advantage that it allows the direct transition from the ground state to the second excited state, which is forbidden in the dipole transition by the selection rules (Poletto *et al.*, 2012).

For electron spin qubits, it has been predicted that the non-linear dependence of the g -tensor on applied electric fields should allow electric-dipole spin resonance (EDSR) at subharmonics of the Larmor frequency for hydrogenic donors in a semiconductor (De, Pryor, and Flatté, 2009; Pingenot, Pryor, and Flatté, 2011). For electrically driven spin qubits confined in a (double) quantum dot, higher-harmonic driving has been proposed that takes advantage of an anharmonic dot confining potential (Danon and Rudner, 2014; Nowak, Szafran, and Peeters, 2012; Osika, Mrenca, and Szafran, 2014; Rashba, 2011; Romhányi, Burkard, and Pályi, 2015) or a spatially inhomogeneous magnetic field (Széchenyi and Pályi, 2014). In order to use higher harmonic generation for coherent control of a system, the corresponding driving rate must exceed the decoherence rate. This requires a non-linearity that is sufficiently strong. Although weak non-linearities are easily obtained and have allowed higher harmonics to be used in continuous wave (CW) spectroscopy for quantum dots hosted in GaAs, InAs, InSb and carbon nanotubes (Forster *et al.*, 2015; Laird *et al.*, 2009; Laird, Pei, and Kouwenhoven, 2013; Nadj-Perge *et al.*, 2012; Pei *et al.*, 2012; Stehlik *et al.*, 2014), coherent spin manipulation using higher harmonics has not been demonstrated previously.

In this chapter, we present experimental evidence of coherent second harmonic manipulation of an electron spin confined in a single quantum dot (QD) hosted in Si/SiGe quantum well. We show that this second-harmonic driving can be used for universal spin control, and we use it to measure the free-induction and Hahn-echo decay of the

electron spin. Furthermore, we study how the second harmonic response varies with the microwave amplitude and phase, and comment on the nature of the non-linearity that mediates the second harmonic driving process in this system.

8.2. DEVICE AND MEASUREMENT TECHNIQUE

The quantum dot is electrostatically induced in an undoped Si/SiGe quantum well structure, through a combination of accumulation and depletion gates (see Sec. 5.3 for full details). The sample and the settings are the same as those used in Ch. 7. A cobalt micro-magnet next to the QD creates a local magnetic field gradient, enabling spin transitions to be driven by electric fields (Kawakami *et al.*, 2014; Obata *et al.*, 2010). All measurements shown here are performed using single-shot read-out via a QD charge sensor (Elzerman *et al.*, 2004) (Sec. 7.2).

First we apply long, low-power microwave excitation to perform quasi-CW spectroscopy (Eq. 4.30). Fig. 8.1(a) shows four observed spin resonance frequencies, $f_0^{(1)}$ through $f_0^{(4)}$, as a function of the external magnetic field. The resonances labeled (1) and (2) represent the response at the fundamental frequency. As in Sec. 7.3, these two closely spaced resonances correspond to the electron occupying either of the two lowest valley states, both of which are thermally populated here. The other two resonances occur at exactly half the frequency of the first two, $f_0^{(1)} = 2f_0^{(3)}$, $f_0^{(2)} = 2f_0^{(4)}$, and represent the second harmonic response.

The effective g -factors extracted from the slopes for the second harmonic response are half those for the first harmonic response (see Fig. 8.1(a) inset). The relevant energy levels and transitions as a function of the total magnetic field, B_{tot} , are visualized in Fig. 8.1(b), where the color scheme used for the resonances is the same as in Fig. 8.1(a). We see two sets of Zeeman split doublets, separated by the splitting between the two lowest-energy valleys, E_V . The transition between the Zeeman sublevels within each doublet can be driven by absorbing a single photon or two photons, as indicated by the single and double arrows.

8.3. ORIGIN OF THE NON LINEARITY

To drive a transition using the second harmonic, a non-linearity is required. In principle, several mechanisms can introduce such a non-linearity in this system (see Sec. 8.S5). First, as schematically shown in Fig. 8.1(c), if the confining potential is anharmonic, an oscillating electric field of amplitude E^{AC} and angular frequency $\omega = 2\pi f_{MW}$ induces effective displacements of the electron wavefunction with spectral components at angular frequencies $n\omega$, with n an integer. In analogy with non-linear optical elements, we can look at this process as generated by an effective non-linear susceptibility of the electron bounded to the anharmonic QD confinement potential.

The gradient in the transverse magnetic field in the dot region (B_{\perp} in green) converts the electron motion into an oscillating transverse magnetic field of the form

$$B_{\perp}^{AC}(t) = B_{\omega} \cos(\omega t) + B_{2\omega} \cos(2\omega t) + \dots \quad (8.1)$$

that can drive the electron spin for $\hbar\omega = E_z$, $2\hbar\omega = E_z$ and so forth (Rashba, 2011). A possible source of anharmonicity arises from the nonlinear dependence of the dipole

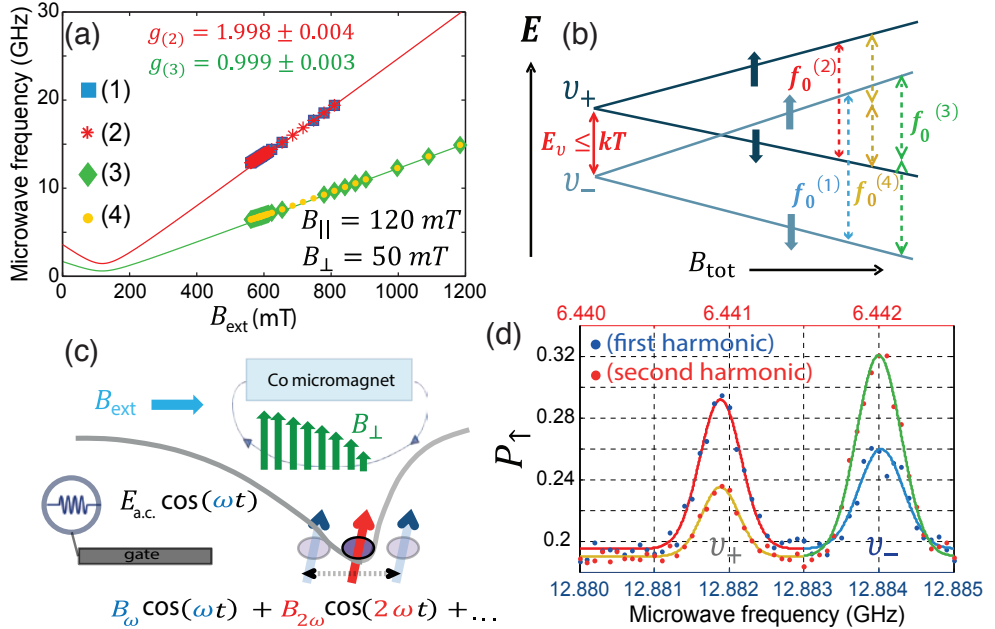


Figure 8.1: (a) Measured resonance frequencies as a function of externally applied magnetic field B_{ext} . The long microwave burst time $t_p = 700 \mu\text{s} \gg T_2^*$ means that the applied excitation is effectively continuous wave (CW). The microwave source output power was $P = -33 \text{ dBm}$ to -10 dBm (-20 dBm to -5 dBm) for the case of fundamental (second) harmonic excitation, decreasing for lower microwave frequency in order to avoid power broadening. The red and green lines represent fits with the relation $hf = g\mu_B \sqrt{(B_{\text{ext}} - B_{\parallel})^2 + B_{\perp}^2}$ respectively to the resonance data labeled (2) and (3) (we excluded points with $B_{\text{ext}} < 700 \text{ mT}$ from the fit because the micromagnet apparently begins to demagnetize there) (Kawakami *et al.*, 2014). (b) Schematic of the energy levels involved in the excitation process, as a function of the total magnetic field at the electron location. The dashed arrows correspond to the four transitions in panel (a), using the same color code. (c) Schematic of an anharmonic confinement potential, leading to higher harmonics in the electron oscillatory motion in response to a sinusoidally varying excitation. (d) Measured spin-up probability, P_{\uparrow} , as a function of applied microwave frequency, f_{MW} , for $B_{\text{ext}} = 560.783 \text{ mT}$ ($P = -30 \text{ dBm}$ for the fundamental response, $P = -12 \text{ dBm}$ for the second harmonics), averaged over 150 repetitions per point times 80 repeated frequency sweeps (160 mins in total). The frequency axis (in red on top) has been stretched by a factor of two for the second harmonic spin response (red datapoints). From the linewidths, we extract a lower bound for the dephasing time $T_2^{*(1)} = 760 \pm 100 \text{ ns}$, $T_2^{*(2)} = 810 \pm 50 \text{ ns}$, $T_2^{*(3)} = 750 \pm 40 \text{ ns}$ and $T_2^{*(4)} = 910 \pm 80 \text{ ns}$. The Gaussian fits through the four peaks use the same color code as in panels (a) and (b).

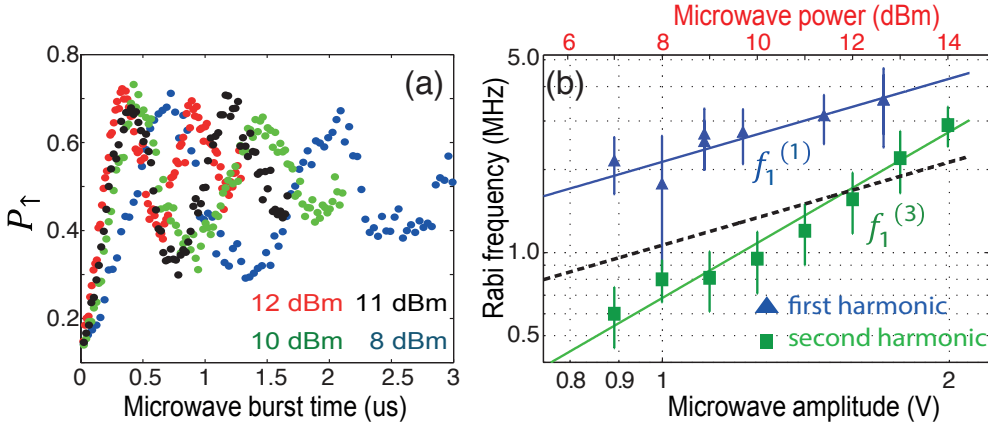


Figure 8.2: Rabi oscillations. (a) Measured spin-up probability, P_{\uparrow} , as a function of microwave burst time ($B_{\text{ext}} = 560.783$ mT, $f_{\text{MW}} = 6.4455$ GHz) at four different microwave powers, corresponding to a rms voltage at the source of 998.8 mV, 1257.4 mV, 1410.9 mV, 1583.0 mV. (b) Rabi frequencies recorded at the fundamental harmonic, $f_1^{(1)}$ (blue triangles, the same as in Fig. 7.S6), and at the second harmonic, $f_1^{(3)}$ (green squares), as a function of the microwave amplitude emitted from the source (top axis shows the corresponding power). For the second harmonic, the amplitude shown corresponds to a 5 dB higher power than the actual output power, to compensate for the 5 dB lower attenuation of the transmission line at 6 GHz versus 12 GHz (Sec. 5.3.2). The green solid (dashed black) line is a fit of the second harmonic data with the relation $\log(f_1^{(3)}) \propto 2\log(V_{AC})$ ($\log(f_1^{(3)}) \propto \log(V_{AC})$). The large error bars in the FFT of the data in Fig. 8.2(a) arise because we perform the FFT on only a few oscillations. $B_{\text{ext}} = 560.783$ mT.

moment between the valley (or valley-orbit) ground (v_-) and excited states (v_+) (Gamble *et al.*, 2013), as a function of E^{AC} .

A second possible source of nonlinearity is a variation of the transverse field gradient, $\frac{dB_{\perp}}{dx, dy}$, with position (see Fig. 8.1(c)). Even if the confining potential were harmonic, this would still lead to an effective transverse magnetic field containing higher harmonics, of the same form as Eq. 8.1.

A third possibility is that not only the transverse magnetic field but also the longitudinal magnetic field varies with position. This leads to an a.c. magnetic field which is not strictly perpendicular to the static field, which is in itself sufficient to allow second harmonic driving (Boscaino *et al.*, 1971; Gromov and Schweiger, 2000; Romhányi, Burkard, and Pályi, 2015), even when the confining potential is harmonic and the field gradients are constant over the entire range of the electron motion.

However, simple estimates indicate that the second and third mechanisms are not sufficiently strong in the present sample to allow the coherent spin manipulation we report below (see Sec. 8.S5). We propose that the first mechanism is dominant in this sample, supported by our observation that the strength of the second harmonic response is sensitive to the gate voltages defining the dot.

8.4. CW ANALYSIS

In Fig. 8.1(d) we zoom in on the four CW spin resonance peaks, recorded at low enough power to avoid power broadening (see Sec. 8.2). Fitting those resonances with Gaus-

sians, we extract the dephasing times $T_2^{*(1,2)} = \frac{\sqrt{2}\hbar}{\pi\delta f_{FWHM}^{(1,2)}}$, $T_2^{*(3,4)} = \frac{\sqrt{2}\hbar}{2\pi\delta f_{FWHM}^{(3,4)}}$, giving values in the range of 750 to 910 ns for all four resonances (see caption of Fig. 8.1(d)). This directly shows that the linewidth (FWHM) extracted for the two-photon process is half that for the one-photon process, as expected (De, Pryor, and Flatté, 2009; Gromov and Schweiger, 2000; Széchenyi and Pályi, 2014).

From the relative peak heights in Fig. 8.1(d), we can estimate the ratio of the Rabi frequencies between the two peaks in each pair (see Sec. 8.S1). In Sec. 7.S5 and Sec. 7.S4, we found that the relative thermal populations of the two valleys ($\epsilon^{(2)} : \epsilon^{(1)} = \epsilon^{(4)} : \epsilon^{(3)}$) were about $0.3 \pm 0.1 : 0.7 \pm 0.1$. Given this, the ratio between the Rabi frequencies, f_1 , extracted from the peak heights is $f_1^{(4)}/f_1^{(3)} = 0.9 \pm 0.2$ for the second harmonics. This is different from the ratio observed in for the fundamental harmonic, $f_1^{(2)}/f_1^{(1)} = 1.53 \pm 0.19$ (Sec. 7.S9)¹.

Such a difference is to be expected. The ratio $f_1^{(4)}/f_1^{(3)}$ is affected by how the degree of anharmonicity in the confining potential differs between the two valleys. In contrast, $f_1^{(2)}/f_1^{(1)}$ depends on how the electrical susceptibility differs between the two valleys (Rahman *et al.*, 2009). In addition, since the valleys have different charge distributions (Gamble *et al.*, 2013), the microwave electric field couples differently to the two valley states, and this difference can be frequency dependent (Kawakami *et al.*, 2013; Oosterkamp *et al.*, 1997). Because the second harmonic Rabi oscillations are driven at half the frequency of the Rabi oscillations driven at the fundamental, this frequency dependence also contributes to a difference between $f_1^{(2)}/f_1^{(1)}$ and $f_1^{(4)}/f_1^{(3)}$. We note that the difference in Rabi frequency ratio between the 1-photon and 2-photon case demonstrates that the second harmonic response is not just the result of a classical up-conversion of the microwave frequency taking place before the microwave radiation impinges on the dot, but takes place at the dot itself.

8.5. COHERENT SPIN OSCILLATIONS

The second harmonic response also permits coherent driving, for which a characteristic power dependence is expected (Gromov and Schweiger, 2000; Strauch *et al.*, 2007; Széchenyi and Pályi, 2014). Fig. 8.2(a) shows Rabi oscillations, where the microwave burst time is varied keeping $f_{MW} = f_0^{(3)}$ for different microwave powers. We note that the contribution to the measured spin-up oscillations coming from the other resonance, (4), is negligible because the respective spin Larmor frequencies are off-resonance by 2 MHz, $f_1^{(3)}/f_1^{(4)} \approx 1$ and its population is \sim three times smaller.

To analyze the dependence of the Rabi frequency on microwave power, we perform a FFT of various sets of Rabi oscillations similar to those in Fig. 8.2(a). Fig. 8.2(b) shows the Rabi frequency thus obtained versus microwave power for driving both at the second harmonic (green) and at the fundamental (blue), taken for identical dot settings (Kawakami *et al.*, 2014). We see that for driving at the frequency of the second harmonic, the Rabi frequency is quadratic in the applied electric field amplitude (linear in power), as expected from theory (Gromov and Schweiger, 2000; Strauch *et al.*, 2007; Széchenyi

¹Note that the ratio between the two Rabi frequencies is independent of the microwave amplitude in both cases, as we have $f_1^{(2)}/f_1^{(1)} = m_2 E^{AC}/m_1 E^{AC} = m_2/m_1$ and $f_1^{(4)}/f_1^{(3)} = q_4 E^{AC^2}/q_3 E^{AC^2} = q_4/q_3$, respectively.

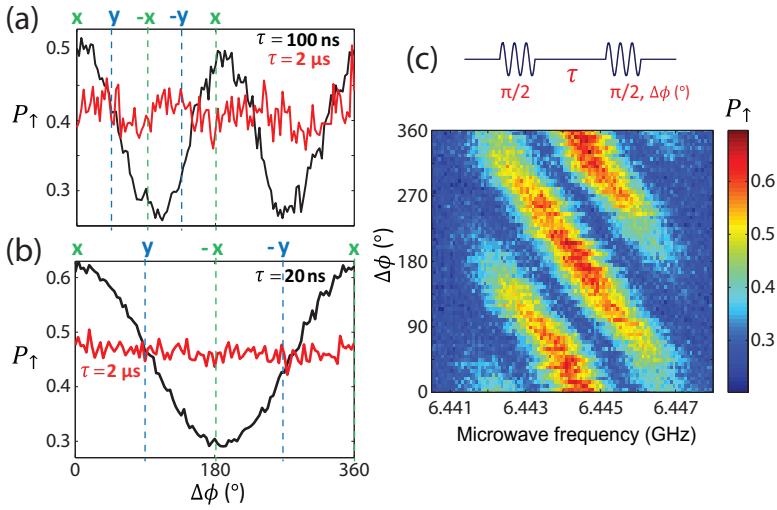


Figure 8.3: Phase control of oscillations. (a) Probability P_{\uparrow} measured after applying two $\pi/2$ rotations via second harmonic excitation, as a function of the relative phase between the two microwave bursts, $\Delta\phi$. The two rotations are separated by $\tau = 100$ ns (black) and $\tau = 2$ μ s (red). ($P = 16.0$ dBm, $B_{\text{ext}} = 560.783$ mT, $f_{\text{MW}} = f_0^{(3)} = 6.44289$ GHz). (b) Similar to panel (a), but now driving the fundamental harmonic for $\tau = 20$ ns (black) and $\tau = 2$ μ s (red). ($P = 12.0$ dBm, $B_{\text{ext}} = 560.783$ mT, $f_{\text{MW}} = f_0^{(1)} = 12.88577$ GHz). Inset: Microwave pulse scheme used for this measurement. (c) Measured spin-up probability, P_{\uparrow} (1000 repetitions for each point), as a function of f_{MW} and the relative phase $\Delta\phi$ between two $\pi/2$ microwave bursts (130 ns, $P = 16.0$ dBm) for second harmonic excitation, with $\tau = 50$ ns. The measurement extends over more than 15 hours.

and Pályi, 2014). When driving at the fundamental resonance, the Rabi frequency is linear in the driving amplitude, as usual. It is worth noting that at the highest power used in this experiment the Rabi frequency obtained from driving the fundamental valley-orbit ground state spin resonance is just a factor of two higher than the one from driving at the second harmonic. This ratio indicates that the use of second harmonic driving is quite efficient in our device. This result is consistent with (Széchenyi and Pályi, 2014), which shows that Rabi frequencies at subharmonic resonances can be comparable to the Rabi frequency at the fundamental resonance, and also with the theory and experiments in (Danon and Rudner, 2014) and (Stehlik *et al.*, 2014), which report resonant response at a second harmonic that can exceed that at the fundamental.

8.6. UNIVERSAL PHASE CONTROL

A further peculiarity in coherent driving using second harmonics is seen when we vary the phase of two consecutive microwave bursts. Fig. 8.3(a) shows the spin-up probability following two $\pi/2$ microwave bursts with relative phase $\Delta\phi$, resonant with $f_0^{(3)}$ and separated by a fixed waiting time τ . For short τ , the signal oscillates sinusoidally in $\Delta\phi$ with a period that is half that for the single-photon case (compare the dashed and dotted black traces in Figs. 8.3(a,b)).

Therefore, in order to rotate the electron spin around an axis in the rotating frame rotated by 90 degrees with respect to a prior spin rotation axis (e.g. a \hat{y} rotation following an \hat{x} rotation in the rotating frame), we need to set $\Delta\phi$ to 45 degrees, instead of 90 degrees, when driving via the second harmonic. Of course, for $\tau \gg T_2^*$, the contrast has vanished, indicating that all phase information is lost during the waiting time (Fig. 8.3(a,b) red traces). Fig. 8.3(c) shows two-pulse measurements as in Fig. 8.3(a) as a function of frequency detuning and phase difference, where we can appreciate the extraordinary stability of the undoped device.

To probe further the coherence properties of the spin, we perform a free induction (Ramsey) decay measurement, see Fig. 8.4(a), as a function of frequency detuning and delay time, τ , between the two bursts. The absence of a central frequency symmetry axis is due to the presence of two superimposed oscillating patterns, originating from the resonances at $f_0^{(3)}$ and $f_0^{(4)}$. Figs. 8.4(c-e) show sections of the Ramsey measurement in Fig. 8.4(a), corresponding to different waiting times τ (see the white dashed lines). The visibility of the Ramsey fringes clearly decreases for longer waiting times between the two $\pi/2$ pulses. Fitting the decay of the visibility of the fringes as a function of τ with a Gaussian ($\propto \exp[-(t/T_2^*)^2]$, see Sec. 8.S3) we find $T_2^* = 780 \pm 110$ ns, in agreement with the value extracted from the linewidth.

Furthermore, and analogously to the observations of Fig. 8.3(a), we report a doubling effect in the frequency of the Ramsey oscillations, f_{Ramsey} , as a function of the detuning $\Delta f_{\text{MW}} = f_{\text{MW}} - f_0^{(3)}$. Fig. 8.4(b) shows $f_{\text{Ramsey}}(\Delta f_{\text{MW}})$, extracted from the data in Fig. 8.4(a) via a FFT over the waiting time τ . The black dashed line indicates the condition $f_{\text{Ramsey}} = 2\Delta f_{\text{MW}}$, closely overlapping with the position of the yellow peaks in the FFT. The black dotted line indicates the condition $f_{\text{Ramsey}} = 2(f_{\text{MW}} - f_0^{(4)})$; this second resonance is not very visible in the data, due to the lower population of the corresponding valley. For comparison, the white dashed line indicates the condition $f_{\text{Ramsey}} = \Delta f_{\text{MW}}$, which is the

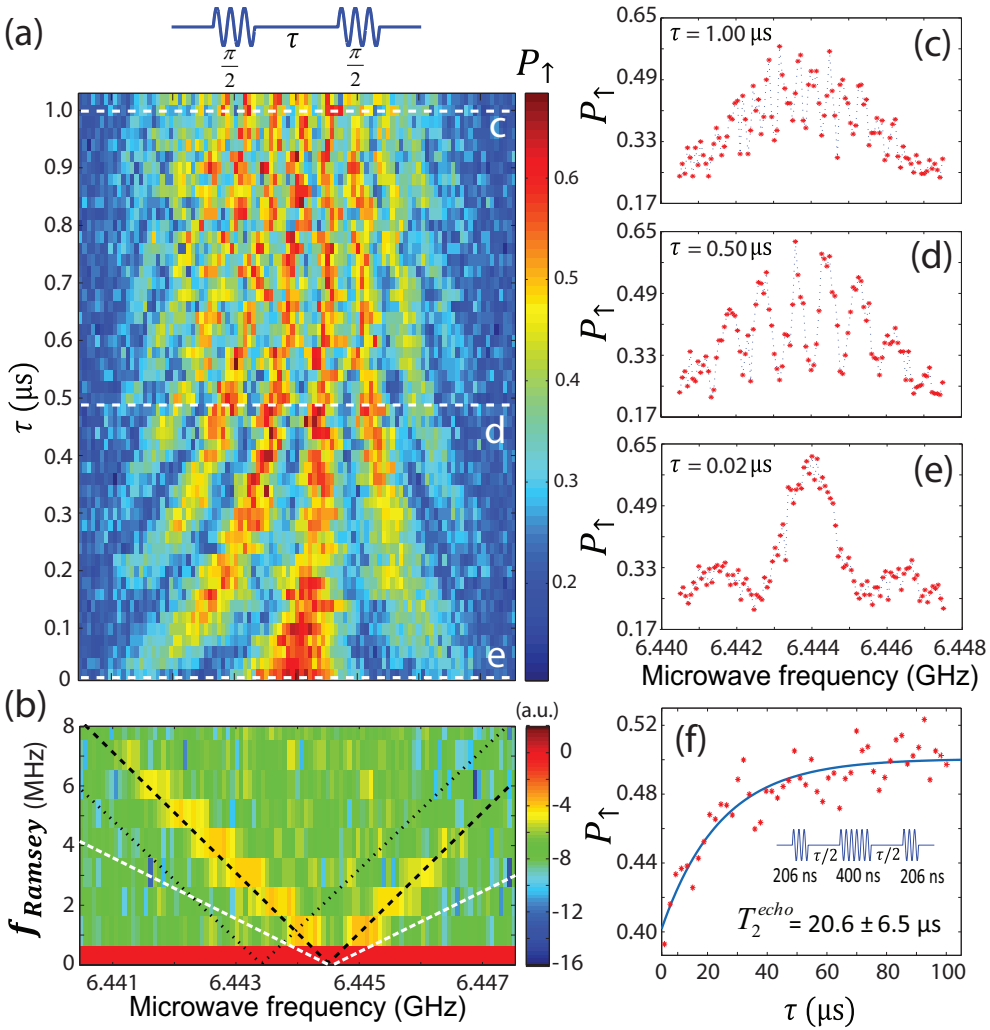


Figure 8.4: Ramsey fringes. (a) Measured spin-up probability, P_{\uparrow} , as a function of f_{MW} and waiting time τ ($B_{\text{ext}} = 560.783$ mT, $P = 13.0$ dBm) between two $\pi/2$ pulses (130 ns) with equal phase, showing Ramsey interference. Each data point is averaged over 300 cycles. Inset: Microwave pulse scheme used for this measurement. (b) Fourier transform over the waiting time, τ , of the data in panel (a), showing a linear dependence on the microwave frequency, with vertex at $f_{\text{MW}} = f_0^{(3)}$ and slope $f_{\text{Ramsey}} = 2\Delta f_{\text{MW}}$ (black dashed lines). The expected position of the FFT of the signal arising from resonance $f_0^{(4)}$ is indicated by the dotted black line. For comparison, the white dashed line represents the relation $f_{\text{Ramsey}} = \Delta f_{\text{MW}}$. (c-e) Sections of the Ramsey interference pattern in (a) along the three white dashed lines; the respective waiting times are indicated also in the inset of each panel. (f) Measured spin-up probability as a function of the total free evolution time, τ , in a Hahn echo experiment (pulse scheme shown in inset). The decay curve is fit well to a single exponential (blue). Here, $f_{\text{MW}} = f_0^{(3)}$, $B_{\text{ext}} = 560.783$ mT.

expected response when driving at the fundamental.

Finally, we perform a spin echo experiment via second harmonic driving. Fig. 8.4(f) shows P_1 as a function of the total free evolution time τ , for a typical Hahn echo pulse sequence (illustrated in the inset) consisting of $\pi/2$, π and $\pi/2$ pulses applied along the same axis, separated by waiting times $\tau/2$ (Hahn, 1950). A fit to a single exponential yields $T_2^{\text{Hahn}} = 20.6 \pm 6.5 \mu\text{s}$ at $B_{\text{ext}} = 560.783 \text{ mT}$, compatible with the T_2^{Hahn} of $23.0 \pm 1.2 \mu\text{s}$ we observed at the same magnetic field when driving via the fundamental harmonic (see Sec. 8.S4).

8.7. CONCLUSION

To summarize, we report coherent second harmonic driving of an electron spin qubit defined in a Si/SiGe quantum dot, including universal single-spin rotations. The non-linearity that permits second harmonic driving is likely related to the anharmonic confining potential for the electron. This means that routine use of second harmonics for spin control would be possible provided there is sufficient control over the degree of anharmonicity of the confining potential. This could be very useful since driving a spin qubit at half its Larmor frequency would substantially simplify the microwave engineering required for high fidelity qubit control.

SUPPLEMENTARY INFORMATION

8.S1. ESTIMATION OF THE RATIO OF RABI FREQUENCIES FROM CW MEASUREMENTS

A typical CW spin resonance measurement is reported in Fig. 8.S1, which shows the spin excited state probability as a function of the applied microwave frequency, f_{MW} , and time. We note that the fluctuations of the two spin resonance frequencies, $f^{(3)}$ and $f^{(4)}$, are highly correlated; this suggests that the two resonances are affected by the same low-frequency source of noise (very likely hyperfine fluctuations) on the \sim minute timescale. The trace for the second harmonic in Fig. 8.1(d) in the main text is obtained by averaging the data in Fig. 8.S1 over the time axis.

As in Sec. 7.S5, the ratio of the steady-state spin-flip probability measured for the two valley states converges at low driving power to $\left(f_1^{(4)}/f_1^{(3)}\right)^2$. The ratio of the measured peak amplitudes between two valley states is the product of $\left(f_1^{(4)}/f_1^{(3)}\right)^2$ and the ratio of the respective populations at the end of the initialization stage, $\epsilon^{(4)}/\epsilon^{(3)}$. From a Gaussian fit to the spin resonance response for the two valleys in Fig. 8.1(d), we extract the ratio of the measured peak amplitudes ~ 0.35 :

$$\left(\frac{f_1^{(4)}}{f_1^{(3)}}\right)^2 \frac{\epsilon^{(4)}}{\epsilon^{(3)}} \sim 0.35. \quad (8.S1)$$

Furthermore, we assume that the ratio between the valley ground and excited state populations after the initialization stage, is the same when driving via the second harmonic

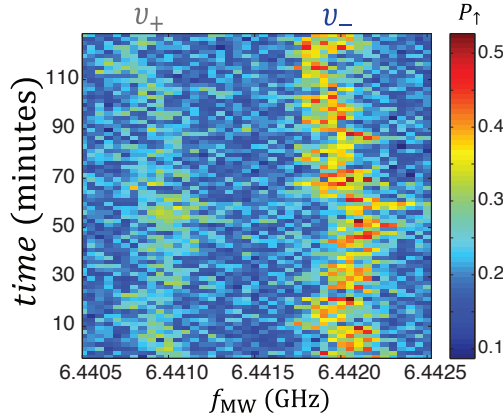


Figure 8.S1: The raw data on which Fig. 1(d) is based. Measured spin-up probability, P_{\uparrow} , as a function of applied microwave drive frequency f_{MW} and time (external field $B_{\text{ext}} = 560.783$ mT, power $P = -12$ dBm, microwave pulse duration $700 \mu\text{s}$). Each horizontal scan in the figure takes ~ 2 minutes (200 cycles, in which each data point takes 2s), and the scan is repeated ~ 60 times. The time reported on the y-axis is counted from the start of the measurement.

as when driving via the fundamental (Sec. 7.S5):

$$\frac{\epsilon^{(4)}}{\epsilon^{(3)}} \equiv \frac{\epsilon^{(2)}}{\epsilon^{(1)}} \sim \frac{0.3}{0.7} \quad (8.S2)$$

From eq. 8.S1 and eq. 8.S2 we obtain

$$\frac{f_1^{(4)}}{f_1^{(3)}} \sim 0.90. \quad (8.S3)$$

We remark that we also assume that the ratio of the Rabi frequencies between two valleys is the same at high microwave power as it is at low microwave power.

8.S2. CHEVRON PATTERN USING SECOND HARMONIC DRIVING

In Fig. 8.S2(a) we report the spin excited state probability oscillations as a function of the microwave burst time and detuning frequency (driving with $P_{\text{MW}} = 11.0$ dBm at the source). The quality of the data (stability of the measurement) is not high enough to extract independently the Rabi frequencies for the two valley states directly from the superimposed Chevron patterns (as was done in (Kawakami *et al.*, 2014) for driving via the fundamental harmonic). However, using the Rabi frequency ratio $f_1^{(4)}/f_1^{(3)} \approx 1$ extracted above, the ratio of initial populations of the two valleys of $\epsilon^{(4)}/\epsilon^{(3)} \sim 0.3/0.7$ discussed above as well, and a Rabi frequency of 1.05 MHz for the valley ground state (estimated from a FFT along the MW burst time of Fig. 8.S2(a)), we can simulate the two superimposed Chevron patterns, see Fig. 8.S2(b). This simulation agrees qualitatively with the data of Fig. 8.S2(a), in particular it captures the slight asymmetry along the detuning axis, and the fact that mostly one Chevron pattern is visible.

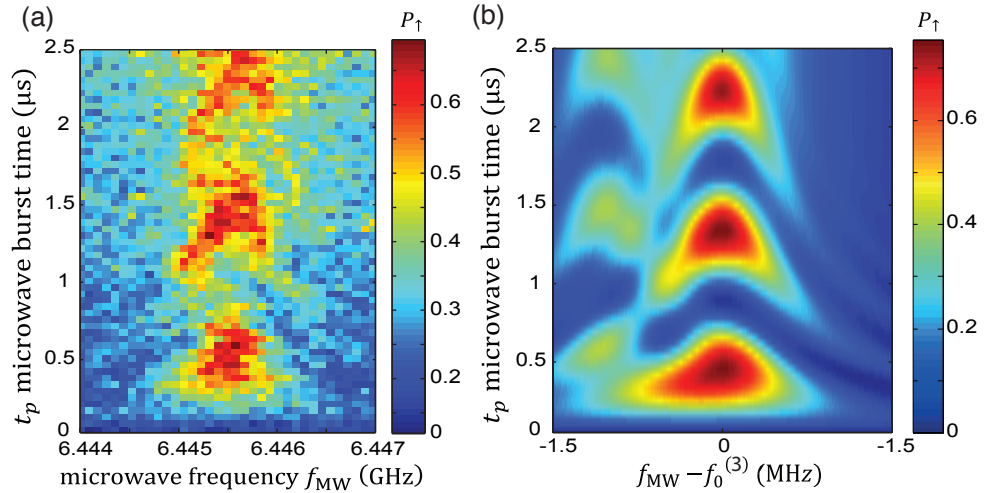


Figure 8.S2: (a) Measured spin-up probability, P_{\uparrow} , as a function of drive frequency f_{MW} and microwave burst time ($B_{\text{ext}} = 560.783$ mT, $P = 11.0$ dBm). (b) Simulated spin-up probability using population fractions 0.3:0.7, Rabi frequencies 1.0 MHz and 1.1 MHz for the v_+ and v_- valley states respectively, and the Larmor frequencies separated by ~ 1.04 MHz, extracted from low-power CW measurements in Fig. 8.1(d).

8.S3. T_2^* ESTIMATION FROM RAMSEY ENVELOPE DECAY AND RAMSEY SIMULATION

In order to get an alternative estimation of the dephasing time T_2^* , we can perform a Ramsey measurement (see Fig. 8.4(a) of the main text) and record the amplitude of the Ramsey oscillations as a function of the waiting time τ between the two $\pi/2$ pulses, keeping $f_{\text{MW}} \approx f_0^{(3)}$. We show this data in Fig. 8.S3, with the blue dotted curve representing the fitting relation $P_{\uparrow} = a \exp[-(t/T_2^*)^2] + c$. From this fit we get a T_2^* of 780 ± 110 ns, compatible with what we estimated from the CW spin resonance linewidth in Fig. 8.1(d). On the same figure we report in black for comparison a fit with the exponential relation $P_{\uparrow} = a \exp(-t/T_2^*) + c$.

8.S4. ECHO DECAY OF A QUBIT DRIVEN FUNDAMENTAL HARMONIC AND COMPARISON TO RESULTS FOR DRIVING AT SECOND HARMONIC

In Fig. 8.S4 we show a Hahn echo measurement realized driving spin resonance at the fundamental harmonic, recorded at the same magnetic field B_{ext} as the measurement reported in Fig. 8.4(e) (driven by second harmonic). The $T_2^{\text{Hahn}}(1ph)$ extracted from a fit with a single exponential decay is similar to the $T_2^{\text{Hahn}}(2ph)$ extracted from Fig. 8.4(e). The decay obeys a single exponential similar to that observed in Sec. 7.5, indicating the presence of a high-frequency decoherence process.

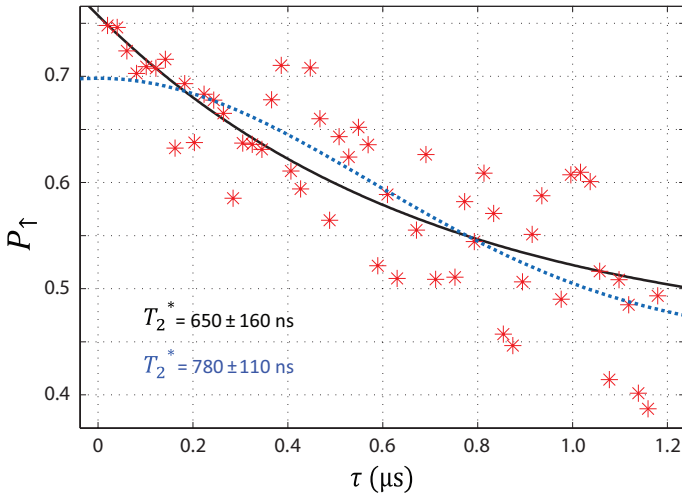


Figure 8.S3: Decay of Ramsey envelope as a function of the waiting time between the two Ramsey pulses. The blue dotted line is a fit of the data with the relation $P_{\uparrow} = a \exp[-(t/T_2^*)^2] + c$, with T_2^* as a free parameter and $c = 0.46$, the average value for $\tau \gg T_2^*$ (see Fig. 8.4), which we also obtain keeping c a free parameter ($c = 0.46 \pm 0.09$; $T_2^* = 790 \pm 330$ ns). The fact that the center of the P_{\uparrow} oscillations is not 0.5 is attributed to initialization and measurement errors.

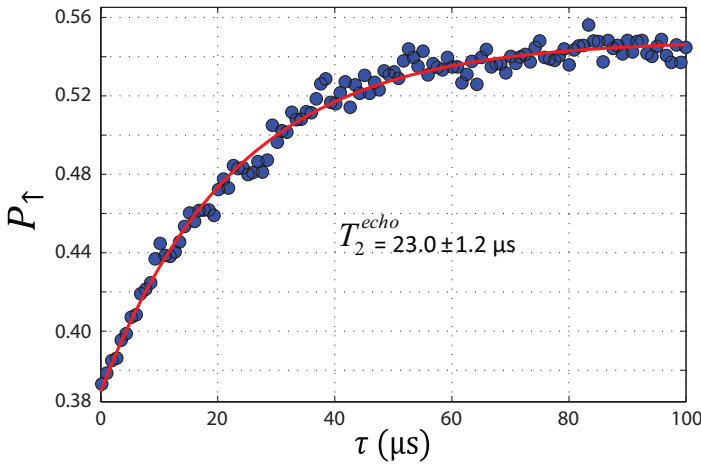


Figure 8.S4: Spin echo measurement for the ground valley-orbit state driven at the fundamental harmonic for $B_{ext} = 560.783$ mT and $f_{MW} = f_0^{(1)} = 2f_0^{(3)}$. The observed T_2^{Hahn} times are similar for driving at the fundamental and second harmonic.

8.S5. MECHANISMS MEDIATING SECOND HARMONIC GENERATION

Here elaborate our discussion on the mechanism that can lead to a second harmonic generation presented in the main text of this chapter and Ch. 3.1.3,

POSITION DEPENDENT MAGNETIC FIELD GRADIENT

From a simulation of the stray magnetic field of the micromagnet (Sec. 3.2, Appendix G), we can put an upper bound on the second derivative of the stray magnetic field with respect to the dot coordinates of $d^2B_{\perp}/dx^2 < 1 \mu\text{T}/(\text{nm})^2$. This is far too small to produce the measured second harmonic Rabi frequencies $\sim 1-5$ MHz, which are as high as the fundamental Rabi frequencies (the ratio is $f_1^{(3)}/f_1^{(1)} \sim 0.5$ for the highest microwave driving field used in the experiment, see Fig. 8.2(b)).

TILTED DRIVE FIELD

As discussed in Ch. 3.1.3 and Appendix. C.1, the second harmonic resonance can be generated by a magnetic field oscillating along the parallel axis to the spin quantization axis. If the gradient of the stray magnetic field parallel to the external magnetic field along the modulated direction is non-zero ($dB_{\parallel}/dx \neq 0$). In our system the magnetic field gradient has components in all three directions of space (Sec. 3.2, Appendix G). More specifically, we have $dB_{\parallel}/dx \approx 0.2$ mT/nm and $dB_{\perp}/dx \approx 0.3$ mT/nm. Given these magnetic field gradients, the amplitude of the magnetic field oscillating along the parallel axis is expected to be the same order of magnitude as the magnetic field oscillating along the perpendicular axis. In this case, according to Eq. 3.23, $f_1^{(3)}/f_1^{(1)} \sim 0.5$ cannot be achieved with this mechanism.

ANHARMONIC CONFINING POTENTIAL

In the absence of detailed knowledge of the shape of the confining potential, it is difficult to quantitatively estimate the magnitude of this effect. However, what we can say is that the details of the confining potential strongly influence the efficiency of second harmonic driving: after tuning the same device into a new gate voltage configuration for the experiments in Ch. 10 (for which the valley splitting is higher than it is here), it has not been possible to observe again clear signatures of second harmonic driving. The new settings will likely also shift the average dot position in the micromagnet stray field, thereby altering the tilt of the effective driving field as well as the position dependent field gradient. However, as discussed in the preceding sections, these two effects are several orders of magnitude too small to explain the observed second harmonic driving. If the degree of anharmonicity of the confining potential dominates second harmonic driving, control of the anharmonicity will be required to make routine use of second harmonic driving in future spin qubit experiments.

9

EDSR DETECTION OF DRESSED ORBITAL STATES IN A QUANTUM DOT

The valley degree of freedom strongly impacts the performance of electron spin qubits in Si/SiGe quantum dots, in particular when the lowest valley-orbit splitting is small compared to the thermal energy. A detailed understanding of these effects is crucial for operating electron spin quantum bits in such systems. The valley degree of freedom was also proposed as a potential quantum bit itself, which requires further experimental study. Here we present experiments on a single electron in a Si/SiGe quantum dot in which microwave electric excitation induces transitions between states with both different electron spin and valley-orbit states. We find a tenfold increase in sensitivity to electric fields and electrical noise compared to pure spin transitions, strongly impacting phase coherence. This increased sensitivity is captured by theoretical modeling of the valley-orbit splitting as a function of electron position in the presence of atomic steps in the quantum well. The ability to drive such inter-valley spin transitions is described theoretically as the result of a non-adiabatic process whereby the valley-orbit state is excited and simultaneously a spin flip is mediated by artificial spin-orbit coupling from a micromagnet next to the quantum dot. Pure spin transitions, whether arising from harmonic or subharmonic generation, are shown to be adiabatic in the orbital sector. Finally, the experiments show a dynamical anti-crossing that we describe theoretically in the form of dressed eigenstates from hybridization of orbital, photon and spin states.

The work in this chapter is done with collaboration with P. Scarlino, T. Jullien, D. R. Ward, D. E. Savage, M. G. Lagally, Mark Friesen, S. N. Coppersmith, M. A. Eriksson and L. M. K. Vandersypen and the manuscript is under preparation.

9.1. INTRODUCTION

A spin-1/2 particle is the canonical two-level quantum system. Its energy level structure is extremely simple, consisting of just the spin-up and spin-down levels. Therefore, when performing spectroscopy on an elementary spin-1/2 particle such as an electron spin, only a single resonance is expected corresponding to the energy separation between the two levels.

Recent measurements have shown that the spectroscopic response of a single electron spin in a quantum dot can be much more complex than this simple picture suggests. This is particularly true when using electric-dipole spin resonance, where an oscillating electric field couples to the spin via spin-orbit coupling (Nowack *et al.*, 2007). First, due to non-linearities in the response to oscillating driving fields, subharmonics can be observed (Forster *et al.*, 2015; Laird *et al.*, 2009; Laird, Pei, and Kouwenhoven, 2013; Nadj-Perge *et al.*, 2012; Pei *et al.*, 2012; Stehlik *et al.*, 2014), and the non-linear response can even be exploited for driving coherent spin rotations (Ch. 8). Second, due to spin-orbit coupling, the exact electron spin resonance frequency in given magnetic field depends on the orbital the electron occupies (Khaetskii and Nazarov, 2001). In silicon or germanium quantum dots, the conduction band valley is an additional degree of freedom (Friesen and Coppersmith, 2010; Friesen, Eriksson, and Coppersmith, 2006; Goswami *et al.*, 2007; Rančić and Burkard, 2016; Zwanenburg *et al.*, 2013), and the electron spin resonance frequency should depend on the valley state as well (Hao *et al.*, 2014; Kawakami *et al.*, 2014; Rančić and Burkard, 2016; Yang *et al.*, 2013). As a result, when valley or orbital energy splittings are comparable to or smaller than the thermal energy, thermal occupation of the respective levels leads to the observation of multiple closely spaced spin resonance frequencies (Ch. 7).

The picture becomes even richer when considering transitions in which not only the spin state but also the orbital quantum number changes. Such phenomena are common in optically active dots (Warburton, 2013), but have been observed also in electrostatically defined (double) quantum dots in the form of relaxation from spin triplet to spin singlet states (Fujisawa *et al.*, 2002; Johnson *et al.*, 2005) and spin-flip photon-assisted tunneling (Braakman *et al.*, 2014; Schreiber *et al.*, 2011). However, transitions involving the valley state have so far remained unexplored in experiment.

Here, we report transitions where both the spin and valley-orbit state flip in a Si/SiGe quantum dot. We demonstrate that we can Stark shift the transition, and we compare the sensitivity to electric fields to the case of pure spin transitions, including the impact on phase coherence. From these measurements we can observe that the valley-orbit coupling strongly affects the coherence properties of the inter-valley spin resonance. We show that a theory incorporating a driven four-level system comprised of two valley-orbit and two spin states subject to strong ac driving provides a consistent description of these transitions, as well as all the previously reported transitions for this system. This theory also explains the observation of a dynamic level repulsion, which can be understood effectively and compactly using a dressed-state formalism.

9.2. DEVICE AND SPECTROSCOPIC MEASUREMENTS

The sample and the settings are the same as those used in Ch. 7.8. A cobalt micromagnet next to the QD creates a local magnetic field gradient, enabling spin transitions to be driven by electric fields (Kawakami *et al.*, 2014; Obata *et al.*, 2010). All measurements shown here are performed using single-shot read-out via a QD charge sensor (Elzerman *et al.*, 2004) (Sec. 7.2). The initialization and read-out procedures require a Zeeman splitting exceeding $k_B T_{el}$ (~ 150 mK, electron temperature estimated from transport measurements), which here restricts us to working at $B_{tot} > 450$ mT.

When varying the applied microwave frequency and external magnetic field, we observe five distinct resonance peaks [Fig. 9.1(a)]¹. The two resonances labeled (1) and (2), not resolved on this scale, are two intra-valley spin resonances, one for each of the two lowest-lying valley states that are thermally occupied (Ch. 7). They exhibit a $T_2^* \sim 1 \mu\text{s}$ and Rabi frequencies of order MHz. The two resonances labeled (3) and (4), similarly not resolved, arise from second harmonic driving of the two intra-valley spin flip transitions. These transitions too can be driven coherently, with Rabi frequencies comparable to those for the fundamental harmonic (Ch. 8).

The focus of the present work is the resonance labeled (5), which has not been discussed before. Its frequency, $f_0^{(5)}$, is ~ 7 GHz lower than the fundamental intra-valley spin resonance frequencies, $f_0^{(1)}$ and $f_0^{(2)}$. From its magnetic field dependence measured above 500 mT, we extract a g -factor of about 1.971 ± 0.002 , close to but different from the g -factors for resonances (1) and (2) ~ 1.99 (Ch. 7.8). The linewidth (Fig. 9.3(a)) is almost ten times larger than that for the intra-valley resonances, giving a correspondingly shorter T_2^* of around 100 ns. Around 500 mT, the slope of resonance (5) changes in a way reminiscent of level repulsions (see Fig. 9.1(b)). Without the change in slope, resonance (5) would have crossed resonances (3) and (4), however the latter do not show any sign of level repulsion and continue their linear dependence on magnetic field.

We interpret these puzzling observations starting with Fig. 9.1(d). Two sets of Zeeman split levels are seen, separated by the energy of the first excited valley-orbit state. The red (1) [(2)] and two blue (3) [(4)] arrows show driving of spin transitions via the fundamental and second harmonic respectively, for the valley-orbit ground [excited] state. We identify resonance (5) with the transition indicated with the black arrows in which both spin and valley(-orbit) flip. It has the same field dependence as resonance (1), but (above 500 mT) it is offset from resonance (1) by a fixed amount, which as we can see from Fig. 9.1(d), is a measure of the valley-orbit splitting, E_V .

¹Here, we present measurements realized for different magnetic field orientations. The components of the external magnetic field are reported in each figure. The specific orientation of the external magnetic field does not play any special role. It is our understanding that the results presented in this work are independent from the specific magnetic field orientation.

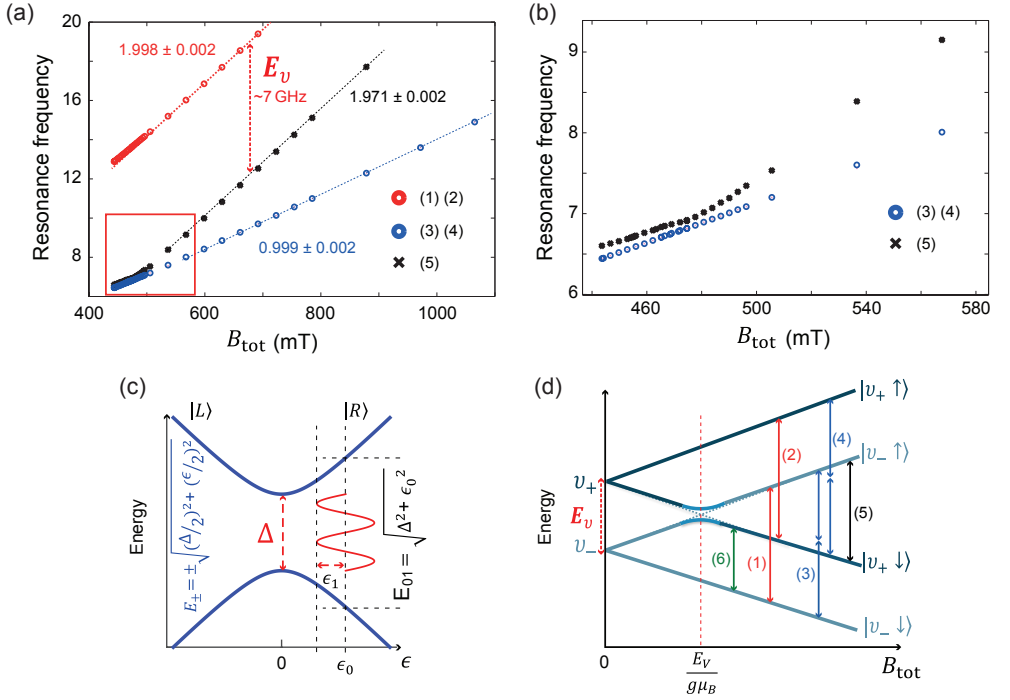


Figure 9.1: (a) Multiple resonance frequencies as a function of the external magnetic field, observed for a single electron spin confined in a gate-defined Si/SiGe quantum dot, driven by low-power microwave excitation applied to one of the quantum dot gates. Resonances (1) and (2) are indistinguishable on this scale, as are resonances (3) and (4). On the horizontal axis, we plot $B_{tot} = \sqrt{(B_{ext}^x + B_{\parallel})^2 + B_{\perp}^2}$, with $B_{\parallel} \sim -120$ mT and $B_{\perp} \sim 50$ mT the estimated components of the stray magnetic field from the micromagnet [magnetized, in this measurement, along the x-direction (see Fig. S3)]. (b) Zoom-in of the region indicated by a red box in panel (a). (c) Schematic energy level diagram of a generic two-level quantum system described by Eq. 9.S1, as a function of detuning ϵ and with a harmonic driving around the central value ϵ_0 with energy eigenvalues E_{\pm} and energy splitting $E_{01} = E_+ - E_-$. (d) The four energy levels considered in this work as a function of B_{tot} , in the absence of photonic dressing, comprised of two valley-orbit states ($|\nu_- \rangle$, $|\nu_+ \rangle$) and two spin states ($|\downarrow \rangle$, $|\uparrow \rangle$). E_V represents the valley-orbit energy splitting. Vertical arrows indicate four processes observed in our simulations, with the same labeling scheme as panel (a). (1) and (2) correspond to single-photon spin flips. (3) and (4) correspond to two-photon spin flips. (5) corresponds to a combined spin flip, valley-orbit excitation, and single-photon absorption. (6) is observed in simulations but not in the experiments, since the condition $E_V \leq k_B T_{el}$ makes the read-out process low-fidelity for this excitation, and corresponds to a nonadiabatic valley-orbit excitation.

9.3. MODEL

We now introduce a simple model Hamiltonian that can be used to understand the observed spectroscopic response. This model explains the presence of both the first and second harmonic driven spin resonance as well as the observed inter-valley spin resonance. We show that resonances such as those observed in experimental Fig. 9.1(a,b) are generic features of a strongly driven four-level system composed of two orbital levels

and two spin levels in which there is a coupling between the orbital levels, such as a tunnel coupling. For our case, it is natural to associate the orbital levels with two different valley-orbit states (see Sec. 9.S1).

Our analysis builds upon the theory proposed by Rashba (Rashba, 2011). When a spin qubit is driven at a frequency ω , it responds at one or more frequencies Ω , which may be the same as ω , but may also be different (see Fig. 9.2(a)). Spin resonance is observed if (i) the spin is flipped², and (ii) $\hbar\Omega = E_Z$, where $E_Z = g\mu_B B_{tot}$ is the Zeeman splitting, g is the Landé g -factor in silicon, μ_B is the Bohr magneton, and B_{tot} is the total magnetic field. In electric dipole spin resonance (EDSR), the spin flip requires a physical mechanism for the electric field to couple to the spin, such as spin-orbit coupling (Tokura *et al.*, 2006). In our experiment, an effective spin-orbit coupling due to the strong magnetic field gradient from the micromagnet is the mechanism responsible for spin flips (Ch. 7). Hence, we can say that EDSR and its associated spin dynamics provide a tool for observing the mapping $\omega \rightarrow \Omega$. However, as discussed in (Rashba, 2011), EDSR does not determine the mapping; determining the resonant frequencies Ω requires including the essential non-linearity in the system, which in this case resides in the orbital sector of the qubit Hamiltonian. We therefore focus on the dynamics of the orbital sector of the Hamiltonian; the mechanism for spin flips is included perturbatively after the charge dynamics have been characterized.

The exact orbital Hamiltonian is difficult to write down from first principles, since it likely involves both orbital and valley components (Ch. 7), and depends on the atomistic details of the quantum well interface (Friesen and Coppersmith, 2010; Friesen, Eriksson, and Coppersmith, 2006; Goswami *et al.*, 2007). Nonetheless, the features of the resonances in Fig. 9.1 emerge quite naturally using a model with one low-lying orbital excited state. Referring to Fig. 9.1(c), in this model, the Hamiltonian for the orbital sector is described by a simple two-state Hamiltonian, which we write as

$$H = \frac{1}{2}(\epsilon\sigma_z + \Delta\sigma_x). \quad (9.1)$$

Here, ϵ is a detuning parameter, Δ is the tunnel coupling between the generic basis states labeled $|L\rangle$ and $|R\rangle$, and σ_x and σ_z are Pauli matrices. We consider a classical ac drive, applied to the detuning parameter:

$$\epsilon(t) = \epsilon_0 + \epsilon_1 \sin(\omega t). \quad (9.2)$$

If the quantum dot confinement were purely parabolic, then changing the detuning would not affect the energy splitting between the eigenstates. However, any nonparabolicity in the dot, which is unavoidable in real devices, will cause the energy splitting to depend on the detuning and will yield a nonlinear response to the driving term, Eq. 9.S4. In our Hamiltonian, this effect enters via the tunnel coupling Δ , which causes the qubit frequency to depend on $\epsilon(t)$.

Our goal is to determine the response of the two-level system to this $\epsilon(t)$. We assume that the basis states are coupled by the applied electric field because they have different

²For resonance (5), the valley state must flip too; therefore, a spin-valley coupling mechanism is required (Hao *et al.*, 2014; Huang and Hu, 2014; Yang *et al.*, 2013).

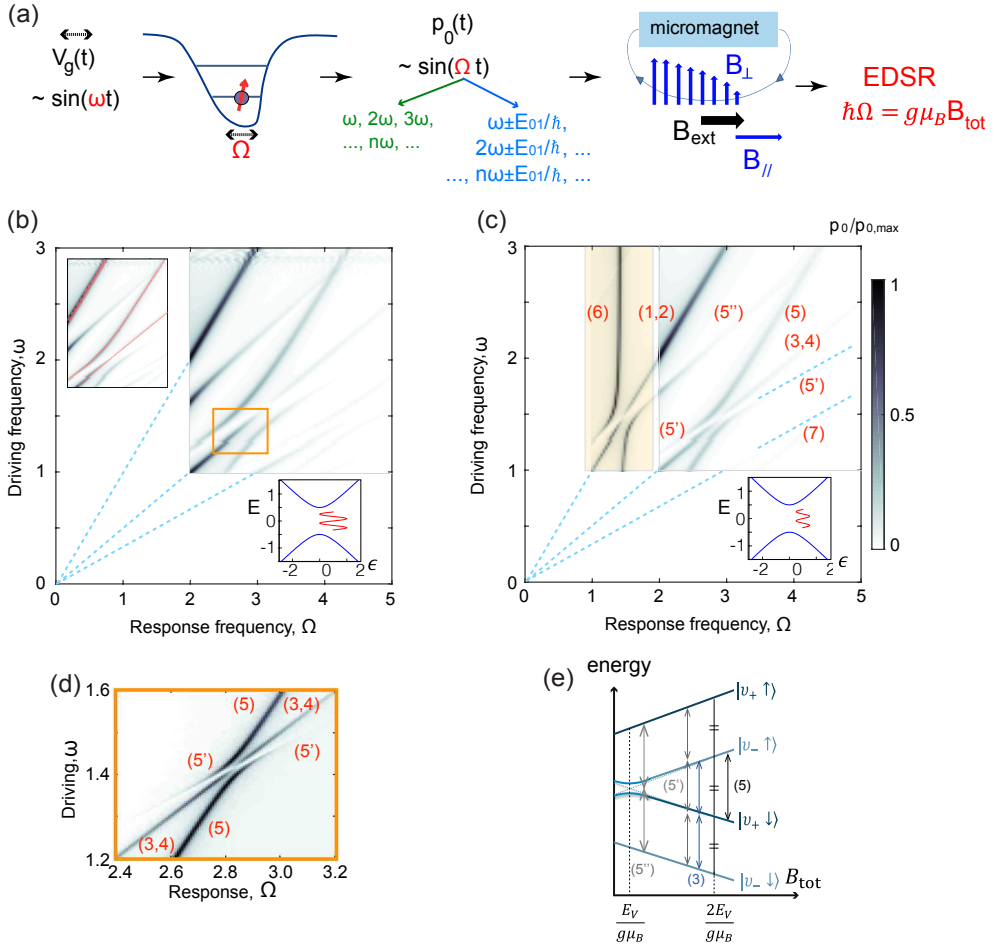


Figure 9.2: Theoretical calculations of resonances in an ac-driven qubit with a low-lying orbital state induced by adiabatic and non-adiabatic processes. (a) Schematic illustrating that an excitation at driving frequency ω leads to several adiabatic (non-adiabatic) response frequencies of the electron dipole moment, $p_0(\Omega) = \text{FFT}[p_0(t)]$, listed in green (blue). The time-dependent electron dipole moment in turn produces spin flips due to the magnetic field gradient when $\hbar\omega$ matches the Zeeman splitting. (b) Simulated resonance spectrum of the ac-driven qubit model of Eqs. (9.S1) and (9.S4), setting $\hbar = 1$. As described in the main text, the dynamics of the dipole moment p_0 , defined in Eq. (9.S5), are solved in the time domain for the driving frequency ω , then Fourier transformed to obtain the response frequency Ω . Here we use $\epsilon_0 = \epsilon_1 = \Delta = 1$. The dashed lines indicate the positions of the fundamental resonance and its first two harmonics (top to bottom). The lower inset shows the relation between the energy levels and the driving term. The upper inset shows the same results as the main panel, with the experimentally relevant resonances highlighted (compare to Fig. 9.1). (c) Resonance spectrum corresponding to the parameters $\epsilon_0 = \Delta = 1$ and $\epsilon_1 = 0.5$. Here, the shaded region was normalized separately from the rest of the figure. The resonance features labeled 1-9 are discussed in the main text (see also Sec. 9.S4 and Sec. 9.S2.2). (d) A blowup of the region shown in the center box of panel (b), using the parameters $\Delta = \epsilon_0 = 1$ and $\epsilon_1 = 0.11$, which gives good agreement with the level repulsion observed in the experiments shown in Figs. 9.1(a) and 9.1(b). (e) The same as Fig. 9.1(d) but focusing on the region around the point where the anti-crossing between the states $|\nu_- \uparrow\rangle$ and $|\nu_+ \downarrow\rangle$ occurs ($B_{\text{tot}} = \frac{E_V}{g\mu_B}$) and where the level repulsion between resonance lines (5) and (5'') occurs ($B_{\text{tot}} = \frac{2E_V}{g\mu_B}$). (5') and (5'') corresponds to the three-photon process and the two-photon process of the transition between $|\nu_- \downarrow\rangle$ and $|\nu_+ \uparrow\rangle$, respectively.

spatial charge distributions, and study the time evolution of the dipole moment of the ground state $|0\rangle$, defined as

$$p_0 = \frac{eL}{2} [|\langle 0|L\rangle|^2 - |\langle 0|R\rangle|^2]. \quad (9.3)$$

Here, L is the distance³ between the charge in states $|L\rangle$ and $|R\rangle$.

Rashba has studied Hamiltonian (Eq. 9.S1) perturbatively in the regime of weak driving and high excitation frequency (Rashba, 2011). In Sec. 9.S1-9.S2, we present a detailed exposition of our extensions of these investigations into the strong driving regime relevant to resonance (5). We find that driving this transition involves non-adiabatic processes whereby the orbital state gets excited, in contrast to the subharmonics reported in Ch. 8, which as we show here involve only adiabatic processes in the charge sector.

Here, we present the results of numerical simulations in this regime and show that the results are consistent with the main features observed experimentally. The dynamical simulations are performed by setting $\hbar = 1$ and solving the Schrödinger equation $i\partial|\psi\rangle/\partial t = H|\psi\rangle$ for Eqs. (9.S1) and (9.S4) and computing $p_0(t)$ as defined in Eq. (9.S5) for a fixed driving frequency⁴ ω . The resulting $p_0(t)$ is Fourier transformed, yielding a $p_0(\Omega)$ whose peaks reflect the resonant response. Finally, we smooth $p_0(\Omega)$ by convolving it with a Gaussian of width 0.025 (in order to take into account noise, which is averaged in the experiment). Because of the spin-orbit coupling, peaks in $p_0(\Omega)$ correspond to frequencies at which an ac magnetic field is generated, so spin flips will occur at a Zeeman frequency given by $E_Z/\hbar = \Omega$. The experiment measures the probability of a spin flip as a function of magnetic field; via the EDSR mechanism, resonances in this probability therefore occur when the peak locations in $p_0(\Omega)$ satisfy $g\mu_B B_{tot} = \hbar\Omega$.

Figs. 9.2(b) and (c) show the results of our simulations for $p_0(\Omega)$ as a function of both driving frequency ω and response frequency Ω over a range of parameters analogous to those shown in Fig. 9.1. From top to bottom, the dashed blue lines correspond to the fundamental resonance (1,2), and the first two subharmonics (3,4,7), which are all visible in the simulations. We also see a resonance, labeled (5), running parallel to the fundamental resonance (the other resonances are discussed in Sec. 9.S4). The upper inset of Fig. 9.2(b) highlights the particular resonances in the main figure that should be compared to the experimental data shown in Fig. 9.1(a,b).

An interesting feature of the resonances, observed both in the experiments and theory (Figs. 9.2(b-d)), is the apparent ‘level repulsion’ between resonance lines (5) and (5’) that takes place near $B_{tot} = 480$ mT. This magnetic field value is much higher than $E_V/g\mu_B \sim B_{tot} = 250$ mT, where the anti-crossing between the states $|\nu_-, \downarrow\rangle$ and $|\nu_+, \uparrow\rangle$ is expected to occur (Yang *et al.*, 2013) (see the red dashed line in Fig. 9.1(d)), but which is outside our measurement window, see above. Instead the observed ‘level repulsion’

³For a charge qubit, L is the lateral separation between the two sides of the double quantum dot. For an orbital qubit, L is the lateral separation of the center of mass of the two orbital states. For a pure valley qubit, L is the vertical separation of the even and odd states (~ 0.16 nm). For a complicated system like a valley-orbit qubit with interface disorder, L will have lateral and vertical components, with the lateral component being usually much larger than the vertical one. In this last case the exact length L will depend on the specifics of the interface disorder; a reasonable guess would be $L \sim 0.5$ -5 nm (see, e.g. Ref. [28]).

⁴For the Hamiltonian parameters indicated in the caption of Fig. 9.2(b), we use time steps in the range 0.061-0.073.

has a purely dynamical origin, as demonstrated by the fact that the anti-crossing is suppressed in Fig. 9.2(c), where the simulation parameters are identical to Fig. 9.2(b), except for a smaller driving amplitude ϵ_1 .

In Sec. 9.S2, we develop a dressed-state theory to describe these strong-driving effects. In this formalism, the quasiclassical driving field of Eq. 9.S4 is replaced by a fully quantum description of the photon field and its coupling to the (valley)-orbital Hamiltonian of the quantum dot. The resulting dressed eigenstates describe the hybridized photon-orbital levels, and more generally, the hybridization of orbital, photon, and spin states. In this way, resonances (1) and (2) in Fig. 9.2(c) correspond to single-photon spin flips, while resonances (3) and (4) correspond to two-photon spin flips. Resonance (5) involves both a spin flip and a valley-orbit excitation. The right-most portion of resonance (5) is parallel to resonance (1,2), indicating that it is a single-photon process. The left-most portion of the resonance (5) (the resonance (5')), is parallel to resonance (7), indicating that it is a three-photon process. The physical mechanisms of the resonances are also indicated in Fig. 9.1(d) and Fig. 9.2(e).

In principle, coupling occurs between all of the dressed states due to the effective spin-orbit coupling in our EDSR experiment. In practice however, the orbital-Rabi frequency is two orders of magnitude larger than the spin-Rabi frequency, so mode hybridization is only observed in resonance (5'), resulting in the level repulsion. The magnitude of this repulsion provides a convenient way to determine the orbital-Rabi frequency, which cannot be measured directly due to the fast dephasing of the excited valley-orbit state (see Sec. 9.S3). In Sec. 9.S2, we estimate this Rabi frequency to be about 0.2 GHz.

9.4. COHERENCE OF THE INTER-VALLEY SPIN TRANSITION

We now examine the possible origin of the ten times larger linewidth of resonance (5) compared to that of the pure spin-flip resonances (1) and (2). Given the partial valley nature of transition (5) and the strong valley-orbit coupling that is typical of Si/SiGe quantum dots (Gamble *et al.*, 2013; Hao *et al.*, 2014; Yang *et al.*, 2013), a plausible candidate decoherence mechanism for this transition is electric field noise.

In order to study the sensitivity to electric fields of the respective transitions, we show in Fig. 9.3(a) the dependence of the frequency of resonances (1) and (5) on the voltage applied to one of the quantum dot gates, V_3 . Clearly, resonance (5) exhibits a much greater sensitivity to gate voltage than resonance (1): ~ 18.5 MHz/mV for $f_0^{(5)}$, versus ~ 0.5 MHz/mV for $f_0^{(1)}$. We also notice that the two resonance shifts as a function of V_3 have opposite sign, which indicates that different mechanisms are responsible. For resonance (1), we believe that the dominant effect of the electric field is the displacement of the electron wave function in the magnetic field gradient from the micromagnets (see Sec. 9.S3.2). This effect also contributes to the frequency shift of resonance (5), but presumably it is masked by the change in valley-orbit splitting (E_V) resulting from the displacement of the electron wave function in the presence of interface disorder (Friesen and Coppersmith, 2010; Shi *et al.*, 2012). For instance, moving the electron towards or away from a simple atomic step at the Si/SiGe interface leads to a change of the valley-orbit energy splitting, as shown by the results of numerical simulations shown

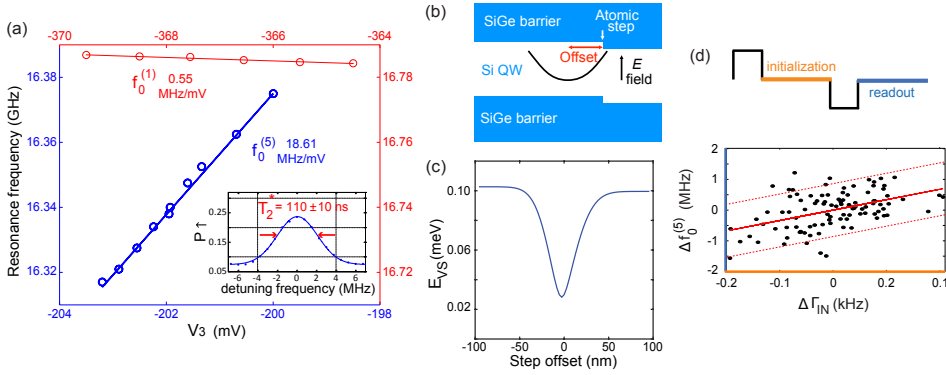


Figure 9.3: Sensitivity of intra-valley and inter-valley spin transitions to electric fields. (a) Measured resonance frequency for the inter-valley ($f_0^{(5)}$) at $B_{ext}^y = 792$ mT, blue data and axes) and intra-valley ($f_0^{(1)}$) at $B_{ext}^y = 550$ mT, red data and axes) spin transition, as a function of gate voltage V_3 . Inset: low-power continuous wave response of the inter-valley spin transition, with T_2^* estimated from the linewidth (see also Fig. 9.S3). (b) Schematic representation of an atomic step in a Si/SiGe quantum well and of a quantum dot parabolic confinement potential (not to scale) laterally offset from the step. (c) Valley-orbit energy splitting found by a 2D tight binding calculation using the geometry shown in panel (b), a 13 nm wide quantum well barrier of 160 meV (corresponding to 30% Ge), a parabolic confinement potential for the dot of size $\sqrt{\langle x^2 \rangle} = 21.1$ nm (corresponding to an orbital energy splitting of $\hbar\omega = 0.45$ meV), and an electric field of 1.5×10^6 V/m (the experimental electric field is not well known). In the plots, a positive step offset corresponds to a step on the right-hand side of the dot. (d) Scatter plot showing two quantities measured every 400 s. The x axis shows the average rate, Γ_{IN} , with which an electron tunnels into the quantum dot during qubit initialization (in orange in the inset); on the y axis is the frequency of resonance (5) relative to its value averaged over the entire measurement (see also Fig. 9.S5). The continuous line represents a linear fit to the data through the point (0,0). The dashed lines represent the 95% confidence interval. The distribution of the points in the scatter plot indicates that the two quantities are correlated. $B_{ext}^x = 590$ mT, $B_{ext}^y = 598.2$ mT, $\Delta f_0^{(5)} = f_0^{(5)} - 15.6894$ GHz, $\Delta \Gamma_{IN} = \Gamma_{IN} - 1.0762$ kHz.

in Fig. 9.3(b,c). As expected, the simulations predict a minimum in the valley-orbit splitting when the wave function is centered around the atomic step, but interestingly it does not vanish, i.e. the opposite signs for the valley-orbit splitting left and right of the atomic step do not lead to complete cancellation (see Sec. 9.S4).

The ~ 35 times greater sensitivity of the spin-valley transition frequency to electric fields may contribute to its ten times larger linewidth compared to the intra-valley spin transition. The linewidth of the intra-valley spin transition is believed to be dominated by the 4.7% ^{29}Si nuclear spins in the host material (Ch. 7,10). The nuclear field also affects the spin-valley transition, but obviously only accounts for a small part of the linewidth here. We propose that the dominant contribution to the linewidth of resonance (5) is low-frequency charge noise.

Although not definitive, some evidence for this interpretation is found in Fig. 9.3(d), which shows a scatter plot of $f_0^{(5)}$ and one of the dot-reservoir tunnel rates, simultaneously recorded over many hours (see Sec. 9.S3.3 for a more detailed description of the measurement scheme). The dot-reservoir tunnel rate serves as a sensitive probe of local electric fields, including those produced by charges that randomly hop around in the vicinity of the quantum dot (see Fig. 9.S5) (Vandersypen *et al.*, 2004). The plot shows a modest correlation between the measured tunnel rate and $f_0^{(5)}$, suggesting that the shifts

in time of both quantities may have a common origin, presumably low-frequency charge noise.

In this case, we can also place an upper bound on T_2^* permitted by charge noise for the intra-valley spin transitions (1,2) in the present sample. Indeed, due to the micro magnet induced gradient in the local magnetic field parallel to B_{ext} , the pure spin transitions are also sensitive to charge noise. Given that $T_2^* \sim 110$ ns for transition (5) and the ratio of ~ 35 in sensitivity to electric fields⁵, charge noise in combination with this magnetic field gradient would limit T_2^* to $\sim 3.8 \mu\text{s}$ for transitions (1,2). It is important to note that this is not an intrinsic limitation, as the stray field of the micro magnet at the dot location can be engineered to have zero gradient of the longitudinal component, so that to first order charge noise does not affect the frequency and T_2^* of transitions (1,2). At the same time, a strong gradient of the transverse component can be maintained, as is necessary for driving spin transitions (Sec. 11.4).

Besides its strong sensitivity to static electric fields, we report a surprising dependence of the frequency of resonance (5) on microwave driving power [Fig. 9.4(b,c)]. Increasing the driving power, the resonance not only broadens but also shifts in frequency, as in an a.c. Stark shift (Brune *et al.*, 1994). This dynamical evolution is very different from the case of the intra-valley spin resonance, which is power broadened but stays at fixed frequency (Ch. 7,10). This frequency shift is, at least for a limited microwave power range, in line with the dynamical level repulsion captured by Eq. S42, where $\Delta E_{\text{asympt}} \propto \epsilon_1^2$ expresses the energy splitting between resonance (5) and its asymptote, $\hbar\omega = E_Z - E_{01}$. This relation is verified in Fig. 9.4(c) for microwave powers of 9 – 17 dBm.

Finally, we attempt to drive coherent oscillations using resonance (5) at high applied microwave power, recording the spin excited state probability as a function of the microwave burst time. Oscillations are not visible, indicating that the highest Rabi frequency we can obtain for resonance (5) is well below the corresponding $1/T_2^*$ of 110 ns. This is consistent with our estimate that the Rabi frequency is of the order of 10 kHz, based on the magnitude of the dynamical level repulsion seen in Fig. 9.1(a,b) and the derivation in Sec. 9.S2.2.

9.5. CONCLUSIONS

Despite its simplicity, the electrical driving of a single electron confined in a single quantum dot can produce a complex spin resonance energy spectrum. This particularly applies for quantum dots realized in silicon, where the presence of the excited valley-orbit state, close in energy and strongly coupled to the ground state, introduces a substantial non-linearity in the system response to microwave electric fields. This allows us to observe a transition whereby both the spin and the valley state are flipped at the same time. We demonstrate how both static external electric fields and electrical noise influence the frequency of this inter-valley spin transition, dominating its coherence properties.

Much of the dynamics of the spin and valley transitions can be captured in a semiclassical picture, including driving using higher harmonics exploiting non-linearities. However, under intermediate or strong driving, new phenomena emerge that cannot be

⁵ $T_2^* \sim 110$ ns was calculated by the standard deviation of the resonance peak $\sigma_f = 2.1$ MHz using Eq. 4.41.

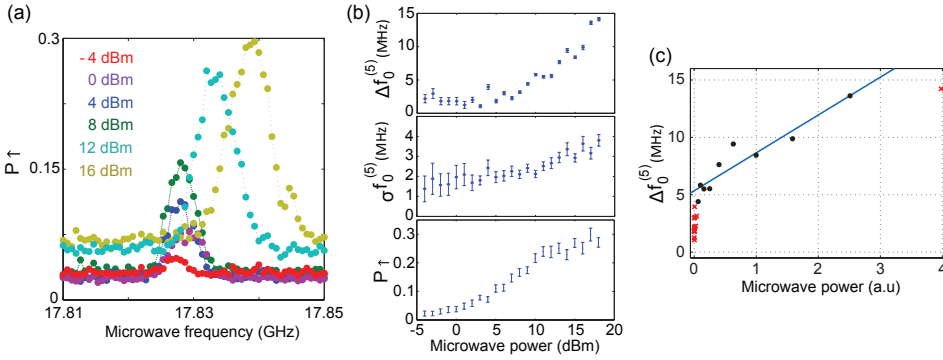


Figure 9.4: (a) Measured spin-up probability as a function of microwave power at $B_{ext}^y = 846$ mT for a fixed microwave burst time of $50 \mu\text{s}$, near the resonance condition for inter-valley spin-flip transition (5). For increasing power, the line does not only become taller and wider but also moves towards higher frequencies. Panel (b) summarizes from top to bottom the center frequency, width and height of the response. $\Delta f_0^{(5)} = f_0^{(5)} - 17.825$ GHz. (c) Top panel of figure (b) replotted using a linear power scale (x-axis $\propto 10^{\text{MW power (dBm)}/5}$). The blue line represents a linear fit to the black data points to the relation $\Delta E_{\text{asympt}} \propto c_1^2$ (eq. S42). The points indicated by the red crosses are excluded from the fit.

easily explained except in terms of pseudospins (dressed states) that fundamentally involve a quantum mechanical coupling between photons and orbital or spin states. Here, we have provided experimental and numerical evidence for the existence of such dressed states of photons and valley-orbit states at strong driving. We have further estimated the strength of this valley-orbit to photon coupling by comparing our analytical theory to the experiments.

This work provides important experimental and theoretical insight in the role of inter-valley transitions for controlling spin dynamics in silicon based quantum dots. It also highlights the limitations of valley-based qubits in the presence of strong valley-orbit coupling, due to their sensitivity to electrical noise.

SUPPLEMENTARY SECTIONS

This first section presents a theoretical discussion of the model used to understand the electric dipole spin resonance experiments presented in the main text. We show that experimental features are generic features of a driven four-level system, comprised of two valley-orbit and two spin degrees of freedom, with a tunnel coupling between the orbital states. The model exhibits conventional resonances, including both fundamental and higher harmonics, as well as novel resonances involving photonically dressed orbital states. We develop an analytical model that describes the key features of the hybridized dynamical states, based on a simple, 4D dressed-state Hamiltonian, and we use this model to determine the Rabi frequency for orbital excitations by fitting to the experimental data.

The main text reports EDSR measurements on an ac-driven spin qubit in a silicon quantum dot. The system is driven in a microwave regime that is intermediate between weak and strong driving, allowing us to observe semiclassical phenomena, such

as conventional spin resonances and spin-flip photon assisted tunneling (PAT) (Braakman *et al.*, 2014; Schreiber *et al.*, 2011), which have been observed previously in quantum dots. However, the experiments also probe new and intriguing phenomena that are purely quantum mechanical, involving the hybridization of photons, orbitals and spin. Such effects are most conveniently described as dressed states. By developing a formalism that is appropriate for our system, we can describe the photonically dressed states as pseudospins, and explain the hybridization effects by means of simple 2D and 4D Hamiltonians. Moreover, although coherent oscillations of the photon-orbital-spin pseudospins are not observed in our experiments (in contrast with photon-spin pseudospins, whose coherent oscillations were reported in Ch. 7), the dressed-state theory still allows us to extract the PAT Rabi frequency.

Our analysis is broken into two parts. In Sec. 9.S1, we describe a simple model for EDSR, and provide an intuitive discussion and overview of the resonances observed in the experiments.

In Sec. 9.S2, we develop a more technical, dressed-state formalism to describe the photonic dressing of the orbital and spin states in our system, which we use to explain and fit the experimental data.

9.S1. MODEL OF THE DYNAMICS

When a spin qubit is driven at a frequency ω , it responds at one or more frequencies Ω , which may be the same as ω , but may also be different. Spin resonance is observed if (i) the spin is flipped, and (ii) $\hbar\Omega = E_Z$, where $E_Z = g_B\mu_B B$ is the Zeeman splitting, g_B is the Landé g -factor in silicon, μ_B is the Bohr magneton, and B is the applied magnetic field. The spin flip requires a physical mechanism, such as spin-orbit coupling in EDSR (Tokura *et al.*, 2006). Indeed, the strong magnetic field gradient of the micromagnet introduces such a coupling (Kawakami *et al.*, 2014; Tokura *et al.*, 2006). Rashba has suggested that the mapping $\omega \rightarrow \Omega$ occurs entirely within the orbital sector, and that EDSR simply provides a tool for observing this mapping (Rashba, 2011). In this Supplemental Section, we adopt Rashba's orbital-based model as our starting point.

Several theoretical explanations have been put forth to explain strong-driving phenomena in EDSR, such as the generation of higher harmonics (Braakman *et al.*, 2014; Rashba, 2011; Stehlik *et al.*, 2014; Széchenyi and Pályi, 2014), and other, more exotic effects such as an even/odd harmonic structure (Stehlik *et al.*, 2014). For silicon dots, the exact orbital Hamiltonian is difficult to write down from first principles, since it involves both orbital and valley components (Ch. 7) and depends on the atomistic details of the quantum well interface (Friesen and Coppersmith, 2010; Friesen, Eriksson, and Coppersmith, 2006; Goswami *et al.*, 2007). Nonetheless, the dynamics can be understood using a minimal model for investigating the physics of the orbital sector, given by the two-level system

$$H = \frac{1}{2}(\epsilon\sigma_z + \Delta\sigma_x), \quad (9.S1)$$

where σ_x and σ_z are Pauli matrices. The basis states in this model may correspond to excited orbitals in a single quantum dot (Tokura *et al.*, 2006), valley states in a single dot (Friesen, Eriksson, and Coppersmith, 2006), localized orbital states in a double dot (Rashba, 2011), or a hybridized combination of these systems (Friesen and Copper-

smith, 2010). In each case, the two basis states have distinct charge distributions that can support EDSR through the mechanism described by Tokura et al. (Tokura *et al.*, 2006)

Eq. (9.S1) is, in fact, the most general theoretical model of a two-level system. Mapping the theoretical model onto a real, experimental system requires specifying the dependence of the effective detuning parameter ϵ and the effective tunnel coupling Δ on the voltages applied to the top gates for a given device. To take a simple example that is relevant for silicon quantum dots, we consider such a mapping for the basis comprised of valley states. In this case, ϵ represents a valley splitting, which can be tuned with a vertical electric field, while Δ represents a valley coupling, which can depend on the interfacial roughness of the quantum well and other materials parameters (Gamble *et al.*, 2013). The centers of mass of the charge distributions of the basis states in this example differ by about a lattice spacing in the vertical direction. It is likely that the silicon dots in the experiments reported here experience an additional valley-orbit coupling, which induces a lateral variation of the charge distributions. In this case, the gate voltage dependence of ϵ and Δ is quite nontrivial; however Eq. (9.S1) should still provide a useful theoretical description. For convenience in the following analysis, we adopt the picture of a charge qubit, for which the basis states correspond to “left” ($|L\rangle$) and “right” ($|R\rangle$). The eigenstates of H are then given by

$$|0\rangle = \frac{\Delta}{\sqrt{\Delta^2 + (\epsilon + E_{01})^2}} |L\rangle - \frac{\epsilon + E_{01}}{\sqrt{\Delta^2 + (\epsilon + E_{01})^2}} |R\rangle, \quad (9.S2)$$

$$|1\rangle = \frac{\Delta}{\sqrt{\Delta^2 + (\epsilon - E_{01})^2}} |L\rangle - \frac{\epsilon - E_{01}}{\sqrt{\Delta^2 + (\epsilon - E_{01})^2}} |R\rangle, \quad (9.S3)$$

and the energy splitting is given by $E_{01} = \sqrt{\Delta^2 + \epsilon^2}$.

To begin, we consider a classical ac driving field, applied to the detuning parameter:

$$\epsilon(t) = \epsilon_0 + \epsilon_1 \sin(\omega t). \quad (9.S4)$$

Our goal is to determine the response of the two-level system to this $\epsilon(t)$. In contrast with Rashba, we will not limit our analysis to the perturbative regime in which $\epsilon_1, E_{01} \ll \hbar\omega$, since the experiments reported here are not in that regime. To proceed, we note that the basis states couple differently to the applied electric field because they have different spatial charge distributions. We specifically consider the time evolution of the dipole moment of the ground state $|0\rangle$, defined as

$$p_0 = \frac{eL}{2} \langle 0 | \sigma_z | 0 \rangle = \frac{eL}{2} [|\langle 0 | L \rangle|^2 - |\langle 0 | R \rangle|^2], \quad (9.S5)$$

where L is the distance between the center of mass of the charge in states $|L\rangle$ and $|R\rangle$. Throughout the discussion that follows, when connecting the output of the model to the experimental data, we will identify E_{01} with the valley-orbit splitting, E_V .

9.S1.1. ADIABATIC EFFECTS

Two fundamentally different types of response to the driving are observed in $p_0(t)$: adiabatic vs. nonadiabatic. We first consider adiabatic processes. The adiabatic eigenstates

of the Hamiltonian, given in Eqs. (9.S2) and (9.S3) yield a corresponding dipole moment, computed from Eq. (9.S5), of

$$p_0 = \frac{eL}{2} \left[\frac{\Delta^2 - (\epsilon + E_{01})^2}{\Delta^2 + (\epsilon + E_{01})^2} \right] = -\frac{eL\epsilon}{2E_{01}}. \quad (9.S6)$$

Substituting Eq. (9.S4) into Eq. (9.S6), we see that the adiabatic response of $p_0(t)$ is a nonlinear function of $\sin(\omega t)$. For example, in the weak driving limit, we can expand Eq. (9.S6) to second order in the small parameter ϵ_1/E_{01} , giving

$$p_0(t) \simeq (\text{const.}) - \left(\frac{eL\Delta^2}{2\bar{E}_{01}^3} \right) \epsilon_1 \sin(\omega t) - \left(\frac{3eL\Delta^2\epsilon_0}{8\bar{E}_{01}^5} \right) \epsilon_1^2 \cos(2\omega t) + \dots \quad (9.S7)$$

Here, \bar{E}_{01} denotes the energy splitting when $\epsilon = \epsilon_0$. We see that the nonlinear dependence of the dipole moment on ϵ_1 translates into a series of response terms at frequencies $\Omega = \omega, 2\omega, 3\omega, \dots$. Since spin resonances only occur when $\hbar\Omega = E_Z$, these should be observed as subharmonics of the fundamental Zeeman frequency: $\omega = E_Z/\hbar, E_Z/2\hbar, E_Z/3\hbar, \dots$. For the two-level system defined by Eq. (9.S1), we note that all resonances depend on the presence of a coupling between the basis states, Δ . In Fig. 9.1(d) of the main text, the fundamental resonance condition and its first subharmonic are sketched as the second and third sets of vertical arrows. We note that adiabatic resonances can be observed in both the strong and weak driving regimes, although the higher harmonics may be suppressed for weak driving, as consistent with Eq. (9.S7).

9.S1.2. NONADIABATIC EFFECTS

We next consider nonadiabatic, or Landau-Zener (LZ) processes (Zener, 1932), which always involve an excitation (or deexcitation) of an orbital state. For the two-state Hamiltonian of Eq. (9.S1), LZ excitations can arise in two ways: (i) a sudden pulse of a control parameter (e.g., ϵ), or (ii) strong periodic driving of the control parameter [e.g., Eq. (9.S4)]. In the first case, the qubit is suddenly projected onto a new adiabatic eigenbasis, which induces a Larmor response at the frequency $\Omega = \pm E_{01}/\hbar$. In the second case, fast periodic excursions of $\epsilon(t)$ at driving frequencies different than E_{01}/\hbar can achieve a similar response. Such ‘conventional’ LZ excitation processes are indicated by the first vertical arrow in Fig. 9.1(d) of the main text⁶.

In the experiments reported here, simple LZ orbital excitations are undetectable, because the excitation energy E_{01} is smaller than the Fermi level broadening. However, the EDSR spin-flip mechanism allows us to generate and detect more complex processes at higher energies. The resonance condition indicated by the fourth set of vertical arrows in Fig. 9.1(d) is particularly important for these experiments; when combined with a spin

⁶In typical resonant driving experiments, the LZ process is actually more general than what is shown in the figure, because it can occur at any B -field. The process indicated in the figure implies an orbital excitation combined with a spin flip, which we discuss below.

flip, it describes one portion of the “resonance (5)” detailed in Figs. 1(a) and (b). Resonances of this type occur when $\hbar\Omega = m\hbar\omega \pm E_{01}$, corresponding to the driving frequencies $\omega = (E_Z \pm E_{01})/\hbar, (E_Z \pm E_{01})/2\hbar, (E_Z \pm E_{01})/3\hbar, \dots$. Since these resonance lines are parallel to the conventional spin resonances, Rashba has called them “satellites” (Rashba, 2011), although he studied a different driving regime for which no satellites were observed in the experiments.

There are two main theoretical approaches for describing such nonadiabatic phenomena. Since the orbital excitation involves an LZ process, it must be described quantum mechanically. However, the ac driving field can be described with a semiclassical, adiabatic theory like the one described in the previous section. In this approach, the qubit gains a “Stückelberg phase” each time it passes through an energy level anticrossing, resulting in interference effects that can be described using standard LZS theory (Shevchenko, Ashhab, and Nori, 2010)⁷. The alternative theoretical approach, described below, uses a dressed state formalism that encompasses all of the same interference effects, and plays a key role in understanding the detailed behavior of the resonance (5). In this case, the process can be described fully quantum mechanically as an orbital excitation combined with a photon absorption. In either description, the orbital excitation is followed by a spin-flip caused by the orbital dynamics.

9.S1.3. SIMULATION RESULTS

Results of numerical simulations of Eq. (9.S1) are presented in Fig. 9.2(b-d) of the main text. Here, we discuss the physical interpretation of these results in more detail.

Fig. 9.2(b-d) in the main text shows the results of our simulations for $p_0(\Omega)$ as a function of both driving frequency ω and response frequency Ω over a range of parameters analogous to those in Fig. 9.1(a). Fig. 9.2(b-d) correspond to three different driving amplitudes, with panel (d) chosen to match the experimental results in Fig. 9.1(b). The dashed blue lines correspond to the conventional ESR signals (the fundamental resonance, and the first two subharmonics, top to bottom), which are all visible in the simulations. In Fig. 9.2(c) (reproduced in Fig. 9.S1), these are labeled (1,2), (3,4), and (7). The inset on the left-hand side of Fig. 9.2(b) highlights the particular resonances that should be compared to the experimental data in Fig. 9.1(a).

In addition to conventional ESR resonances, several LZ resonances can be seen in the simulations. Three LZ resonances, labeled (5), (5') and (5''), are observed in Fig. 9.2(c). These lines correspond to the resonance conditions given by $\omega = (E_Z - E_{01})/\hbar$, $\omega = (E_Z + E_{01})/3\hbar$ and $\omega = (E_Z + E_{01})/2\hbar$, respectively. The latter resonance is clearly visible in the experiment, and corresponds to the resonance labeled (5) at high frequencies in Fig. 9.1.

An interesting feature of the LZ resonances is the apparent level repulsion between the resonance peaks (see Fig. 9.1(b)). Several of these anticrossings are seen in Fig. 9.2. The effect is purely dynamical, as demonstrated by the fact that the anticrossing is suppressed in going from panels (b) to (d), as consistent with the smaller driving amplitudes. In the dressed-state formalism, these dynamical modes correspond to resonances of the hybridized photon-orbital states, where the state composition changes suddenly.

⁷Note that the standard theory assumes the qubit is driven all the way through the energy level anticrossing in Eq. (9.S1); however, the interference effects observed in our simulations occur even without passing through the anticrossing.

Several excitations are observed in the simulations of Fig. 9.2 that are not also observed in the experiments. For example, the vertical line labeled (6) in Fig. 9.2(c) corresponds to the nonresonant (Larmor) LZ excitation discussed in Sec. 9.S1.2. This excitation occurs at an energy $\hbar\Omega$ that is too small to be detected experimentally. Resonance (5'') is suppressed in the simulations, compared to resonance (5), and it is not observed at all in the experiments. A level anticrossing is observed between resonances (6) and (5') in the simulations, which also occurs outside the experimental measurement window. Resonance (5') (highlighted with a dashed line) is somewhat faint in Fig. 9.2(c), but more prominent in Fig. 9.2(b). Several other features can be observed in the lower-right corner of Fig. 9.2(b), which are very faint, and can also be classified according to the resonance scheme discussed above.

9.S2. DRESSED STATES

Previous approaches to strong driving have assumed that the driving amplitude ϵ_1 and the driving frequency $\hbar\omega$ are both much larger than the minimum energy gap Δ (Oliver *et al.*, 2005). However, the simulation results shown in Fig. 9.2, which provide a good description of the experiments in Fig. 9.1, suggest that our system falls into an intermediate regime, where the dimensionless parameters all have similar magnitudes, $\Delta, \epsilon_0, \hbar\omega \sim 1$, and $\epsilon_1 \sim 0.1$. Below, we develop a new dressed state formalism that is appropriate for such an intermediate parameter regime, while treating ϵ_1 as weakly perturbative. This formalism successfully describes all the resonance features observed in Fig. 9.2. In keeping with our emphasis on orbital physics, we will first consider only the charge and photon sectors, and introduce the spin afterwards.

9.S2.1. ORBITAL-PHOTON SYSTEM

The time-dependent Hamiltonian given by Eqs. (9.S1) and (9.S4) is semiclassical (i.e., the electric field is treated classically). The same Hamiltonian was investigated in (Oliver *et al.*, 2005), in the context of strong driving. A fully quantum version of the same problem was considered in (Nakamura, Pashkin, and Tsai, 2001) and (Wilson *et al.*, 2007), also in the context of strong driving. The solutions to the semiclassical and quantum Hamiltonians are identical, suggesting that the two approaches are interchangeable. The quantum version is more elegant however, and it is more directly compatible with the dressed state formalism. We therefore adopt the quantum Hamiltonian as our starting point, rather than Eq. (9.S1). The full quantum Hamiltonian is given by

$$H = \frac{1}{2}(\epsilon_0\sigma_z + \Delta\sigma_x) + \hbar\omega a^\dagger a + g\sigma_z(a + a^\dagger). \quad (9.S8)$$

Here, a^\dagger and a are the creation and annihilation operators for microwave photons of frequency ω , and g is the electron-photon coupling constant (we ignore the vacuum fluctuations of the electric field). The semiclassical and quantum Hamiltonians are related through the correspondence (Nakamura, Pashkin, and Tsai, 2001)

$$g = \epsilon_1/4\sqrt{\langle N \rangle}, \quad (9.S9)$$

where $N = a^\dagger a$ is the photon number operator. We expect that $\langle N \rangle \gg 1$ for gate-driven microwave fields. The ac detuning amplitude can be related to the ac voltage applied

to a top gate, V_{ac} , through the relation $\epsilon_1 = eV_{\text{ac}}(C_g/C_\Sigma)$, where C_g is the capacitance between the dot and the top gate and C_Σ is the total capacitance of the dot.

It is important to note the form of the coupling term in Eq. (9.S8), which arises because the ac signal is applied to the detuning parameter. The resulting Hamiltonian cannot be solved exactly, and several approaches have been used to simplify the problem. In the weak driving limit, it is common to combine a unitary transformation with a rotating wave approximation to reduce the coupling in Eq. (9.S8) to a transverse form: $g(\sigma_+ a + \sigma_- a^\dagger)$ (Childress, Sørensen, and Lukin, 2004). The latter has been used to describe the interactions between a dot and a microwave stripline (Frey *et al.*, 2012). Alternatively, in the strong driving limit, it is common to retain the longitudinal coupling form of Eq. (9.S8) while treating Δ as a perturbation. This approach has been used to describe the dynamics of a dot in a gate-driven microwave field (Nakamura, Pashkin, and Tsai, 2001; Wilson *et al.*, 2007). In the intermediate driving regime, which is most relevant for the experiments reported here, neither of these approaches is appropriate.

As discussed in Sec. 9.S1.2, the LZ satellite peaks in Fig. 9.2 are displaced vertically from the conventional spin resonances (the center peaks) by $E_{01}/m\hbar$. For example, the satellite peak labeled (5) in Fig. 9.2(c) is displaced by⁸ $\sqrt{2}$ from the fundamental resonance (1,2), while the satellite labeled (5'') is displaced by $\sqrt{2}/2$ from the conventional first harmonic (3,4). This suggests that we should first diagonalize the uncoupled ($g = 0$) Hamiltonian, giving $\tilde{H}_0 = -\frac{E_{01}}{2}\tilde{\sigma}_z + \hbar\omega a^\dagger a$, where $\tilde{\sigma}_z$ is the Pauli matrix along the orbital quantization axis. The eigenstates of \tilde{H}_0 are labeled $|c\rangle|N\rangle$, where $(\tilde{\sigma}_z/2)|c\rangle = c|c\rangle$ and $c = \pm 1/2$, and the energy eigenvalues are given by $-cE_{01} + N\hbar\omega$. The full Hamiltonian becomes

$$\tilde{H} = -\frac{E_{01}}{2}\tilde{\sigma}_z + \hbar\omega a^\dagger a + g(\cos\theta\tilde{\sigma}_x - \sin\theta\tilde{\sigma}_z)(a + a^\dagger), \quad (9.S10)$$

where we have defined $\tan\theta = \epsilon_0/\Delta$.

To dress the orbital states, we consider the Hamiltonian $\tilde{H}_l = \tilde{H}_0 - g\sin\theta\tilde{\sigma}_z(a + a^\dagger)$, whose coupling is purely longitudinal. This Hamiltonian has exact solutions, given by (Cohen-Tannoudji, Dupont-Roc, and Grynberg, 1998),

$$|c; N\rangle_l = \exp[-2cg\sin\theta(a^\dagger - a)/\hbar\omega]|c\rangle|N\rangle, \quad (9.S11)$$

with the corresponding energies

$$E_N^c = -cE_{01} + N\hbar\omega - \frac{(g\sin\theta)^2}{\hbar\omega}. \quad (9.S12)$$

Here, the subscript l indicates a longitudinal dressed state.

Evaluating the full Hamiltonian \tilde{H} in the dressed state basis, we obtain diagonal terms given by Eq. (9.S12), and off-diagonal terms given by

$${}_l\langle c; N|g\cos\theta\tilde{\sigma}_x(a + a^\dagger)|c; N + m\rangle_l = 0, \quad (9.S13)$$

$${}_l\langle -c; N|g\cos\theta\tilde{\sigma}_x(a + a^\dagger)|c; N\rangle_l = 0, \quad (9.S14)$$

$${}_l\langle -c; N|g\cos\theta\tilde{\sigma}_x(a + a^\dagger)|c; N + m\rangle_l = \hbar v_{N,m}/2 \quad (\text{with } m \geq 1), \quad (9.S15)$$

⁸The simulations are dimensionless and the corresponding energy splitting is given by $E_{01} = \sqrt{\epsilon_0^2 + \Delta^2} = \sqrt{2}$.

where

$$\frac{h\nu_{N,m}}{2} = g \cos\theta e^{-2\alpha^2} \sum_{p=0}^N \left[1 + \frac{4\alpha^2(N-p)}{(m+p)(m+p+1)} \right] \times \frac{(-1)^{m+p-1} (2\alpha)^{m+2p-1} \sqrt{N!(N+m)!}}{p!(m+p-1)!(N-p)!}, \quad (9.S16)$$

and

$$\alpha = -\frac{2cg \sin\theta}{\hbar\omega}. \quad (9.S17)$$

We note that Eq. (9.S13) follows from the facts that (i) the orbital character of $|c; N\rangle_l$ is the same as $|c\rangle|N\rangle$, and (ii) $\langle c|\tilde{\sigma}_x|c\rangle = 0$. Equations (9.S14) and (9.S15) are obtained using standard techniques (Cohen-Tannoudji, Dupont-Roc, and Grynberg, 1998).

We can obtain an approximate form for the Rabi frequency $\nu_{N,m}$ for orbital oscillations. Since our simulations indicate that $\epsilon_1 \ll \hbar\omega$, and we have assumed that $\langle N \rangle \gg 1$, Eqs. (9.S9) and (9.S17) imply that $\alpha \ll 1$. Since the distribution of photon number states comprising $|c; N\rangle_l$ is sharply peaked around $\langle N \rangle$, we can approximate $N \simeq \langle N \rangle$, yielding

$$\frac{h\nu_{N,m}}{2} \simeq g \cos\theta \left[1 + \frac{4\alpha^2 \langle N \rangle}{m(m+1)} \right] \frac{(-2\alpha)^{m-1}}{(m-1)!} \langle N \rangle^{m/2}. \quad (9.S18)$$

Finally, in the limit $\alpha\sqrt{\langle N \rangle} \ll 1$, we find

$$\nu_{N,m} \simeq \frac{\omega/2\pi}{(m-1)! \tan\theta} \left(\frac{\epsilon_1 \sin\theta}{2\hbar\omega} \right)^m. \quad (9.S19)$$

Thus, ignoring geometrical factors, we obtain the general scaling relation $\nu_{N,m} \simeq \epsilon_1^m / (\hbar\omega)^{m-1}$.

The dressed state formalism is convenient for identifying and analyzing resonant phenomena. For example, the resonance condition for an m -photon orbital excitation is simply given by $E_{N+m}^{+1/2} \simeq E_N^{-1/2}$, or $m\hbar\omega \simeq E_{01}$. When this condition is satisfied, the full Hamiltonian approximately decouples into a set of 2D manifolds given by

$$H_{2D} = \begin{pmatrix} E_{01} & \frac{h\nu_{N,m}}{2} \\ \frac{h\nu_{N,m}}{2} & m\hbar\omega \end{pmatrix}, \quad (9.S20)$$

where we have subtracted a constant diagonal term. For a system initially in the orbital state $c = 1/2$, Eq. (9.S20) describes oscillations between $c = 1/2$ and $-1/2$, with the Rabi frequency $\nu_{N,m}$. These resonances are referred to as photon assisted tunneling (PAT), and are well known in quantum dots (Kouwenhoven *et al.*, 1994a). In the present context, "tunneling" refers to the generalized tunneling parameter Δ in Eq. (9.S1), which represents the coupling between the different orbital states.

9.S2.2. SPIN-ORBITAL-PHOTON SYSTEM

Following Rashba, we have argued that the experimental EDSR spectrum can be explained entirely within the orbital sector. The argument is summarized as follows: (1) the orbital (two-level) system is driven at a frequency ω ; (2) nonlinearities in the orbital system generate responses at multiples of ω , corresponding to multiphoton processes; (3) strong driving modifies the response by generating additional satellite peaks at frequencies $\pm E_{01}/\hbar$; (4) the response frequencies in the orbital sector are transferred directly to the spin sector, where they become the driving frequencies for spin rotations

via the EDSR mechanism. By associating the response frequency Ω in the orbital system with the characteristic frequency $g\mu_B B/\hbar$ in the spin system, we were able to obtain excellent agreement with the experiments, without invoking any other assumptions about the spin physics. In an alternative explanation of the spin harmonics, we could consider unrelated nonlinearities in the spin sector, independent of the orbital sector. Two arguments against such an approach are as follows. First, since nonlinearities occur in the orbital system anyway, Occam's razor suggests using the simplest, weak-driving model for the spin dynamics. Second, while the spin Rabi frequencies obtained in our previous EDSR experiments are < 10 MHz (Ch. 7,8), the Rabi frequencies for orbital oscillations are > 100 MHz (see Sec. 9.S2.3); it is therefore very reasonable to consider strong, photon-mediated driving for the orbital system, but weak driving for the spin system, mediated by the orbital dynamics.

We can formalize such a "simple-spin" model by adopting a standard spin Hamiltonian,

$$H_{\text{spin}} = -\frac{1}{2} g_B \mu_B \hat{\mathbf{B}}(\hat{\mathbf{r}}[\sigma_z]) \cdot \boldsymbol{\tau}. \quad (9.S21)$$

Here, $\hat{\mathbf{B}}$ is a superoperator representing the inhomogeneous magnetic field, $\hat{\mathbf{r}}$ is the electron position operator, which is related linearly to the dipole moment operator in Eq. (9.S5), and $\boldsymbol{\tau}$ is the Pauli operator for a (spin-1/2) electron. The explicit dependence of $\hat{\mathbf{r}}$ on σ_z indicates that $\hat{\mathbf{r}}$ acts only on the orbital variables. We emphasize that there is no direct coupling between spins and photons in this model.

The quantization axis for the spins is defined as the average of the magnetic field operator:

$$\mathbf{B}_{\text{avg}} = \langle \hat{\mathbf{B}}(\hat{\mathbf{r}}) \rangle, \quad (9.S22)$$

with the corresponding Zeeman energy, $E_Z = g\mu_B B_{\text{avg}}$. The deviation of $\hat{\mathbf{B}}(\hat{\mathbf{r}})$ from its average value (e.g., due to driving) is given by

$$\delta \hat{\mathbf{B}}(\hat{\mathbf{r}}) = \hat{\mathbf{B}}(\hat{\mathbf{r}}) - \mathbf{B}_{\text{avg}}. \quad (9.S23)$$

Clearly, $\delta \hat{\mathbf{B}}(\hat{\mathbf{r}})$ contains information about the magnetic field gradient, which is the source of spin-orbit coupling in EDSR. Transforming $\boldsymbol{\tau}$ to the quantization frame yields $\tilde{\tau}_z = \boldsymbol{\tau} \cdot \mathbf{B}_{\text{avg}}/B_{\text{avg}}$, where $(\tilde{\tau}_z/2)|s\rangle = s|s\rangle$ and $s = \pm 1/2$. Note that we have identified $s = +1/2$ as the low-energy spin state, in analogy with the orbital system.

In the simple-spin model, the photons dress the orbital state but not the spin state. We may therefore simply extend the longitudinal dressed states to include the bare spin: $|c; s; N\rangle_l \equiv |c; N\rangle_l |s\rangle$. In this basis, the diagonal elements of the full Hamiltonian are given by

$$E_N^{c,s} = N\hbar\omega - cE_{01} - sE_Z. \quad (9.S24)$$

Note that we have dropped the constant energy shift $g^2/\hbar\omega$ from Eq. (9.S12) since it is present for all the basis states and plays no role in a following analysis. In general, $\delta \hat{\mathbf{B}}$ is neither parallel nor perpendicular to \mathbf{B}_{avg} . Hence, our spin-orbit coupling terms are of the form $\{\tilde{\sigma}_x, \tilde{\sigma}_z\} \otimes \{\tilde{\tau}_x, \tilde{\tau}_z\}$. The off-diagonal perturbation in the fully quantum Hamiltonian is now given by

$$V = g \cos \theta \tilde{\sigma}_x (a + a^\dagger) + \sum_{j,k}^{x,z} f_{j,k} \tilde{\sigma}_j \tilde{\tau}_k, \quad (9.S25)$$

where the first term describes the orbital-photon coupling, and the second term describes the spin-orbit coupling. The spin-orbit coupling constants $f_{j,k}$ depend, in part, on geometrical factors such as the relative alignment of the magnetic field gradient with respect to the dipole moment of the orbital states. The term $f_{x,x} \tilde{\sigma}_x \tilde{\tau}_x$ is the conventional EDSR matrix element (Tokura *et al.*, 2006), describing the flip-flop transition between the orbital and spin states. The constant $f_{z,x}$ is of particular interest for the resonance (5). It describes a hybridization of spin states ($\tilde{\tau}_x$), which depends on the orbital occupation, but does not hybridize the orbital states ($\tilde{\sigma}_z$). These coupling constants arise through the valley-orbit coupling mechanism, which depends on the local disorder realization at the quantum well interface. Since we do not know the disorder potential for our device, we do not attempt to calculate $f_{j,k}$ here. However, we provide estimates for several of these parameters below, based on our experimental measurements. The other contributions to the spin-orbit matrix elements can be evaluated using Eqs. (9.S13)-(9.S15), and the additional results

$${}_l \langle c; N | \tilde{\sigma}_x | c; N + m \rangle_l = {}_l \langle -c; N | \tilde{\sigma}_z | c; N + m \rangle_l = 0, \quad (9.S26)$$

$${}_l \langle c; N | \tilde{\sigma}_z | c; N + m \rangle_l = 2c \delta_{m,0}, \quad (9.S27)$$

$${}_l \langle -c; N | \tilde{\sigma}_x | c; N + m \rangle_l \simeq \left(2\alpha \sqrt{\langle N \rangle} \right)^{2m} J_m \left(-4\alpha \sqrt{\langle N \rangle} \right), \quad (9.S28)$$

which are also obtained using standard techniques (Cohen-Tannoudji, Dupont-Roc, and Grynberg, 1998). Here, $J_m(x)$ is an integer Bessel function.

In the simple-spin model, no photons are absorbed via spin-orbit coupling, so only the $m = 0$ terms will be considered in Eqs. (9.S26)-(9.S28). There are therefore three types of direct (i.e, first-order) transitions allowed by Eq. (9.S25): (i) PAT transitions, with no spin flip, like those described in Eq. (9.S15), (ii) spontaneous flip-flops between the spin and orbital states ($f_{x,x}$ processes), or (iii) phase exchange ($f_{z,z}$) processes, without photon absorption or emission. Note that direct transitions of the $f_{x,z}$ or $f_{z,x}$ type are also allowed; however, they do not conserve energy, and are therefore highly suppressed in resonant transitions. The only relevant first-order matrix elements are therefore

$${}_l \langle -c; s; N | V | c; s; N + m \rangle_l = h\nu_{N,m}/2 \quad (m \geq 1), \quad (9.S29)$$

$${}_l \langle c; s; N | V | c; s; N \rangle_l = 2c f_{z,z}, \quad (9.S30)$$

$${}_l \langle -c; -s; N | V | c; s; N \rangle_l \simeq f_{x,x} J_0 \left(4\alpha \sqrt{\langle N \rangle} \right). \quad (9.S31)$$

Note that Eq. (9.S29) corresponds to PAT, while Eqs. (9.S30) and (9.S31) describe pure spin-orbit coupling, which hybridizes the spin and orbital states, even in the absence of a driving term.

We now consider second-order processes in the perturbation, V . All photon-driven processes with spin flips must be second-order, involving two distinct steps. In the first, an orbital state is excited (deexcited) while absorbing (emitting) one or more photons; this is a nonresonant LZ process. In the second, a spin flip occurs, accompanied by a second orbital flip (an $f_{x,x}$ process), or a phase change of the orbital state (an $f_{z,x}$ process). Processes of the $f_{x,z}$ and $f_{z,z}$ type are also allowed; however they do not cause spin flips, and will not be considered in our EDSR analysis. We first consider a pure-spin resonance

generated by the sequence $|c; s; N + m\rangle \rightarrow |-c; s; N\rangle \rightarrow |c; -s; N\rangle$. Here, the difference between the initial and final states involves a spin excitation and m absorbed photons. The intermediate state $|-c; s; N\rangle$ is off-resonant, and may be eliminated to obtain an effective, second-order matrix element, given by

$${}_I \langle c; -s; N | V | c; s; N + m \rangle_I \simeq \frac{h\nu_{N,m} f_{x,x}}{4(sE_Z - cE_{01})} J_0(4\alpha\sqrt{\langle N \rangle}). \quad (9.S32)$$

Here, we have evaluated the energy denominator at the resonant condition $m\hbar\omega = 2sE_Z$. Similarly, we can consider a ‘‘resonance (5)’’ type process generated by the sequence $|c; s; N + m\rangle \rightarrow |-c; s; N\rangle \rightarrow |-c; -s; N\rangle$. In this case, the difference between the initial and final states involves a spin excitation, a charge excitation, and m absorbed photons. The effective, second-order matrix element for this process is given by

$${}_I \langle -c; -s; N | V | c; s; N + m \rangle_I \simeq -\frac{h\nu_{N,m} f_{z,x} c}{2sE_Z}, \quad (9.S33)$$

corresponding to the resonance condition $m\hbar\omega = 2(sE_Z + cE_{01})$. In the limit $\alpha\sqrt{\langle N \rangle} \lesssim 1$, which seems appropriate for our experiments (see below), we therefore obtain

$${}_I \langle c; -s; N | V | c; s; N + m \rangle_I \simeq \frac{h\nu_{N,m} f_{x,x}}{4(sE_Z - cE_{01})} \equiv \frac{hf_m}{2}, \quad (9.S34)$$

$${}_I \langle -c; -s; N | V | c; s; N + m \rangle_I \simeq -\frac{h\nu_{N,m} f_{z,x} c}{2sE_Z} \equiv \frac{hf'_m}{2}. \quad (9.S35)$$

Here, f_m represents the Rabi frequency for a pure-spin resonance, and f'_m represents the Rabi frequency for a combined spin-orbit resonance (like the resonance (5)).

Keeping all other parameters fixed, we can estimate the power scaling of the Rabi frequencies (9.S34) and (9.S35) by using Eqs. (9.S9), (9.S17), and (9.S18). Assuming the limit $\alpha\sqrt{\langle N \rangle} \rightarrow 0$, we find that $f_1, f'_1 \propto \epsilon_1$, $f_2, f'_2 \propto \epsilon_1^2$, etc.; these theoretical results are consistent with experimental results reported in Ch. 8. Based on Eq. (9.S34), we also predict a simple form for the ratio

$$\frac{f_2}{f_1} \simeq \frac{\nu_{N,2}}{\nu_{N,1}} \simeq -2\alpha\sqrt{\langle N \rangle}. \quad (9.S36)$$

Using the results for f_1 and f_2 in Ch. 8, we estimate this ratio to be in the range $2\alpha\sqrt{\langle N \rangle} \simeq 1/3$ - $1/2$ for typical experiments, which confirms our previous assumptions.

We can estimate the ratio of the Rabi frequencies between different orbital states (i.e., different values of c), but the same EDSR mode (the same value of m). Taking $c = \pm 1/2$ in Eq. (9.S34), we obtain the ratio

$$\frac{f_m^{(1)}}{f_m^{(2)}} \simeq \frac{E_Z + E_{01}}{E_Z - E_{01}}. \quad (9.S37)$$

Here, we have adopted the notation of Ch. 8 where $f_1^{(1)}$ ($f_1^{(2)}$) corresponds to $c = 1/2$ ($c = -1/2$) for the case $m = 1$. In Ch. 8, it was found that $f_1^{(1)}/f_1^{(2)} = 1.7$ when $B_{ext} =$

561 mT. Using these values, Eq. (9.S37) predicts that $E_{01} = 17 \mu\text{eV}$ or 4 GHz. We note that, although Ch. 8 used the same device as we do here, the gates were tuned differently, which could potentially yield to different values for the valley splitting. The spectroscopy shown in Fig. 9.1 of the main text gives a more direct estimate of $E_{01} = 7$ GHz. The agreement is reasonable; however, Eq. (9.S37) also predicts that $f_m^{(1)}/f_m^{(2)}$ should not depend on m , while Ch. 8 estimates a ratio of $f_2^{(1)}/f_2^{(2)} = 0.9$ for the first subharmonic resonance ($f_1^{(3)}/f_1^{(4)}$ in their notation). This experimental result is clearly inconsistent with Eq. (9.S37), which should be greater than 1. We point out, however, that the error bars reported in Ch. 8 were large enough to permit $f_2^{(1)}/f_2^{(2)} > 1$. Moreover, we note again that strong driving was employed in Ch. 8, so that the arguments leading to Eq. (S37) could begin to break down.

The scaling behavior $f_1 \sim f_{x,x}\epsilon_1/(E_Z - E_{01})$ suggested by Eq. (9.S34) is consistent with (Tokura *et al.*, 2006). We can now obtain a rough estimate for the EDSR coupling constant $f_{x,x}$ by combining the current experimental results with those reported in Ch. 8. In Ch. 8, a typical value of $f_1^{(1)} = 2.5$ MHz was obtained (note that $f_1^{(1)}$ should be smaller in the current experiment, although we do not know its value). In the current experiments, we find that $E_Z - E_{01} \approx 7$ GHz (see Fig. 9.1), and $\nu_{N,1} \approx 0.2$ GHz (see Sec. 9.S2.3, below). From Eq. (9.S34), we then obtain the estimate $f_{x,x} \approx 90$ MHz. We can also estimate the parameter $f_{z,x}$. As discussed above, this coupling constant describes the orbital (i.e., valley)-induced hybridization of the spin states, and determines the strength of the resonance (5). Specifically, it arises from contributions to the g -factor tensor that are transverse to the applied field, and which differ slightly between the two different valley states. It is not possible to compute these valley-induced perturbations without knowledge of the disorder potential. In general however, the disorder will not be aligned with the magnetic field, so the transverse component of the perturbation in the g -factor tensor should differ from the total perturbation by a simple geometrical factor of order $O[1]$. In Ch. 7, the total difference in the g -factors for the two valley states was found to be $\Delta g/g \approx 0.015\%$. Hence, we can estimate the valley-dependent hybridization of the spin states to be $2f_{z,x} = \Delta g\mu_B B$. At the magnetic field corresponding to the kink in resonance (5) in Fig. 9.1 of the main text, we have $B_{\text{tot}} \approx 480$ mT, yielding $f_{z,x} \approx 1$ MHz, or $f_{z,x}/f_{x,x} \approx 1\%$. Finally, we can estimate a typical Rabi frequency for the resonance (5) from Eq. (9.S35), giving $f_1' \approx 10$ kHz. This explains why it is not possible to observe coherent oscillations of the resonance (5) in our experiments.

To close this section, we discuss the basic features of the simulation results shown in Fig. 9.S1, in terms of the first and second-order matrix elements obtained in Eqs. (9.S29)-(9.S31) and (9.S34)-(9.S35). First, it is helpful to recall how the spin enters this discussion, since the orbital Hamiltonian used in the simulations, Eq. (9.S1), does not explicitly include spin. It is important to note that Fig. 9.S1 does not represent resonant phenomena; it is simply the Fourier transform of the response of the orbital dipole moment to an ac drive. In the simple-spin model, this response is converted into an ac magnetic signal, with a strength determined by the spin-orbit coupling parameters $f_{j,k}$ in Eqs. (9.S30) and (9.S31), yielding an EDSR response in the spin sector. Since there is no spin-orbit coupling in the simulations, we can learn nothing about the spin Rabi frequencies. However, the response spectrum in Fig. 9.S1 should still provide an accurate mapping of the EDSR spectrum.

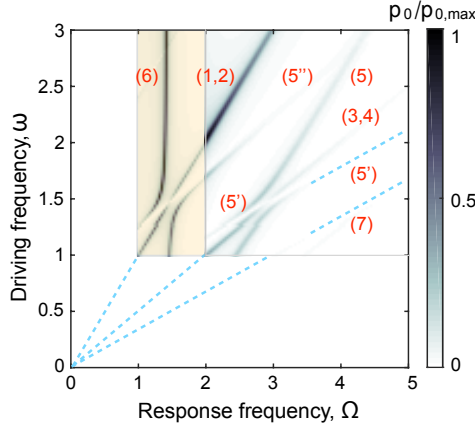


Figure 9.S1: Simulation results, reproduced from Fig. 9.2(c) in the main text. Here, the resonances labeled (1) through (7) are described in Sec. 9.S4.

To take some examples, the features label (1,2) and (3,4) in Fig. 9.S1 correspond to conventional EDSR, with spin excitations occurring at the resonance conditions $E_{N+m}^{c,s} = E_N^{c,-s}$ (or $m\hbar\omega = 2sE_Z$) when $m = 1$ and 2 , respectively. These features correspond to the experimental resonances labeled the same way in Fig. 1(a) of the main text. The corresponding Rabi frequencies are given by f_m in Eq. (9.S34), and were measured to be in the range of a few MHz in Ch. 8. The feature labeled (7) in Fig. 9.S1 corresponds to a 3-photon spin resonance, with $m = 3$; this feature is not observed in the experiments. The features labeled (5), (5'), and (5'') occur at the resonance conditions $E_{N+m}^{c,s} = E_N^{-c,-s}$ [or $m\hbar\omega = 2(sE_Z + cE_{01})$], and involve simultaneous spin and orbital excitations. In previous work, such processes were referred to as “spin-flip PAT” (Braakman *et al.*, 2014; Schreiber *et al.*, 2011). In the current experiment, they are responsible for resonances (5) and (5'). The corresponding Rabi frequencies are given by f'_m in Eq. (9.S35), and have not been measured yet experimentally. In principle, the PAT transitions, which occur at the resonance condition $E_{N+m}^{c,s} = E_N^{-c,s}$ (or $m\hbar\omega = 2cE_{01}$) in Eq. (9.S29), could also be observed in the simulations. However, these transitions correspond to discrete points along the line labeled (6) in Fig. 9.S1, which makes them difficult to detect. Moreover, the response frequency for PAT (E_{01}/h) is smaller than Fermi level broadening, so it cannot be detected in our read-out scheme. It is therefore interesting that PAT plays a key role in our understanding of the hybridization between dressed states, as discussed in Sec. 9.S2.3, and that the repulsion between the dynamical modes allows us to estimate the magnitude of the PAT Rabi frequency, $v_{N,m}$.

One of the most interesting features in Fig. 9.S1 is labeled (6), and corresponds to a pure-LZ transition, with an orbital state excitation but no photon absorption. Since $m = 0$, according to Eq. (9.S15), this cannot be described by a direct, first-order process. Instead, it involves a combination of photon-mediated processes, with a *net* photon absorption of $m = 0$. A minimal process of this type must be third-order, since second-order processes would involve an orbital excitation, followed by a deexcitation, leaving the orbital in its initial state. Since the electrons in experiments have spins (in contrast

with our simulations), there is also another mechanism that can cause feature (6): a spin-orbit flip-flop occurring at the resonance condition $E_N^{c,s} = E_N^{-c,-s}$ (or $sE_Z = -cE_{01}$). This is the direct, first-order process, described by Eq. (9.S31), in which the orbital state spontaneously deexcites while causing a spin excitation. Feature (6) should therefore appear in both the simulations and the experiments, but with different physical origins and different Rabi frequencies. This is a moot point for experiments however, since low-energy processes cannot be resolved by our measurement scheme.

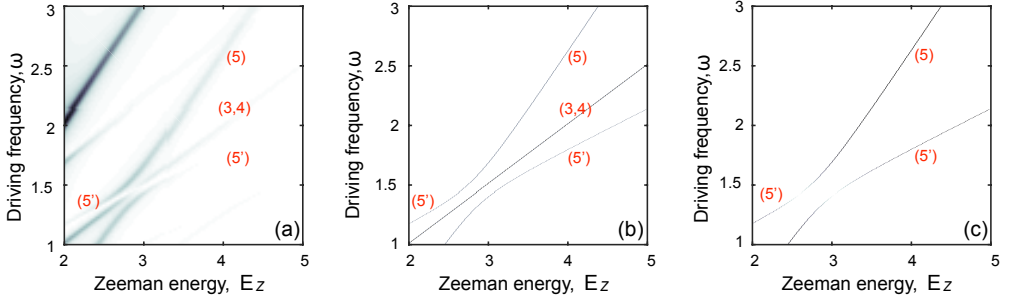


Figure 9.S2: Two types of theory estimates for the EDSR resonance spectra. (a) Simulation results, reproduced from Fig. 9.S1, with the resonances of interest labeled. To make contact with the dressed-state theory, we have equated the response frequency Ω to the Zeeman energy E_Z . (b) Spin-state resonances obtained from the 4D dressed-state Hamiltonian, Eq. (9.S39). Here, we use $E_{01} = \sqrt{2}$ and $h\nu_1 = 0.22$. (c) Orbital-state resonances obtained for the same parameters.

9.S2.3. HYBRIDIZATION OF THE DRESSED STATES

Dressed states allow us to analyze one of the most intriguing features of the data: the kink in the resonance (5), where the resonance line appears to switch between two well-defined slopes, as shown in Fig. 9.1(b) of the main text. The two asymptotic resonance lines correspond to the conditions $E_{N+3}^{+1/2,+1/2} \simeq E_N^{-1/2,-1/2}$ (or $3\hbar\omega \simeq E_Z + E_{01}$) far to the left of the kink, and $E_{N'+1}^{-1/2,+1/2} \simeq E_{N'}^{+1/2,-1/2}$ (or $\hbar\omega \simeq E_Z - E_{01}$) far to the right. The intersection of these two resonance lines occurs when $E_Z = 2\hbar\omega = 2E_{01}$, or $N' = N + 1$, and defines a quadruple resonance. The Hamiltonian for this 4D manifold is given by

$$H_{4D} = \begin{pmatrix} E_N^{-1/2,-1/2} & \frac{h\nu_{N,1}}{2} & \frac{hf_2}{2} & \frac{hf'_3}{2} \\ \frac{h\nu_{N,1}}{2} & E_{N+1}^{+1/2,-1/2} & \frac{hf'_1}{2} & \frac{hf_2}{2} \\ \frac{hf_2}{2} & \frac{hf'_1}{2} & E_{N+2}^{-1/2,+1/2} & \frac{h\nu_{N+2,1}}{2} \\ \frac{hf'_3}{2} & \frac{hf_2}{2} & \frac{h\nu_{N+2,1}}{2} & E_{N+3}^{+1/2,+1/2} \end{pmatrix}. \quad (9.S38)$$

We can gain intuition about the experiments and simulations by considering a simplified version of H_{4D} . First, we note that $\nu_{N,1} \simeq \nu_{N+2,1} \equiv \nu_1$ when $\langle N \rangle \gg 1$. To investigate the dominant behavior, since $\nu_1 \gg f_m, f'_m$, we consider the limit $f_m, f'_m = 0$. The

resulting Hamiltonian

$$H_{4D} \simeq \begin{pmatrix} E_{01} + E_Z & \frac{\hbar\nu_1}{2} & 0 & 0 \\ \frac{\hbar\nu_1}{2} & \hbar\omega + E_Z & 0 & 0 \\ 0 & 0 & 2\hbar\omega + E_{01} & \frac{\hbar\nu_1}{2} \\ 0 & 0 & \frac{\hbar\nu_1}{2} & 3\hbar\omega \end{pmatrix} - \frac{E_{01} + E_Z}{2} \quad (9.S39)$$

does not permit any dynamical hybridization of spin states, and can therefore be used to directly identify the spin resonance conditions.

We find that Eq. (9.S39) reproduces all the main features of the experimental and simulation results near the kink in the resonance (5), as indicated in Fig. 9.S2. The features observed in Figs. 9.S2(b) and (c) reflect sudden changes in the compositions of the eigenstates. To obtain these plots, we first diagonalize H_{4D} to obtain its four eigenstates as a function of E_Z . We then compute probability $P^{(j)}(s)$ for the j th state to have spin s . Here, the states are labeled according to their energy ordering, as they would be for eigenstates of the full 4D Hamiltonian in Eq. (9.S38). Near a spin resonance, the spin-up or spin-down character of the ordered eigenstates changes abruptly. To see these sudden changes in the simulations, we sum the numerical derivatives, $\sum_j |\partial P^{(j)}(s)/\partial E_Z|$. The resulting spectrum displays sharp peaks at the resonance locations, as illustrated in Fig. 9.S2(b). Comparison with the simulation results, reproduced in Fig. 9.S2(a), shows that only one parameter ($\hbar\nu_1/E_{01} \simeq 0.16$) is needed to capture the main features of the resonance (5). Including the other off-diagonal terms in Eq. (9.S38) leads to small feature changes, such as broadening of the resonance peaks, but does not change the underlying spectrum.

The dynamically induced shifts of the dressed state energies (i.e., ac Stark shifts) are dominated by the orbital coupling terms $\nu_{N,m}$, because $\nu_{N,m} \gg f_m$. Hence, they are easily computed from Eq. (9.S39) by diagonalizing the two 2D subsystems. Diagonalizing the Hamiltonian in this way yields the four energies

$$\frac{E_Z + \hbar\omega}{2} \pm \sqrt{\left(\frac{E_{01} - \hbar\omega}{2}\right)^2 + \left(\frac{\hbar\nu_1}{2}\right)^2}, \quad (9.S40)$$

$$\frac{5\hbar\omega - E_Z}{2} \pm \sqrt{\left(\frac{E_{01} - \hbar\omega}{2}\right)^2 + \left(\frac{\hbar\nu_1}{2}\right)^2}. \quad (9.S41)$$

In particular, the energy splitting between the resonance (5) (i.e., the upper feature, including the kink) and its asymptote, $\hbar\omega = E_Z - E_{01}$, is given by

$$\Delta E_{\text{asympt}} \simeq \frac{(\hbar\nu_1)^2}{2(E_Z - 2E_{01})}, \quad (9.S42)$$

and the energy splitting at the anticrossing between resonances (3,4) and (5) is given by $\Delta E_X = \hbar\nu_1/\sqrt{3}$. Using the asymptotic formula for the Rabi frequencies, Eq. (9.S19), and in particular, $\nu_1 \simeq \epsilon_1 \cos\theta/2\hbar$, we find that $\Delta E_X \simeq \epsilon_1 \cos\theta/2\sqrt{3}$ in the regime of experimental interest. We can also obtain analytical expressions for the resonance conditions by equating the energy expressions in Eqs. (9.S40) and (9.S41). For the resonant feature

labeled (3,4) in Fig. 9.S2, we obtain the condition $\hbar\omega = E_Z/2$. For the resonance features labeled (5) and (5'), we obtain the conditions

$$\hbar\omega = \frac{1}{3}(2E_Z - E_{01}) \pm \frac{1}{3}\sqrt{(E_Z - 2E_{01})^2 + 3(\hbar v_1)^2}. \quad (9.S43)$$

It is interesting to note that, while the parameters f_m control the spin dynamics and the EDSR Rabi frequencies, the dressed state energies $E_N^{c,s}$ determine the gross features of the resonance spectrum, and the PAT Rabi frequency v_1 determines the fine features of the resonance (5). From Eqs. (9.S38) and (9.S39), we see that the dynamical level repulsion in the resonance (5) (i.e., the kink) occurs between dressed states with the same spin but different orbital states. The kink is therefore caused by orbital physics. The correspondence between Figs. 9.S2(a) and 9.S2(b) indicates that all of the resonances in this manifold involve a spin flip. We have also computed the analogous orbital resonances for the same 4D manifold, corresponding to sudden changes in the charge state, as obtained from the expression $\sum_j |\partial P^{(j)}(c)/\partial E_Z|$. The results are shown in Fig. 9.S2(c). In this case, the central resonance (3,4) disappears, indicating that it is a pure-spin resonance.

Although coherent EDSR oscillations were observed in Ch. 8, with Rabi frequencies in the range $f_1, f_2 \simeq 0.6\text{-}4$ MHz, it was not possible to observe coherent PAT oscillations because of their relatively low energy scale. However, we can now estimate the PAT Rabi frequency by fitting the analytical theory of Eq. (9.S39) to the experimental resonance spectrum in Fig. 9.1(b) of the main text, obtaining the result $v_1 \simeq 0.2$ GHz. This confirms our previous assumption that $f_1 \ll v_1$. We can also estimate the remaining parameters in the theoretical model of Eqs. (9.S1) and (9.S4). From Eqs. (9.S9) and (9.S18), we obtain $\epsilon_1 \simeq 0.5$ GHz $\simeq 2$ μ eV. Using the experimental result $E_{01} \simeq 7$ GHz $\simeq 29$ μ eV and the rough estimate $\epsilon_0 \simeq \Delta$ (deduced from our simulations), we also obtain $\epsilon_0 \simeq \Delta \simeq E_{01}/\sqrt{2} \simeq 5$ GHz $\simeq 20$ μ eV. The parameters ϵ_0 and ϵ_1 that describe the detuning of the orbital basis states due to the driving field are difficult to determine from first principles in silicon devices because they are determined by the degree of valley-orbit mixing, which depends sensitively on the details of the interfacial disorder (Gamble *et al.*, 2013; Kharche *et al.*, 2007). In contrast, the energy splitting between the orbital states E_{01} and the PAT frequency v_1 can be extracted directly from the experiments.

9.S3. ADDITIONAL MEASUREMENTS AND ANALYSIS

9.S3.1. VARIATIONS IN TIME OF THE SPIN-VALLEY TRANSITION FREQUENCY

In Fig. 9.S3 we report repeated measurements of resonance (5) recorded over time, in order to investigate the low frequency noise fluctuations. In the main central panel we report, in blue, the spin resonance peak obtained by averaging directly, over time, the data of panel (a), inside the blue square frame. From its full width at half maximum (FWHM) we can get a lower bound for T_2^* , in this case of 100 ns. Alternatively we can also perform a Gaussian fit for each of the time traces in panel (a) and then shift the center of each dataset in order to align the centers of each resonance peak on top of each other, as reported in panel (b). If we now perform the averaging we get the red Gaussian, reported in the main central panel(a), from which we can extract a T_2^* of 150 ns. This last averaging strategy is equivalent to filtering out the very low frequency component of the

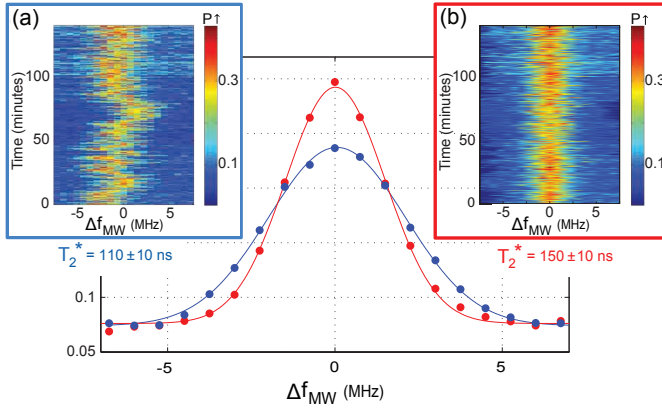


Figure 9.S3: The main panel represents a CW (low MW power) measurement of the inter-valley spin resonance, done for $B_{ext}^y = 860$ mT. The blue and red traces are obtained averaging over time the data reported respectively in panels (a) and (b). Both panels report the CW resonance, away from 18.223 GHz, recorded over time (y-axis). Each point is averaged over 10 ms and there are 150 points per trace. We observe that over time the resonance shifts in frequency. Averaging the bare data in panel (a) we get the blue trace. Fitting with a Gaussian we can get a lower bound for the T_2^* of ~ 110 ns. Furthermore, we can operate a different kind of averaging procedure: we can fit each trace with a Gaussian, get the center of each fit, shift each set of data to center all of the resonance traces (see panel (b)) and average all of them. In this way we get the red trace in the main panel, that gives us a T_2^* of ~ 150 ns. In the first method, we average on a timescale of a few hours, in the second on a timescale of tens of seconds only. The difference between the two average procedures points at the importance of very-low-frequency noise.

noise (\sim mHz), clearly visible in panel (a).

In what follows we report 3 different measurements realized in order to investigate the sensitivity of resonance (5) to the electrostatic environment and to electrical noise.

9.S3.2. INFLUENCE OF THE STATIC AND PULSED GATE VOLTAGES

Controlling the electrostatic potential by the voltage applied to the gates defining the QD confinement potential, we can systematically shift in frequency resonance (5) (see Fig. 9.3). The inset of Fig. 9.S4(a) shows the peak of resonance (5) for five different voltage configurations of the gate 3 (V_3 , represented by different colors). The main panel reports a measurement of the g-factor in each of the gate voltage configurations reported in the lower inset of Fig. 9.S4(a). The extracted g-factors are compatible with each other, considering their associated errors, as reported in Fig. 9.S4(b). This implies that, by changing the gate voltage we can modify the Larmor frequency of the 2-level system involved in the resonance process, without appreciably modifying the Zeeman energy⁹. This suggests that, in this case, we are directly modifying the valley splitting (modelled by moving the QD towards a step defect in the QW, as schematically represented in Fig. 9.3(b)).

We can estimate the effective wave function displacement in space (mainly in the

⁹ Changing the gate voltage also will result in a changing of QD position in the micromagnet magnetic field gradient but the derivative of the gradient with respect to the position is quite small as we can estimate from simulation and measure from the blue data in Fig. 9.S4.

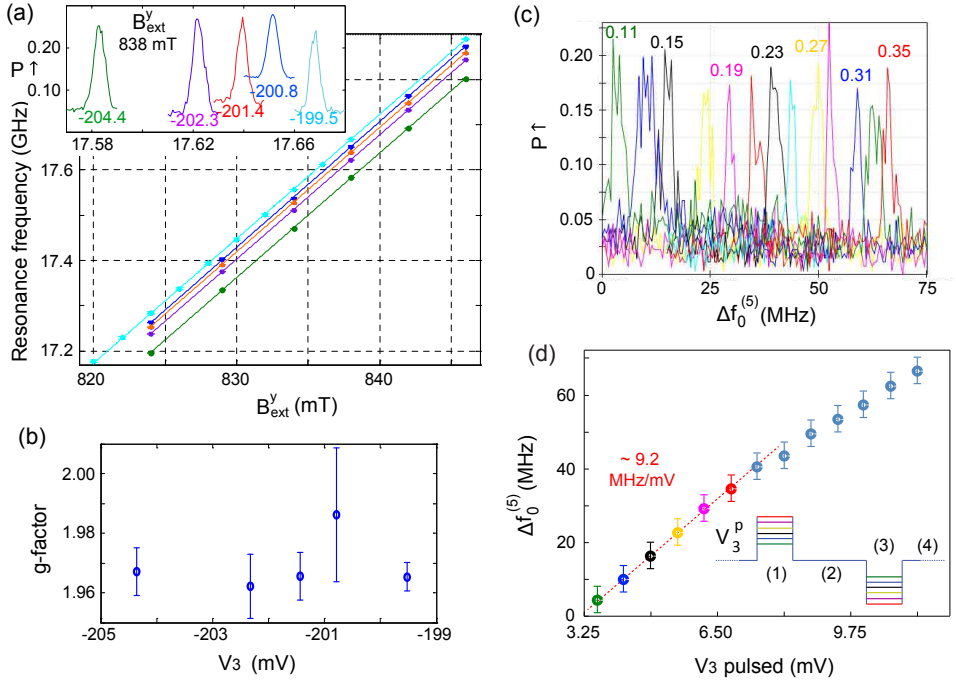


Figure 9.S4: (a) g-factor measurements for different voltage applied to gate 3 (V_3), reported in mV with different colors in the inset; the extracted g-factors for each value of V_3 are reported in panel (b). The fact that the g-factor stays constant suggests that the mechanism responsible for the gate dependence of the Larmor frequency $f_0^{(5)}$ is not related to the shift of the electron wave function in the micromagnet stray field (see main text). In panel (c) we show that it is possible to shift the resonance frequency also by changing the voltage amplitude during the manipulation stage. We keep the pulse shape symmetric, compensating by using the same voltage pulse amplitude, but with opposite sign, during the initialization stage [see inset of panel (d)]. The number reported on each resonance represents the voltage pulse amplitude (in V) at the output of the AWG. (d) Shift in the resonance frequency $f_0^{(5)}$ as a function of a gate voltage pulse applied to gate V2 (the color code of the 6 voltage pulse levels corresponds to the first 6 resonances reported in panel (c)). Here, $\Delta f_0^{(5)} = f_0^{(5)} - 21$ GHz and for the x-axis we used the conversion factor 32.5 mV/V extracted from calibration measurements.

QW plane) generated by modifying the voltage applied to the gate 3 by 1 mV, by using the shift of the Larmor frequency of the intra-valley spin resonance (red trace in Fig. 9.3(a)) due to the magnetic field gradient. From the simulation of the magnetic field gradient we can estimate an upper bound for the magnetic field gradient of ~ 0.2 mT/nm (in the y-direction \sim gate 3), equivalent to ~ 56 MHz/nm in silicon. This energy gradient gives a position lever-arm of ~ 0.01 nm/mV, considering the slope of ~ 0.55 MHz/mV of the red curve in Fig. 9.3(a). Furthermore, by making use of the measured value 18.5 MHz/mV for $f_0^{(5)}$ (see blue trace in Fig. 9.3(a)) and of the estimation above ~ 0.01 nm/mV, we can conclude that $\Delta E_{01}/\Delta|\mathbf{r}| \sim 1.8$ GHz/nm (where \mathbf{r} is the vector representing the motion of the electron generated in the Si QW by the changing of the voltage on gate 3).

An equivalent way to explore this effect is reported in Figures 9.S4(c-d) where keeping a constant static d.c. voltage configuration, we change the amplitude of the voltage

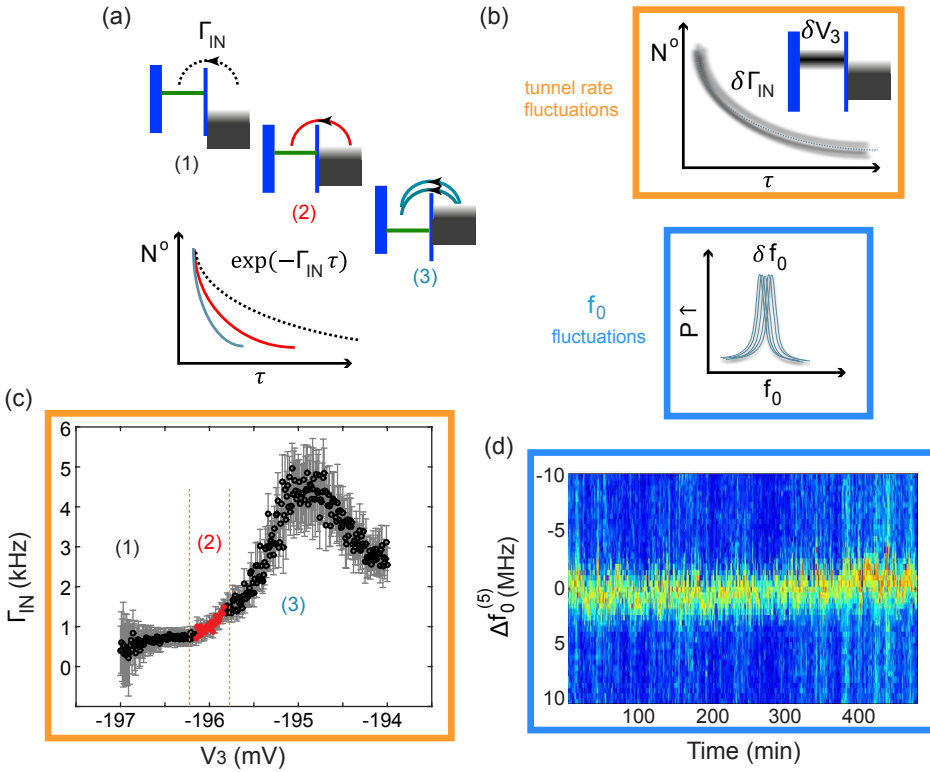


Figure 9.S5: (a) Schematic representing the variation of the tunnel-in rate Γ_{IN} , as a function of the relative detuning between the electrochemical potential in the dot and the Fermi level in the reservoir, controlled by V_3 . (b) Schematic of the effect of the magnetic noise and electrical noise, causing respectively a Larmor frequency fluctuation (lower panel) and tunnel rate fluctuations (upper panel). (c) Tunnel-IN rate, Γ_{IN} , recorded during the initialization stage as a function of V_3 . We are operating around the read-out position indicated by the red points in panel (c) (for which we can estimate a sensitivity of $\frac{d\Gamma_{IN}}{dV_3} \sim 1.7$ kHz/mV) (d) CW measurement of the inter-valley resonance at low MW power (as in Fig 9.S3) over time, in order to study the low frequency (tens of mHz) noise spectrum affecting the inter-valley spin resonance frequency. ($B_{ext}^x = 590$ mT; $B_{ext}^y = 598.2$ mT).

pulse applied on gate 3 to bring the system in Coulomb Blockade during the manipulation stage. As summarized in Fig. 9.S4(d), by increasing the pulse amplitude V_2^p , the resonance peak systematically moves toward lower frequencies. The lever-arm of this process ($\Delta f / \Delta V_2^p$) is around 9 MHz/mV. This measurement demonstrates the dynamic Stark shifting of resonance (5) and creates opportunities for site-selective addressing (voltage pulse induced addressability). The difference in $\Delta f / \Delta V_3$ between the d.c. and pulsed case can be ascribed to the fact that for the measurement reported in Fig. 9.3(a) we have to compensate the change in V_3 by changing the voltage on another gate, in order to keep a good initialization and read-out fidelity. Instead, for the pulsed case we just modify the voltage pulse amplitude on the gate 3 in the manipulation stage (and the empty stage, to keep the symmetry of the pulse), without any further compensation.

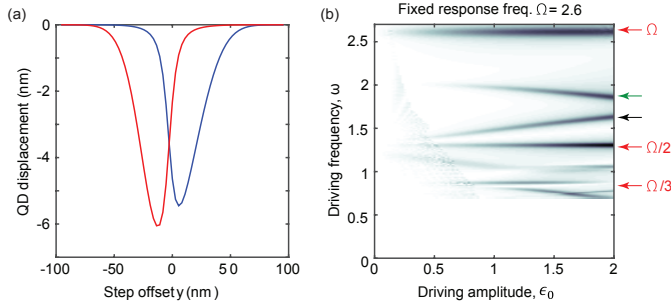


Figure 9.S6: (a) Tight binding simulations of the displacement of the electron center of mass respective to the quantum dot for the ground (blue) and the first excited (red) valley states in the presence of an atomic step, for the parameters discussed in the text. (b) A resonance spectrum for driving frequency vs. microwave amplitude, obtained for a fixed value of the response frequency. The red arrows indicate the fundamental resonance (Ω) and its first two subharmonics ($\Omega/2$ and $\Omega/3$), whose values are largely unaffected by the microwave power. The green and black arrows indicate Landau-Zener-mediated, dynamical processes, which are highly sensitive to the driving strength. The resonance at the green arrow evolves into $\hbar\omega = (E_Z + E_{01})/2$ at larger response frequencies. The resonance at the black arrow corresponds to the inter-valley spin resonance (5) and evolves into $\hbar\omega = (E_Z - E_{01})$.

9.S3.3. INFLUENCE OF ELECTRIC FIELD NOISE

The measurements reported above reveal that the electrostatic configuration considerably affects the inter-valley resonance frequency. Next we consider the effect of the electrical noise on the coherence of the inter-valley spin resonance.

We already have clear evidence of the importance of the electric noise from the upper bound of T_2^* of resonance (5), estimated from the FWHM measurement reported in in Fig. 9.S3, which is 10 times shorter than what it should be if just hyperfine fluctuations dominated (Ch. 7). This results from the higher sensitivity of resonance (5) to the electrical environment, so also to the electrical noise. In the hypothesis that the hyperfine (hf) and the electric noise (el) are independent, we can write the total noise affecting this resonance as $\delta S_{tot} = \sqrt{(\delta S_{hf})^2 + (\delta S_{el})^2}$, from which

$[T_2^*]_{el} \sim 1/\sqrt{([T_2^*]_{tot})^{-2} - ([T_2^*]_{hf})^{-2}} \sim 100$ ns. Therefore, we can deduce that the coherence properties of the inter-valley spin resonance are almost completely dominated by the electric noise (here for $[T_2^*]_{hf}$ we use the value 950 ns extracted for the inter-valley spin resonance in Ch. 7).

Now, we present a measurement realized to study the correlation between the low frequency fluctuations of resonance (5) and low frequency electric noise (low with respect to the electron tunnel rate during the read-out stage). In this respect we made use of the following measurement technique (see Fig. 9.S5):

i) the tunnel rate for an electron jumping inside (or outside) a QD from (into) an electron reservoir is a sensitive function of the relative energy alignment between the Fermi level of the electron reservoir and the electrochemical potential of the single electron inside the QD (Vandersypen *et al.*, 2004). Fig. 9.S5(a) reports a schematic representation of Γ_{IN} (the single electron tunnel rate IN (y-axis)), as a function of the voltage on gate 3 (V_3) that controls the relative alignment of the two levels (measured data represented in

Fig. 9.S5(c)). Making V_3 more positive the tunnel rate will increase, due to the participation of the excited state in the tunneling process. Each tunnel rate is extracted by recording and processing on the fly (using an FPGA) the tunnel events during the initialization stage (~ 5 ms) and fitting an exponential to the histogram of the number of events versus time τ (Fig. 9.S5(a)). Here τ is the time between the start of the initialization stage and the actual tunnel-in event. For the experiment we used V_3 around -196 mV (red points in Fig. 9.S5(c)), which has been optimized for a good read-out and initialization process. As schematically represented inside the orange frame of Fig. 9.S5(b), if we model the electric noise from the environment as a relative fluctuation of V_3 (δV_3), we can write $\delta\Gamma_{IN} \sim \frac{\partial\Gamma_{IN}}{\partial V_3} \delta V_3$. In this way we use $\delta\Gamma_{IN}$, the tunnel rate fluctuations during the initialization stage (of the 4-stages pulse sequence), as a probe of electric noise.

ii) The same 4-stage voltage pulse scheme allows us to perform rotation of the electron spin and to read it out in the last stage. Due to the coupling with the environmental noise, the spin Larmor frequency, $f_0^{(5)}$, fluctuates (see blue frame of Fig. 9.S5(b)) over time, as reported in the CW measurement over time in Fig. 9.S5(d). We fit each resonance trace to a Gaussian in order to extract the center of it (Larmor frequency).

iii) We repeat this measurement over time (each trace takes tens of seconds), in order to get enough statistics, and plot, as reported in Fig. 9.3(d), the extracted Γ_{IN} (x-axis) and Larmor frequency fluctuation Δf_0 (y-axis) traces, for each measurement cycle.

A more rigorous estimate of the correlation in time between $\Gamma_{IN}(t)$ and $\Delta f_0(t)$, evaluated according to the Pearson product-moment correlation coefficient¹⁰ gives a value ~ -0.5 indicating a modest correlation in time.

The sensitivity of this procedure is related to the ability to distinguish small charge fluctuations and it is a function of the static gate voltage configuration (V_3) chosen for the measurement. In fact, from Fig. 9.S5(c) we can clearly notice that we are not working yet in the most sensitive gate voltage configuration (maximal $\partial\Gamma_{IN}/\partial V_3$). Instead, the specific electrostatic configuration has been chosen in order to optimize the spin initialization and read-out.

9.S4. SIMULATION OF VALLEY-ORBIT SPLITTING VERSUS DOT POSITION

The simulation reported in Fig. 9.3(c) of the main text represents the result of a 2D tight binding calculation. The fact that the simulation is 2D rather than 3D affects just the magnitude of E_{01} , but not its qualitative dependence on the step offset. The quantum well barrier has been chosen to be 160 meV, corresponding to 30% Ge. We assumed a parabolic confinement potential for the dot (for simplicity) of size $\sqrt{\langle x^2 \rangle} = 21.1$ nm, corresponding to an orbital energy splitting of $\hbar\omega = 0.45$ meV (Ch. 7). The electric field and the quantum well width have been chosen to be 1.5×10^6 V/m and 13 nm, respectively. The experimental quantum well is nominally 12 nm and the experimental electric field is not well known.

There are 3 competing effects that determine the energy splitting between the two

¹⁰It represents a measure of the linear correlation (dependence) between two variables X and Y, giving a value between +1 and -1 inclusive, where +1 stands for total positive correlation, 0 no correlation, and -1 total negative correlation.

lowest eigenstates, which we usually refer as ‘valley splitting’, for simplicity. (i) The first is the actual valley splitting, which is maximized when the electron sees no step. However, the ground and excited states move to the left or right differently as a function of the step offset. (ii) The second effect is related to the electrostatic energy. When the electron sits to the left of the step, it gains a little energy because the energy is given by eEz , where z is the vertical position. For a single atom step with $E = 1.5 \times 10^6$ V/m, this energy scale is 0.20 meV, so it competes with the valley splitting, whose characteristic value in the plots is about 0.22 meV. This competition is always present, for any value of the electric field, because the electrostatic energy and the valley splitting both have a linear dependence on E . (iii) The third competing effect is the confinement energy of the parabolic dot: when the electron center of mass moves to the left or right, this increases the average energy of the electron in the parabola. For the maximum shift of ~ 20 nm shown in Fig. 9.S6(a), this confinement energy scale is ~ 0.1 meV, so all the energy scales are comparable. The competition between these different effects causes the left-right symmetry of the plots to be broken. The competition also makes it difficult to gain much intuition about the final results. Without the competing effects, we would expect the valley splitting to go to zero as the ground state changes from ‘even’ to ‘odd’ in the valley parameter. But the electron always wants to maximize the energy splitting between the two eigenstates, and the competing effects (in particular, the shifting of the electrons to the left and right) allow it to keep a nonzero energy splitting at all times. It is interesting that this minimum valley splitting (~ 25 μ eV) is very close to the one we observed in our experiments.

From Fig. 9.2(b-c) we notice that the first subharmonic resonance (3,4) seems to fade for high response frequencies. In the simulations reported in Fig. 9.S6(b) we study the visibility of the spin resonances as a function of the driving amplitude (for a fixed value of the response frequency Ω). We notice that the subharmonic resonance (red arrow, $\Omega/2$) seems to fade when it crosses the Landau-Zener resonance (black arrow). This can simply indicate entering the strong driving regime, where the Landau-Zener process (which is a dynamical effect) dominates the regular harmonics (which are simply due to the non-linearities in the Hamiltonian).

10

GATE FIDELITY AND COHERENCE TIME OF AN ELECTRON SPIN IN A SI/SiGe QUANTUM DOT

The gate fidelity and the coherence time of a qubit are important benchmarks for quantum computation. We construct a qubit using a single electron spin in a Si/SiGe quantum dot and control it electrically via an artificial spin-orbit field from a micromagnet. We measure an average single-qubit gate fidelity of $\approx 99\%$ using randomized benchmarking, which is consistent with dephasing from the slowly evolving nuclear spins in the substrate. The coherence time measured using dynamical decoupling extends up to $\approx 400 \mu\text{s}$ for 128 decoupling pulses, with no sign of saturation. We find evidence that the coherence time is limited by noise in the 10 kHz – 1 MHz range, possibly because charge noise affects the spin via the micromagnet gradient. This work shows that an electron spin in a Si/SiGe quantum dot is a good candidate for quantum information processing as well as for a quantum memory, even without isotopic purification.

10.1. INTRODUCTION

The performance of a qubit is characterized by how accurately operations on the qubit are implemented and for how long its state is preserved. For improving qubit performance, it is important to identify the nature of the noise which introduces gate errors and leads to loss of qubit coherence. Ultimately, what counts is to balance the ability to drive fast qubit operations and the need for long coherence times (Fowler *et al.*, 2012).

Electron spins in Si quantum dots are now known to be one of the most promising qubit realizations for their potential to scale up and their long coherence times (Kawakami *et al.*, 2014; Kim *et al.*, 2014; Maune *et al.*, 2012; Morton *et al.*, 2011; Muhonen *et al.*,

The work in this chapter has been published as: E. Kawakami, T. Jullien, P. Scarlino, D. R. Ward, D. E. Savage, M. G. Lagally, V. V. Dobrovitski, Mark Friesen, S. N. Coppersmith, M. A. Eriksson and L. M. K. Vandersypen arXiv:1492.0477.

2014; Tyryshkin *et al.*, 2012; Veldhorst *et al.*, 2014, 2015b; Zwanenburg *et al.*, 2013). Using magnetic resonance on an electron spin bound to a phosphorus impurity in isotopically purified ^{28}Si (Muhonen *et al.*, 2014) or confined in a ^{28}Si MOS quantum dot (Veldhorst *et al.*, 2014) ≈ 0.3 MHz Rabi frequencies, gate fidelities over 99.5%, and spin memory times of tens to hundreds of ms have been achieved. Also electrical control of an electron spin has been demonstrated in a (natural abundance) Si/SiGe quantum dot. This was achieved by applying an AC electric field that oscillates the electron wave function back and forth in the gradient magnetic field of a local micromagnet (Ch. 7). The advantage of electrical control over magnetic control is that electric fields can be generated without the need for microwave cavities or striplines and allows better spatial selectivity, which simplifies individual addressing of qubits. However, the magnetic field gradient also makes the qubit sensitive to electrical noise, so it is important to examine whether the field gradient limits the spin coherence time and the gate fidelity.

In our previous work (Ch. 7), the effect of electrical noise on spin coherence and gate fidelity was overwhelmed by transitions between the lowest two valley-orbit states. Since different valley-orbit states have slightly different Larmor frequencies, such a transition will quickly randomize the phase of the electron spin. If valley-orbit transitions can be (largely) avoided, then the question becomes what limits coherence and fidelities instead.

Here we measure the gate fidelity and spin echo times for an electron spin in a Si/SiGe quantum dot in a regime where the electron stably remains in the lowest valley-orbit state for long times, and where the corresponding resonance condition is well separated from that associated with the other valley-orbit state. In order to learn more about the dominant noise sources in this new regime, we use dynamical decoupling experiments to extract the noise spectrum in the range of 5 kHz - 1 MHz, and we compare this spectrum with spectra derived from numerical simulations for various noise sources. We also study the influence of the various noise sources on the gate fidelity.

10.2. DEVICE AND MEASUREMENT SETUP

The device used in this work is the same as in the previous work (Ch. 7-9) but the applied gate voltages are set differently to obtain a higher valley-orbit splitting. A static external magnetic field of 794.4 mT is applied along the direction as indicated in Fig. 10.1. Spin rotations are achieved by applying microwave excitation to one of the gates, which oscillates the electron wave function back and forth in the magnetic field gradient produced by two cobalt micromagnets fabricated on top of the device. The measurement scheme consists of 4 stages: initialization, manipulation, read-out and emptying, as shown in Fig. 5.5. Differently from the measurements in Ch. 7-9, the 4-stage voltage pulse is applied to gate 8 and the microwave excitation is applied to gate 3 (Fig. 10.1). The initialization and read-out stages take 4-5 ms and the manipulation and emptying stages last 1-1.5 ms.

10.3. HIGH-QUALITY RABI OSCILLATIONS

Rabi oscillations are recorded by varying the burst time and the microwave frequency. With the present gate voltage settings, the spin resonance frequencies corresponding to

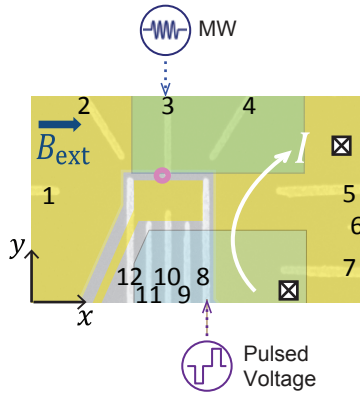


Figure 10.1: False color device image showing a fabricated pattern of split gates, labeled 1-12. The region shown is outlined with dotted lines in Fig. 5.1. For the experiments in this chapter, we used the same sample as in Ch. 7-9 but we create a single quantum dot (QD) and a sensing dot (SD). The current I through the SD is measured as a function of time for a fixed voltage bias of $-600 \mu\text{eV}$. The location of the QD is estimated to be around the pink circle from the measurements of resonant frequencies as a function of the direction of the external magnetic field (not shown in this thesis).

the two lowest valley-orbit states are separated by $\approx 5 \text{ MHz}$ (at $B_{\text{ext}} = 794.4 \text{ mT}$), so that two well separated chevron patterns characteristic for Rabi oscillations are observed [see Fig. 10.2(a)]. This difference of $\approx 5 \text{ MHz}$ results mainly from slightly different electron g -factors between the two valley-orbit states. The population of the valley-orbit ground state is estimated to be $\approx 80\%$ from Fig. 10.2(a), which is higher than in our previous work (Ch. 7), and implies a higher valley-orbit splitting¹. Fig. 10.2(b) shows a Rabi oscillation of a single spin with the electron in the ground valley-orbit state. The Rabi frequency extracted from the data is 1.345 MHz . The decay of the oscillation is what we would expect assuming a statistical distribution of resonance conditions with a line width of 0.63 MHz (FWHM), which is the number extracted from the continuous wave response (not shown). This line width corresponds to $T_2^* \approx 1 \mu\text{s}$, and is presumably dominated by the 4.7% ^{29}Si spins in the substrate, similar to what reported in Ch. 7. Here there is no evidence of intervalley switching with or without spin flip, or the combined effects of electrical noise and the magnetic field gradient.

10.4. DYNAMICAL DECOUPLING

Next we examine the spin memory time of this electrically controlled spin qubit. In our previous work (Ch. 7,8), due to switching between the two valley-orbit states, the Hahn echo decay was exponential with coherence time $\approx 40 \mu\text{s}$. Furthermore, we were unable to extend the coherence time using multiple echo pulses. Due to the difference in Lar-

¹Due to many unknown parameters, it is difficult to obtain a reliable estimate of the valley-orbit splitting. Nevertheless, assuming that the values of these parameters are equal between the previous work (Ch. 7), and this work, the higher population of the ground valley-orbit state implies a higher valley-orbit splitting. See Sec. 10.S11 for more details.

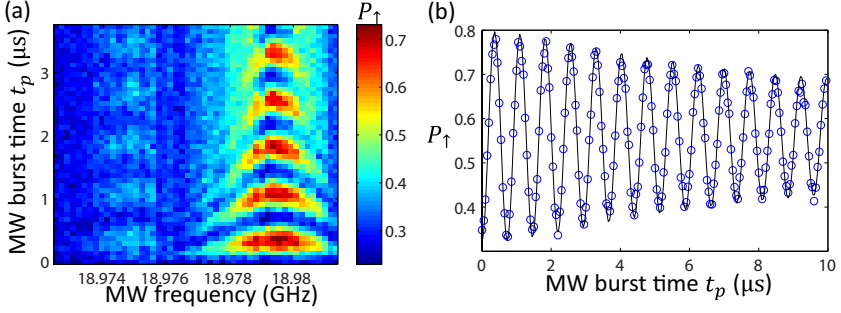


Figure 10.2: (a) Measured spin-up probability, P_{\uparrow} , as a function of f_{MW} and burst time t_p (microwave power at the source $P = 18.85$ dBm), showing two Rabi chevron patterns corresponding to the two valley-orbit states. The resonance frequency of the valley-orbit ground state is 18.9795 GHz and that of the excited state is 18.9750 GHz. The signal coming from the excited state is much smaller due to its lower population. (b) Measured spin-up probability, P_{\uparrow} , showing a Rabi oscillation for the ground valley-orbit state (blue circles). During the manipulation stage, on-resonance microwave excitation (at $f_{MW} = 18.9795$ GHz) was applied for a time t_p and off-resonance microwave ($f_{MW} = 18.9195$ GHz) was applied for a time $t'_p = 10\mu\text{s} - t_p$, in order to keep the total duration of the microwave bursts fixed to $10\mu\text{s}$ for every data point. The black line shows a numerical fit with a model that includes a constant driving field in the rotating frame (which is a fit parameter) and (quasi-)static noise modeled by a Gaussian distribution of resonance offsets with width 0.63 MHz (FWHM).

mor frequency between two valley-orbit states, as soon as a switch from one to the other valley-orbit state occurred, phase information could not be recovered by echo pulses. In this work, we observe significantly extended coherence times presumably because the switching between valleys is slower in the present gate voltage configuration.

We study the spin memory characteristics using two types of two-axis dynamical decoupling sequences, based on the XY4 (Maudsley, 1986), $(XY4)^n$ (sometimes called vCDD (Álvarez, Souza, and Suter, 2012)) and XY8 (Gullion, Baker, and Conradi, 1990) protocols. The insets in Fig. 10.3(a,b) show the $(XY4)^n$ and XY8 pulse sequences for 16π pulses. We use X and Y to denote π rotations about \hat{x} and \hat{y} , and \bar{X} and \bar{Y} for rotations about $-\hat{x}$ and $-\hat{y}$. Such two-axis decoupling sequences are chosen in order to reduce the effect of pulse imperfections and to equally preserve the spin components along all directions in the $\hat{x} - \hat{y}$ plane (de Lange *et al.*, 2010), which is important for quantum information processing. One-axis decoupling sequences such as CPMG (Carr and Purcell, 1954; Meiboom and Gill, 1958) may artificially preserve a specific spin component for a longer time than two-axis decoupling sequences, but with a reduced coherence time of the orthogonal spin component (Bluhm *et al.*, 2010b; Souza, Álvarez, and Suter, 2012; Wang *et al.*, 2012). The visibility of the echo amplitude decreases for larger numbers of π pulses, N_{π} , due to the pulse imperfections. Therefore, to facilitate direct comparison of the decay rates with different numbers of π pulses, in Fig. 10.3(a,b) we show the data, normalized to the echo amplitude at $t_{\text{wait}} = 0$, as a function of the total wait time t_{wait} for $(XY4)^n$ and XY8, respectively.

To analyze these decay curves, we adopt a semiclassical approach, in which the decay curve of the echo amplitude is written as

$$P(t_{\text{wait}}) = \exp[-W(t_{\text{wait}})] \quad (10.1)$$

with

$$W(t_{\text{wait}}) = \int_{-\infty}^{\infty} \frac{S(\omega)}{2\pi} \frac{F(\omega)}{\omega^2} d\omega. \quad (10.2)$$

$S(\omega)$ is the noise spectrum that produces an effective magnetic field fluctuation $\delta b(t)$ along the same direction as the quantization axis (de Sousa, 2009). More concretely, the relation between $S(\omega)$ and $\delta b(t)$ is described as $S(\omega) = \int_{-\infty}^{\infty} \gamma_e^2 \langle \delta b(0) \delta b(t) \rangle e^{i\omega t} dt$ with γ_e the gyro-magnetic ratio of the electron. $F(\omega)$ is the filter function of the pulse sequence (Cywinski *et al.*, 2008; Uhrig, 2007). First we assume that the noise spectrum dominating the decoherence is described by a power law,

$$S(\omega) = \frac{K}{\omega^{\alpha-1}}, \quad (10.3)$$

as seen in GaAs quantum dots (Medford *et al.*, 2012) and NV centers in diamond (de Lange *et al.*, 2010). Under this assumption, if the filter function $F(\omega)$ is sufficiently narrow around $\omega = \frac{\pi N_\pi}{t_{\text{wait}}}$ (which we verified is the case for $N_\pi \geq 4$), the decay curve can be written as (Bylander *et al.*, 2011)

$$P(t_{\text{wait}}) = \exp \left[- \left(\frac{t_{\text{wait}}}{T_2} \right)^\alpha \right], \quad (10.4)$$

with $T_2 = T_2^0 N_\pi^{(1-\frac{1}{\alpha})}$ and $T_2^0 = \left(\frac{2}{K} \right)^{\frac{1}{\alpha}} \pi^{1-\frac{1}{\alpha}}$. Fig. 10.3(c) shows T_2 as a function of the number of π pulses obtained by fitting Eq. [4] to the decay curves. The longest T_2 time reached is $\approx 400 \mu\text{s}$ with XY8 and $N_\pi = 128$ (data shown in Sec. 10.S9). We fitted $T_2 = T_2^0 N_\pi^{(1-\frac{1}{\alpha})}$ to the data (leaving out the case $N_\pi = 1$, the Hahn echo) and the resulting fit is shown in green in Fig. 10.3(c).

We can derive the noise spectrum from the decay curves in Fig. 10.3(a,b) using the fact that the filter function is narrow around $\omega = \frac{\pi N_\pi}{t_{\text{wait}}}$ for $N_\pi \geq 4$, (de Sousa, 2009) (Sec. 10.S3). The circles in Fig. 10.3(d) show the noise spectrum extracted from six decay curves in Fig. 10.3(b). The colors of the circles in Fig. 10.3(d) correspond to the colors used in Fig. 10.3(b) for different N_π . The green solid line in Fig. 10.3(d) is based on Eq. (10.3) with T_2^0 and α obtained from the fit (green line) to the data in Fig. 10.3(c). Its decay is close to a $1/f$ decay. Although this line shows an overall good agreement with the noise spectrum extracted from the decay curves, it does not match with the flat region at $\omega/2\pi \lesssim 30$ kHz.

In order to capture both the flat and decaying parts of the spectrum and obtain more insight into the nature of the noise spectrum, we now write the noise spectrum in the form

$$S(\omega) = \frac{A}{1 + (\omega\tau_c)^{\alpha-1}}, \quad (10.5)$$

where τ_c is the correlation time of the fluctuations in the environment that dominate the dynamical decoupling decay. We fit Eq. (10.1) to the six decay curves (leaving out $N_\pi = 1$) in Fig. 10.3(b) simultaneously, using also Eq. (10.2) and Eq. (10.5), with A and τ_c as the only fitting parameters. We first perform this fit (numerically) using $\alpha = 2$, close to the previously fitted value $\alpha = 1.8$ obtained using Eq. (10.3), but the fits deviate from the measured echo decays (see Fig. S5(e)). A better fit to the echo decay data using

Eq. (10.5) is obtained for $\alpha = 3$ (Fig. 10.3(b)), in which case Eq. (10.2) can be expressed analytically (Wang *et al.*, 2012). The fits in Fig. 10.3(b) yield $A = (2.5 \pm 0.2) \cdot 10^4 \text{ rad}^2\text{s}^{-1}$ and $\tau_c = 2.46 \pm 0.17 \mu\text{s}$. The resulting fit, plotted as a thick black line in Fig. 10.3(d), shows reasonable agreement with $S(\omega)$ obtained from the experimental data.

Extrapolating the fitted noise spectrum to frequencies below 5 kHz, where we do not have experimental data, the noise spectral density looks flat; this would result in an exponential Ramsey decay with $T_2^* \approx 80 \mu\text{s}$ (de Sousa, 2009). However, the measured Ramsey decay is Gaussian and has a much shorter $T_2^* \approx 1 \mu\text{s}$. Therefore the noise power at low frequencies must exceed the solid horizontal black line in Fig. 10.3(d) (Sec. 10.S1).

We now turn to the noise mechanisms and examine whether the hyperfine coupling of the electron spin with the evolving nuclear spins can explain the observed noise spectrum. Nuclear spin dynamics have two main mechanisms, hyperfine-mediated and dipole-dipole interactions between nuclear spins. Decoherence due to the hyperfine-mediated interactions is negligible in Si at $B \approx 800 \text{ mT}$ (Cywinski, Witzel, and Das Sarma, 2009) (Sec. 10.S1). However, magnetic dipole-dipole induced nuclear spin dynamics cannot be neglected. We performed numerical simulations of the spectrum of the nuclear spin noise and of the Hahn echo decay for a dot with 4.7% of ^{29}Si nuclei (natural abundance) within the coupled pair-cluster expansion (Yang and Liu, 2009) for several choices of the quantum dot parameters. A calculated spectrum is approximated to an analytical expression: $\frac{2\sigma_\omega^2\tau_n}{1+(\omega\tau_n)^2}$ with the correlation time of the nuclear spin bath $\tau_n \sim 10^4 \text{ ms}$ and the amplitude $\sigma_\omega \sim 10^6 \text{ rad/s}$ is shown by the dotted line in Fig. 10.3(d). The measured Gaussian-shape Ramsey decay with $T_2^* \sim 1 \mu\text{s}$ is consistent with this spectrum so presumably the randomly oriented ^{29}Si nuclear spins dominate the noise at low frequencies (Kawakami *et al.*, 2014; de Sousa, 2009) (see Sec. 10.S1 for details). They also dominate the gate fidelities discussed below. However, at higher frequencies, even though the noise spectrum calculated from the nuclear spin dynamics has the same shape as Eq. 10.5 with $\alpha = 3$, the amplitude and the correlation time are significantly different from the noise spectrum measured by the dynamical decoupling. With the calculated correlation time and the amplitude for the nuclear spins, the Hahn echo decay time T_2 would be above 0.5 ms, which is much longer than the measured value of $70 \mu\text{s}$. Nuclear spin noise thus cannot explain the observed Hahn echo decay.

We therefore conclude that the noise spectrum consists of at least two contributions: nuclear spin noise at low frequencies and another mechanism at higher frequencies. At higher frequencies, the noise spectrum decays as $1/f^2$ taking $\alpha = 3$, but we see that a $\approx 1/f$ decay (green line) also fits the frequency dependence of the data points well. It is possible that this part of the spectrum is dominated by charge noise, which couples to the spin due to the magnetic field gradient from the micromagnets. Thus charge noise may effectively induce magnetic $1/f$ or $1/f^2$ noise. To give a feeling for numbers, a two-level magnetic field fluctuation of $\pm 0.4 \mu\text{T}$, which given the micromagnet gradient corresponds to a $\approx 4 \text{ pm}$ shift back and forth in the dot position, gives a Lorentzian noise spectrum that matches the solid line in Fig. 10.3(d) (Eq. 10.5 with $\alpha = 3$, $A = (2.5 \pm 0.2) \cdot 10^4 \text{ rad}^2\text{s}^{-1}$ and $\tau_c = 2.46 \pm 0.17 \mu\text{s}$) (Bergli, Galperin, and Altshuler, 2009).

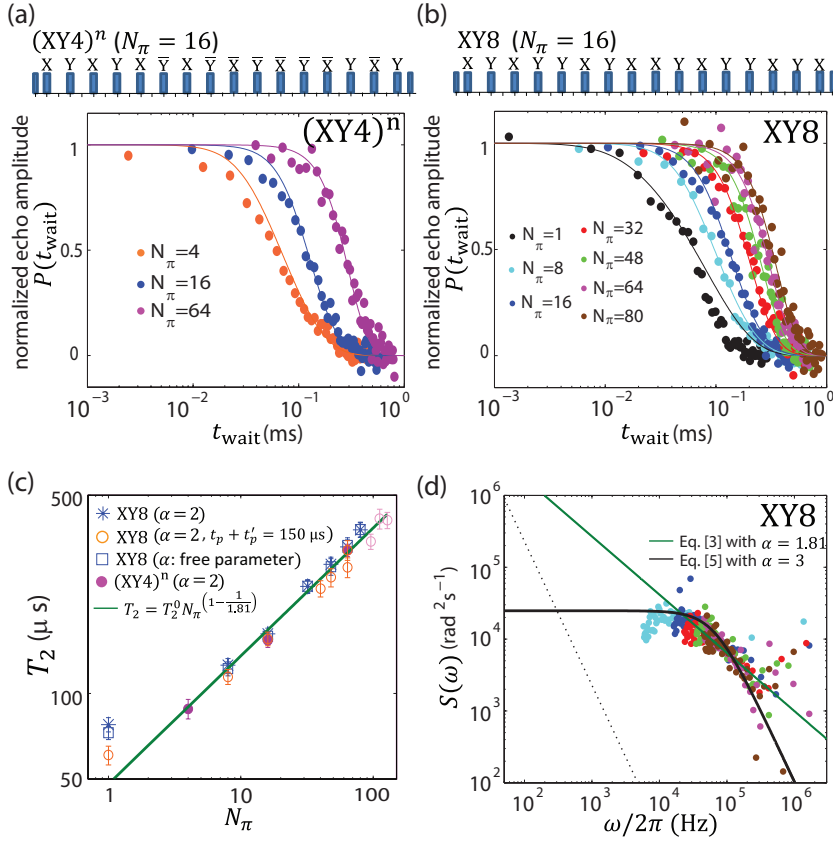


Figure 10.3: (a) Normalized spin echo amplitude as a function of the total waiting time t_{wait} using the $(XY4)^n$ pulse sequence for $N_\pi = 4$ (orange points), 16 (blue points), and 64 (purple points) pulses (concatenated level $n = 1, 2$ and 3, respectively). The inset shows the $(XY4)^n$ pulse sequence for $N_\pi = 16$ ($n = 2$). The first and the last pulses are $\pi/2$ pulses and the 16 pulses in the middle are π pulses. X, \bar{X} , \bar{Y} or Y indicate the phase of the pulses. The solid lines present fits using Eq. (10.1) with Eq. (10.2) and Eq. (10.5) for $\alpha = 3$. (b) Similar to (a) but using a Hahn echo sequence for $N_\pi = 1$ and a XY8 sequence for $N_\pi = 8, 16, 32, 48, 64, 80$. The inset shows XY8 pulse sequence for $N_\pi = 16$. Fits as in (a), except that the solid line for $N_\pi = 1$ is the decay curve with A and τ_c obtained from the fit to the other 6 decay curves in (b). (c) Coherence time, T_2 , as a function of the number of π pulses N_π using XY8 (blue asterisks, blue squares and orange circles) and $(XY4)^n$ (purple circles). See Sec. 10.S9 for the pulse sequences used for pink open circles. The T_2 values are obtained by fitting Eq. (10.4) to the decay curves. The choice of α did not much affect the extracted T_2 . The values shown are for $\alpha = 2$ except for the blue squares for which α is left as a fitting parameter. The green line presents a fit to the data (leaving out $N_\pi = 1$) using $T_2 = T_2^0 N_\pi^{(1-1/\alpha)}$. From this fit, we obtained $T_2^0 = 48 \pm 8\ \mu\text{s}$ and $\alpha = 1.81 \pm 0.14$. (d) Noise spectrum extracted from Fig. 10.3(b). The green solid line corresponds to Eq. (10.3) with $T_2^0 = 48\ \mu\text{s}$ and $\alpha = 1.81$. The black line presents a fit using Eq. (10.5), see main text. The dotted black line represents the calculated noise spectrum produced by the ^{29}Si nuclear spin dynamics (see Sec. 10.S1 for the details of the calculation).

10.5. RANDOMIZED BENCHMARKING

We measured the average gate fidelity using Standard Randomized Benchmarking (SRB), which is known as an efficient way to measure the gate fidelity without suffering from

initialization and read-out errors (Knill *et al.*, 2008; Magesan, Gambetta, and Emerson, 2012). The specific procedure is as follows. After initializing the electron to the spin-down state, we apply randomized sequences of m Clifford gates and a final Clifford gate C_{m+1} that is chosen so that the final target state in the absence of errors is either spin-up or spin-down. Every Clifford gate is implemented by composing π and $\pi/2$ rotations around two axes, following (Barends *et al.*, 2014). Applying randomized sequences of imperfect Clifford gates acts as a depolarizing channel (Knill *et al.*, 2008; Magesan, Gambetta, and Emerson, 2012). The depolarization parameter p reflects the imperfection of the average of 24 Clifford gates. Under certain assumptions, for m successive Clifford gates the depolarization parameter is p^m .

We measure the spin-up probability both for the case where spin-up is the target state, $P_{\uparrow}^{|\uparrow\rangle}$, and for the case where spin-down is the target state, $P_{\uparrow}^{|\downarrow\rangle}$, for 119 different randomized sequences for each choice of m , and varying m from 2 to 220. The difference of the measured spin-up probability for these two cases, $P_{\uparrow}^{|\uparrow\rangle} - P_{\uparrow}^{|\downarrow\rangle}$, is plotted with red circles in Fig. 10.4(a). Theoretically, $P_{\uparrow}^{|\uparrow\rangle} - P_{\uparrow}^{|\downarrow\rangle}$ is expressed as (Muhonen *et al.*, 2015; Veldhorst *et al.*, 2014):

$$P_{\uparrow}^{|\uparrow\rangle} - P_{\uparrow}^{|\downarrow\rangle} = ap^m \quad (10.6)$$

where a is a prefactor that does not depend on the gate error. As seen in Eq. (10.6), differently from quantum process tomography (Chuang and Nielsen, 1997; Kim *et al.*, 2014, 2015), the measurement of the gate fidelity is not affected by the initialization and read-out infidelities, assuming these infidelities are constant throughout the measurement. In order to keep the read-out and initialization fidelities constant for different m , we kept the total microwave burst time $t_p + t'_p = 150 \mu\text{s}$. Due to the longer total microwave burst time, the read-out and initialization infidelities are higher than in Fig. 10.2. This is the reason that initially $P_{\uparrow}^{|\uparrow\rangle} - P_{\uparrow}^{|\downarrow\rangle}$ is 20% instead of 45%.

Fig. 10.4(a) shows that the measured decay does not follow a simple exponential p^m . This behavior is reproduced by numerical simulations of the randomized benchmarking experiment, using the same set of randomized sequences as used in the experiments and assuming that the magnetic field fluctuations are characterized by $\delta b(t)$, the combination of the high-frequency noise $\delta b'(t)$ and the (quasi-)static noise δb_0 :

$$\delta b(t) = \delta b_0 + \delta b'(t), \quad (10.7)$$

where δb_0 again has a Gaussian distribution with FWHM of 0.63 MHz and $\delta b'(t)$ is expressed by Eq. (10.5) using $\alpha = 3$, $A = 2.5 \cdot 10^4 \text{ rad}^2\text{s}^{-1}$, $\tau_c = 2.46 \mu\text{s}$. The simulation results are shown in Fig. 10.4(b) and show good agreement with experiment.

To evaluate explicitly the relative contribution of δb_0 and $\delta b'(t)$ to the randomized benchmarking decay, we repeated the numerical simulation including at first only the high-frequency noise $\delta b'(t)$, in which case the decay is extremely slow. Next we include only the (quasi-)static noise δb_0 and find almost exactly the same decay as with the combination of the two noise contributions. This indicates that the (quasi-)static noise is mainly responsible for the gate error while the contribution from the high-frequency noise is small (Sec. 10.S7). This is consistent with an earlier report (Fogarty *et al.*, 2015), in which it was also shown that ensemble averaging over individual exponential decays

can lead to a non-exponential decay. Repeated measurements in the presence of low-frequency noise effectively lead to such ensemble averaging.

Since the measured SRB decay is not of the form ap^m , we should be cautious using the fidelity numbers extracted from this procedure (Epstein *et al.*, 2014). We see that both in experiment and simulation, the decay begins to deviate from a single exponential (straight line in the semi-log plot) for on-resonance microwave bursts with $t_p \gtrsim 8\mu\text{s}$. These are the data points with open circles in Fig. 10.4. We fitted to the decay curves for $t_p < 8\mu\text{s}$ to ap^m and obtained $p = 0.9620 \pm 0.0051$. From this, the average fidelity of a Clifford gate is $1 - (1 - p)/2 = 98.10 \pm 0.26\%$ and the average fidelity for a single π or $\pi/2$ rotation around \hat{x} or \hat{y} is calculated to be $1 - (1 - p)/2/1.875 = 98.99 \pm 0.14\%$.

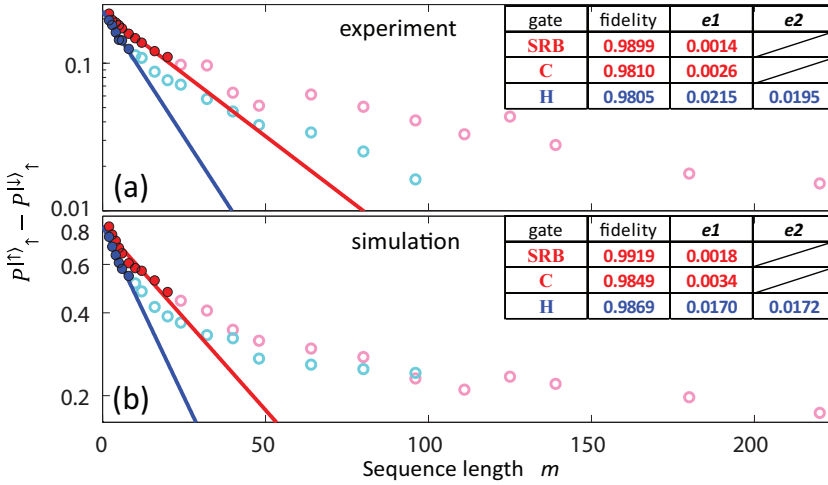


Figure 10.4: Randomized benchmarking. The difference between the spin-up probability with spin-up as the target state and with spin-down as the target state, $p_{\uparrow}^{(m)} - p_{\downarrow}^{(m)}$, is plotted as a function of the number of Clifford gates, m . The Standard Randomized Benchmarking curve (red circles) is measured after applying randomized sequences of m Clifford gates and a final Clifford gate C_{m+1} . The Interleaved Randomized Benchmarking curve is measured by interleaving the Hadamard gate with the same random sequence of Clifford gates (blue circles). The experimental results are shown in (a) and the results of numerical simulations (see main text) are shown in (b). The experiments and simulations use the same 119 random sequences from $m = 2$ to 220. Each experimental data point is the average of 250 single-shot cycles. For the numerical simulation, we averaged over 1000 repetitions, and for each repetition we sample δb_0 and include a different time-domain realization of $\delta b'(t)$. In the simulation, the read-out and initialization fidelities are assumed to be perfect. The π rotation time is 366 ns for the experiments and 360 ns for the simulation. The delay time between pulses is set to be 5 ns for both the measurements and the simulations. The red and blue curves present fits of the form Ap^m to the data with $t_p < 8\mu\text{s}$. The gate fidelities extracted from the fits are shown in the insets. The first row (SRB) and the second row (C) show the average fidelity per single gate and per Clifford gate, respectively, obtained from the SRB measurements. The third row (H) shows the fidelity of the Hadamard gate obtained from IRB. $e1$ and $e2$ are as defined in Table 10.1.

We also characterized the fidelity of individual gates using interleaved randomized benchmarking (IRB). In this procedure, a specific gate is interleaved between randomized Clifford gates. The depolarizing parameter now becomes bigger than in SRB due to the imperfections of the interleaved gate. From the difference in the depolarizing

experiment

gate	fidelity	e1	e2
T ($\pi/4$ rotation around \hat{z})	0.9891	0.0282	0.0272
H (π rotation around $(\hat{x} + \hat{z})/2$)	0.9805	0.0215	0.0195
x ($\pi/2$ rotation around \hat{x})	0.9893	0.0285	0.0368
z ($\pi/2$ rotation around \hat{z})	0.9813	0.0198	0.0231
X (π rotation around \hat{x})	0.9842	0.0622	0.0325
Z (π rotation around \hat{z})	0.9917	0.0670	0.0401

Table 10.1: The measured gate fidelities for five representative gates, extracted using Interleaved Randomized Benchmarking. e_1 and e_2 are errors in the fidelities. e_1 is calculated from the 95% confidence interval on the fit coefficient p and e_2 is an upper bound arising from imperfect random gates, calculated according to the formulas in (Magesan, Gambetta, and Emerson, 2012). As the T gate is not a Clifford gate, we interleaved 2 successive T gates, following (Barends *et al.*, 2014).

parameter between SRB and IRB, the fidelity of the interleaved gate is extracted. In Fig. 10.4(a), the blue circles show the case where the Hadamard gate is the interleaved gate. The Hadamard gate is implemented by a π rotation around the \hat{x} axis and a $\pi/2$ rotation around the $-\hat{y}$ axis. By fitting $a_H p_H^m$ to the decay curve (again for $t_p < 8 \mu\text{s}$), $p_H = 0.9245 \pm 0.0197$ is obtained. The fidelity of the Hadamard gate is calculated to be $1 - (1 - p_H/p)/2 = 98.05 \pm 2.15\%$. In the same way, we measured the fidelities for several other common gates (Table 10.1). While also for IRB, the decay is not exponential, the gate fidelities extracted from IRB for the first $8 \mu\text{s}$ appear roughly consistent with the fidelities extracted from SRB.

10.6. DISCUSSION AND CONCLUSION

We have shown that the average single gate fidelity for a single electron spin confined in a $^{\text{nat}}\text{Si}/\text{SiGe}$ quantum dot approaches the fault-tolerance threshold for surface codes (Fowler *et al.*, 2012). The low frequency noise that limits gate fidelity is well explained by the nuclear spin randomness given the natural abundance of ^{29}Si . Therefore we can increase gate fidelities by reducing the abundance of ^{29}Si using isotopically enriched ^{28}Si (Muhonen *et al.*, 2014; Veldhorst *et al.*, 2014) or by using composite pulses (Vandersypen and Chuang, 2005). Also the read-out fidelity can be boosted to the fault-tolerance threshold by using Pauli spin blockade read-out (Shulman *et al.*, 2012) and RF reflectometry (Bart *et al.*, 2016d). The longest coherence time measured using dynamical decoupling is $\approx 400 \mu\text{s}$. We revealed that the noise level is flat in the range of 5 kHz - 30 kHz and decreases with frequency in the range of 30 kHz - 1 MHz. In this frequency range (5 kHz - 1 MHz), the measured noise level is higher than expected from the dynamics of the ^{29}Si nuclear spins. Instead, charge noise in combination with a local magnetic field gradient may be responsible. If charge noise is dominant, dynamical decoupling decay times can be further extended by positioning the electron spin so that the gradient of the longitudinal component of the magnetic field gradient vanishes, while keeping the transverse component non-zero as needed for driving spin rotations. At that point, we can reap the full benefits from moving to ^{28}Si enriched material for maximal coherence times as well.

SUPPLEMENTARY SECTIONS

10.S1. MODELING OF DECOHERENCE AND NOISE PRODUCED BY NUCLEAR SPINS

In order to analyze decoherence and noise produced by the nuclear spins, we performed numerical modeling of the Hahn echo decay and of the spectrum of the nuclear spin noise. To model the quantum dot we generate a crystallite of silicon by representing the underlying diamond lattice as two fcc sublattices shifted with respect to each other by the vector $[1/4, 1/4, 1/4]$. The size of the crystallite is $(2L_x + 1) \times (2L_y + 1) \times (2L_z + 1)$ along the x -, y -, and z -axis, respectively. For simulation results shown below we used the external field directed along the x -axis as in the experiments and $L_x = L_y = 18$ and $L_z = 8$ which is large enough, so that the results do not depend much on the crystallite size; we also did not see any significant changes with changing the orientation of the dot with respect to the external field directed along the z -axis. The sites inside the crystallite are randomly populated with spins $1/2$ (which represent ^{29}Si nuclei) with abundance of 4.68%, so the total number of nuclear spins in the crystallite was about 8700. For convenience, below we express the coordinates (x, y, z) in the units of d , where $d = 0.543$ nm is the lattice constant of the cubic lattice.

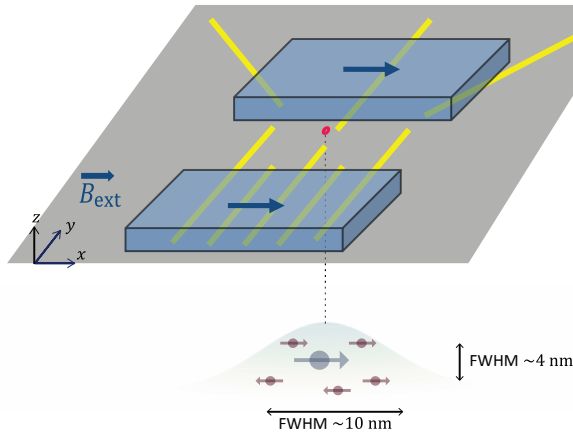


Figure 10.S1: Schematic of the position of electron respect to the micromagnets and surface gates. The shown electron wavefunction spread represents Eq. 10.S1 for the case (i) $x_0 = 0.4 \cdot L_x$, $y_0 = 0.4 \cdot L_y$, and $z_0 = 0.4 \cdot L_z$. The drawing of the electron wavefunction spread is scaled around 100 times larger than that of the micromagnets and the surface gates. The estimated position of the center mass of the electron on the $x - y$ plane is indicated with a red circle $((x, y, z) = (x_c, y_c, 0))$ and the dot is positioned around 150 nm below the surface gates ($z_c = -147$ nm, see Sec. 5.3).

The envelope of the electron density within the dot is modeled as a 3-dimensional Gaussian distribution, centered at the central unit cell of the crystallite:

$$\rho_{env}(x, y, z) = \rho_0 \exp\left(\frac{-(x - x_c)^2}{2x_0^2}\right) \exp\left(\frac{-(y - y_c)^2}{2y_0^2}\right) \exp\left(\frac{-(z - z_c)^2}{2z_0^2}\right), \quad (10.S1)$$

with various deviations x_0 , y_0 , and z_0 . Below, we present the results for two representative cases: (i) $x_0 = 0.4 \cdot L_x$, $y_0 = 0.4 \cdot L_y$, and $z_0 = 0.4 \cdot L_z$, denoted as the larger dot, and (ii) $x_0 = 0.2 \cdot L_x$, $y_0 = 0.2 \cdot L_y$, and $z_0 = 0.2 \cdot L_z$, denoted as the smaller dot. The hyperfine coupling constants are proportional to the electron density, so that the Hamiltonian of the hyperfine coupling between nuclear spins and the electron spin is

$$H = \sum_{i=1}^{N_n} A_i I_{ix} S_x \quad (10.S2)$$

with $A_i = A_{\text{sum}} \rho_{\text{env}}(x, y, z) = A_{\text{sum}} |\phi(x_i, y_i, z_i)|^2$ where $\phi(x_i, y_i, z_i)$ is an envelope function (Eq. D.13) and x_i , y_i , and z_i are the coordinates of the i -th nucleus, its spin operator is I_{ix} , while S_x is the electron spin operator (note that the external field is directed along the x -axis), and $N_n \sim 8700$ is the total number of ^{29}Si nuclear spins in the crystalite. The proportionality coefficient A_0 is normalized to produce the standard deviation in electron Larmor frequency $\sigma_\omega = \sqrt{\sum_i A_i^2}/2$ equal to 1.7 Mrad/s, i.e. approximately $2\pi \cdot 271$ kHz, which corresponds to the measured line width (or, equivalently, to $T_2^* = 800$ μs or to a random static field of 9.6 μT). Calculated value of A_0 for a larger dot is almost consistent with a theoretically calculated A_0 for natural silicon (Assali *et al.*, 2011).

The nuclear spins are subjected to an external field $B_{\text{ext}} = 800$ mT and a gradient stray field from the micromagnet. The gradient field varies both in magnitude and in direction, and is much smaller than B_{ext} . If the transverse part of the stray field is neglected then the Zeeman part of the Hamiltonian of the i -th nuclear spin is

$$H_{Z,i} = \gamma_n \hbar I_{ix} B(x_i), \quad (10.S3)$$

where γ_n is the gyromagnetic ratio of the ^{29}Si nucleus, and $B(x_i) = B_{\text{ext}} + x_i G_{\parallel}$, where G_{\parallel} is the gradient of the longitudinal x -component of the stray magnetic field; in our experiments $\gamma_n G_{\parallel} = 5.78$ krad/s (approximately $2\pi \cdot 0.92$ kHz) per unit cell.

The transverse part of the stray field, which varies from one nuclear spin to another, may lead to decoherence in a manner similar to the electron spin echo envelope modulation (ESEEM) mechanism (Schweiger and Jeschke, 2001). This decoherence mechanism has been considered by Beaudoin and Coish (Beaudoin and Coish, 2013), and we show below that for the parameters of our experiment the contribution of this decoherence channel is negligible. Indeed, if we omit the coupling between the nuclear spins, then the Hamiltonian of the electron spin coupled to a bath of nuclear spins in a gradient field will be

$$H_1 = \sum_{i=1}^{N_n} (\hbar A_i I_{ix} S_x + \gamma_n \hbar I_{ix} B(x_i) + \gamma_n \hbar I_{iy} B_y(x_i)), \quad (10.S4)$$

where we omitted the Zeeman term for the electron spin by considering dynamics of the electron spin in its rotating frame, and leaving only the secular terms (Schweiger and Jeschke, 2001; Slichter, 1990). We also assumed for simplicity that the transverse part of the gradient field is directed along the y -axis, and that the transverse field changes only along the x -axis. Shortly we will see that these assumptions do not change the conclusions, and only help clarify the arguments.

The motion of the nuclear spins under the Hamiltonian H_1 above can be analyzed explicitly: S_x is a constant of motion, so that we can consider the subspaces with $S_x = +1/2$

and $S_x = -1/2$ separately; in each subspace the Hamiltonian H_1 becomes a sum of terms describing individual nuclear spins. E.g., it can be shown that, under the standard assumption of completely unpolarized initial state of the nuclear spins, the free decay of the electron spin coherence is proportional to $\text{Tr}_n \left[U_{1+}(t) U_{1-}^\dagger(t) \right]$,

and the Hahn echo decay for the electron spin is proportional to

$\text{Tr}_n \left[U_{1+}(t_{\text{wait}}/2) U_{1-}(t_{\text{wait}}/2) U_{1+}^\dagger(t_{\text{wait}}/2) U_{1-}^\dagger(t_{\text{wait}}/2) \right]$, where the evolution operators $U_{1\pm}(t) = \exp(-iH_{1\pm}t)$; here the operators H_{1+} and H_{1-} are the parts of the Hamiltonian H_1 corresponding to the subspaces $S_x = +1/2$ and $S_x = -1/2$ respectively, and Tr_n denotes trace over the nuclear spins.

In our experimental situation, where $\gamma_n B_{\text{ext}} \gg A_k$ and $B_{\text{ext}} \gg B_y$ for a typical nuclear spin in the quantum dot, the Hahn echo signal decays from its initial value (normalized to 1) to the minimum (Childress *et al.*, 2006; Cywinski, Witzel, and Das Sarma, 2009) given by $\exp \left[-\sum_{i=1}^{N_n} (A_i \gamma_n B_y(x_i))^2 / (\gamma_n B_{\text{ext}})^4 \right]$, which can be evaluated as $\exp[-\sigma_\omega^2 (\gamma_n \delta B_y)^2 / (\gamma_n B_{\text{ext}})^4]$, where δB_y is the typical spread of the transverse field over the quantum dot, which is of the order of $\delta B_y \sim l \cdot (dB_\perp/dx) \sim 3$ mT if we assume the size of the dot $l \sim 10$ nm and $dB_\perp/dx \sim 0.3$ mT/nm. Also taking into account the values $\sigma_\omega \sim 1.7 \cdot 10^6$ rad/s and $B_{\text{ext}} \sim 800$ mT, we find that the overall decay of the Hahn echo due to ESEEM-like mechanism is negligible: instead of decay, the Hahn echo experiences a small modulation. Thus, the effect of the transverse field on the decoherence can be neglected. The variations in the direction of the local quantization axes leads only to a small renormalization of the hyperfine coupling constants A_i and of the dipole-dipole couplings between the nuclear spins.

Thus, in order to analyze the decay of the electron spin Hahn echo, we should take into account the dipolar interaction between the nuclear spins, which lead to pairwise flip-flops of the nuclear spins, and present more efficient decoherence channel than the individual flips of the nuclear spins caused by the transverse stray fields. The dipolar coupling is given by the sum over the pairs

$$H_{nn} = \sum_{i < j} b_{ij} (1 - 3 \cos^2 \theta_{ij}) \left(I_{ix} I_{jx} - \frac{1}{2} I_{iz} I_{jz} - \frac{1}{2} I_{iy} I_{jy} \right), \quad (10.S5)$$

with $b_{ij} = \frac{\mu_0 \hbar^2 \gamma_n^2}{4\pi R_{ij}^3}$ (Eq. 3.33), where $R_{ij} = r_{ij} d$ is the distance between the two nuclei, and θ_{ij} is the angle between the line connecting the nuclei and the x -axis. The numerical modeling of the nuclear spin dynamics was performed using the coupled cluster expansion (CCE) (Yang and Liu, 2009) within second order (i.e., considering only the clusters made of nuclear spin pairs). We have also included the electron spin-mediated coupling between the nuclear spins (Cywinski, Witzel, and Das Sarma, 2009) in the numerical modeling, of the form

$$H_{nn}^{(2)} = \sum_{i < j} \beta_{ij} S_z \left(\frac{1}{2} (I_{iz} I_{jz} + I_{iy} I_{jy}) \right), \quad (10.S6)$$

with $\beta_{ij} = \frac{A_i A_j}{2\omega_0}$ with ω_0 the Larmor frequency of the electron spin. As expected, this coupling did not produce any noticeable effect, since the magnitude of the electron spin-mediated coupling is much smaller than the direct dipolar interaction between nuclei.

Indeed we can roughly estimate the typical strength of the dipolar interaction between nuclear spins as $\frac{\mu_0}{4\pi}\gamma_n^2\hbar/\bar{R}^3 \approx 66$ rad/s where \bar{R}^{-3} is the density of nuclear spins, while the typical electron spin-mediated coupling is of the order of $A_k^2/(2\omega_0) \sim 2\sigma_\omega/(N_s\omega_0)$, which is about 0.1-0.01 rad/s for $B_{\text{ext}} \sim 500$ mT; here N_s is the number of the nuclear spins effectively coupled to the electron, which is about 4500 for the larger dot and 560 for the smaller dot, so that the magnitude of the electron spin-mediated coupling is several orders smaller than the dipolar coupling for such a large magnetic field. As expected from this estimation, the electron spin-mediated coupling did not produce a noticeable effect in the calculation result. The Hahn echo decays calculated within the pair-cluster CCE are shown in Fig. 10.S2 for the larger and the smaller quantum dots (defined above). The Hahn echo decay times are of order of 0.5–1 ms, which is much longer than the experimentally measured T_2 time. Similar results have been obtained for other system parameters we explored.

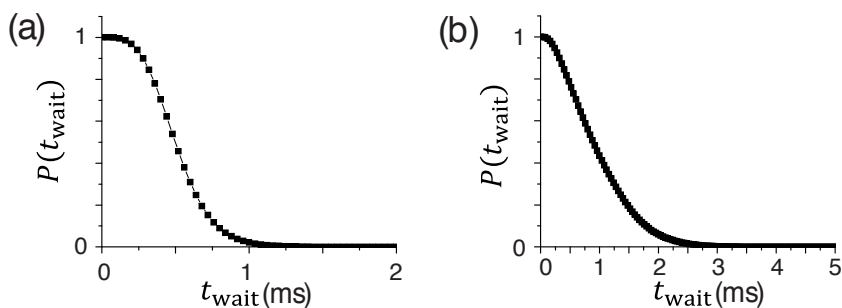


Figure 10.S2: Hahn Echo amplitudes $P(t_{\text{wait}})$ for the larger dot (a) and the smaller dot (b) as a function of the total waiting time t_{wait} .

In order to gain deeper insight into the nature of the noise created by the nuclear spins, we used the pair-cluster CCE to calculate the correlator of the nuclear spin noise. Let us first note that the concept of the nuclear spin noise, which acts on the electron spin and decoheres it, is a semi-classical concept. For instance, it presumes that the properties of the nuclear spin noise (such as the correlation function) are well defined and independent of the electron spin. This description is not always adequate: much decoherence comes from the quantum back-action of the electron spin on the nuclear bath, so that the motion of the nuclear spins depends on the electron spin state. Nevertheless, the model of the random nuclear noise has its advantages, and often gives a reasonable semi-quantitative description of decoherence for a range of experimentally interesting situations (Reinhard *et al.*, 2012).

Thus, we investigate the correlation function of the spin noise. Specifically, for a given state of the electron spin $s = +, -$ (along the x-axis or in the direction opposite to the x-axis) we calculate the correlator

$$C(t) = \langle \eta_s(0)\eta_s(t) \rangle = \sum_{i,k} A_i A_k \langle I_{ix} I_{kx}(t) \rangle_s \quad (10.S7)$$

where $\langle \dots \rangle_s$ denotes the quantum-mechanical average with the completely disordered initial state of the nuclear spin bath and the electron spin in the state s and

$\eta(t) = \sum_i^{N_n} A_i I_{ix}(t) = \gamma_e \delta b(t)$ with γ_e gyro-magnetic ratio of the electron and $\delta b(t)$ effective magnetic field fluctuation along the z axis due to the nuclear spin bath. We performed simulations with the pair-cluster CCE method, using the Heisenberg representation for the nuclear spin operators $I_{mx}(t)$. Since the correlation function $C(t)$ has the value $C(0) = \sigma_\omega^2$ at $t = 0$ (where $\sigma_\omega = 2\pi \cdot 271$ kHz), it is convenient to plot the normalized correlator $C_N(t) = C(t)/\sigma_\omega^2$; these simulation results are plotted in Fig. 10.S3.

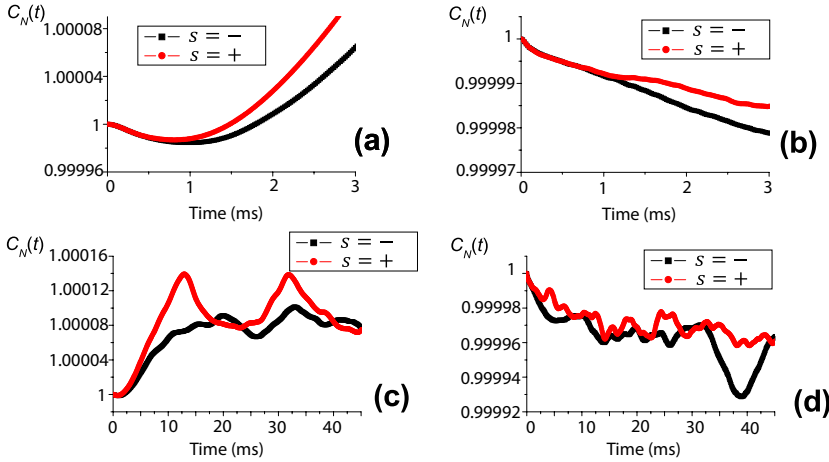


Figure 10.S3: Normalized correlation functions $C_N(t)$ for different orientations of the electron spin, for the two quantum dots: (a) and (c) — for the larger quantum dots; (b) and (d) — for the smaller quantum dot. Panels (a) and (c) show the same results, but for different time ranges, the same is true for the panels (b) and (d).

Our results show that the noise correlators corresponding to different electron spin states can be very different, implying back-action of the electron spin on the nuclear spin bath. Indeed, the hyperfine coupling constants, even for quite large quantum dots, are large in comparison with the dipole-dipole couplings between the nuclear spins. However, the echo decay is determined by the noise dynamics *at the timescale of the echo decay*, which is of the order of a few milliseconds. At this timescale the noise correlators corresponding to different electron spin states do not differ too much, and give meaningful semi-quantitative information about the properties of the nuclear spin bath.

In particular, we describe the nuclear bath as a classical Ornstein-Uhlenbeck (Gaussian, Markovian, stationary) noise source (Wang et al., 2012) with amplitude σ_ω and correlation time τ_n , so that its correlation function is $C(t) = \sigma_\omega^2 \exp(-t/\tau_n)$. In this context, the intuitive meaning of τ_n is thus the correlation time of the nuclear spin bath on short timescales (< 1 ms). We use the notation τ_n when the correlation time refers specifically to correlation time of the nuclear spin bath in order to avoid the confusion with the experimentally measured correlation time τ_c . The spectrum of this noise is

$$S(\omega) = 2\sigma_\omega^2 \tau_n \frac{1}{1 + (\omega\tau_n)^2}, \quad (10.S8)$$

where for natural silicon the correlation time is of order of seconds to minutes. For such a slow noise, satisfying the condition $\sigma_\omega \tau_n \gg 1$, the free coherence decay (Ramsey decay)

has Gaussian form. Indeed, as known from the statistical theory of the spin resonance decay (Klauder and Anderson, 1962; Kubo, Toda, and Hashitsume, 1991), for the static noise the shape of the Ramsey decay is given by the Fourier transform of the (instant) distribution function of the random process η . For the electron spin coupled to a large bath of nuclear spins via contact hyperfine coupling, this distribution function is Gaussian, with the standard deviation σ_ω :

$$P(\eta) = \frac{1}{\sqrt{2\pi\sigma_\omega^2}} \exp[-\eta^2/(2\sigma_\omega^2)]. \quad (10.S9)$$

Correspondingly, the Ramsey decay has Gaussian form, with the decay time $T_2^* = \sqrt{2}/\sigma_\omega$. Furthermore, for the slow noise (satisfying the condition $\sigma_\omega\tau_n \gg 1$) the Hahn echo decay time T_2 is proportional to $(\sigma_\omega^2/\tau_n)^{-1/3}$ (Klauder and Anderson, 1962), so that

$$\frac{\tau_n}{T_2} \sim \left(\frac{T_2}{T_2^*}\right)^3, \quad (10.S10)$$

i.e. for the quantum dot under consideration, the correlation time of the nuclear noise is of order of $2 \cdot 10^8$ times longer than T_2^* .

In other words, for the Ramsey decay of the electron spin the filter function $F(\omega, t)$ in Eq. 2 of the main text involves the frequencies ranging from 0 to the frequencies of order of $1/T_2^*$. In this region the noise spectrum looks like a very sharp peak (its width is of order of $1/\tau_n$, which is 10^{-8} times smaller than the whole range of relevant frequencies), and can be approximated as a delta-function. The integral in Eq. 2 in this case leads to the Ramsey decay of Gaussian shape with the decay time $T_2^* = \sqrt{2}/\sigma_\omega$, which is consistent with the measured Ramsey decay.

Due to extreme slowness of the noise, on the timescale of the Hahn echo decay, the change in the correlation function $\langle \eta_s(0)\eta_s(t) \rangle$ is minuscule, and this is indeed what is seen in Fig. S2: although the correlation functions $C(t)$ are quite irregular on the timescales of order of 10–50 ms, the overall change in the noise amplitude over the experimentally relevant timescale, < 1 ms, is very small, and can be well approximated by a decaying exponential $C_N(t) = \exp(-t/\tau_n)$. From this fitting we extract the values of τ_n , and substitute them into the simplified theoretical expression for the Hahn echo decay (Klauder and Anderson, 1962)

$$P(t_{\text{wait}}) = \exp\left(-\frac{t_{\text{wait}}^3 \sigma_\omega^2}{12\tau_n}\right). \quad (10.S11)$$

Fig. 10.S4 illustrates the comparison between such estimates and the original CCE-simulated echo curves (shown above in Fig. 10.S2). The values of τ_n were obtained from fitting the curves $C_N(t)$ to the decaying exponent in the region of $0 < t < 0.5$ ms. This is the range of times where the echo decay happens, and where the correlators for the electron spin states "down" ($s = -$) and "up" ($s = +$) are close to each other and are well described by decaying exponent. The resulting values are $\tau_n = 4.464 \cdot 10^4$ ms for the larger dot, and $\tau_n = 8.475 \cdot 10^4$ ms for the smaller dot. The condition $\sigma_\omega\tau_n \gg 1$ is satisfied for both cases. The red curves in Fig. S3 describe well the Hahn echo decay during the first millisecond,

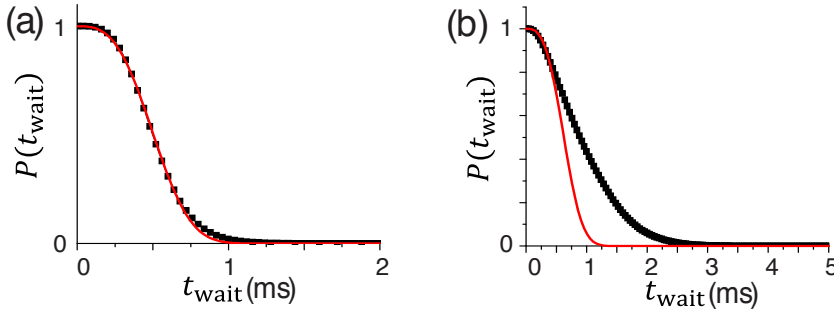


Figure 10.S4: Calculated Hahn echo amplitudes (black squares) for the larger dot (a) and for the smaller dot (b), obtained from the CCE simulations, are compared with the theoretical estimates (Eq. 10.S11): shown as red lines.

where the approximation of the nuclear noise is valid, and where the back-action from the electron spin is not too strong.

Thus, we conclude that the model of the nuclear spin noise is semi-quantitatively applicable to the considered quantum dots. However, the experimentally measured Hahn echo decay time is an order of magnitude shorter than the CCE simulations predict for the nuclear spin-induced echo decay. Similarly, we can extract the noise spectrum using the exponential fittings of $C(t)$ described above: the result is shown in Fig. 10.3(d) of the main text. Again, we see that the noise produced by the nuclear spins is too slow in comparison with the experimentally measured one, and is unlikely to be an important source of decoherence in the Hahn echo and the dynamical decoupling experiments in our quantum dot system.

10.S2. HEATING OF THE ELECTRON RESERVOIR AS A FUNCTION OF MICROWAVE BURST TIME

Fig. 10.S5(a) shows a Rabi oscillation of the ground valley-orbit state varying the microwave burst time up to $\approx 160 \mu\text{s}$. We take the offset of a Rabi oscillation in the measured spin-up probability as B and its amplitude as A as shown in Fig. 10.S5(b). The offset B increases with longer microwave burst time, while in Fig. S4(a) there is no change in the amplitude A other than the decrease expected by quasi-static noise, is observed. These results indicate that the microwave bursts heat the electron reservoir.

To quantify this effect, we characterize the spin read-out and initialization fidelities of the excited valley-orbit state (ground valley-orbit state) by three parameters, α_1 , β_1 and γ_1 (α_2 , β_2 and γ_2) Sec. 7.S7. By taking the population of two valley-orbit states as $\epsilon_1 : \epsilon_2$, the amplitude, A , and the offset, B , are expressed with

$$A = \epsilon_2(1 - 2\gamma_2)(1 - \beta_2 - \alpha_2) \quad (10.S12)$$

and

$$B = B_1 + B_2, \quad (10.S13)$$

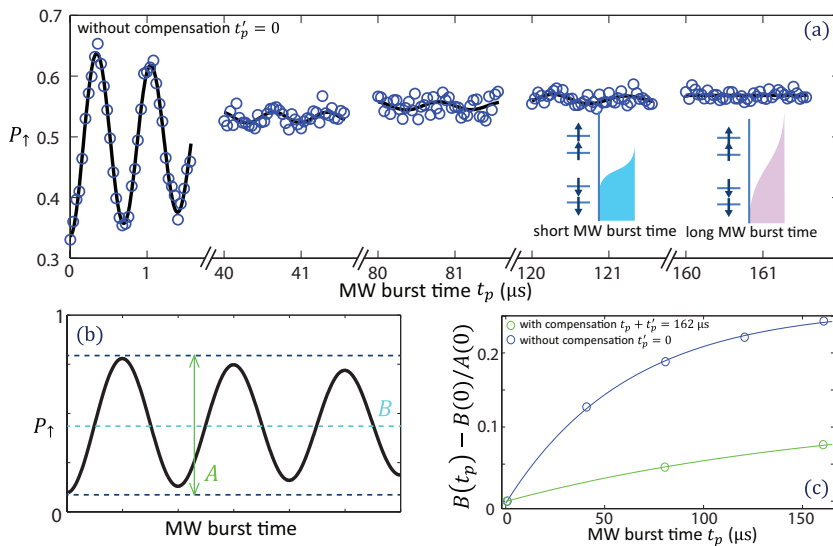


Figure 10.S5: (a) Measured spin-up probability, P_{\uparrow} , showing a Rabi oscillation for the ground valley-orbit state (blue circles) without off-resonance microwaves applied. The black lines show fits with damped cosine curves assuming that the offset, B , can be regarded constant for short time ($1.5 \mu\text{s}$). The insets show schematics of the four energy levels (two spin states and two valley states) in the dot and the electron reservoir for a short microwave burst time and for a long microwave burst time. (b) The offset B and the amplitude A in the measured spin-up probability of a Rabi oscillation. The deviation of the amplitude A from 1 and that of the offset B from 0.5 are due to the initialization and read-out infidelities. (c) The increase of the offset $B(t_p) - B(0)$ normalized by the initial amplitude $A(0)$ as a function of the microwave burst time t_p , without off-resonance microwaves (blue circles), and with off-resonance microwaves (green circles) so that the duration of the microwave bursts is fixed to $162 \mu\text{s}$.

with

$$B_1 = \epsilon_1 [(1 - \beta_1)\gamma_1 + \alpha_1(1 - \gamma_1)] \quad (10.S14)$$

and

$$B_2 = \epsilon_2 \frac{1 - \beta_2 + \alpha_2}{2}. \quad (10.S15)$$

A is determined only by the parameters for the ground valley-orbit state. Since no change in A is observed, we conclude that the read-out and initialization fidelities for the ground valley-orbit state are not significantly affected by increased burst times. For the same reason, B_2 should not greatly change. Thus the increase in B_1 is the dominant source for the increase in B . As shown in the insets of Fig. 10.S5, we assume that the electron temperature of the reservoir is increased with longer microwave burst time. The spin-down excited valley-orbit state is the closest dot energy level to the Fermi level of the reservoir and thus is affected the most by the increase of the electron temperature.

Fig. 10.S5(c) shows the change of the offset, $B(t_p) - B(0)$, normalized by the initial amplitude, $A(0)$, as a function of the microwave burst time. The blue circles are extracted from Fig. 10.S5(a) and green circles are extracted from a similar measurement

as in (a) but with off-resonance microwave excitation applied in order to keep the total duration of the microwave bursts fixed to $162 \mu\text{s}$. The increase of the offset is heavily suppressed by applying the off-resonance microwave but not completely suppressed. This remaining increase may be due to a change in the population between the two valley-orbit states with long microwave burst time. With the total microwave time $< 8 \mu\text{s}$ (condition assumed for the evaluation of the gate fidelities with randomized benchmarking), this remaining increase is small enough to be ignored. Therefore the measured gate fidelities are not affected by this effect. Also for the dynamical decoupling measurement, the longest total microwave duration used is $\approx 8 \mu\text{s}$ and we have not observed any significant difference in the dynamical decoupling coherence time with versus without off-resonance microwave excitation as discussed below.

10.S3. EXTRACT THE NOISE SPECTRAL DENSITY FROM THE ECHO DECAYS

Here we show how the noise spectral density is extracted from the experimental echo decay data. When a dynamical decoupling pulse sequence whose time separation between π pulses is fixed and symmetric i.e. the timing of k th π pulse is $t_k = \frac{t_{\text{wait}}}{N_\pi}$, the filter function $F(\omega, t_{\text{wait}}, N_\pi)$ peaks at $\omega_0 = \frac{2\pi}{4\tau}$ with $\tau = \frac{t_{\text{wait}}}{2N_\pi} (k - \frac{1}{2})$.

Following Bylander et al. (Bylander et al., 2011), if the filter function $F(\omega)$ is sufficiently narrow around ω_0 , we can treat the noise as constant within the bandwidth of the filter function and then Eq. 10.2 is reduced to

$$W(t_{\text{wait}}) \approx S(\omega_0) \int_{-\infty}^{\infty} \frac{1}{2\pi} \frac{F(\omega, t_{\text{wait}}, N_\pi)}{\omega^2} d\omega. \quad (10.S16)$$

According to the numerical simulation we confirmed that Eq. (10.S16) is valid for $N \geq 4$. From Eq. 10.1 we know that

$$W(t_{\text{wait}}) = -\log P(t_{\text{wait}}) \quad (10.S17)$$

and so $S(\omega_0)$ is determined by the logarithm of the normalized echo amplitude at time $t_{\text{wait}} = 2\tau N_\pi$ divided by the integral of the filter function:

$$S\left(\omega_0 = \frac{2\pi}{4\tau}\right) \approx \frac{-\log P(t_{\text{wait}})}{\int_{-\infty}^{\infty} \frac{1}{2\pi} \frac{F(\omega)}{\omega^2} d\omega} = \frac{-2\log P(t_{\text{wait}})}{t_{\text{wait}}}. \quad (10.S18)$$

10.S4. FURTHER ANALYSIS OF THE ECHO DECAYS

The circles in Fig. 10.S6(a,b) and (d,e) show the echo decay curves using $(XY4)^n$ and XY8 pulse sequences, respectively (the same data as in Fig. 10.3(a)). In the main text, we fitted the echo data to Eq. 10.1 with Eq. 10.2 and Eq. 10.5 keeping α fixed to 3. Here, we explore alternative ways of fittings. The solid lines in Fig. 10.S6(a,d) are fits using Eq. 10.4 with α and T_2 as fitting parameters. In Fig. 10.S6(a), $\alpha = 1.14, 1.64$ and 2.22 and $T_2 = 83.6, 149$ and $320 \mu\text{s}$ are obtained for $N_\pi = 4, 16$ and 64 , respectively. In Fig. 10.S6(d), $\alpha = 1.50, 1.59, 1.82, 1.85, 2.03, 2.31$ and 2.38 and $T_2 = 72.7, 122, 159, 239, 280, 333$ and $378 \mu\text{s}$ are obtained for $N_\pi = 1, 8, 16, 32, 48, 64$ and 80 respectively. α becomes larger with higher

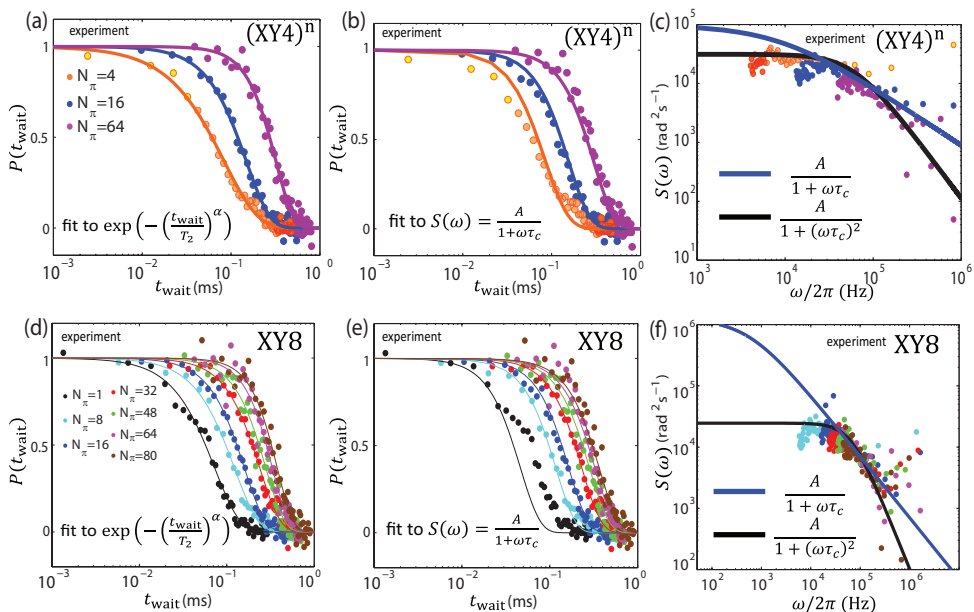


Figure 10.S6: Results of different fits of echo decay curves for $(XY4)^n$ and XY8 pulse sequences. The circles in (a,b) and in (d,e) show the echo decay curves using $(XY4)^n$ and XY8 pulse sequences, the same data as in Fig. 10.3(a) and (b), respectively. (a,d) The solid lines are the fits using Eq. 10.4 with α and T_2 as fitting parameters. The experimental data shown with circles in (a-d) are normalized according to these fits. (b,e) The solid lines are the numerical fits using Eq. 10.1 with Eq. 10.2 and Eq. 10.5 for $\alpha = 2$. See the text for the fitting results. (c,f) The circles show the noise spectrum extracted from the experimental data of $(XY4)^n$ and XY8, respectively. The blue solid lines present Eq. 10.5 for $\alpha = 2$ with A and τ_c obtained from the fits in (b,e). The black solid lines present Eq. 10.5 for $\alpha = 3$ with A and τ_c obtained from the fits shown in Fig. 10.3(a,b). (a-c) The decay curve for $N_\pi = 4$ and the noise spectrum extracted from this decay curve are shown with 3 different colored circles: yellow, orange and strong orange for short, middle and long waiting time, respectively, in order to demonstrate which parts of decay data correspond to the extracted spectrum noise.

numbers of π pulses because the echo decay curve becomes determined more by the decaying parts of the noise spectrum rather than the flat part.

The solid lines in Fig. 10.S6(b,e) are fits using Eq. 10.1 with a numerical integration of Eq. 10.2 and Eq. 10.5 for $\alpha = 2$. The fits yield $A = (9.8 \pm 4.7) \cdot 10^4 \text{ rad}^2 \text{ s}^{-1}$ in (b) and $\tau_c = 17.4 \pm 8.29 \mu\text{s}$ and $A = (124.5 \pm 827) \cdot 10^4 \text{ rad}^2 \text{ s}^{-1}$ and $\tau_c = 280 \pm 18.7 \mu\text{s}$ in (e).

The circles in Fig. 10.S6(c) and (f) show the noise spectrum extracted from the experimental data of $(XY4)^n$ and XY8, respectively. The blue solid lines in Fig. 10.S6(c) and (f) present Eq. 10.5 for $\alpha = 2$ with A and τ_c obtained from fitting the decay curves in Fig. 10.S6(b) and (e), respectively. The black solid line in Fig. 10.S6(c) (Fig. 10.S6(f)) shows Eq. 10.5 for $\alpha = 3$ with $A = 2.5 \pm 0.2 \cdot 10^4 \text{ rad}^2 \text{ s}^{-1}$ and $\tau_c = 2.46 \pm 0.17 \mu\text{s}$ ($A = 3.1 \pm 0.2 \cdot 10^4 \text{ rad}^2 \text{ s}^{-1}$ and $\tau_c = 2.64 \pm 0.19 \mu\text{s}$), which are obtained from the fitting of the decay curves using the analytical expression as shown in Fig. 10.3(a) (Fig. 10.3(b)). Furthermore we found that the result of the fitting using the numerical integration of Eq. 10.5 for $\alpha = 3$ coincides with that of the fit using the analytical expression. We conclude that Eq. 10.5 with $\alpha = 3$ (Lorentian spectrum) captures the echo decay data for

a wider frequency range than with $\alpha = 2$.

10.S5. GENERATION OF NOISE FOR THE NUMERICAL SIMULATIONS

In this section, we explain how the noise fluctuation, $\beta(t) = \gamma_e \delta b'(t)$, which exhibits a spectral density $S(\omega)$, is generated. We assume that $\beta(t)$ is constant for a short time Δt . We first generate $u^\alpha(t_i)$, discrete points of a noisy time trace corresponding to a white noise spectrum, with the mean $E = 0$ and the standard deviation $\sigma_0 = 1$, where α indexes a different set of noise sequence (different set of measurement) and $t_i = i \Delta t$ ($i = 1, 2, \dots, N$) using the Mathematica function `RandomVariate[NormalDistribution[E, σ_0]]`.

The discrete Fourier transform of $u^\alpha(t_i)$ is defined as

$$\tilde{u}^\alpha(\omega_j) = \frac{1}{\sqrt{N}} \sum_i u^\alpha(t_i) \exp(-i\omega_j t_i) \quad (10.S19)$$

with $\omega_j = \frac{2\pi j}{\Delta t N}$.

To obtain a discrete time trace $\beta(t)$ corresponding to the spectrum density $S(\omega)$, we take the inverse Fourier transform of the product of $\tilde{u}^\alpha(\omega_j)$ and $\sqrt{S'(\omega_j)}$:

$$\beta_l^\alpha = \beta^\alpha(t_l) = \sum_{j=1}^N \frac{1}{\sqrt{N}} \tilde{u}^\alpha(\omega_j) \sqrt{S'(\omega_j)} \exp(i\omega_j t_l), \quad (10.S20)$$

where $t_l = l \Delta t$ and $S'(\omega_j)$ corresponds to $S(\omega_j)/\Delta t$ folded about $\omega_j = N/2 + 1$:

$$S'(\omega_j) = \begin{cases} S(\omega_j)/\Delta t & j = 1, 2, \dots, N/2 + 1 \\ S(\omega_{N+2-j})/\Delta t & j = N/2 + 2, \dots, N \end{cases}. \quad (10.S21)$$

10.S6. METHOD OF THE NUMERICAL SIMULATION

In Sec. 10.S1, the quantization axis (\sim the direction of the external magnetic field) is taken as x axis to be consistent with the coordinate on the device in Fig. 10.1 but in this section we take the quantization axis as z axis, in the same way as Ch. 4.

The two-level Hamiltonian describing a single spin under microwave excitation $\omega_1 \sin(\omega_0 t + \phi)$, setting $\hbar = 1$, can be written in the rotating frame of its Larmor frequency ω_0 as

$$H_R(t) = \omega_1(t) \left(\frac{\sigma_x}{2} \cos \phi(t) - \frac{\sigma_y}{2} \sin \phi(t) \right) + \eta(t) \frac{\sigma_z}{2} \quad (10.S22)$$

with $\eta(t) = \gamma_e \delta b(t)$ and $\delta b(t)$ a fluctuating magnetic field along the same direction as the quantization axis, \hat{z} . We take ω_1 and ϕ to be a function of time since we turn on and turn off the microwave excitation and change the microwave phase according to the quantum gates.

Here we treat the evolution of the density operator according to Eq. (10.S22) numerically, assuming that $H_R(t)$ can be considered as constant for a short time Δt :

$$H_{Ri}(t_i) = \omega_{1i} \left(\frac{\sigma_x}{2} \cos \phi_i - \frac{\sigma_y}{2} \sin \phi_i \right) + \eta_i \frac{\sigma_z}{2}, \quad (10.S23)$$

with $t_i = i\Delta t$. Then the density operator at time $t = n\Delta t$ becomes

$$\rho(n\Delta t) = \langle \mathcal{O}_{i=1}^n \mathcal{U}_i(\rho_0) \rangle_\alpha = \frac{1}{M} \sum_\alpha [\mathcal{O}_{i=1}^n \mathcal{U}_i^\alpha(\rho_0)], \quad (10.S24)$$

where ρ_0 is the initial state and \mathcal{U}_i is the superoperator representation:

$$\mathcal{U}_i(\rho) = U_i \rho U_i^\dagger \quad (10.S25)$$

$$\mathcal{O}_{i=1}^n \mathcal{U}_i(\rho) = \mathcal{U}_n \circ \dots \circ \mathcal{U}_3 \circ \mathcal{U}_2 \circ \mathcal{U}_1(\rho) = U_n \dots U_3 U_2 U_1 \rho U_1^\dagger U_2^\dagger U_3^\dagger \dots U_n^\dagger \quad (10.S26)$$

with

$$U_i = \exp(-iH_R(t_i)\Delta t). \quad (10.S27)$$

The ω_{1i} is a step function with the value of the Rabi frequency ω_1 : it is set to ω_1 when microwaves are applied and 0 otherwise. ϕ_i is set depending on the phase of the applied microwave. η_i is the sum of the static noise β_0^α and the high-frequency noise β_i^α :

$$\eta_i^\alpha = \beta_0^\alpha + \beta_i^\alpha, \quad (10.S28)$$

where β_0^α has a Gaussian distribution with standard deviation 0.268 MHz (FWHM = 0.63 MHz) and β_i^α is generated by Eq. (10.S20) with $S(\omega) = \frac{A}{1+(\omega\tau_c)^2}$, $A = 2.5 \cdot 10^4 \text{ rad}^2 \text{ s}^{-1}$ and $\tau_c = 2.46 \mu\text{s}$ as discussed in the main text. In Eq. 10.S28, we explicitly write that η gives a different value with different α . The simulations for randomized benchmarking and dynamical decoupling were performed with $M = 1000$, $\Delta t = 5 \text{ ns}$, $N = 200000$, $\omega_1 = \frac{2\pi}{360\text{ns}}$ unless otherwise stated. From $\Delta t = 5 \text{ ns}$, the highest frequency taken into account for β_i^α is 200 MHz and from $N \cdot \Delta t = 1 \text{ ms}$, the lowest frequency is 1 kHz. The frequency range of 1 kHz-200 MHz is a larger range than the one explored with the dynamical decoupling experimentally.

10.S7. NUMERICAL SIMULATION FOR RANDOMIZED BENCHMARKING

The main results of the simulation are shown in the main text.

Here the average gate fidelity for a single gate ($m = 1$) with the same noise used for Fig. 10.4(b) is calculated. The initial quantum state ρ_0 , after undergoing a depolarizing channel produced by applying one set of imperfect Clifford gates and perfect inverse Clifford gates, becomes

$$\rho = \frac{1}{24} \sum_{i=1}^{24} \mathcal{C}_i^{\text{ideal}\dagger} \circ \mathcal{C}_i^{\text{real}}(\rho_0) = p\rho_0 + (1-p)\frac{\mathbb{1}}{2}, \quad (10.S29)$$

where $\mathcal{C}_i^{\text{ideal}}$ is the superoperator of a perfect Clifford gate without noise and $\mathcal{C}_i^{\text{real}}$ is the superoperator of an imperfect Clifford gate affected by the noise described by Eq. (10.S28).

By taking the POVM operator as $E = |\uparrow\rangle\langle\uparrow|$ and $\rho_0 = |\downarrow\rangle\langle\downarrow|$ ², the measured spin-up probability becomes

$$P_{\uparrow} = \text{Tr}[E\rho] = \text{Tr}\left[|\uparrow\rangle\langle\uparrow|\left(p|\downarrow\rangle\langle\downarrow| + (1-p)\frac{\mathbb{1}}{2}\right)\right] = \frac{1-p}{2}. \quad (10.S30)$$

Finally the average gate fidelity for an isolated gate ($m = 1$) is calculated as $1 - P_{\uparrow}/1.875 = 97.8\%$ (There are 45 single qubit gates used across 24 Cliffords (Barends *et al.*, 2014). In order to obtain the average gate fidelity of a single qubit gate, the error is divided by 45/24.), which is lower than the average gate fidelity per single gate $\approx 99\%$ obtained by the fits to the curves in Fig. 10.4(a,b), which is the averaged gate fidelity when several gates are concatenated ($m = 2$ to 10). The improvement of the gate fidelity with a higher number of gates stems from the fact that some RB sequences have the effect of partial error suppression of low-frequency noise (Ball *et al.*, 2015; Epstein *et al.*, 2014). We consider the averaged gate fidelity over the gates for $m = 2$ to 10 as the fidelity of interest because the average gate fidelity per single gate for $m = 1$ cannot be measured by randomized benchmarking and since more than 2 gates are usually applied in the real quantum computation.

Fig. 10.S7 shows the results of the numerical simulations of the spin-up probability with spin-up as the target state $P_{\uparrow}^{|\uparrow\rangle}$ including only the high-frequency noise $\delta b'(t)$ (red circles), only the (quasi-)static noise δb_0 (green squares), and both $\delta b_0 + \delta b'(t)$ (blue circles). With only the high-frequency noise, the decay is very slow. In this case, the flat region of the Lorentian spectrum mainly contributes to the gate errors and thus the noise can be regarded as uncorrelated, which results in the whole decay curve following a single power law and the extracted average gate fidelity per single gate from the fit of $ap^m + 0.5$ is $> 99.99\%$, which means that the high-frequency noise $\delta b'(t)$ would not limit the gate fidelity with the isotopically purified Si sample. The decay curve with only the (quasi-)static noise and that with the combination of two show almost the same decay. It indicates that the (quasi-)static noise is mainly responsible for the simulated and measured gate errors.

10.S8. NUMERICAL SIMULATION FOR DYNAMICAL DECOUPLING

We have used 3 different types of dynamical decoupling pulse sequences: XY4 (Maudsley, 1986), XY8 (Gullion, Baker, and Conradi, 1990) and $(XY4)^n$ (Álvarez, Souza, and Suter, 2012). CPMG timing is used as the time interval between pulses for all the three sequences and so their filter functions are the same, while the phases of the π pulses,

²In fact, not depending on how E and ρ_0 are taken, the calculated gate fidelity should be the same.

simulation and the experiment. The fitted lines to the decay curves for XY4, XY8 and $(XY4)^n$ match with each other very well and the T_2 time (see caption in Fig. 10.S8) is almost equal for all the sequences. This is expected given that the filter function is the same. However the standard errors on the fitting parameters are more than 10 times higher with XY4 than with $(XY4)^n$, due to the reduced visibility and to the oscillations for short t_{wait} . In conclusion, even if it is still possible to determine T_2 in the presence of pulse imperfections, one needs to use a pulse sequence which is robust to the pulse imperfections like $(XY4)^n$ in order to determine T_2 with high accuracy. In addition, in terms of quantum information processing, it is important to preserve a quantum state. $(XY4)^n$ is the preferred pulse sequence in this sense since it succeeds in filtering out the high-frequency noise while canceling out the pulse errors due to the low-frequency noise at the same time.

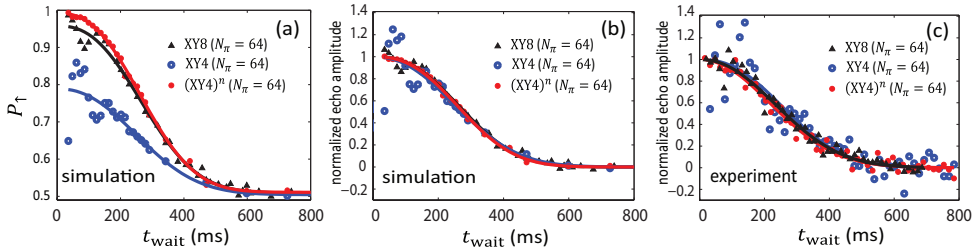


Figure 10.S8: (a-c) the echo decays with XY4, XY8 and $(XY4)^n$ for $N_\pi = 64$ (a) echo decays calculated from the numerical simulation. The solid lines are the fits with Eq. 10.4. $T_2 = 320 \pm 92$, 325 ± 12 and $319 \pm 7 \mu\text{s}$ and $\alpha = 2.28 \pm 1.78$, 2.50 ± 0.30 and 2.53 ± 0.18 are obtained, for XY4, XY8 and $(XY4)^n$, respectively. (b) The echo decay data are normalized according to the fits with Eq. 10.4. (c) Measured echo decay normalized according to the fits with Eq. 10.4.

In Fig. 10.S9(a), the simulated echo decays for Hahn ($N_\pi = 1$), XY4 ($N_\pi = 4$) and XY8 ($N_\pi = 8$) are shown. Fig. 10.S9(b,c) show the noise spectrum extracted from the simulated echo decay curves presented in Fig. 10.S8(b) and Fig. 10.S9(a) using the same methods as used in Fig. 10.3(d).

The solid black lines in Figs. S8(b) and (c) represents the noise spectrum used to produce the echo decays in the numerical simulations in Fig. S8(a). The deviation of the extracted noise spectrum from the input noise spectrum is due to the oscillations seen in the echo decays and normalization problems. The noise spectrum extracted from $(XY4)^n$ echo decay follows the input noise spectrum the best. In the region of $10^5 < \omega/2\pi$, the deviations of the extracted noise for XY4 ($N_\pi = 4$) and XY8 ($N_\pi = 8$) are above the input noise spectrum (Fig. 10.S9(b,c)). This is related to normalization problems. The inset of Fig. 10.S9(a) shows that the data points for each echo decay are below each respective fitted line for short waiting times. This results in an extracted noise spectrum that is higher than the input noise spectrum, in particular for the high frequency range (as seen in the shaded region in Fig. 10.S9(b)). This problem arises from the difficulty of proper normalization of the simulated data points and for the artifact of the oscillations at short t_{wait} . Thus even if at higher frequencies, Eq. [3] with $\alpha \sim 2$ seems to work better to capture the power spectrum in Fig. 10.3(d) of the main text, it happens due to this normalization problem. Besides that, there is another normalization problem. When

the echo decays are normalized, some data points where t_{wait} is short (for example, 4 points for XY4 ($N_\pi = 64$) and 2 points for XY8 ($N_\pi = 64$),) of Fig. 10.S8(b) go above 1. In these cases, for the logarithmic plot in Fig. 10.S9(b), $-\log P(t_{\text{wait}})$ in Eq. (10.S18) is replaced with $|\log P(t_{\text{wait}})|$. These points are not reliable.

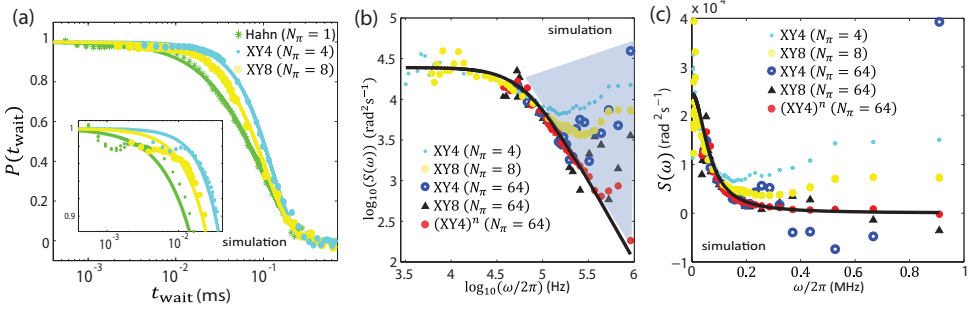


Figure 10.S9: (a) Simulated echo decays with Hahn ($N_\pi = 1$), XY4 ($N_\pi = 4$) and XY8 ($N_\pi = 8$). The inset shows the zoom-up of the beginning of the decays. The solid lines present the fits with Eq. 10.4. (b,c) Noise spectrum extracted from numerical simulated echo decays using XY4 ($N_\pi = 4$), XY8 ($N_\pi = 8$), XY4 ($N_\pi = 64$), XY8 ($N_\pi = 64$) and $(XY4)^n$ ($N_\pi = 64$) pulse sequences. The solid black line is the noise spectrum which is used in the simulation to produce the echo decays. In (b), decimal logarithmic scales are used along x and y axis.

10.S9. ADDITIONAL DATA FOR DYNAMICAL DECOUPLING

Here we provide additional dynamical decoupling data. First, the blue circles in Fig. 10.S10 show data analogous to purple circles in Fig. 10.3(c) but with an off-resonance microwave burst added in order to keep the total microwave burst time fixed. The T_2 does not significantly change when adding the off-resonance microwave. Second, we show as black circles the echo decay using the XY4 pulse sequence. The green line and pink circles are the same as in Fig. 10.3(c). The pink circles show T_2 with the number of π pulses, 96, 112 and 128 for $\alpha = 2$. In Fig. 10.S10(b), the red circles shows the decay curve with $N_\pi = 128$ and the red line shows the fit with Eq. 10.4 for $\alpha = 2$. From this fit, $T_2 = 404 \pm 34 \mu\text{s}$ is obtained. $(\bullet)^R$ stands for applying the pulse sequence (\bullet) in reverse order. We note that extending the $(XY4)^n$ pulse sequence beyond $N_\pi = 64$ would take us immediately to 256 pulses. The pulse sequences used for $N_\pi = 96$ is $(XY4)^2 + (XY4)^3 + ((XY4)^2)^R$, for $N_\pi = 112$ is repeating $(XY4)^2$ 7 times, and for $N_\pi = 128$ is $(XY4)^3 + ((XY4)^3)^R$.

10.S10. ORIGIN OF THE HIGH-FREQUENCY NOISE SPECTRUM

In the main text, we state that the measured high-frequency noise can be explained by a two-level magnetic field fluctuation of $\pm 0.4 \mu\text{T}$. If this fluctuation arises from a two-level charge fluctuator that shifts the dot position in the micromagnet gradient, it would correspond to a $\pm 4 \text{ pm}$ shift back and forth in the dot position. In this section, we consider other possible descriptions for or origins of the measured high-frequency noise.

First, we consider whether noise from the voltage source can be responsible for the measured high-frequency part of the noise spectrum. We consider this gate voltage noise Gaussian. Gaussian noise with a Lorentzian spectrum gives the same noise spectrum as

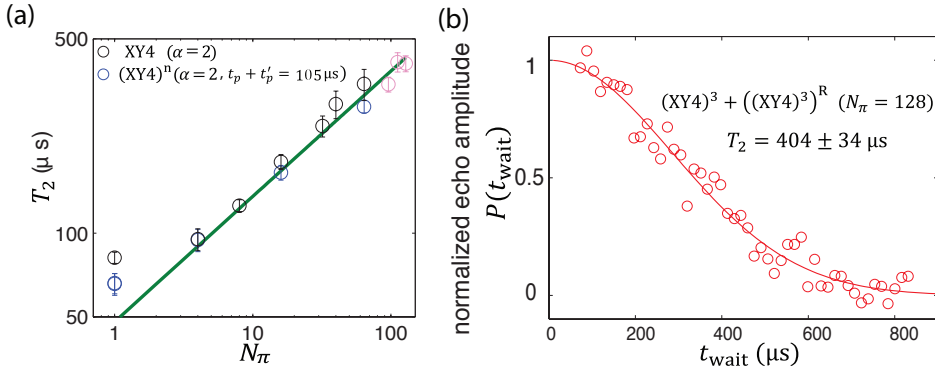


Figure 10.S10: (a) Coherence time, T_2 , as a function of the number of π pulses using XY8 without (black circles) and with (blue circles) off-resonance microwave. The green line is the same as in Fig. 10.3(c). (b) Echo decay with 128 π pulses. The fit with a Gaussian curve (red line) gives $T_2 \approx 400 \mu\text{s}$.

RTN if the standard deviation of the Gaussian noise equals half the amplitude of the random telegraph noise (RTN). Thus, here we consider Gaussian noise with standard deviation $0.4 \mu\text{T}$. From a separate measurement, we measured 0.55 MHz/mV as the shift in resonance frequency resulting from changing the voltage on the gate that is coupled most strongly to the dot. Using this conversion factor, $0.4 \mu\text{T}$ corresponds to $\sim 20 \mu\text{V}$ in this gate voltage. The specification of the voltage source fluctuations at room temperature is $8 \mu\text{V}$ (standard deviation), which is of the same order of magnitude as the estimated gate-voltage fluctuation. Furthermore, there is an additional effect of voltage noise on the other gates. However, the wires connecting the sources to the gates are heavily filtered, including with low-pass filters with a cut-off frequency of 20 Hz at the 20 mK stage. The standard deviation of the noise is considerably reduced after those filters. Thus we conclude that it is unlikely that the voltage source is responsible for the measured high-frequency noise.

Secondly, we compare the measured high-frequency magnetic noise spectrum in this work with the magnetic noise expected when combining the micromagnet gradient and the high-frequency charge noise spectrum $S_c(\omega)$ reported for Si/SiGe quantum dots (Eng *et al.*, 2015) and GaAs/AlGaAs quantum dots (Dial *et al.*, 2013). Using the conversion factor $\frac{df}{dV} = 0.55 \text{ MHz/mV}$, we plot $S(\omega) = \left(\frac{df}{dV}\right)^2 S_c(\omega)$ in Fig. 10.S11. For the case of (Eng *et al.*, 2015), this noise spectrum is only slightly smaller than that extracted in the present work. It is thus conceivable that the dynamical decoupling decay is limited by high-frequency charge noise in the presence of the (longitudinal) magnetic field gradient from the micromagnet.

For completeness, the measured T_2^* translates to a 270 kHz (standard deviation) quasi-static magnetic noise. In the main text, we stated that this could be explained by the slowly varying nuclear spins. Following an analogous reasoning as for high-frequency noise, we consider the role of low-frequency charge noise in explaining T_2^* . The standard deviation of the quasi-static charge noise is measured to be $\sim 5 - 300 \mu\text{V}$ depending on the device (Dial *et al.*, 2013; Eng *et al.*, 2015; Petersson *et al.*, 2010; Shi *et al.*, 2013;

Veldhorst *et al.*, 2015b). This corresponds to $\sim 3 - 170$ kHz magnetic noise using the conversion factor $\frac{df}{dV} = 0.55$ MHz/mV. The highest values are almost high enough to be able to explain the T_2^* as well.

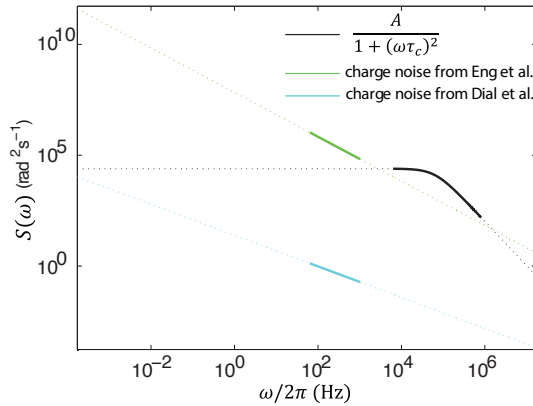


Figure 10.S11: The black line presents Eq. 10.5 for $\alpha = 3$ with A and τ_c obtained from the fits show in Fig. 10.3(a,b). The green line (the light blue line) presents the charge noise result measured in (Eng *et al.*, 2015) ((Dial *et al.*, 2013)) translated into magnetic noise via 0.55 MHz/mV. The solid lines show the measured frequency region and the dotted lines show the extrapolated frequency region.

10.S11. ESTIMATION OF THE VALLEY-ORBIT SPLITTING

It is difficult to estimate the valley-orbit splitting in the current work. We deduced that the valley-orbit splitting became higher from the fact that the valley-scattering slowed down and the population of the ground valley-orbit state increased compared to the previous work (Ch. 7-9).

We assume that the excited valley-orbit state is populated during the initialization stage, i.e., electrons are initialized to the excited valley-orbit state with 20% probability. If we can furthermore assume that only electron tunneling from the reservoir to the spin-down ground and excited valley-orbit states are relevant (i.e., we can ignore electron tunnelings from dot to the reservoir and from the reservoir to the spin-up states) and that the spin-down ground and excited valley-orbit states are both deep in the Coulomb blockade regime, we can estimate that the valley-orbit splitting is around 12 GHz (please see below for the details of this estimate). However, this assumption may not be valid for the initialization position used in the experiment. The electron temperature of the reservoir is around 3 GHz (150 mK) and the Zeeman splitting is around 19 GHz. Given these numbers together with the hypothetical valley-orbit splitting 12 GHz, all the three numbers are very close and we can not find an initialization position where all the above assumptions are satisfied.

In order to quantify the valley-orbit splitting correctly when the above assumption is not valid, we need to solve the rate equations considering electron tunneling from the reservoir to the excited valley-orbit state, from the reservoir to the ground valley-orbit state, from the excited valley-orbit state to the reservoir and from the ground valley-orbit

state to the reservoir. In this case, there are too many parameters which are difficult to estimate from our measurements to obtain a reliable estimate of the valley-orbit splitting.

ESTIMATION OF THE VALLEY-ORBIT SPLITTING UNDER THE ASSUMPTION THAT ONLY ELECTRON TUNNELINGS FROM THE RESERVOIR TO THE SPIN-DOWN GROUND AND EXCITED VALLEY-ORBIT STATES ARE RELEVANT

If we can assume that only electron tunneling from the reservoir to the spin-down ground and excited valley-orbit states are relevant, the rate equations for the populations of the spin-down, ground and excited valley-orbit states become

$$\epsilon_{\downarrow v_+} = \frac{\Gamma_{\downarrow v_+}}{\Gamma_{\downarrow v_+} + \Gamma_{\downarrow v_-}} (1 - \exp(-(\Gamma_{\downarrow v_+} + \Gamma_{\downarrow v_-})t)), \quad (10.S34)$$

$$\epsilon_{\downarrow v_-} = \frac{\Gamma_{\downarrow v_-}}{\Gamma_{\downarrow v_+} + \Gamma_{\downarrow v_-}} (1 - \exp(-(\Gamma_{\downarrow v_+} + \Gamma_{\downarrow v_-})t)), \quad (10.S35)$$

where $\Gamma_{\downarrow v_i}$ is the tunneling rate from the reservoir to the spin-down excited valley-orbit state ($i = v_+$) or to the spin-down ground valley-orbit state ($i = v_-$), and t is the time spent during the initialization stage.

After spending a long enough time ($t \gg \frac{1}{\Gamma_{\downarrow v_+} + \Gamma_{\downarrow v_-}}$) at the initialization stage, the population ratio of the excited valley-orbit state to the ground valley-orbit state is reduced to

$$\frac{\epsilon_{\downarrow v_+}}{\epsilon_{\downarrow v_-}} \sim \frac{\Gamma_{\downarrow v_+}}{\Gamma_{\downarrow v_-}}. \quad (10.S36)$$

The tunneling rate is given by the convolution of the Fermi-Dirac distribution, the energy dependent tunneling function and transmission function (Amasha *et al.*, 2008; Kawakami *et al.*, 2013; Simmons *et al.*, 2011b). Assuming that the transmission function is approximated to be a delta function around the dot level, the tunneling rate is reduced to

$$\Gamma_{\downarrow v_i} = \frac{\Gamma_i \exp\left(-\frac{V}{E_i}\right)}{1 + \exp\left(-\frac{V}{k_B T}\right)}, \quad (10.S37)$$

which is a function of the detuning of the dot level with respect to the Fermi level of the reservoir V and, where $i = v_+, v_-$, E_i is the linearized energy dependent tunneling coefficient that relates to the transparency of the barrier (Amasha *et al.*, 2008; Simmons *et al.*, 2011b), and T is the electron temperature of the reservoir.

In the gate configuration used in Ch. 7-9, we have measured the valley-orbit splitting to be $E_V \sim 28 \mu\text{eV}$ (~ 7 GHz). (In Ch. 9, we explain how we measured this valley-orbit splitting. Please note that we were not able to measure the valley-orbit splitting in the same way in the gate configuration of this work.) The population ratio was measured to be $\frac{\epsilon_{\downarrow v_+}}{\epsilon_{\downarrow v_-}} = \frac{30}{70}$ and the electron temperature of the reservoir was measured to be $T \sim 150$ mK (~ 3 GHz).

If we assume that $\Gamma_{v_-} = \Gamma_{v_+} = \Gamma$ and $E_{v_-} = E_{v_+} = E$, the equation above is reduced to

$$\Gamma_{\downarrow v_+}(V) = \Gamma_{\downarrow v_-} = \Gamma_l = \frac{\Gamma \exp\left(-\frac{V}{E}\right)}{1 + \exp\left(-\frac{V}{k_B T}\right)}. \quad (10.S38)$$

This assumption is validated by the fact that we were not able to distinguish two valley states by measuring the electron tunneling rate from the reservoir to any dot level as a function of a gate voltage. Using the equation above, the population ratio between two valley-orbit states is simplified to

$$\frac{\epsilon_{\downarrow v_+}}{\epsilon_{\downarrow v_-}} = \frac{\Gamma_{\downarrow v_+}(v + E_V)}{\Gamma_{\downarrow v_-}(v)}. \quad (10.S39)$$

If both the spin-down, ground and excited valley-orbit states are deep in the Coulomb blockade ($v \gg k_B T$), it can be further approximated to be

$$\frac{\epsilon_{\downarrow v_+}}{\epsilon_{\downarrow v_-}} \sim \exp\left(\left(\frac{1}{E} - \frac{1}{k_B T}\right)E_V\right). \quad (10.S40)$$

From this equation, we obtain a linearized energy dependent tunneling coefficient for the gate configuration used in Ch. 7-9, $E \sim 21 \mu\text{eV}$.

We assume that the linearized energy dependent tunneling coefficient is the same for the gate configuration used in Ch. 7-9 and this work. This assumption is validated by the fact that the electron tunneling rate from the reservoir to any dot level changes as a function of a gate voltage in a similar way for both the gate configuration used in Ch. 7-9 and this work. Finally, in order to obtain $\frac{\epsilon_{\downarrow v_+}}{\epsilon_{\downarrow v_-}} = \frac{20}{80}$, using $E \sim 21 \mu\text{eV}$ and the equation above, the valley-orbit splitting should be $E_V \sim 47 \mu\text{eV}$ ($\sim 12 \text{ GHz}$).

11

CONCLUSIONS AND OUTLOOK

In this chapter we summarize the work presented in this thesis, together with the progress the community as a whole has made recently towards the implementation of qubits using single electron spins in Si. Future directions and work to be done towards the realization of a quantum computer using these qubits is also discussed.

11.1. CONCLUSION

The question we had 5 years ago was whether, given they are a promising candidate as a qubit in theory, single electron spins in Si/SiGe quantum dots could be experimentally implemented as qubits. The experiments shown in this thesis partially answered "yes". At least we satisfied some of necessary conditions towards the realization of a quantum computer. For example, the demonstration of a universal 1-qubit gate and its high fidelity shown in Ch. 7 and Ch. 10 is a major first step towards the achievement of a larger scale Si quantum computer.

This achievement relies on the detection and read-out techniques of spin states developed in GaAs/AlGaAs quantum dots and newly developed defect-free and noise less Si/SiGe devices. The last technical breakthrough that was needed after overcoming earlier problems with leaky gates and unreliable contacts, was moving from doped Si/SiGe heterostructures to undoped Si/SiGe heterostructures (Borselli *et al.*, 2011). It dramatically reduced charge noise in Si/SiGe heterostructures, which had been the main concern for realizing qubits in Si/SiGe quantum dots.

Our experiments brought potential problems of using single electron spins in Si/SiGe quantum dots as qubits to light. One example amongst others is leakage to an excited valley state as discussed in Ch. 7 and Ch. 9.

We also explored the coherent manipulation of a spin state using second harmonic driving in Ch. 8 and the inter-valley inter-spin transition in Ch. 9. The former showed as high-quality coherent oscillations as the fundamental harmonic driving and thus it can be used for a qubit manipulation if an anharmonicity can be engineered at our disposal. However the latter did not show a coherent oscillation due to a large hybridization between valley states and orbital states. This result showed rich solid state physics in Si, but

did not come up to the expectation of making use of valley states as qubit states instead of regarding it as a nuisance (Culcer *et al.*, 2012; Rohling and Burkard, 2012).

In the following section, we discuss more details on our achievements and outlooks in terms of using single electron spins in Si/SiGe quantum dots as qubits.

11.2. DiVINCENZO CRITERIA

In this section, we interpret the experimental results shown in this thesis in light of the DiVincenzo criteria which we introduced in Sec. 1.2.

(1) Scalable system with well-defined qubits

In Ch. 7 and Ch. 10, we demonstrated the realization of a qubit in an isotopically natural Si/SiGe quantum dot using electrical control. As for the scalability, up to 3 Si/SiGe quantum dots in the few-electron regime (Eng *et al.*, 2015) and individual electrical control of 2 qubits (Takeda *et al.*, 2016) are experimentally demonstrated. In a similar system, in SiMOS quantum dots, individual control of 2 qubits with magnetic control and a 2-qubit gate using the exchange interaction between 2 electrons is demonstrated (Veldhorst *et al.*, 2015b).

We have observed leakage to valley excited states due to the small valley splitting compared to the electron temperature of the Fermi reservoir, which makes the effective initialization fidelity lower (Ch. 7 and Ch. 10) and the coherence time shorter (Ch. 7) than with the larger valley splitting. While we were not able to increase the valley splitting in a systematic way, it has been experimentally demonstrated that the valley splitting can be made larger by changing the voltages on the surface gates in SiMOS (Yang *et al.*, 2013) and in Si/SiGe (Takeda, 2015) (Ch. 10).

(2) Initialization to a pure state

In Ch. 7 we demonstrated that the initialization fidelity to a spin-down state is 95%. Due to non-zero initialization to a valley excited state, the initialization fidelity to a spin-down valley ground state is $\sim 70\%$ for the experiment in Ch. 7 and $\sim 80\%$ for the experiment in Ch. 10. As discussed in Ch. 1, low purity of the initial state downgrades the speed of quantum calculation. If the purity is so low that no entanglement exists during the calculation, the quantum calculation cannot be faster than the classical calculation.

Besides the purity, we should consider the initialization speed. The initialization currently takes ~ 4 to 5 ms. The initialization time should be shortened for the ancilla qubits used in quantum error correction to a time shorter than the dephasing time.

(3) Universal set of quantum gates

We have demonstrated a universal 1-qubit gate (Ch. 7) and measured the average 1-qubit gate fidelity $\sim 99\%$ for 1-qubit gate (Ch. 10), which is just above the threshold for topological quantum error correction (Fowler *et al.*, 2012).

Another group showed that, using an isotopically natural Si/SiGe quantum dot (Takeda *et al.*, 2016) as well, an average 1-qubit gate fidelity of $\sim 99.6\%$ for 1-qubit gates was measured with two times longer T_2^* time and 10 times faster Rabi frequency than in our measurement. In an isotopically purified SiMOS quantum dot (Veldhorst *et al.*,

2014), an average 1-qubit gate fidelity $\sim 99.6\%$ for 1-qubit gate was reported with 100 times longer T_2^* and 4 times slower Rabi frequency than in our measurement.

A 2-qubit gate (CNOT) is also demonstrated in an isotopically purified SiMOS quantum dots (Veldhorst *et al.*, 2015b). The gate fidelity of a two-qubit gate is not measured yet but it is expected to be as high as 99%.

(4) Read-out of each qubit state

Our considerations for the read-out fidelity and speed are similar to the initialization fidelity and speed.

In Ch. 7, we demonstrated a read-out fidelity of 95%. In this case, it costs 3 repetitions of the measurement to obtain 99% fidelity.

As for the speed, the read-out takes ~ 4 to 5 ms. This time should be shortened for the ancilla qubits used in quantum error correction for the same reason as the initialization time needs to be shortened.

(5) Long coherence times

In Ch. 7, we measured the intrinsic coherence time in an isotopically natural Si/SiGe quantum dot $T_2^* \sim 1 \mu\text{s}$ and it can be extended to $T_2 \sim 40 \mu\text{s}$ with Hahn echo technique. Presumably, T_2 time was limited by the switching between two valley states (Sec. 7.S13) and Hahn echo decay was exponential. Later, in Ch. 10, we retuned the configuration of the gate voltages of the same sample and presumably the switching between two valley states became slower. Thanks to this improvement, we succeeded in demonstrating that the coherence time can be extended up to $T_2 \sim 400 \mu\text{s}$ using dynamical decoupling techniques. In the new configuration, the experimental demonstration of the extension of the coherence time was limited by the imperfection of microwave pulses. Takeda *et al.*, found $T_2^* \sim 2 \mu\text{s}$ in an isotopically natural Si/SiGe quantum (Takeda *et al.*, 2016). Their dot size may be four times larger than ours (Eq. 3.43). T_2^* in an isotopically purified SiMOS quantum dot was measured to be $120 \mu\text{s}$ (Veldhorst *et al.*, 2014). The ^{29}Si isotopic ratio in the SiMOS device was reduced ~ 60 times compared to the isotopic ratio in natural Si (reduced from 4.67% to 800ppm), which results in ~ 60 times¹ longer T_2^* . The coherence time was extended up to $T_2 \sim 28$ ms using dynamical decoupling technique in this isotopically purified sample.

(6) and (7) Transfer of a quantum state between stationary and flying qubits & Transmit of flying qubits between specified locations

We did not work for these two criteria in this thesis but these two criteria are important for both the scalability of a quantum computer and the communication of quantum information to build a quantum network.

It might be difficult to physically fit enough number of qubits for a quantum computation on one chip, but transferring a quantum state from a chip to another would allow us to realize a scalable quantum computer. There are many recent theoretical and experimental works towards the demonstration of the coherent quantum state

¹In fact, according to Eq. 3.43, we expect that T_2^* becomes $\sqrt{60}$ times longer with 60 times smaller ^{29}Si isotopic ratio instead of 60 times longer T_2^* for a fixed dot size.

transfer between a qubit on a chip to a photon via superconducting resonator using cavity quantum electrodynamics (Cassidy *et al.*, 2014; Deng *et al.*, 2015; Frey *et al.*, 2012; Hu, Liu, and Nori, 2012; Petersson *et al.*, 2012; Samkharadze *et al.*, 2015).

For the quantum network, there is great interest in using photons to convey quantum information over long distances. However, the photon absorption by fiber-optic cables causes some loss of information. By using quantum repeaters, which can be realized by trapped ions (Brumfiel, 2009) or NV centers in diamond (Bernien *et al.*, 2013), transfer of quantum information is essentially realized by quantum teleportation and the distance that single photons travel can be shortened, which results in less information loss.

11.3. HOW GOOD IS GOOD ENOUGH?

We claim that the control fidelity of a physical qubit should be higher than 99% and we experimentally demonstrated that this condition can be already met for a 1-qubit gate in Ch. 10. We would not have any hope to realize a quantum computer (i.e., any hope to obtain a sufficiently low logical error rate in order to execute Shor's factoring algorithm with a reasonable chance of success (Fowler *et al.*, 2012)) if we had a gate fidelity of 80% unless a lower threshold quantum error correction method is invented, but at the same time, we do not know if a gate fidelity 99% is already good enough. How can we know a good enough number? The same question should be asked for initialization fidelity and initialization speed, read-out fidelity and read-out speed, gate speed, coherence times and e.t.c. A longer coherence time is preferable but how long should it be? How much purity of a quantum state is required in order to avoid a serious slow down in the calculation? In addition to that, these thresholds are correlated to each other (Fowler *et al.*, 2012). If we have a high read-out fidelity, the threshold for the gate fidelity can be relaxed. Do we need to make more efforts to improve the read-out fidelity or the gate fidelity? If we have a high gate fidelity, the number of required qubits is decreased. 10^4 physical qubits are required in order to obtain a target logical error rate of 10^{-14} with the gate fidelity 99%, while "only" 170 physical qubits with the gate fidelity 99.999% for the same logical error rate. Do we need to make more efforts to increase the number of qubits or to improve the gate fidelity? Answering these questions is beyond the scope of this thesis but we hope that in the near future we can come up with a blueprint for a Si quantum computer providing the threshold values for all the elements.

The selling point of a quantum computer is the ability to solve a certain problem which cannot be tackled by a classical computer. The required number of logical qubits depends on the size of the problem to be solved. Another question is what kind of problem should be targeted for the first blueprint of a Si quantum computer. We would propose the factorization of RSA-768. In the next paragraphs, we compare the factorization of RSA-768 using a classical computer and using a quantum computer, while considering how many qubits and how high gate fidelity are required to solve this problem.

A large semiprime which has 232 decimal digits, or 768 bits, (RSA-768)² was factored classically over the span of 2 years (Kleinjung *et al.*, 2010) with a collection of parallel classical computers. In this demonstration, a total of 10^{20} operations were required to

²RSA is the name of one of the first practical public-key cryptosystems.

factor RSA-768.

With a quantum computer not less than 1154 logical qubits are required to factor RSA-768 (Zalka, 2006) without using oversimplifying quantum factoring (Smolin, Smith, and Vargo, 2013). Combining with the fact that 170 physical qubits are required for the physical qubit gate fidelity 99.999% for one logical qubit as discussed above, $\sim 2 \times 10^5$ physical qubits are required. Once you prepare this number of high-fidelity qubits, only 10^6 operations are required to factor RSA-768 with a quantum computer, which means that the problem can be solved in ~ 3 ms with a 1 GHz clock speed and in one year with a 10^{10} times slower clock speed, ~ 0.1 Hz, than that typically used in a nowadays classical computer (see also Fig. 1 of (Van Meter and Horsman, 2013)). Fig. 11.1 shows how fast the number of physical qubits and the average gate fidelity of physical qubits should be increased in the future in order to factorize RSA-768 with a quantum computer within 30 years.

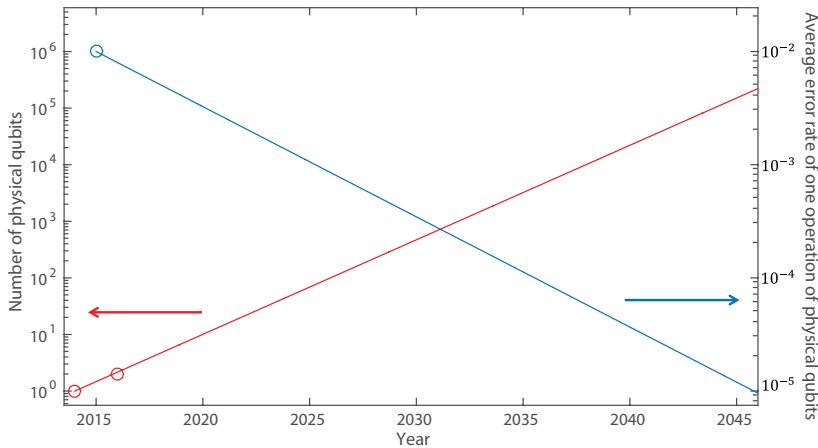


Figure 11.1: Quantum Moore's law required in order to achieve factorization of RSA-768 in 30 years. The red line is the growing line of the number of qubits as a function of year. Two red circles present 1 physical qubit in 2014 (Kawakami *et al.*, 2014) and 2 physical qubits in 2016. The blue line is the falling line of the average error rate of one operation of physical qubits. The blue circle presents 10^{-2} error rate in 2015 (Ch. 10).

11.4. OUTLOOK

Even if, as discussed in the previous section, it is not clear yet which elements should be improved to which extent, in the following we consider the options and difficulties in improving each element.

- Isotopic purification

As already discussed above, the dephasing time T_2^* and T_2 can be extended further by the isotopic purification of the Si substrate to Si atoms which have non-zero nuclear spins (^{28}Si or ^{30}Si). Muhonen *et al.* (2014) reported that the coherence time using the dynamical decoupling (i.e., high-frequency magnetic noise) is not determined by the residual 800ppm ^{29}Si but presumably by the magnetic noise induced

by the superconducting magnets. This experimental result implies that we may also need to be careful with other magnetic noise or electric noise coming from the experimental setup like microwave sources, d.c. electronics, dilution refrigerators, and substrates when we use an isotopically purified sample in order to get maximum benefit from the low concentration of ^{29}Si .

- Reduce the charge noise

As proposed in (Loss and DiVincenzo, 1998), a two-qubit gate is realized using the exchange interaction between two electrons (Veldhorst *et al.*, 2015b). The exchange interaction is very sensitive to the charge noise, which degrades a two-qubit gate fidelity. The ratio of the exchange interaction $J(\epsilon)$ to the standard deviation of the quasi-static charge noise σ_ϵ converted into a magnetic noise $\sigma_\epsilon dJ(\epsilon)/d\epsilon$ is $\frac{J(\epsilon)}{\sigma_\epsilon dJ(\epsilon)/d\epsilon} \sim 100$ in GaAs quantum dots (Dial *et al.*, 2013) and $\frac{J(\epsilon)}{\sigma_\epsilon dJ(\epsilon)/d\epsilon} \sim 40$ in SiMOS quantum dots (Veldhorst *et al.*, 2015b)³, where ϵ is the voltage on one of the surface gates. The fidelity of a two-qubit gate has not been directly measured yet but from this ratio, the fidelity of one operation of a two-qubit gate is expected to be⁴ $\sim 99\%$. In order to increase this ratio for a better two-qubit gate fidelity, we should decrease σ_ϵ , or increase $\frac{J(\epsilon)}{dJ/d\epsilon}$.

GaAs quantum dot	Si quantum dot
8 μV (Dial <i>et al.</i> , 2013)	70 μV (Eng <i>et al.</i> , 2015) (Si/SiGe)
$\sim 100 \mu\text{V}$, 4 μeV (Baart <i>et al.</i> , 2016b)	$\sim 230 \mu\text{V}$ (Ch. 9) ⁵ (Si/SiGe)
3.7 μeV (Petersson <i>et al.</i> , 2012)	6.4 μeV (Wu <i>et al.</i> , 2014) (Si/SiGe)
	$\sim 270 \mu\text{V}$ (Veldhorst <i>et al.</i> , 2015b) (SiMOS)

Table 11.1: Various measured standard deviation of quasi-static charge noise σ_ϵ . The values with the unit μeV are scaled on the chemical potential of a dot and the values with the unit μV are scaled on the voltage on one of the surface gates. The noise in SiMOS quantum dots (Veldhorst *et al.*, 2015b), is slightly higher than the other values in GaAs quantum dots or Si/SiGe quantum dots presumably because the surface gates are closer to the electrons than the other devices.

Table 11.1 presents various measured quasi-static charge noises σ_ϵ in GaAs quantum dots, in SiMOS quantum dots and in Si/SiGe quantum dots. The charge noise in Si quantum dots are not overall worse than that in GaAs quantum dots but it rather depends on devices. The gate dielectric, donors in the substrate, and de-

³In GaAs quantum dots (Dial *et al.*, 2013), $\frac{J}{dJ/d\epsilon} \sim 1 \text{ mV}$, $\sigma_\epsilon \sim 8 \mu\text{V}$ and in SiMOS quantum dots (Veldhorst *et al.*, 2015b), $\frac{J}{dJ/d\epsilon} \sim 10 \text{ mV}$, $\sigma_\epsilon \sim 270 \mu\text{V}$.

⁴Contrary to the case of one-qubit gate as discussed in Ch. 10, we do not expect that the fidelity of a two-qubit gate becomes better with a higher number of two-qubit gates but worse even for a correlated charge noise, since the noise is along the same spin axis as the exchange interaction.

⁵According to Fig. 9.S3 and the discussions in Sec. 9.S3.3, the linewidth of the inter-valley spin-flip resonance peak is $\sigma_f = 2.1 \text{ MHz}$, which corresponds to $T_2^* = 110 \text{ ns}$ using Eq. 4.41. Assuming that this linewidth is determined by the resonance frequency fluctuation due to the valley splitting fluctuation caused by charge noise, using the measured $\frac{df}{d\epsilon} = 9.2 \text{ MHz/mV}$ (Fig. 9.S4) and $\sigma_f = 2.1 \text{ MHz}$, we can translate it into an equivalent standard deviation of the charge noise $\sigma_\epsilon \sim 230 \mu\text{V}$ (for the specific gate used to perform the measurement reported in Fig. 9.S4).

fects at the interface might be the origins of the charge noise. The improvement on the heterostructure growth (for example, we can suppress the formation of defects in the heterostructure by elastic strain engineering (Roberts *et al.*, 2006) and we may be able to reduce the defects in the dielectric by changing the material of the dielectric (Zimmerman *et al.*, 2014)) would remove these origins. So far the charge noise coming from the setup seems much smaller than the charge noise coming from the device itself (Sec. 10.S10) and thus can be ignored.

If we operate a single qubit operation when the exchange interaction is not completely off, single qubit gate fidelities are also degraded by the charge noise since the resonance frequency is affected by the exchange interaction. We should operate single qubit operations at the point where the differential of the exchange interaction with respect to a gate voltage $\frac{dJ}{d\epsilon}$ is low enough or is at least lower than the differential of the Larmor frequency with respect to the gate voltage $\frac{df}{d\epsilon}$ which results from the gradient of the magnetic field component parallel to the external magnetic field required for the addressability (see also the next paragraph), in order not to degrade the single qubit gate fidelity due to the exchange interaction.

- Micromagnet design

As discussed in Sec. 2.4, we create the magnetic field gradients by micromagnets for two purposes: to create (a) the gradient of the magnetic field parallel to the external magnetic field along the direction which the qubits line up for addressability and (b) the gradient of the magnetic field perpendicular to the external magnetic field along the direction which an electron is modulated by a microwave excitation for EDSR.

(a) parallel magnetic field gradient

We need high enough parallel magnetic field gradient $\frac{dB_{\parallel}}{dr}$, where r defines the direction in which qubits are lined up, for the addressability of different qubits. $\frac{dB_{\parallel}}{dr}$ induces $\frac{df}{d\epsilon}$, which, together with the charge noise, generates magnetic noise. The standard deviation of this magnetic noise is calculated to be $\sigma_{\epsilon} \frac{df}{d\epsilon}$, while the standard deviation of the magnetic noise due to the nuclear spins in the isotopically purified SiMOS sample (with 800ppm residual concentration of ^{29}Si) was measured to be $\sigma_f = 12$ kHz (Veldhorst *et al.*, 2015b). Thus, using $\sigma_{\epsilon} = 100$ μV (see Table 11.1), the total magnetic field gradient should be $\frac{df}{d\epsilon} < 0.12$ MHz/mV in order to make maximum use of the low concentration of ^{29}Si . There is an optimized point for the magnetic field gradient considering the trade-off between the addressability for a given Rabi frequency (Sec. E.1.2) and the magnetic noise for a given ^{29}Si concentration as discussed above. By designing the micromagnets to realize such a magnetic field gradient, we can maximize the single qubit gate fidelity.

(b) perpendicular magnetic field gradient

In order to obtain a high Rabi frequency, we would like to have a high perpendicular magnetic field gradient ($\frac{dB_{\perp}}{dr}$, where r here is a modulation direction of the dot position and $\frac{dB_{\perp}}{dx}$ in Eq. 3.15). In the experiments shown in this thesis, we applied the external magnetic field along the x axis (Sec. 3.2, Fig. G.2). With this direc-

tion of the external magnetic field, we obtain $\frac{dB_{\perp}}{dx} = 0.3 \text{ mT/nm}$ at the dot position which happened to be displaced from the intended position. The maximum measured Rabi frequency was $\sim 5 \text{ MHz}$.

The lateral positions and shapes of the micromagnets were designed so that when the external magnetic field is applied along the y axis (Sec. G.2), the dot was created on the intended position (in the middle of two micromagnets along the y axis), and the electron is modulated along the y axis, the perpendicular magnetic field gradient is maximized ($\frac{dB_{\perp}}{dy} \sim 1 \text{ mT/nm}$). In Sec. 6.6, we estimated the maximum reachable Rabi frequency in this situation is $\sim 50 \text{ MHz}$, and the measured Rabi frequency in recent measurements by our group (not shown in this thesis) is consistent with this estimation.

Besides playing with the lateral positions and shapes of the micromagnets, we can also increase the perpendicular magnetic field gradient by placing the micromagnets closer to 2DEG, for example by making the dielectric layer thinner, or using a different ferromagnetic material which has a larger saturated magnetization. For example the saturated magnetization of CoFe, which depends on the composition ratio, can reach $\sim 2.5 \text{ T}$ (Fu, Cheng, and Yang, 2005), while that of Co is 1.8 T (Pioro-Ladrière *et al.*, 2007). The saturated magnetization of CoFe is measured to be 1.93 T in the context of using it as an ingredient for EDSR (Lachance-Quirion *et al.*, 2015).

- PSB read-out and RF read-out

The initialization and read-out infidelities using the Elzerman scheme (Elzerman *et al.*, 2004) are attributed to the three factors: finite electron temperature of the reservoir, lifetime broadening of the quantum dot levels (linearized energy dependent tunneling coefficient that relates to the transparency of the barrier; Amasha *et al.* (2008); Simmons *et al.* (2011a)), and the noise on the signal. If (a) the Zeeman splitting is much larger than the electron temperature of the reservoir or the lifetime broadening: $\epsilon_z \gg k_B T_{el}, E_{\uparrow}, E_{\downarrow}$, where ϵ_z is the Zeeman splitting, T_{el} is the electron temperature of the reservoir, k_B is Boltzmann constant, and E_{\uparrow} (E_{\downarrow}) is the linearized energy dependent tunneling coefficient that relates to the transparency of the barrier of the spin-up state (spin-down state) (Amasha *et al.*, 2008; Simmons *et al.*, 2011a), (b) the signal to noise ratio is large enough: $S/N \gg 1$ with the reasonably wide signal bandwidth set around the tunneling rate and (c) the initialization time and the read-out time are set much longer than the inverse of the tunneling rates: $t_{\text{read}} \gg \Gamma_{\text{out}}^{-1}$, $t_{\text{init}} \gg \Gamma_{\text{in}}^{-1}$, where Γ_{out} (Γ_{in}) is the tunneling out rate of an electron from the dot to the reservoir (the tunneling in rate of an electron from the reservoir to the dot), the initialization and read-out fidelity can reach $\sim 100\%$. (A short T_1 can degrade the read-out fidelity and a leakage to an excited valley-orbit state can degrade the initialization fidelity. However we ignore these two effects here since these two values can be tuned by perpendicular electric field (Yang *et al.*, 2013).)

How can we satisfy all the three conditions at the same time? For condition (a), we can simply apply a higher magnetic field in order to obtain a high ϵ_z but then Larmor frequency of the electron also becomes higher and we face difficulties in

high-frequency microwave engineering. By using Pauli Spin Blockade (PSB) read-out (Koppens *et al.*, 2005; Ono *et al.*, 2002; Shulman *et al.*, 2012) (see also Sec. 2.4) instead of Elzerman read-out (Elzerman *et al.*, 2004), Zeeman splitting does not have to be higher than the electron temperature since it uses a parity check of two neighboring spins (Brunner *et al.*, 2011; Koppens *et al.*, 2006; Nowack *et al.*, 2007; Ono *et al.*, 2002). In this case, the energy requirement is that single-dot singlet-triplet splitting should be much larger than the phonon temperature. The disadvantage of this method is to sacrifice one dot, which otherwise can be used as one of the physical qubits, for the read-out.

In the experiments shown in this thesis, in order to satisfy conditions (b,c), we set the signal bandwidth DC-30 kHz, the tunneling rate around 10 kHz, and the initialization and read-out time 4–5 ms. We had to choose this narrow bandwidth in order to obtain a high enough S/N and had to wait long enough time so that an electron jumps out/in with a high enough probability.

As discussed in the previous section, it is preferred to have a short initialization and read-out time. In order to satisfy condition (c) with a short initialization and read-out time, the tunneling rate should be high (the tunneling rate is, in principle, tunable). In order to satisfy condition (b) with a high tunneling rate, we can use radiofrequency (RF) reflectometry (Baart *et al.*, 2016a; Barthel *et al.*, 2010), which allows to increase the signal bandwidth to around a higher frequency and to increase the S/N since there are low-noise amplifiers available at RF frequencies.

- Long-distance qubit-qubit coupling

So far the number of quantum dots had been extended along a line (Baart *et al.*, 2016c; Shulman *et al.*, 2012). In order to implement the surface code as a quantum error correction, it is preferable to place quantum dots in a two-dimensional lattice so that one qubit has the nearest-neighbor interaction with more than two qubits. In (Thalentineau *et al.*, 2012), 4 quantum dots are placed in a square-like configuration. However, there is not enough space in which to place a large number of gates needed to define a further number of quantum dots. A strategy to meet this challenge is to implement distant interactions between the qubits. It can be realized via a photon using a superconducting resonator as discussed in DiVincenzo criteria (6) but there are also other ideas for implementing long-distance qubit-qubit coupling on a chip using a compact design compared to the coupling scheme based on a superconducting resonator. For example, a long-distance coupling between spin qubits can be generated by a long-range capacitive coupling induced by a long floating metallic gate (Chan *et al.*, 2002) combined with a spin-orbit interaction (Trifunovic *et al.*, 2012) or dipolar interactions with a long floating ferromagnet (Trifunovic, Pedrocchi, and Loss, 2013).

- Smaller gate design

From our experiences of tuning the gate voltages to form dots, it is difficult to have two quantum dots at the intended positions having a reasonable tunnel coupling and a reasonable coupling between the dots which confine electrons serving as qubits and sensing dots with the gate design used in the experiments presented in this thesis. This difficulty of tunability can be a big problem to scale the number of

qubits. Thus we propose to make the gate design smaller in order to place everything in a smaller space (Eng *et al.*, 2015; Veldhorst *et al.*, 2014; Ward *et al.*, 2016; Zajac *et al.*, 2015), which requires a further improvement on the nanofabrication technique for a higher resolution of electron-beam lithography. By doing so, as a side benefit, the size of the dots will also be decreased and it will increase the possibility of obtaining a higher valley splitting, since the electron wave function would overlap with a fewer number of atomic steps (see Sec. 2.5.2).

EPILOGUE

Even if, as shown in the previous chapter, there is still a lot of work to be completed, it may not be a vacuity anymore to talk about the world with a quantum computer. When I was working with field engineers from Oxford Instruments to install cryogenic systems, I got the following imaginations.

10 years from now, Qutech sells Si quantum computers. In the section on specifications, in the brochure of the Qutech quantum computer, you will find the clock speed for 1-qubit gate and 2-qubit gate, reliability of computation output (quantum efficiency), etc. The price will vary depending on the number of qubits provided or the concentration of residual ^{29}Si in the Si substrate. Clients can customize the layout of quantum dots depending on their applications.

Tuning the configuration of gate voltages to define quantum dots will be part of the job done by a field engineer (let's name his name Phil) during the installation of the quantum computer on site. Of course, Phil uses the automated tuning program (Baart *et al.*, 2016a). After successfully defining the same number of quantum dots as written in the specification, now he finds the Larmor frequencies and the Rabi frequencies for electrons in each dots. There should be also an automated program for that by that time. The maximum Rabi frequencies should meet what is written in the specifications and the Larmor frequencies of electrons in neighboring dots should be further apart, otherwise clients may complain because it would degrade the clock speed and the 1-qubit gate fidelity. Next, Phil moves to the characterization of exchange interactions between electrons in neighboring dots. Again there will be an automated program for that. Exchange interactions should be higher than what is written in the specification and noise on the exchange interaction should be lower than what is written in the specification, otherwise clients may complain because it would degrade the clock speed and the 2-qubit gate fidelity. If the exchange interaction is low, it may be because of the low valley splitting. The low valley splitting may be due to the defects at the interface. Thus Phil may contact headquarter to send him another sample with a smoother interface. At the same time, he first tries to make the valley splitting higher by changing the gate voltages, because the client does not like a delay in the schedule. If he changes the gate voltages, the dot position moves and Larmor frequencies are shifted. He should repeat all the calibrations again hoping that the Rabi frequencies are high enough and keeping the exchange interactions high enough at the same time.

Phil's work may be completed here after the calibration of physical qubits. However, clients may also choose options that the calibrations of virtual qubits, logical qubits or even a demonstration of a simple quantum algorithm is done by a field engineer.

I think it will really happen.

A

SPIN OPERATORS

A.1. PAULI MATRICES

A.1.1. DEFINITION

Pauli matrices, σ_x , σ_y and σ_z are given by:

$$\sigma_x = \begin{pmatrix} 0 & 1 \\ 1 & 0 \end{pmatrix}, \sigma_y = \begin{pmatrix} 0 & -i \\ i & 0 \end{pmatrix}, \sigma_z = \begin{pmatrix} 1 & 0 \\ 0 & -1 \end{pmatrix}. \quad (\text{A.1})$$

In the case of spin-1/2, the spin operators are described as

$$S_x = \frac{\hbar}{2}\sigma_x, \quad S_y = \frac{\hbar}{2}\sigma_y, \quad S_z = \frac{\hbar}{2}\sigma_z, \quad (\text{A.2})$$

where \hbar is the reduced plank constant. Hence, the eigenvectors of the Pauli matrices and the spin operators are the same, which can be taken as follows:

$$\begin{aligned} |+\sigma_z\rangle &= |S_z\rangle &= \begin{pmatrix} 1 \\ 0 \end{pmatrix} \equiv |1\rangle \\ |-\sigma_z\rangle &= |S_z\rangle &= \begin{pmatrix} 0 \\ 1 \end{pmatrix} \equiv |0\rangle \\ |+\sigma_x\rangle &= |S_x\rangle &= \frac{1}{\sqrt{2}} \begin{pmatrix} 1 \\ 1 \end{pmatrix} = \frac{1}{\sqrt{2}}(|1\rangle + |0\rangle) \\ |-\sigma_x\rangle &= |S_x\rangle &= \frac{1}{\sqrt{2}} \begin{pmatrix} 1 \\ -1 \end{pmatrix} = \frac{1}{\sqrt{2}}(|1\rangle - |0\rangle) \\ |+\sigma_y\rangle &= |S_y\rangle &= \frac{1}{\sqrt{2}} \begin{pmatrix} 1 \\ i \end{pmatrix} = \frac{1}{\sqrt{2}}(|1\rangle + i|0\rangle) \\ |-\sigma_y\rangle &= |S_y\rangle &= \frac{1}{\sqrt{2}} \begin{pmatrix} 0 \\ -i \end{pmatrix} = \frac{1}{\sqrt{2}}(|1\rangle - i|0\rangle) \end{aligned} \quad (\text{A.3})$$

The eigenvalues corresponding to $|+\sigma_i\rangle$ ($|+S_i\rangle$) are $+1$ ($+\frac{\hbar}{2}$) and for $|-\sigma_i\rangle$ ($| -S_i\rangle$) they are -1 ($-\frac{\hbar}{2}$) for $i = x, y, z$.

A.1.2. COMMUTATION RELATIONS

The Pauli matrices satisfy the following commutation and anticommutation relations:

$$[\sigma_a, \sigma_b] = \sigma_a \sigma_b - \sigma_b \sigma_a = 2i \varepsilon_{abc} \sigma_c, \quad (\text{A.4})$$

$$\{\sigma_a, \sigma_b\} = \sigma_a \sigma_b + \sigma_b \sigma_a = 2\delta_{ab} \cdot \mathbb{1}. \quad (\text{A.5})$$

where ε_{abc} is the Levi-Civita's symbol, δ_{ab} is the Kronecker's delta, and $\mathbb{1}$ is the identity matrix.

These equations are summarized to:

$$\sigma_a \sigma_b = \delta_{ab} \cdot \mathbb{1} + i \sum_c \varepsilon_{abc} \sigma_c, \quad (\text{A.6})$$

$$\sigma_1 \sigma_2 = -\sigma_2 \sigma_1 = i \sigma_3, \quad (\text{A.7})$$

$$\sigma_2 \sigma_3 = -\sigma_3 \sigma_2 = i \sigma_1, \quad (\text{A.8})$$

$$\sigma_3 \sigma_1 = -\sigma_1 \sigma_3 = i \sigma_2, \quad (\text{A.9})$$

$$\sigma_1 \sigma_1 = \mathbb{1}. \quad (\text{A.10})$$

$$(\text{A.11})$$

A.2. DENSITY OPERATOR

Any quantum state of a single spin ($S = \frac{1}{2}$)¹ can be expressed with the density operator as follows :

$$\rho = \frac{1}{2} \mathbb{1} + \frac{1}{2} \boldsymbol{\sigma} \cdot \mathbf{r}, \quad (\text{A.13})$$

where $\boldsymbol{\sigma} = (\sigma_x, \sigma_y, \sigma_z)$, $\mathbf{r} = (r_x, r_y, r_z)$, and $\mathbb{1}$ is the identity matrix. ρ is a pure state when $|\mathbf{r}| = 1$ and can be rewritten as the outer product of state vectors: $\rho = |\Psi\rangle \langle \Psi|$. ρ is a statistical mixture of pure states (simply called mixed state) when $|\mathbf{r}| < 1$. A mixed state cannot be rewritten as the outer product of any state vectors.

The expectation value (see Appendix A.3) of the observable S_i is thus equal to $\frac{1}{2} r_i$

$$\langle S_i \rangle = \text{Tr}(\rho S_i) = \frac{1}{2} r_i \quad (\text{A.14})$$

where $i = x, y, z$. $\frac{1}{2}$ in Eq. A.14 comes from the eigenvalue of $|S_i\rangle$.

¹For n-spin system, any state can be expressed with

$$\rho = \frac{1}{2^n} (\mathbb{1}^{\otimes n} + \boldsymbol{\sigma}^{\otimes n} \mathbf{r}^{\otimes n}) \quad (\text{A.12})$$

where $\boldsymbol{\sigma}^{\otimes n}$ is the Pauli matrix vector for n-spin system, whose $4^n - 1$ components are all n -fold tensor products of single qubit Pauli matrices $\mathbb{1}, \sigma_x, \sigma_y, \sigma_z$ except for $\mathbb{1}^{\otimes n}$

A.3. EXPECTATION VALUE

In quantum theory, an experimental setup is described by the observable A to be measured, and the quantum state ρ of the system. The expectation value of A in the state ρ is denoted as $\langle A \rangle_\rho$ and is given as the trace of A multiplied by ρ :

$$\langle A \rangle_\rho = \text{Trace}(\rho A). \quad (\text{A.15})$$

When ρ is a pure state, it can be written as $\rho = |\Psi\rangle\langle\Psi|$. In this case, the expectation value of A in the state $|\Psi\rangle$ is defined as

$$\langle A \rangle_\Psi = \langle\Psi|A|\Psi\rangle. \quad (\text{A.16})$$

If one knows a complete set of eigenvectors a_j for A , with eigenvalues E_{a_j} , then Eq. A.16 can be expressed as

$$\langle A \rangle_\Psi = \sum_j E_{a_j} |\langle\Psi|a_j\rangle|^2. \quad (\text{A.17})$$

The eigenvalues E_{a_j} are the possible outcomes of each experiment, and the coefficient $|\langle\Psi|a_j\rangle|^2$ is the probability that this outcome will occur. The above formulas are valid for pure states only.

A.4. TIME EVOLUTION OPERATOR

In the rotating frame (Appendix B.4), the microwave excitation with amplitude ω_1 , phase ϕ , and carrier frequency $\Delta\omega$ detuned from the Larmor frequency, can be represented by the time-independent Hamiltonian

$$H_{\Delta\omega, \omega_1, \phi} = \omega_1 \left(\frac{\sigma_x}{2} \cos\phi - \frac{\sigma_y}{2} \sin\phi \right) + \Delta\omega \frac{\sigma_z}{2}. \quad (\text{A.18})$$

Subsequently the spin system evolves according to the time evolution operator

$$R(\Delta\omega, \omega_1, \phi, t) \equiv \exp(-iH_{\Delta\omega, \omega_1, \phi} t) \\ = \begin{cases} \cos\left(\frac{\omega_{\text{eff}} t}{2}\right) \mathbb{1} - i \sin\left(\frac{\omega_{\text{eff}} t}{2}\right) (c_z \sigma_z + c_x \sigma_x + c_y \sigma_y) & (\omega_{\text{eff}} \neq 0) \\ \mathbb{1} & (\omega_{\text{eff}} = 0) \end{cases} \quad (\text{A.19})$$

with $\omega_{\text{eff}} = \sqrt{\Delta\omega^2 + \omega_1^2}$, $\omega_1 = 2\pi f_1$, $c_z = \Delta\omega/\omega_{\text{eff}}$, $c_x = \omega_1 \cos(\phi)/\omega_{\text{eff}}$ and $c_y = \omega_1 \sin(\phi)/\omega_{\text{eff}}$.

A.4.1. ROTATION OPERATOR AROUND x , y , AND z AXES

The rotation operators of a single $S = 1/2$ spin system² are given as follows:

$$R_x(\theta) \equiv \exp(-i\theta S_x) = \cos\frac{\theta}{2} \mathbb{1} - i \sin\frac{\theta}{2} \sigma_x = \begin{pmatrix} \cos\frac{\theta}{2} & -i \sin\frac{\theta}{2} \\ -i \sin\frac{\theta}{2} & \cos\frac{\theta}{2} \end{pmatrix} \quad (\text{A.21})$$

²For a 2-spin system,

$$R_{\alpha\beta}(\theta) = \exp(-i\theta S_\alpha^A S_\beta^B) = \cos\frac{\theta}{4} \mathbb{1}^{AB} - i \sin\frac{\theta}{4} \sigma_\alpha^A \sigma_\beta^B \quad (\text{A.20})$$

with $\alpha, \beta, \gamma = x, y, z$.

$$R_y(\theta) \equiv \exp(-i\theta S_y) = \cos \frac{\theta}{2} \mathbb{1} - i \sin \frac{\theta}{2} \sigma_y = \begin{pmatrix} \cos \frac{\theta}{2} & -\sin \frac{\theta}{2} \\ \sin \frac{\theta}{2} & \cos \frac{\theta}{2} \end{pmatrix} \quad (\text{A.22})$$

$$R_z(\theta) \equiv \exp(-i\theta S_z) = \cos \frac{\theta}{2} \mathbb{1} - i \sin \frac{\theta}{2} \sigma_z = \begin{pmatrix} e^{-i\theta/2} & 0 \\ 0 & e^{i\theta/2} \end{pmatrix} \quad (\text{A.23})$$

Frequently used relations between the rotation and spin operators for a single³ are given below.

$$R_z^\dagger(\theta) \begin{Bmatrix} S_z \\ S_x \\ S_y \\ S_\pm \end{Bmatrix} R_z(\theta) = \exp(i\theta S_z) \begin{Bmatrix} S_z \\ S_x \\ S_y \\ S_\pm \end{Bmatrix} \exp(-i\theta S_z) = \begin{Bmatrix} S_z \\ S_x \cos \theta - S_y \sin \theta \\ S_y \cos \theta + S_x \sin \theta \\ S_\pm \exp(\pm i\theta) \end{Bmatrix} \quad (\text{A.25})$$

$$R_x^\dagger(\theta) \begin{Bmatrix} S_z \\ S_x \\ S_y \\ S_\pm \end{Bmatrix} R_x(\theta) = \exp(i\theta S_x) \begin{Bmatrix} S_z \\ S_x \\ S_y \\ S_\pm \end{Bmatrix} \exp(-i\theta S_x) = \begin{Bmatrix} S_z \cos \theta + S_y \sin \theta \\ S_x \\ S_y \cos \theta - S_z \sin \theta \\ i S_z \sin \theta + S_\pm \cos^2 \theta / 2 - S_\mp \sin^2 \theta / 2 \end{Bmatrix} \quad (\text{A.26})$$

$$R_y^\dagger(\theta) \begin{Bmatrix} S_z \\ S_x \\ S_y \\ S_\pm \end{Bmatrix} R_y(\theta) = \exp(i\theta S_y) \begin{Bmatrix} S_z \\ S_x \\ S_y \\ S_\pm \end{Bmatrix} \exp(-i\theta S_y) = \begin{Bmatrix} S_z \cos \theta - S_x \sin \theta \\ S_x \cos \theta + S_z \sin \theta \\ S_y \\ -S_z \sin \theta + S_\pm \cos^2 \theta / 2 + S_\mp \sin^2 \theta / 2, \end{Bmatrix} \quad (\text{A.27})$$

where $S_\pm = S_x \pm iS_y$ are the raising and lowering operators, which satisfy the commutation relations:

$$[S_z, S_\pm] = \pm S_\pm, \quad [S_+, S_-] = 2S_z \quad (\text{A.28})$$

³For a 2-spin system,

$$\exp(i\theta S_\alpha^A S_\beta^B) S_\gamma^A \exp(-i\theta S_\alpha^A S_\beta^B) = \begin{cases} S_\gamma^A \cos \frac{\theta}{2} + 2[S_\gamma^A, S_\alpha^A] S_\beta^B \sin \frac{\theta}{2} & (\alpha \neq \gamma) \\ S_\gamma^A & (\alpha = \gamma) \end{cases} \quad (\text{A.24})$$

with $\alpha, \beta, \gamma = x, y, z$ and $[S_a^A, S_b^A] = i\epsilon_{abc} S_c^A$ (Eq. A.4)

B

TIME EVOLUTION OF A QUANTUM STATE

In this section, we present the the time evolution of a quantum state in the Schrödinger picture.

B.1. EQUATION OF MOTION OF A QUANTUM STATE

B.1.1. CASE OF PURE STATE: SCHRÖDINGER EQUATION

The Schrödinger equation is an equation of motion that describes how the quantum state of a physical system changes in time. The most general form, the time-dependent Schrödinger equation (i.e., where the Hamiltonian is dependent on time), states

$$i\hbar \frac{\partial}{\partial t} |\Psi(t)\rangle = H|\Psi(t)\rangle, \quad (\text{B.1})$$

where \hbar is the reduced plank constant and $|\Psi(t)\rangle$ is the wavefunction, representing the probability amplitude of the quantum state, $i\hbar \frac{\partial}{\partial t}$ is the energy operator (i is the imaginary unit and \hbar is the reduced Planck constant (also known as Dirac constant)), and H is the Hamiltonian operator.

Setting $\hbar = 1$, Eq. B.1 becomes

$$i \frac{\partial}{\partial t} |\Psi(t)\rangle = H|\Psi(t)\rangle. \quad (\text{B.2})$$

We usually denote the time-evolution operator (also called propagator) from time t_0 to t as $U(t, t_0)$, where

$$|\Psi(t)\rangle = U(t, t_0) |\Psi(t_0)\rangle, \quad (\text{B.3})$$

and so Eq. (B.1) becomes

$$i \frac{\partial}{\partial t} U(t, t_0) = HU(t, t_0). \quad (\text{B.4})$$

B.1.2. GENERAL CASE: LIOUVILLE-VON NEUMANN EQUATION

Eq. (B.1) and Eq. (B.3) are only valid for a pure state. For general cases, the state may be "mixed" and the Schrödinger equation Eq. (B.1) is replaced by the Liouville-von Neumann equation

$$i\frac{\partial\rho}{\partial t} = [H, \rho] \quad (\text{B.5})$$

This is the equation of motion of any quantum system (valid for both a pure state and a mixed state). Note that all the arguments in this thesis are developed in the Schrödinger picture.

In the same way, Eq. (B.3) is replaced by

$$\rho(t) = U(t, t_0)\rho(t_0)U^\dagger(t, t_0). \quad (\text{B.6})$$

B.2. TIME EVOLUTION OPERATOR FOR TIME-INDEPENDENT HAMILTONIAN

If the Hamiltonian is time-independent, we can easily solve Eq. (B.4), and we get

$$U(t, t_0) = \exp(-iH(t - t_0)). \quad (\text{B.7})$$

In this case, Eq. (B.6) can also be rewritten in a simple form:

$$\rho(t) = e^{-iH(t-t_0)}\rho(t_0)e^{iH(t-t_0)}. \quad (\text{B.8})$$

B.3. TIME EVOLUTION OPERATOR FOR TIME-DEPENDENT HAMILTONIAN

In the case where the Hamiltonian is time-dependent, Eq. (B.7) is generalized down to

$$\begin{aligned} U(t, t_0) &= 1 - i \int_{t_0}^t H(t')U(t', t_0)dt' \\ &= 1 + (-i) \int_{t_0}^t dt_1 H(t_1) + (-i)^2 \int_{t_0}^t dt_1 \int_{t_0}^{t_2} dt_2 H(t_1)H(t_2) + \dots \end{aligned} \quad (\text{B.9})$$

Eq. (B.9) is converted into a simple form, using Wick-Dyson operator T ,

$$U(t, t_0) = T \left[\exp \left(-i \int_{t_0}^t H(t') dt' \right) \right]. \quad (\text{B.10})$$

B.4. ROTATING REFERENCE FRAME

Here, we introduce "rotating reference frame" [Sakurai \(1993\)](#) [Haeberlen \(1976\)](#). In what follows, t_0 is equal to 0 and $U(t, 0)$ is simplified to $U(t)$.

Suppose that the total Hamiltonian can be divided into two parts:

$$H = H_0 + H(t) \quad (\text{B.11})$$

H_0 is a time-independent Hamiltonian while $H(t)$ can be any (time-dependent or time-independent) Hamiltonian.

We now make the ansatz

$$\rho_R(t) = U_0^\dagger \rho(t) U_0, \quad \text{with } U_0 = \exp(-iH_0 t). \quad (\text{B.12})$$

Eq. (B.12) leads the left side of the equation of motion in Eq. (B.5) to

$$\begin{aligned} i\dot{\rho} &= i\dot{U}_0 \rho_R U_0^\dagger + iU_0 \dot{\rho}_R U_0^{-\dagger} + iU_0 \rho_R \dot{U}_0^\dagger \\ &= H_0 U_0 \rho_R U_0^\dagger + iU_0 \dot{\rho}_R U_0^\dagger - U_0 \rho_R U_0^\dagger H_0 \\ &= [H_0, U_0 \rho_R U_0^\dagger] + iU_0 \dot{\rho}_R U_0^\dagger, \end{aligned} \quad (\text{B.13})$$

and the right side to

$$[H, \rho] = [H_0 + H(t), U_0 \rho_R U_0^\dagger]. \quad (\text{B.14})$$

Comparing Eq. (B.13) and Eq. (B.14), we get

$$iU_0 \dot{\rho}_R U_0^\dagger = [H(t), U_0 \rho_R U_0^\dagger]. \quad (\text{B.15})$$

Multiplying this equation from the left with U_0^\dagger and from the right with U_0 gives

$$\begin{aligned} i\dot{\rho}_R &= U_0^\dagger H(t) U_0 \rho_R U_0^\dagger U_0 - U_0^\dagger U_0 \rho_R U_0^\dagger H(t) U_0 \\ &= [H_R(t), \rho_R], \end{aligned} \quad (\text{B.16})$$

with

$$H_R(t) \equiv U_0^\dagger H(t) U_0. \quad (\text{B.17})$$

This represents the equation of motion of a quantum state (Liouville-Neumann equation) in the rotating reference frame.

B.5. ELECTRON SPIN RESONANCE

B.5.1. TWO LEVEL SYSTEM AS QUBIT

The two-level Hamiltonian describing a single spin which has a Zeeman splitting ω_0 under the microwave excitation (frequency ω_{MW} and the amplitude $2\omega_1$ with the phase ϕ) excitation perpendicular to the Zeeman splitting can be written as

$$H = -\omega_0 S_z + 2\omega_1 (\cos(\omega_{\text{MW}} t + \phi) S_x). \quad (\text{B.18})$$

B.5.2. ROTATING WAVE APPROXIMATION

In this section, the reference frame is changed to one which rotates with the microwave frequency ω_{MW} for the convenience of further analytic solution. By taking H_0 and $H(t)$ in Eq. B.11 as

$$H_0 = -\omega_{\text{MW}} S_z \quad (\text{B.19})$$

and

$$H(t) = \Delta\omega S_z + 2\omega_1 (\cos(\omega_{\text{MW}} t + \phi) S_x) \quad (\text{B.20})$$

with $\Delta\omega = -\omega_0 + \omega_{\text{MW}}$, Eq. B.17 becomes

$$\begin{aligned}
 H_{\text{R}}(t) &= U_0^\dagger H(t) U_0 = \exp(iH_0 t) H(t) \exp(-iH_0 t) \\
 &= R_z^\dagger(\omega_{\text{MW}} t) (2\omega_1 (\cos(\omega_{\text{MW}} t + \phi)) S_x + \Delta\omega S_z) R_z(-\omega_{\text{MW}} t) \\
 &= R_z^\dagger(\omega_{\text{MW}} t) (2\omega_1 (\cos(\omega_{\text{MW}} t + \phi)) S_x) R_z(-\omega_{\text{MW}} t) + \Delta\omega S_z \\
 &= \omega_1 \frac{e^{-i\phi} S_- + e^{i\phi} S_+}{2} + \omega_1 \frac{e^{i(2\omega_{\text{MW}} t + \phi)} S_- + e^{-i(2\omega_{\text{MW}} t + \phi)} S_+}{2} + \Delta\omega S_z. \quad (\text{B.21})
 \end{aligned}$$

We have used the relation¹

$$\begin{aligned}
 2\omega_1 (\cos(\omega_{\text{MW}} t + \phi)) S_x &= \omega_1 (e^{i(\omega_{\text{MW}} t + \phi)} + e^{-i(\omega_{\text{MW}} t + \phi)}) \frac{S_+ + S_-}{2} \\
 &= \omega_1 \frac{e^{-i(\omega_{\text{MW}} t + \phi)} S_- + e^{i(\omega_{\text{MW}} t + \phi)} S_+}{2} + \omega_1 \frac{e^{i(\omega_{\text{MW}} t + \phi)} S_- + e^{-i(\omega_{\text{MW}} t + \phi)} S_+}{2}. \quad (\text{B.22})
 \end{aligned}$$

The second term in Eq. B.21 oscillates much faster than the detuning ($2\omega_{\text{MW}} \gg \Delta\omega$) and thus can be ignored. Finally, the Hamiltonian on the rotating frame approximation is

$$H_{\text{R}}(t) = \omega_1 (\cos\phi S_x - \sin\phi S_y) + \Delta\omega S_z. \quad (\text{B.23})$$

¹ $\frac{e^{-i\phi}}{2} \frac{\sigma_+}{2} + h.c. = \cos\phi \frac{\sigma_x}{2} + \sin\phi \frac{\sigma_y}{2}$

C

MULTIPHOTON ESR

Electron Spin Resonance (ESR) is a technique to flip or alter an electron spin state by applying a magnetic field oscillating along the orthogonal direction to the spin-quantization axis. When the photon energy of the oscillating magnetic field matches the spin splitting, the condition for ESR is satisfied. If there is a perpendicular oscillating magnetic field in addition to the orthogonal oscillating magnetic field, an electron spin state can also be changed when the photon energy of the oscillating magnetic field matches the spin splitting divided by whole numbers. In the following section, we demonstrate the mechanism of such a multiphoton electron spin resonance and derive the Rabi frequency of the two-photon electron spin resonance.

C.1. MULTIPHOTON ELECTRON SPIN RESONANCE DUE TO A PERPENDICULAR OSCILLATING MAGNETIC FIELD

The conventional Hamiltonian for ESR (Eq. 3.13) along with the perpendicular oscillating magnetic field becomes

$$H = -\omega_0 S_z + 2\omega_1 \cos(\omega_{\text{MW}} t + \phi) S_x + 2\omega'_1 \cos(\omega_{\text{MW}} t + \phi) S_z. \quad (\text{C.1})$$

In the case of micromagnet EDSR in a quantum dot, the third term appears due to the magnetic field gradient along the same direction as the external magnetic field (Sec. 3.1.1).

$$H_R = \Delta\omega S_z + \omega_1 \frac{S_+ + S_-}{2} + \omega_1 \frac{S_- e^{i2\omega_{\text{MW}} t} + h.c.}{2} + \omega'_1 \cos(\omega_{\text{MW}} t) S_z \quad (\text{C.2})$$

with $\Delta\omega = \omega_0 - \omega_{\text{MW}}$. Now the reference frame is changed again to one which rotates¹ with the frequency $\omega'_1 \cos(\omega_{\text{MW}}t)$:

$$H_{RR} = W^\dagger (H_R - \omega'_1 \cos(\omega_{\text{MW}}t) S_z) W \quad (\text{C.3})$$

with $W = \exp\left(-i\eta \frac{\sigma_z^{\text{spin,orb}}}{2}\right)$ and $\eta = \int \omega'_1 \cos(\omega_{\text{MW}}t) dt = \frac{\omega'_1}{\omega_{\text{MW}}} \sin(\omega_{\text{MW}}t)$ (Shevchenko, Ashhab, and Nori, 2010).

$$H_{RR} = W^\dagger \left(\Delta\omega S_z + \omega_1 \frac{S_+ + S_-}{2} + \omega_1 \frac{S_- e^{i2\omega_{\text{MW}}t} + h.c.}{2} \right) W \quad (\text{C.4})$$

$$= \Delta\omega S_z + \omega_1 \frac{S_+ e^{i\eta} + h.c.}{2} + \omega_1 \frac{S_- e^{i2\omega_{\text{MW}}t} e^{-i\eta t} + h.c.}{2} \quad (\text{C.5})$$

$$= \Delta\omega S_z + \omega_1 \frac{\sum_{n=-\infty}^{\infty} J_n\left(\frac{\omega'_1}{\omega_{\text{MW}}}\right) S_+ e^{in\omega_{\text{MW}}t} + h.c.}{2} + \omega_1 \frac{\sum_{n=-\infty}^{\infty} J_n\left(\frac{\omega'_1}{\omega_{\text{MW}}}\right) S_- e^{i(2-n)\omega_{\text{MW}}t} + h.c.}{2}, \quad (\text{C.6})$$

where $J_n(\alpha)$ is a n -th kind Bessel function. Eq. C.6 describes the generation of higher harmonic resonances. For example, for the second harmonic resonance, when $\Delta\omega = \omega_{\text{MW}}$, i.e., $\omega_{\text{MW}} = \frac{\omega_0}{2}$, the third term with $n = 1$ induces the resonance. The Rabi frequency for the second harmonic resonance is $\omega_2 = \omega_1 J_1\left(\frac{\omega'_1}{\omega_{\text{MW}}}\right)$. When $\omega'_1 \ll \omega_{\text{MW}}$, it can be approximated to $\omega_2 \sim \frac{\omega_1 \omega'_1}{2\omega_{\text{MW}}}$. Thus the ratio in Rabi frequency between the fundamental resonance and the second harmonic resonance is

$$\frac{\omega_2}{\omega_1} = \frac{\omega'_1}{2\omega_{\text{MW}}}. \quad (\text{C.7})$$

The same relation is derived in (Gromov and Schweiger, 2000) using Floquet theory. In the case of micromagnet EDSR in a quantum dot, $\omega'_1 \ll \omega_{\text{MW}}$.

¹In Sec. B.4, we treated the case where the transformation into the rotating reference frame is generated by the time evolution operator with a time-independent Hamiltonian. The discussion in Sec. B.4 still holds even if H_0 in Eq. B.11 is time-dependent. In this case, U_0 in Eq. B.12 is replaced by $U_0 = T \left[\exp\left(-i \int_{t_0}^t H_0 dt'\right) \right]$. Here the Wick-Dyson operator (Eq. B.10) can be omitted as the Hamiltonians inside the integral at different times commute for all the time.

D

DECOHERENCE MECHANISM

D.1. DECOHERENCE DUE TO THE OVERHAUSER FIELD

D.1.1. DECAY DUE TO QUASI-STATIC OVERHAUSER FIELD

First, we demonstrate the derivation of Eq. 3.40 (Eq. D.11) in more detail. We take a superposition state $\rho_0 = \frac{1}{2}\mathbb{1} + S_x$ and see how it evolves with H_O (Eq. 3.30) over time. From Eq. 4.3, Eq. 4.5 and Eq. A.24, we know that the evolution of ρ after time t is¹

$$\rho(t) = \frac{1}{2}\mathbb{1} + \exp\left(i\sum_i A_i I_{iz} S_z t\right) S_x \exp\left(-i\sum_i A_i I_{iz} S_z t\right) \quad (\text{D.3})$$

$$= \frac{1}{2}\mathbb{1} + S_x \cos\left(\sum_i A_i I_{iz} t\right) - iS_y \sin\left(\sum_i A_i I_{iz} t\right). \quad (\text{D.4})$$

In order to extract the decay of a quantum state $P(t)$, which is introduced in Eq. 4.58, only the second term, which contains S_x matters:

$$P(t) = \text{Tr}\left(\sigma_x S_x \cos\left(\sum_i A_i I_{iz} t\right)\right) = \prod_i^{N_n} \cos\left(\frac{A_i}{2} t\right) \quad (\text{D.5})$$

$$= \prod_i^{N_n} \frac{1}{2} \left(e^{\frac{i}{2} A_i t} + e^{-\frac{i}{2} A_i t} \right) \quad (\text{D.6})$$

$$= \sum_{\xi_1=\pm 1, \xi_2=\pm 1, \dots, \xi_{N_n}=\pm 1} \frac{1}{2} \exp\left(\frac{i}{2} t (\xi_1 A_1 + \xi_2 A_2 + \dots + \xi_{N_n} A_{N_n})\right). \quad (\text{D.7})$$

¹using the notation:

$$\cos(aS_z^A + bS_z^B) = \cos\left(\frac{a}{2}\right) \cos\left(\frac{b}{2}\right) - 2S_z^A \sin\left(\frac{a}{2}\right) 2S_z^B \sin\left(\frac{b}{2}\right) \quad (\text{D.1})$$

and

$$\sin(aS_z^A + bS_z^B) = 2S_z^A \sin\left(\frac{a}{2}\right) \cos\left(\frac{b}{2}\right) - 2S_z^B \cos\left(\frac{a}{2}\right) \sin\left(\frac{b}{2}\right). \quad (\text{D.2})$$

Here we assumed that the nuclear spins are unpolarized (finite temperature approximation) and thus all the combinations of $(\xi_i, \xi_{i+1}, \dots, \xi_{N_n})$ happen with the same probability. The exponent of e in Eq. D.7 can be rewritten as $\frac{1}{2}t\sigma_z z$ by defining z as

$$\frac{\sum_i^{N_n} \xi_i A_i}{\sigma_z} \equiv z \quad (\text{D.8})$$

(de Sousa, 2009) with

$$\sigma_z = \sqrt{\sum_i^{N_n} A_i^2}. \quad (\text{D.9})$$

Assuming that $N_n \rightarrow \infty$ with each individual $A_i \rightarrow 0$, z is reduced to the sum of a large number of random variables. The central limit theorem tells that the normalized random variable z has a standard Normal distribution in the limit $N_n \rightarrow \infty$, so the decay is

$$P(t) \rightarrow \int \frac{1}{\sqrt{2\pi}} e^{-\frac{z^2}{2}} e^{\frac{1}{2}t\sigma_z z} dz \quad (\text{D.10})$$

$$= e^{-\frac{1}{8}z^2 t^2}. \quad (\text{D.11})$$

The decay shows a Gaussian shape. We denote the time constant of this decay induced by quasi-static bath as the intrinsic decoherence time² and use the notation T_2^* :

$$T_2^* = \frac{2\sqrt{2}}{\sigma_z}. \quad (\text{D.12})$$

From Eq. D.11 and Eq. D.12, we can further infer that the quasi-static noise of $\eta(t)$ has a Gaussian distribution with the standard deviation $\frac{\sigma_z}{2}$ (see Sec. 4.4).

D.1.2. RELATION BETWEEN QUASI-STATIC NUCLEAR SPIN NOISE DECAY AND THE NUMBER OF NUCLEAR SPINS

Secondly, we demonstrate the derivation of Eq. 3.43 (Eq. D.21) in more detail.

In a periodic lattice, the electron wave function $\Psi(\mathbf{R})$ is written as the product of an envelope function ϕ and a Bloch function $u(\mathbf{R})$, so the hyperfine coupling constant Eq. 3.29 is rewritten as

$$A_i = A_{\text{sum}} |\phi(\mathbf{R}_i)|^2 \quad (\text{D.13})$$

with $A_{\text{sum}} = \frac{\mu_0}{4\pi} \frac{8\pi}{3} \gamma_e \gamma_n \hbar |u(\mathbf{R}_i)|^2$. Here we already introduce the notation A_{sum} . Later in Eq. D.18, it is demonstrated that A_{sum} is equal to the sum of hyperfine coupling constant between the electron and each Si atom overlapped with the electron wavefunction, i.e., $A_{\text{sum}} = \frac{\mu_0}{4\pi} \frac{8\pi}{3} \gamma_e \gamma_n \hbar |u(\mathbf{R}_i)|^2 = \sum_i^N A_i$, where N is the number of overlapped Si atoms with the electron wavefunction. The Bloch function $u(\mathbf{R})$ varies on the atomic scale and periodically on the unit cell. Thus $|u(\mathbf{R}_i)|^2$ has the same value at any lattice position: $|u(\mathbf{R}_i)|^2 = |u(\mathbf{R}_j)|^2$. We normalize $u(\mathbf{R})$ as

$$\int_{v_0} |u(\mathbf{R})|^2 d^3 r = 1 \quad (\text{D.14})$$

²Eq. D.12 is valid for a quasi-static bath with a single nuclear species and its angular momentum quantum number 1/2, so it is valid for Silicon but not for GaAs (Cywinski, 2011; de Sousa, 2009; Zhang *et al.*, 2007). In any case, $1/T_2^*$ is given by $\approx \sigma_z$.

with the volume of the unit cell³ v_0 . Here we introduce a parameter χ , the relative weight of the electron wavefunction at a Si atomic site,

$$\int_{v_0} |u(\mathbf{R}_i)|^2 d^3r = v_0 |u(\mathbf{R}_i)|^2 = \chi. \quad (\text{D.15})$$

From the necessity that $\int_V |\Psi(\mathbf{R})|^2 d^3r = 1$ with all the space V and Eq. D.14, the envelope function is normalized as

$$\int_V |\phi(\mathbf{R})|^2 d^3r = v_0. \quad (\text{D.16})$$

Further assuming that the envelope function is smooth over one unit cell, Eq. D.16 can be rewritten as

$$\sum_i^N |\phi(\mathbf{R}_i)|^2 v_0 = v_0. \quad (\text{D.17})$$

Applying Eq. D.17 to Eq. D.13, we can demonstrate that A_{sum} is the sum of hyperfine couplings of all the atoms overlapped with the electron wave function

$$\sum_i^N A_i = A_{\text{sum}} \sum_i^N |\phi(\mathbf{R}_i)|^2 = A_{\text{sum}}. \quad (\text{D.18})$$

From Eq. D.15, A_{sum} can be further rewritten then as

$$A_{\text{sum}} = \frac{\mu_0}{4\pi} \frac{8\pi}{3} \gamma_e \gamma_n \hbar \frac{\chi}{v_0}. \quad (\text{D.19})$$

We now see that A_{sum} depends on only the characteristic of the crystalline structure but not on how you confine the electron, as long as the electron wavefunction overlaps with a large enough number of atoms. Eq. D.18 is further rewritten as (Merkulov, Efros, and Rosen, 2002)

$$\sum_i^N A_i^2 = A_{\text{sum}}^2 \sum_i^N |\phi(\mathbf{R}_i)|^4 = A_{\text{sum}}^2 \frac{\sum_i^N |\phi(\mathbf{R}_i)|^2}{N} = \frac{A_{\text{sum}}^2}{N}. \quad (\text{D.20})$$

Using Eq. D.20, σ_z is finally reduced to

$$\sigma_z = \sqrt{\sum_i^{N_n} A_i^2} = \sqrt{c \sum_i^N A_i^2} = \sqrt{c} \frac{A_{\text{sum}}}{\sqrt{N}} = \frac{A}{\sqrt{N_n}}. \quad (\text{D.21})$$

c is the nuclear spin concentration and thus $A = c A_{\text{sum}}$ and $N_n = cN$. A_{sum} depends on the material. N is proportional to the size of the dot. The way to make T_2^* longer is to make the dot size larger, change the material for smaller A_{sum} or do the isotope purification for smaller c (Abe *et al.*, 2010).

³This normalization is different from (Assali *et al.*, 2011; Nowack, 2009). We followed (Cywinski, 2011).

E

ANALYTIC EXPRESSION FOR RABI OSCILLATION AND RAMSEY FRINGE

E.1. RABI OSCILLATION

In this section, we present additional information on analytic expressions of Rabi oscillations.

E.1.1. RABI OSCILLATION WITH ON-RESONANCE MICROWAVE

We are first interested in the spin-up probability of Rabi oscillations when microwave of which frequency is near the Larmor frequency is applied. The main discussion is in Sec. 4.3. In this appendix section, we derive Eq. 4.27 (Eq. E.5) and Eq. 4.30 (Eq. E.10) as analytic solutions of Eq. 4.25 in the case of $\omega_1 \gg \sigma_\omega$ and $\omega_1 \ll \sigma_\omega$, respectively.

ANALYTIC EXPRESSION FOR STRONG DRIVING $\omega_1 \gg \sigma_\omega$

We consider the case $\omega_1 \gg \sigma_\omega$ to demonstrate the derivation of Eq. 4.27 (Eq. E.5). We restrict ourselves to the case where $|\omega_{\text{MW}} - \omega_0| \ll \omega_1$ for simplicity. Thanks to this restriction we can take $\eta \ll \omega_1$, since $G(\eta)$ is small otherwise and thus its contribution to the integral can be ignored. By taking $\eta \ll \omega_1$ and under the assumed condition $\omega_1 \gg \sigma_\omega$, the following approximation is valid:

$$T(\eta + (\omega_{\text{MW}} - \omega_0)) = \sin^2 \left(\frac{t}{2} \sqrt{\omega_1^2 + (\eta + (\omega_{\text{MW}} - \omega_0))^2} \right) \approx \sin^2 \left(\frac{t}{2} \sqrt{\omega_1^2 + (\omega_{\text{MW}} - \omega_0)^2} \right). \quad (\text{E.1})$$

Using this approximation, Eq. 4.25 can be rewritten as

$$P_{10} \approx \sin^2 \left(\frac{t}{2} \sqrt{\omega_1^2 + (\omega_{\text{MW}} - \omega_0)^2} \right) \int_{-\infty}^{\infty} \frac{1}{\sqrt{2\pi}\sigma_\omega} \exp \left(-\frac{\eta^2}{2\sigma_\omega^2} \right) \frac{\omega_1^2}{\omega_1^2 + (\eta + (\omega_{\text{MW}} - \omega_0))^2} d\eta \quad (\text{E.2})$$

$$= T(\omega_{\text{MW}} - \omega_0)(G * L)(\omega_{\text{MW}} - \omega_0) \quad (\text{E.3})$$

Under the assumed assumption $\omega_1 \gg \sigma_\omega$, $G(\eta)$ has a sufficiently narrow peak around 0 compared to $L(\eta)$ and thus

$$P_{\uparrow 0} \approx T(\omega_{\text{MW}} - \omega_0) L(\omega_{\text{MW}} - \omega_0) \int_{-\infty}^{\infty} G(\eta) \eta \quad (\text{E.4})$$

$$= \sin^2 \left(\frac{t}{2} \sqrt{\omega_1^2 + (\omega_{\text{MW}} - \omega_0)^2} \right) \frac{\omega_1^2}{\omega_1^2 + (\omega_{\text{MW}} - \omega_0)^2}. \quad (\text{E.5})$$

ANALYTIC EXPRESSION FOR WEAK DRIVING $\omega_1 \ll \sigma_\omega$

We consider the case $\omega_1 \ll \sigma_\omega$. Under this condition, $L(\eta)T(\eta)$ has a sufficiently narrow peak around 0 compared to $G(\eta)$ and thus

$$P_{\uparrow 0} = (G * LT)(\omega_{\text{MW}} - \omega_0) \quad (\text{E.6})$$

$$\approx G(\omega_{\text{MW}} - \omega_0) \int_{-\infty}^{\infty} L(\eta) T(\eta) d\eta \quad (\text{E.7})$$

$$= \frac{1}{\sqrt{2\pi}\sigma_\omega} \exp \left(-\frac{(\omega_{\text{MW}} - \omega_0)^2}{2\sigma_\omega^2} \right) \int_{-\infty}^{\infty} \frac{\omega_1^2}{\omega_1^2 + \eta^2} \sin^2 \left(\frac{t}{2} \sqrt{\omega_1^2 + \eta^2} \right) d\eta \quad (\text{E.8})$$

$$\approx \frac{1}{\sqrt{2\pi}\sigma_\omega} \exp \left(-\frac{(\omega_{\text{MW}} - \omega_0)^2}{2\sigma_\omega^2} \right) \frac{1}{2} \left(\int_{-\infty}^{\infty} \frac{\omega_1^2}{\omega_1^2 + \eta^2} d\eta - \int_{-\infty}^{\infty} \frac{\omega_1^2}{\omega_1^2 + \eta^2} \cos(t\eta) d\eta \right) \quad (\text{E.9})$$

$$= \frac{1}{\sqrt{2\pi}\sigma_\omega} \exp \left(-\frac{(\omega_{\text{MW}} - \omega_0)^2}{2\sigma_\omega^2} \right) \frac{\pi\omega_1}{2} (1 - \exp(-\omega_1|t|)) \quad (\text{E.10})$$

E

E.1.2. RABI OSCILLATION WITH OFF-RESONANCE MICROWAVE

Secondly, we are interested in a spin-up probability when microwave of which frequency is detuned away from the Larmor frequency is applied. For individual addressing of multiple qubits, such a spin-up probability should be suppressed.

ANALYTIC EXPRESSION WITH $|\omega_{\text{MW}} - \omega_0| \gg \omega_1 \gg \sigma_\omega$

We derive a spin-up probability when microwave frequency is detuned further away from the Larmor frequency ($|\omega_{\text{MW}} - \omega_0| \gg \omega_1$) in the case of strong driving ($\omega_1 \gg \sigma_\omega$). Differently from the main text, we also consider the case where a microwave pulse is not only rectangular but has any shape $f(t)$.

In this subsection, we describe the Hamiltonian for a Rabi oscillation in the rotating reference frame at $\omega_0 + \eta(t)$ (Eq. 4.14 is the Hamiltonian for a Rabi oscillation in the rotating reference frame at the microwave carrier frequency ω_{MW}) for later convenience:

$$H_{\text{Rabi}}(t) = \omega_1 \left(\cos((\omega_{\text{MW}} - \omega_0 - \eta(t))t) f(t) S_x + \sin((\omega_{\text{MW}} - \omega_0 - \eta(t))t) f(t) S_y \right) \quad (\text{E.11})$$

$$\sim \omega_1 \cos((\omega_{\text{MW}} - \omega_0)t) f(t) S_x, \quad (\text{E.12})$$

where the approximation is valid for $|\omega_{\text{MW}} - \omega_0| \gg \sigma_\omega$ and $1/(\omega_{\text{MW}} - \omega_0) \gg t$. The spin-

up probability is calculated to be

$$P_{\uparrow 0} = \sin^2 \left(\frac{1}{2} \int_{-\infty}^{\infty} \omega_1 \cos((\omega_{\text{MW}} - \omega_0)t) f(t) dt \right) \quad (\text{E.13})$$

$$= \sin^2 \left(\frac{\omega_1}{2} F(\omega_{\text{MW}} - \omega_0) \right) \quad (\text{E.14})$$

$$\sim \frac{\omega_1^2}{4} (F(\omega_{\text{MW}} - \omega_0))^2, \quad (\text{E.15})$$

where $F(\omega)$ is the Fourier transform of $f(t)$ and the approximation is valid when $\frac{\omega_1}{2} F(\omega_{\text{MW}} - \omega_0) \sim 0$.

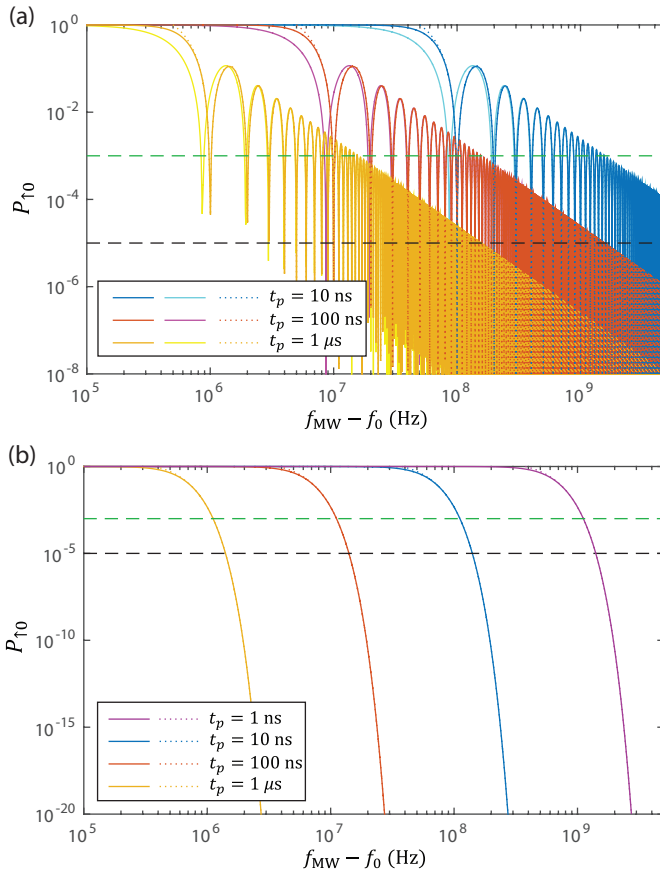


Figure E.1: Spin-up probability as a function of microwave frequency detuning for a rectangular π pulse in (a) and for a Gaussian π pulse in (b). (a,b) Purple, blue, red, and yellow lines represent Eq. E.14 for $t_p=1$ ns, 10 ns, 100 ns, and 1 μ s, respectively. Purple, blue, red and yellow dotted lines represent Eq. E.15 for $t_p=1$ ns, 10 ns, 100 ns, and 1 μ s, respectively. The data with $t_p=1$ ns is not shown in (a). The black and green horizontal dashed lines shows $P_{\uparrow 0} = 10^{-5}$ and $P_{\uparrow 0} = 10^{-3}$, respectively. (a) Light blue, pink, and light yellow lines represent Eq. E.5¹ for $t_p=10$ ns, 100 ns, and 1 μ s, respectively.

We plotted the spin-up probability when $\omega_1 t_p = \pi$ in the case of a rectangular pulse:

$$f(t) = \text{rect}\left(\frac{t}{t_p}\right), \quad (\text{E.16})$$

$$F(\omega) = t_p \frac{\sin\left(\frac{\omega t_p}{2}\right)}{\frac{\omega t_p}{2}}, \quad (\text{E.17})$$

by setting $t_p=10$ ns, 100 ns, and 1 μ s in Fig. E.1(a) and in the case of a Gaussian pulse:

$$f(t) = \exp\left(-\frac{\pi t^2}{t_p^2}\right), \quad (\text{E.18})$$

$$F(\omega) = t_p \exp\left(-\frac{t_p^2 \omega^2}{4\pi}\right), \quad (\text{E.19})$$

in Fig. E.1(b), by setting $t_p=1$ ns, 10 ns, 100 ns, and 1 μ s.

Fig. E.1 shows Gaussian shaped pulses can suppress unwanted spin-rotation better than rectangular pulses in all the cases. The identity pulse fidelity for a spin-down state as an initial state is given by

$$F(\mathcal{E}(|\downarrow\rangle\langle\downarrow|)|\downarrow\rangle\langle\downarrow|) = \text{Tr}(\mathcal{E}(|\downarrow\rangle\langle\downarrow|)|\downarrow\rangle\langle\downarrow|) = 1 - P_{10} \quad (\text{E.20})$$

In order to obtain this fidelity higher than 99.999%, P_{10} should be lower than 10^{-5} (black dashed line in Fig. E.1). Such conditions are directly applied for multiple qubits operated by an a.c. magnetic field sent to a global antenna or when leakage outside the qubit manifold is considered since the amplitude of a.c. magnetic field is the same order for untargeted qubits or untargeted transition. However, for multiple qubits operated by an a.c. electric field sent to different gates for each qubit, as investigated in this thesis, the condition is more relaxed since the amplitude of the electric field E^{AC} on untargeted qubits is much smaller than E^{AC} on a targeted qubit. In the case of fundamental harmonic driving (Ch. 7), if E^{AC} is 10 times smaller for untargeted qubits than for a targeted qubit, Rabi frequency ω_1 for untargeted qubits becomes 10 times smaller (Eq. 3.15). Thus, according to Eq. E.15, P_{10} becomes 100 times smaller. In this case, in order to obtain the identity pulse fidelity higher than 99.999%, we should look at the green dashed line in Fig. E.1.

E.2. RAMSEY FRINGE

In this section, we present additional information on analytic expressions of Ramsey fringes.

We derive 4.39 and Eq. 4.44 as analytic solutions of Eq. 4.35 in the case of $\omega_1 \gg \sigma_\omega$ and $\omega_1 \sim \sigma_\omega$, respectively.

¹Eq. E.5 is also valid for $|\omega_{MW} - \omega_0| \gg \sigma_\omega$ since the approximation in Eq. E.1 is also valid when $|\omega_{MW} - \omega_0| \gg \sigma_\omega$.

$\omega_1 \gg \sigma_\omega$

First we consider the case $\omega_1 \gg \sigma_\omega$ and we restrict ourselves to the case where $|\omega_{\text{MW}} - \omega_0| \ll \omega_1$ for simplicity in the same way as done in the Rabi oscillation section. We can take $\eta \ll \omega_1$ again and thus $\sin\left(\frac{\tau}{2}\Delta\omega\right) \sim 0$. By taking the second term of Eq. 4.34 as 0, The spin-up probability for a specific noise η becomes

$$p_{10} = 4 \sin^2 \theta \sin^2 \left(\frac{t_p}{2} \sqrt{\omega_1^2 + \Delta\omega^2} \right) \left[\cos \left(\frac{\tau}{2} \Delta\omega \right) \cos \left(\frac{t_p}{2} \sqrt{\omega_1^2 + \Delta\omega^2} \right) \right]^2 \quad (\text{E.21})$$

$$= \frac{\omega_1^2}{\omega_1^2 + \Delta\omega^2} \sin^2 \left(t_p \sqrt{\omega_1^2 + \Delta\omega^2} \right) \cos^2 \left(\frac{\tau}{2} \Delta\omega \right) \quad (\text{E.22})$$

and the spin-up probability including the effect of the time evolution of the noise becomes

$$P_{10} = (G * LT'R)(\omega_{\text{MW}} - \omega_0) \quad (\text{E.23})$$

with $T'(\eta) = \sin^2 \left(t_p \sqrt{\omega_1^2 + \eta^2} \right)$ and $R(\eta) = \cos^2 \left(\frac{\tau}{2} \eta \right)$.

In the same way as done in the Rabi oscillation section, Eq. E.1 is valid also here and under the assumed assumption $\omega_1 \gg \sigma_\omega$, $G(\eta)$ has a sufficiently narrow peak around 0 compared to $L(\eta)$ and thus Eq. E.23 becomes

$$P_{10} = T'(\omega_{\text{MW}} - \omega_0) L(\omega_{\text{MW}} - \omega_0) \int_{-\infty}^{\infty} G(\eta) R(\eta) d\eta \quad (\text{E.24})$$

$$= \frac{\omega_1^2}{\omega_1^2 + (\omega_{\text{MW}} - \omega_0)^2} \sin^2 \left(t_p \sqrt{\omega_1^2 + (\omega_{\text{MW}} - \omega_0)^2} \right) \frac{1 + e^{-\frac{\sigma_\omega^2 \tau^2}{2}}}{2} \quad (\text{E.25})$$

 $\omega_1 \sim \sigma_\omega$

We consider the case $\omega_1 \sim \sigma_\omega$ and we restrict ourselves to the case where $\omega_{\text{MW}} \sim \omega_0$ and $\omega_1 t_p = \frac{\pi}{2}$. We can take $\eta \ll \omega_1$ again and the spin-up probability for a specific noise η can be written with Eq. E.22 and the spin-up probability including the effect of the time evolution of the noise can be written with Eq. E.23.

$$P_{10} = (G * LT'R)(\omega_{\text{MW}} - \omega_0) \quad (\text{E.26})$$

$$= \int_{-\infty}^{\infty} \frac{1}{\sqrt{2\pi}\sigma_\omega} \exp \left(-\frac{(\eta + (\omega_{\text{MW}} - \omega_0))^2}{2\sigma_\omega^2} \right) \frac{\omega_1^2}{\omega_1^2 + \eta^2} \sin^2 \left(\frac{\pi}{2} \sqrt{\frac{\omega_1^2 + \eta^2}{\omega_1^2}} \right) \cos^2 \left(\frac{\tau}{2} \eta \right) d\eta \quad (\text{E.27})$$

$$\approx \int_{-\infty}^{\infty} \frac{1}{\sqrt{2\pi}\sigma_\omega} \exp \left(-\frac{(\eta + (\omega_{\text{MW}} - \omega_0))^2}{2\sigma_\omega^2} \right) \exp \left(-\frac{\eta^2}{\omega_1^2} \right) \cos^2 \left(\frac{\tau}{2} \eta \right) d\eta \quad (\text{E.28})$$

$$= \frac{1}{2} \frac{e^{-\left(\frac{(\omega_{\text{MW}} - \omega_0)^2}{2\sigma_\omega^2} + \frac{(\omega_{\text{MW}} - \omega_0)^2}{2(\sigma_\omega^2 + \omega_1^2)}\right)}}{\sqrt{1 + \left(\frac{\sigma_\omega^2}{\omega_1^2}\right)}} \left[1 + \exp \left(-\frac{1}{2} \frac{\sigma_\omega^2 \tilde{\omega}_1^2}{\sigma_\omega^2 + \tilde{\omega}_1^2} \tau^2 \right) \cos \left(\frac{\tilde{\omega}_1^2}{\sigma_\omega^2 + \tilde{\omega}_1^2} (\omega_{\text{MW}} - \omega_0) \right) \tau \right] \quad (\text{E.29})$$

with $\tilde{\omega}_1 = \omega_1 / \sqrt{2}$. From Eq. E.27 to Eq. E.28, we used the approximation

$$\frac{\omega_1^2}{\omega_1^2 + \eta^2} \sin^2 \left(\frac{\pi}{2} \sqrt{\frac{\omega_1^2 + \eta^2}{\omega_1^2}} \right) \sim \exp \left(-\frac{\eta^2}{\omega_1^2} \right) \text{ (Lu et al., 2011)}. \text{ The time constant of the Gaussian}$$

decay is $T_2^* = \frac{\sqrt{2}}{\sigma_\omega} \sqrt{1 + \frac{\sigma_\omega^2}{\omega_1^2}}$. This equation shows that a small Rabi frequency induces an artificial extension on the decay time.

F

PHYSICAL CONSTANTS

F.1. PHYSICAL CONSTANTS

Value of h (Plank constant)	Unit
$6.626068996 \times 10^{-34}$	J·s
$4.13566733 \times 10^{-15}$	eV·s
$6.62606896 \times 10^{-27}$	erg·s

Value of $\hbar (=h/2\pi)$ (Dirac constant)	Unit
$1.054571628 \times 10^{-34}$	J·s
$6.58211899 \times 10^{-16}$	eV·s
$1.054571628 \times 10^{-27}$	erg·s

Value of γ_e (gyro-magnetic ratio of the electron)	Unit
$-g_e \cdot \mu_B = -2 \cdot 9.274 \times 10^{-24}$	J/T
$-2 \cdot 9.274 \times 10^{-24} / \hbar = -1.76 \times 10^{11}$	rad· Hz/T
-28.0	GHz/T

Value of k_B (Boltzmann constant)	Unit
$1.3806503 \times 10^{-23}$	J/K
0.08614	$\mu\text{eV/mK}$

F.2. ENERGY CONVERSION

B (T)	for an electron ($g = 2$)			for a ^{29}Si nuclear spin		
	f (GHz)	hf (μeV)	$T = \frac{hf}{k_B}$ (mK)	f (GHz)	hf (μeV)	$T = \frac{hf}{k_B}$ (mK)
1	28.0	116	1340	8.47	35.0	406
0.95	26.6	110	1280	8.04	33.3	386
0.9	25.2	104	1210	7.62	31.5	366
0.85	23.8	98.4	1140	7.2	29.8	345
0.8	22.4	92.6	1080	6.77	28.0	325
0.75	21.0	86.9	1010	6.35	26.3	305
0.7	19.6	81.1	941	5.93	24.5	285
0.65	18.2	75.3	874	5.50	22.8	264
0.6	16.8	69.5	807	5.08	21.0	244
0.55	15.4	63.7	739	4.66	19.3	224
0.5	14.0	57.9	672	4.23	17.5	203
0.45	12.6	52.1	605	3.81	15.8	183
0.4	11.2	46.3	538	3.39	14	163
0.35	9.80	40.5	471	2.96	12.3	142
0.3	8.40	34.7	403	2.54	10.5	122
0.25	7.00	29.0	336	2.12	8.75	102
0.2	5.60	23.2	269	1.69	7.00	81.3
0.15	4.20	17.4	202	1.27	5.25	61.0
0.1	2.80	11.6	134	0.847	3.50	40.6
0.05	1.40	5.79	67.2	0.423	1.75	20.3
0.118	1.00	4.14	48.0	0.302	1.25	14.5

G

MAGNETIC FIELD GRADIENT CREATED BY MICRO-MAGNETS

In this appendix chapter, we first show the magnetic field gradient created by micro-magnets when the external magnetic field is applied along the x axis or y axis. Here we take the heterostructure growth direction as z axis and x and y axes as shown in the figures below.

G.1. MAGNETIC FIELD GRADIENTS THE EXTERNAL MAGNETIC FIELD IS APPLIED ALONG THE x AXIS

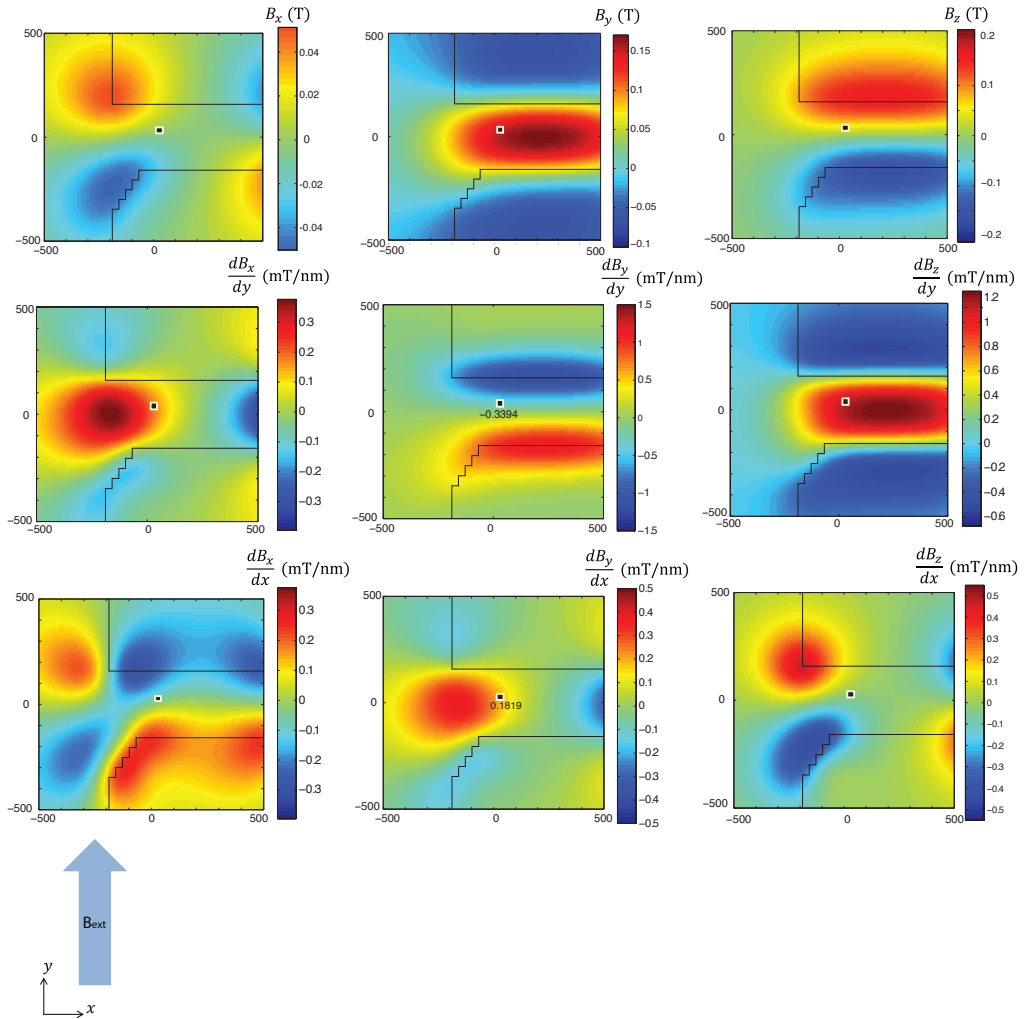
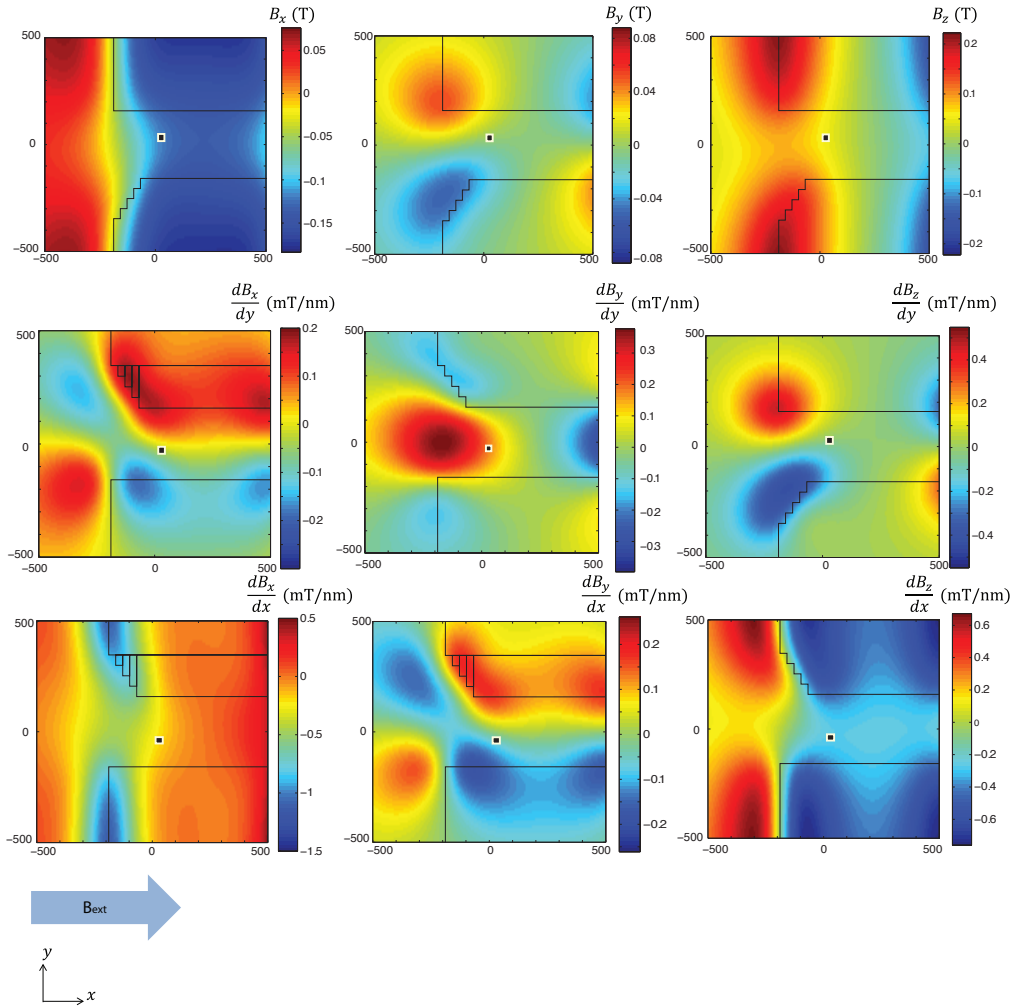


Figure G.1: Numerically computed x , y and z components of the magnetic field and their gradients along the x and y axes induced by the micromagnets when the external magnetic field along the y axis in the plane of the Si quantum well, for fully magnetized micromagnets. The black solid lines indicate the edges of the micromagnet as simulated. The black rectangles shows the estimated position of the dot.

G.2. MAGNETIC FIELD GRADIENTS THE EXTERNAL MAGNETIC FIELD IS APPLIED ALONG THE y AXIS



G

Figure G.2: The same as in Fig. G.1 when the external magnetic field along the x axis.

BIBLIOGRAPHY

- Abe, E., Isoya, J., and Itoh, K. M., [Physica B: Condensed Matter](#) **376-377**, 28 (2006).
- Abe, E., Tyryshkin, A. M., Tojo, S., Morton, J. J. L., Witzel, W. M., Fujimoto, A., Ager, J. W., Haller, E. E., Isoya, J., Lyon, S. A., Thewalt, M. L. W., and Itoh, K. M., [Physical Review B](#) **82**, 121201 (2010).
- Ahn, J., Weinacht, T. C., and Bucksbaum, P. H., [Science](#) **287**, 463 (2000).
- Akhtar, W., Filidou, V., Sekiguchi, T., Kawakami, E., Itahashi, T., Vlasenko, L., Morton, J. J. L., and Itoh, K. M., [Physical Review Letters](#) **108**, 097601 (2012).
- Álvarez, G. A., Souza, A. M., and Suter, D., [Physical Review A](#) **85**, 052324 (2012), [arXiv:1203.0252](#) .
- Amasha, S., MacLean, K., Radu, I. P., Zumbühl, D. M., Kastner, M. A., Hanson, M. P., and Gossard, A. C., [Physical Review B](#) **78**, 041306 (2008).
- Assali, L. V. C., Petrilli, H. M., Capaz, R. B., Koiller, B., Hu, X., and Das Sarma, S., [Physical Review B](#) **83**, 165301 (2011).
- Baart, T. A., Eendebak, P. T., Reichl, C., Wegscheider, W., and Vandersypen, L. M. K., (2016a), [arXiv:1603.02274](#) .
- Baart, T. A., Fujita, T., Reichl, C., Wegscheider, W., and Vandersypen, L. M. K., (2016b), [arXiv:1603.03433](#) .
- Baart, T. A., Jovanovic, N., Reichl, C., Wegscheider, W., and Vandersypen, L. M. K., (2016c), [arXiv:1606.00292](#) .
- Baart, T. A., Shafiei, M., Fujita, T., Reichl, C., Wegscheider, W., and Vandersypen, L. M. K., [Nature Nanotechnology](#) **11**, 330 (2016d).
- Ball, H., Stace, T. M., Flammia, S. T., and Biercuk, M. J., (2015), [arXiv:1504.05307](#) .
- Banholzer, W. F. and Anthony, T. R., [Thin Solid Films](#) **212**, 1 (1992).
- Barends, R., Kelly, J., Megrant, A., Veitia, A., Sank, D., Jeffrey, E., White, T. C., Mutus, J., Fowler, A. G., Campbell, B., Chen, Y., Chen, Z., Chiaro, B., Dunsworth, A., Neill, C., O'Malley, P., Roushan, P., Vainsencher, A., Wenner, J., Korotkov, A. N., Cleland, A. N., and Martinis, J. M., [Nature](#) **508**, 500 (2014).
- Barthel, C., Kjærgaard, M., Medford, J., Stopa, M., Marcus, C. M., Hanson, M. P., and Gossard, A. C., [Physical Review B](#) **81**, 161308 (2010).

- Beaudoin, F. and Coish, W. A., [Physical Review B **88**, 085320 \(2013\)](#).
- Becker, P., Schiel, D., Pohl, H.-J., Kaliteevski, A. K., Godisov, O. N., Churbanov, M. F., Devyatikh, G. G., Gusev, A. V., Bulanov, A. D., Adamchik, S. A., Gavva, V. A., Kovalev, I. D., Abrosimov, N. V., Hallmann-Seiffert, B., Riemann, H., Valkiers, S., Taylor, P., Bièvre, P. D., and Dianov, E. M., [Measurement Science and Technology **17**, 1854 \(2006\)](#).
- Benioff, P., [Journal of Statistical Physics **22**, 563 \(1980\)](#).
- Bergli, J., Galperin, Y. M., and Altshuler, B. L., [New Journal of Physics **11**, 025002 \(2009\)](#).
- Bernien, H., Hensen, B., Pfaff, W., Koolstra, G., Blok, M. S., Robledo, L., Taminiiau, T. H., Markham, M., Twitchen, D. J., Childress, L., and Hanson, R., [Nature **497**, 86 \(2013\)](#).
- Biercuk, M. J., Uys, H., VanDevender, A. P., Shiga, N., Itano, W. M., and Bollinger, J. J., [Nature **458**, 996 \(2009\)](#).
- Bloch, I., [Nature Physics **1**, 23 \(2005\)](#).
- Bloch, I., Dalibard, J., and Nascimbène, S., [Nature Physics **8**, 267 \(2012\)](#).
- Bluhm, H., Foletti, S., Mahalu, D., Umansky, V., and Yacoby, A., [Physical Review Letters **105**, 216803 \(2010a\)](#).
- Bluhm, H., Foletti, S., Neder, I., Rudner, M., Mahalu, D., Umansky, V., and Yacoby, A., [Nature Physics **7**, 109 \(2010b\)](#).
- Borhani, M. and Hu, X., [Physical Review B **85**, 125132 \(2012\)](#).
- Borselli, M. G., Eng, K., Croke, E. T., Maune, B. M., Huang, B., Ross, R. S., Kiselev, A. A., Deelman, P. W., Alvarado-Rodriguez, I., Schmitz, A. E., Sokolich, M., Holabird, K. S., Hazard, T. M., Gyure, M. F., and Hunter, A. T., [Applied Physics Letters **99**, 063109 \(2011\)](#).
- Boscaino, R., Ciccarello, I., Cusumano, C., and Strandberg, M. W. P., [Physical Review B **3**, 2675 \(1971\)](#).
- Bowdrey, M. D., Oi, D. K., Short, A. J., Banaszek, K., and Jones, J. A., [Physics Letters A **294**, 258 \(2002\)](#).
- Boykin, T. B., Klimeck, G., Eriksson, M. A., Friesen, M., Coppersmith, S. N., von Allmen, P., Oyafuso, F., and Lee, S., [Applied Physics Letters **84**, 115 \(2004\)](#).
- Braakman, F. R., Danon, J., Schreiber, L. R., Wegscheider, W., and Vandersypen, L. M. K., [Physical Review B **89**, 075417 \(2014\)](#).
- Braun, M. and Burkard, G., [Physical Review Letters **101**, 036802 \(2008\)](#).
- Bravyi, S. and Kitaev, A., [Physical Review A **71**, 022316 \(2005\)](#).
- Brown, K. R., Kim, J., and Monroe, C., (2016), [arXiv:1602.02840](#).

- Bruder, C. and Schoeller, H., [Physical Review Letters](#) **72**, 1076 (1994).
- Brumfiel, G., [Nature](#) (2009), 10.1038/news.2009.50.
- Brumfiel, G., [Nature](#) **491**, 322 (2012).
- Brune, M., Nussenzveig, P., Schmidt-Kaler, F., Bernardot, F., Maali, A., Raimond, J. M., and Haroche, S., [Physical Review Letters](#) **72**, 3339 (1994).
- Brune, P., Bruder, C., and Schoeller, H., [Physical Review B](#) **56**, 4730 (1997).
- Brunner, R., Shin, Y.-S., Obata, T., Pioro-Ladrière, M., Kubo, T., Yoshida, K., Taniyama, T., Tokura, Y., and Tarucha, S., [Physical Review Letters](#) **107**, 146801 (2011).
- Bylander, J., Gustavsson, S., Yan, F., Yoshihara, F., Harrabi, K., Fitch, G., Cory, D. G., Nakamura, Y., Tsai, J.-S., and Oliver, W. D., [Nature Physics](#) **7**, 565 (2011).
- Carr, H. and Purcell, E., [Physical Review](#) **94**, 630 (1954).
- Cassidy, M., Kammhuber, J., Car, D., Plissard, S., Bakkers, E., Dicarlo, L., and Kouwenhoven, L., in *APS Meeting Abstracts* (2014).
- Chan, I. H., Westervelt, R. M., Maranowski, K. D., and Gossard, A. C., [Applied Physics Letters](#) **80**, 1818 (2002).
- Chekhovich, E. A., Makhonin, M. N., Tartakovskii, A. I., Yacoby, A., Bluhm, H., Nowack, K. C., and Vandersypen, L. M. K., [Nature materials](#) **12**, 494 (2013).
- Childress, L., Gurudev Dutt, M. V., Taylor, J. M., Zibrov, A. S., Jelezko, F., Wrachtrup, J., Hemmer, P. R., and Lukin, M. D., [Science](#) **314**, 281 (2006).
- Childress, L., Sørensen, A. S., and Lukin, M. D., [Physical Review A](#) **69**, 042302 (2004).
- Chow, J. M., Gambetta, J. M., Tornberg, L., Koch, J., Bishop, L. S., Houck, A. A., Johnson, B. R., Frunzio, L., Girvin, S. M., and Schoelkopf, R. J., [Physical Review Letters](#) **102**, 090502 (2009).
- Chuang, I. L. and Nielsen, M. A., [Journal of Modern Optics](#) **44**, 2455 (1997), [arXiv:quant-ph/9610001](#) .
- Chuang, I. L., Vandersypen, L. M. K., Zhou, X., Leung, D. W., and Lloyd, S., [Nature](#) **393**, 143 (1998).
- Churchill, H. O. H., Bestwick, A. J., Harlow, J. W., Kuemmeth, F., Marcos, D., Stwertka, C. H., Watson, S. K., and Marcus, C. M., [Nature Physics](#) **5**, 321 (2009).
- Clarke, J. and Wilhelm, F. K., [Nature](#) **453**, 1031 (2008).
- Clerk, A. A., Devoret, M. H., Girvin, S. M., Marquardt, F., and Schoelkopf, R. J., [Reviews of Modern Physics](#) **82**, 1155 (2010).

- Cohen-Tannoudji, C., Dupont-Roc, J., and Grynberg, G., eds., *Atom–Photon Interactions* (Wiley-VCH Verlag GmbH, Weinheim, Germany, 1998).
- Culcer, D., Saraiva, A. L., Koiller, B., Hu, X., and Das Sarma, S., *Physical Review Letters* **108**, 126804 (2012).
- Cywinski, L., *Acta Physica Polonica A* **119**, 576 (2011), 1009.4466 .
- Cywinski, L., Lutchyn, R. M., Nave, C. P., and Das Sarma, S., *Physical Review B* **77**, 174509 (2008).
- Cywinski, L., Witzel, W. M., and Das Sarma, S., *Physical Review Letters* **102**, 057601 (2009).
- Dankert, C., Cleve, R., Emerson, J., and Livine, E., *Physical Review A* **80**, 012304 (2009).
- Danon, J. and Rudner, M. S., *Physical Review Letters* **113**, 247002 (2014).
- Datta, S., *Electronic Transport in Mesoscopic Systems*, Cambridge Studies in Semiconductor Physi (Cambridge University Press, 1997).
- Davies, J. H., *The Physics of Low-dimensional Semiconductors: An Introduction* (1998).
- De, A., Pryor, C. E., and Flatté, M. E., *Physical Review Letters* **102**, 017603 (2009).
- Dehollain, J. P., Simmons, S., Muhonen, J. T., Kalra, R., Laucht, A., Hudson, F., Itoh, K. M., Jamieson, D. N., McCallum, J. C., Dzurak, A. S., and Morello, A., *Nature Nanotechnology* (2015), 10.1038/nnano.2015.262.
- Deng, G.-W., Wei, D., Li, S.-X., Johansson, J. R., Kong, W.-C., Li, H.-O., Cao, G., Xiao, M., Guo, G.-C., Nori, F., Jiang, H.-W., and Guo, G.-P., *Nano letters* **15**, 6620 (2015).
- Denk, W., Strickler, J., and Webb, W., *Science* **248**, 73 (1990).
- Dennis, E., Kitaev, A., Landahl, A., and Preskill, J., *Journal of Mathematical Physics* **43**, 4452 (2002).
- Deutsch, D., *Proceedings of the Royal Society A: Mathematical, Physical and Engineering Sciences* **400**, 97 (1985).
- Deutsch, D. and Jozsa, R., *Proceedings of the Royal Society A: Mathematical, Physical and Engineering Sciences* **439**, 553 (1992).
- Devoret, M. H. and Schoelkopf, R. J., *Science* **339**, 1169 (2013).
- Devoret, M. H., Wallraff, A., and Martinis, J. M., (2004), [arXiv:cond-mat/0411174](https://arxiv.org/abs/cond-mat/0411174) .
- Dial, O. E., Shulman, M. D., Harvey, S. P., Bluhm, H., Umansky, V., and Yacoby, A., *Physical Review Letters* **110**, 146804 (2013).
- DiVincenzo, D. P., *Topics in Quantum Computers*, edited by L. L. Sohn, L. P. Kouwenhoven, and G. Schön, Mesoscopic Electron Transport (Springer Netherlands, Dordrecht, 1997).

- DiVincenzo, D. P., (2000), [arXiv:quant-ph/0002077](#) .
- Dobrovitski, V. V., Feiguin, A. E., Hanson, R., and Awschalom, D. D., [Physical Review Letters](#) **102**, 237601 (2009).
- Dovinos, D. and Williams, D., [Physical Review B](#) **72**, 085313 (2005).
- Eckstein, J. N. and Levy, J., [MRS Bulletin](#) **38**, 783 (2013).
- Elzerman, J. M., Hanson, R., Willems Van Beveren, L. H., Witkamp, B., Vandersypen, L. M. K., and Kouwenhoven, L. P., [Nature](#) **430**, 431 (2004), [arXiv:cond-mat/0411232](#) .
- Emerson, J., [Canadian Journal of Physics](#) (2008).
- Emerson, J., Alicki, R., and Zyczkowski, K., [Journal of Optics B: Quantum and Semiclassical Optics](#) **7**, S347 (2005).
- Emerson, J., Silva, M., Moussa, O., Ryan, C., Laforest, M., Baugh, J., Cory, D. G., and Laflamme, R., [Science](#) **317**, 1893 (2007).
- Eng, K., Ladd, T. D., Smith, A., Borselli, M. G., Kiselev, A. A., Fong, B. H., Holabird, K. S., Hazard, T. M., Huang, B., Deelman, P. W., Milosavljevic, I., Schmitz, A. E., Ross, R. S., Gyure, M. E., and Hunter, A. T., [Science advances](#) **1**, e1500214 (2015).
- Epstein, J. M., Cross, A. W., Magesan, E., and Gambetta, J. M., [Physical Review A](#) **89**, 062321 (2014).
- Feher, G., [Physical Review](#) **103**, 834 (1956).
- Feher, G., [Physical Review](#) **114**, 1219 (1959).
- Feynman, R. P., [International Journal of Theoretical Physics](#) **21**, 467 (1982).
- Fogarty, M. A., Veldhorst, M., Harper, R., Yang, C. H., Bartlett, S. D., Flammia, S. T., and Dzurak, A. S., [Physical Review A](#) **92**, 022326 (2015).
- Forster, F., Mühlbacher, M., Schuh, D., Wegscheider, W., and Ludwig, S., [Physical Review B](#) **91**, 195417 (2015).
- Fowler, A. G., Mariantoni, M., Martinis, J. M., and Cleland, A. N., [Physical Review A](#) **86**, 032324 (2012).
- Foxman, E., McEuen, P., Meirav, U., Wingreen, N., Meir, Y., Belk, P., Belk, N., Kastner, M., and Wind, S., [Physical Review B](#) **47**, 10020 (1993).
- Franken, P., Hill, A., Peters, C., and Weinreich, G., [Physical Review Letters](#) **7**, 118 (1961).
- Frey, T., Leek, P. J., Beck, M., Blais, A., Ihn, T., Ensslin, K., and Wallraff, A., [Physical Review Letters](#) **108**, 046807 (2012).

- Friesen, M., Chutia, S., Tahan, C., and Coppersmith, S. N., [Physical Review B](#) **75**, 115318 (2007).
- Friesen, M. and Coppersmith, S. N., [Physical Review B](#) **81**, 115324 (2010).
- Friesen, M., Eriksson, M. A., and Coppersmith, S. N., [Applied Physics Letters](#) **89**, 202106 (2006).
- Fu, Y., Cheng, X., and Yang, Z., [physica status solidi \(a\)](#) **202**, 1150 (2005).
- Fujisawa, T., Austing, D. G., Tokura, Y., Hirayama, Y., and Tarucha, S., [Nature](#) **419**, 278 (2002).
- Fujisawa, T., Oosterkamp, T. H., van der Wiel, W. G., Broer, B. W., Aguado, R., Tarucha, S., and Kouwenhoven, L. P., [Science](#) **282**, 932 (1998).
- Fujita, T., Morimoto, K., Kiyama, H., Allison, G., Larsson, M., Ludwig, A., Valentin, S. R., Wieck, A. D., Oiwa, A., and Tarucha, S., (2015), [arXiv:1504.03696](#) .
- Gamble, J. K., Eriksson, M. A., Coppersmith, S. N., and Friesen, M., [Physical Review B](#) **88**, 035310 (2013).
- Goldman, J., Ladd, T., Yamaguchi, F., and Yamamoto, Y., [Applied Physics A](#) **71**, 11 (2000).
- Gordon, J. P. and Bowers, K. D., [Physical Review Letters](#) **1**, 368 (1958).
- Goswami, S., Slinker, K. A., Friesen, M., McGuire, L. M., Truitt, J. L., Tahan, C., Klein, L. J., Chu, J. O., Mooney, P. M., van der Weide, D. W., Joynt, R., Coppersmith, S. N., and Eriksson, M. A., [Nature Physics](#) **3**, 41 (2007).
- Gromov, I. and Schweiger, A., [Journal of magnetic resonance \(San Diego, Calif. : 1997\)](#) **146**, 110 (2000).
- Grover, L. K., [Pramana](#) **56**, 333 (2001).
- Gullion, T., Baker, D. B., and Conradi, M. S., [Journal of Magnetic Resonance](#) **89**, 479 (1990).
- Haeberlen, U., [High resolution NMR in solids: selective averaging](#) (Academic Press, 1976) Chap. Averaging in Ordinary Coordinate and Spin Spaces, p. 45.
- Hahn, E., [Physical Review](#) **80**, 580 (1950).
- Hanson, R., Petta, J. R., Tarucha, S., and Vandersypen, L. M. K., [Reviews of Modern Physics](#) **79**, 1217 (2007).
- Hao, X., Ruskov, R., Xiao, M., Tahan, C., and Jiang, H., [Nature communications](#) **5**, 3860 (2014).
- Hayashi, T., Fujisawa, T., Cheong, H. D., Jeong, Y. H., and Hirayama, Y., [Physical Review Letters](#) **91**, 226804 (2003).

- Heinz, T. F., Chen, C. K., Ricard, D., and Shen, Y. R., [Physical Review Letters](#) **48**, 478 (1982).
- Hendrichs, S., *Si/SiGe quantum dots for highly coherent spin qubits*, Master's thesis, Delft University of Technology (2011).
- Higginbotham, A. P., Larsen, T. W., Yao, J., Yan, H., Lieber, C. M., Marcus, C. M., and Kuemmeth, F., [Nano letters](#) **14**, 3582 (2014).
- Hoffmann, E. A. and Linke, H., [Journal of Low Temperature Physics](#) **154**, 161 (2009).
- Horodecki, M., Horodecki, P., and Horodecki, R., [Physical Review A](#) **60**, 1888 (1999).
- Hu, X., Liu, Y.-x., and Nori, F., [Physical Review B](#) **86**, 035314 (2012).
- Huang, P. and Hu, X., [Physical Review B](#) **90**, 235315 (2014).
- Itoh, K., Hansen, W., Haller, E., Farmer, J., Ozhogin, V., Rudnev, A., and Tikhomirov, A., [Journal of Materials Research](#) **8**, 1341 (1993).
- Itoh, K. M., [Solid State Communications](#) **133**, 747 (2005).
- Itoh, K. M., Kato, J., Uemura, M., Kaliteevskii, A. K., Godisov, O. N., Devyatych, G. G., Bulanov, A. D., Gusev, A. V., Kovalev, I. D., Sennikov, P. G., Pohl, H.-J., Abrosimov, N. V., and Riemann, H., [Japanese Journal of Applied Physics](#) **42**, 6248 (2003).
- Johnson, a. C., Petta, J. R., Taylor, J. M., Yacoby, a., Lukin, M. D., Marcus, C. M., Hanson, M. P., and Gossard, a. C., [Nature](#) **435**, 925 (2005).
- Jones, J. A., Mosca, M., and Hansen, R. H., [Nature](#) **393**, 344 (1998).
- Jones, N. C., *Layered Architectures for Quantum Computers and Quantum Repeaters*, edited by Y. Yamamoto and K. Semba, Principles and Methods of Quantum Information Technologies, Vol. 911 (Springer Japan, Tokyo, 2016).
- Jones, N. C., Van Meter, R., Fowler, A. G., McMahon, P. L., Kim, J., Ladd, T. D., and Yamamoto, Y., [Physical Review X](#) **2**, 031007 (2012).
- Jozsa, R., [Journal of Modern Optics](#) **41**, 2315 (1994).
- Kane, B. E., [Nature](#) **393**, 133 (1998).
- Kawakami, E., Scarlino, P., Schreiber, L. R., Prance, J. R., Savage, D. E., Lagally, M. G., Eriksson, M. A., and Vandersypen, L. M. K., [Applied Physics Letters](#) **103**, 132410 (2013).
- Kawakami, E., Scarlino, P., Ward, D. R., Braakman, F. R., Savage, D. E., Lagally, M. G., Friesen, M., Coppersmith, S. N., Eriksson, M. A., and Vandersypen, L. M. K., [Nature nanotechnology](#) **9**, 666 (2014).
- Keizer, H., *Towards single-shot read-out of two-electron spin states in lateral few electron quantum dots*, Master's thesis, Delft University of Technology (2007).

- Kelly, J., Barends, R., Fowler, A. G., Megrant, A., Jeffrey, E., White, T. C., Sank, D., Mutus, J. Y., Campbell, B., Chen, Y., Chen, Z., Chiaro, B., Dunsworth, A., Hoi, I.-C., Neill, C., O'Malley, P. J. J., Quintana, C., Roushan, P., Vainsencher, A., Wenner, J., Cleland, A. N., and Martinis, J. M., *Nature* **519**, 66 (2015).
- Khaetskii, A. V. and Nazarov, Y. V., *Physical Review B* **64**, 125316 (2001).
- Kharche, N., Prada, M., Boykin, T. B., and Klimeck, G., *Applied Physics Letters* **90**, 092109 (2007).
- Khodjasteh, K. and Lidar, D. A., *Physical Review Letters* **95**, 180501 (2005).
- Khodjasteh, K. and Viola, L., *Physical Review Letters* **102**, 080501 (2009).
- Kielipinski, D., Monroe, C., and Wineland, D. J., *Nature* **417**, 709 (2002).
- Kim, D., Shi, Z., Simmons, C. B., Ward, D. R., Prance, J. R., Koh, T. S., Gamble, J. K., Savage, D. E., Lagally, M. G., Friesen, M., Coppersmith, S. N., and Eriksson, M. A., *Nature* **511**, 70 (2014).
- Kim, D., Ward, D. R., Simmons, C. B., Savage, D. E., Lagally, M. G., Friesen, M., Coppersmith, S. N., and Eriksson, M. A., *npj Quantum Information* **1**, 15004 (2015).
- Kim, J., Maunz, P., Kim, T., Hussman, J., Noek, R., Mehta, A., Monroe, C., Ralph, T., and Lam, P. K., in *QUANTUM COMMUNICATION, MEASUREMENT AND COMPUTING (QCMC): The Tenth International Conference*, Vol. 1363 (AIP Publishing, 2011) pp. 190–193.
- Klauder, J. R. and Anderson, P. W., *Physical Review* **125**, 912 (1962).
- Kleinjung, T., Aoki, K., Franke, J., Lenstra, A. K., Thomé, E., Bos, J. W., Gaudry, P., Kruppa, A., Montgomery, P. L., Osvik, D. A., Riele, H., Timofeev, A., and Zimmermann, P., *Advances in Cryptology*, edited by T. Rabin (Springer Berlin Heidelberg, Berlin, Heidelberg, 2010) Chap. Factorization of a 768-Bit RSA Modulus, pp. 333–350.
- Knill, E., *Nature* **434**, 39 (2005).
- Knill, E., Leibfried, D., Reichle, R., Britton, J., Blakestad, R., Jost, J., Langer, C., Ozeri, R., Seidelin, S., and Wineland, D., *Physical Review A* **77**, 012307 (2008).
- Koh, T. S., Gamble, J. K., Friesen, M., Eriksson, M. A., and Coppersmith, S. N., *Physical Review Letters* **109**, 250503 (2012).
- Konig, K., *Journal of Microscopy* **200**, 83 (2000).
- Koppens, E., Nowack, K., and Vandersypen, L., *Physical Review Letters* **100**, 236802 (2008).
- Koppens, F. H. L., Buizert, C., Tielrooij, K. J., Vink, I. T., Nowack, K. C., Meunier, T., Kouwenhoven, L. P., and Vandersypen, L. M. K., *Nature* **442**, 766 (2006).

- Koppens, F. H. L., Folk, J. a., Elzerman, J. M., Hanson, R., van Beveren, L. H. W., Vink, I. T., Tranitz, H. P., Wegscheider, W., Kouwenhoven, L. P., and Vandersypen, L. M. K., *Science* **309**, 1346 (2005).
- Koppens, F. H. L., Klauser, D., Coish, W. A., Nowack, K. C., Kouwenhoven, L. P., Loss, D., and Vandersypen, L. M. K., *Physical Review Letters* **99**, 106803 (2007).
- Kouwenhoven, L., Jauhar, S., Orenstein, J., McEuen, P., Nagamune, Y., Motohisa, J., and Sakaki, H., *Physical Review Letters* **73**, 3443 (1994a).
- Kouwenhoven, L., Johnson, A., van der Vaart NC,, Harmans, C., and Foxon, C., *Physical Review Letters* **67**, 1626 (1991).
- Kouwenhoven, L. P., Jauhar, S., McCormick, K., Dixon, D., McEuen, P. L., Nazarov, Y. V., van der Vaart, N. C., and Foxon, C. T., *Physical Review B* **50**, 2019 (1994b).
- Kubo, R., Toda, M., and Hashitsume, N., *Statistical Physics II*, Springer Series in Solid-State Sciences, Vol. 31 (Springer Berlin Heidelberg, Berlin, Heidelberg, 1991).
- Lachance-Quirion, D., Camirand Lemyre, J., Bergeron, L., Sarra-Bournet, C., and Pioro-Ladrière, M., *Applied Physics Letters* **107**, 223103 (2015).
- Ladd, T. D., Goldman, J. R., Yamaguchi, F., Yamamoto, Y., Abe, E., and Itoh, K. M., *Physical Review Letters* **89**, 017901 (2002).
- Ladd, T. D., Jelezko, F., Laflamme, R., Nakamura, Y., Monroe, C., and O'Brien, J. L., *Nature* **464**, 45 (2010).
- Laird, E. A., Barthel, C., Rashba, E. I., Marcus, C. M., Hanson, M. P., and Gossard, A. C., *Semiconductor Science and Technology* **24**, 064004 (2009).
- Laird, E. A., Pei, F., and Kouwenhoven, L. P., *Nature nanotechnology* **8**, 565 (2013).
- de Lange, G., Wang, Z. H., Ristè, D., Dobrovitski, V. V., and Hanson, R., *Science* **330**, 60 (2010).
- Levitt, M. H., *Progress in Nuclear Magnetic Resonance Spectroscopy* **18**, 61 (1986).
- Linden, N. and Popescu, S., *Physical Review Letters* **87**, 047901 (2001).
- Loss, D. and DiVincenzo, D. P., *Physical Review A* **57**, 120 (1998).
- Lu, J., Hoehne, F., Stegner, A. R., Dreher, L., Stutzmann, M., Brandt, M. S., and Huebl, H., *Physical Review B* **83**, 235201 (2011).
- Magesan, E., Gambetta, J. M., and Emerson, J., *Physical Review Letters* **106**, 180504 (2011).
- Magesan, E., Gambetta, J. M., and Emerson, J., *Physical Review A* **85**, 042311 (2012).

- Magesan, E., Gambetta, J. M., Johnson, B. R., Ryan, C. A., Chow, J. M., Merkel, S. T., da Silva, M. P., Keefe, G. A., Rothwell, M. B., Ohki, T. A., Ketchen, M. B., and Steffen, M., [Physical Review Letters](#) **109**, 080505 (2012).
- Mani, P., Nakpathomkun, N., Hoffmann, E. A., and Linke, H., [Nano letters](#) **11**, 4679 (2011).
- Maudsley, A., [Journal of Magnetic Resonance](#) (1969) **69**, 488 (1986).
- Maune, B. M., Borselli, M. G., Huang, B., Ladd, T. D., Deelman, P. W., Holabird, K. S., Kiselev, A. A., Alvarado-Rodriguez, I., Ross, R. S., Schmitz, A. E., Sokolich, M., Watson, C. A., Gyure, M. F., and Hunter, A. T., [Nature](#) **481**, 344 (2012).
- Medford, J., Beil, J., Taylor, J. M., Bartlett, S. D., Doherty, A. C., Rashba, E. I., DiVincenzo, D. P., Lu, H., Gossard, A. C., and Marcus, C. M., [Nature nanotechnology](#) **8**, 654 (2013).
- Medford, J., Cywiński, L., Barthel, C., Marcus, C. M., Hanson, M. P., and Gossard, A. C., [Physical Review Letters](#) **108**, 086802 (2012).
- Meiboom, S. and Gill, D., [Review of Scientific Instruments](#) **29**, 688 (1958).
- Merkulov, I. A., Efros, A. L., and Rosen, M., [Physical Review B](#) **65**, 205309 (2002).
- Monroe, C., Meekhof, D., King, B., Itano, W., and Wineland, D., [Physical Review Letters](#) **75**, 4714 (1995).
- Morello, A., Pla, J. J., Zwanenburg, F. A., Chan, K. W., Tan, K. Y., Huebl, H., Möttönen, M., Nugroho, C. D., Yang, C., van Donkelaar, J. A., Alves, A. D. C., Jamieson, D. N., Escott, C. C., Hollenberg, L. C. L., Clark, R. G., and Dzurak, A. S., [Nature](#) **467**, 687 (2010).
- Morton, J. J. L., McCamey, D. R., Eriksson, M. A., and Lyon, S. A., [Nature](#) **479**, 345 (2011).
- Morton, J. J. L., Tyryshkin, A. M., Brown, R. M., Shankar, S., Lovett, B. W., Ardavan, A., Schenkel, T., Haller, E. E., Ager, J. W., and Lyon, S. a., [Nature](#) **455**, 1085 (2008).
- Muhonen, J. T., Dehollain, J. P., Laucht, A., Hudson, F. E., Kalra, R., Sekiguchi, T., Itoh, K. M., Jamieson, D. N., McCallum, J. C., Dzurak, A. S., and Morello, A., [Nature nanotechnology](#) **9**, 986 (2014).
- Muhonen, J. T., Laucht, A., Simmons, S., Dehollain, J. P., Kalra, R., Hudson, F. E., Freer, S., Itoh, K. M., Jamieson, D. N., McCallum, J. C., Dzurak, A. S., and Morello, A., [Journal of physics. Condensed matter : an Institute of Physics journal](#) **27**, 154205 (2015).
- Nadj-Perge, S., Pribiag, V. S., van den Berg, J. W. G., Zuo, K., Plissard, S. R., Bakkers, E. P. A. M., Frolov, S. M., and Kouwenhoven, L. P., [Physical Review Letters](#) **108**, 166801 (2012).
- Nakamura, Y., Pashkin, Y. A., and Tsai, J. S., [Nature](#) **398**, 786 (1999).
- Nakamura, Y., Pashkin, Y. A., and Tsai, J. S., [Physical Review Letters](#) **87**, 246601 (2001).

- Nielsen, M. and Chuang, I., *Quantum Computation and Quantum Information: 10th Anniversary Edition* (Cambridge University Press, 2011).
- Nielsen, M. A., *Physics Letters A* **303**, 249 (2002).
- Nigg, D., Müller, M., Martinez, E. A., Schindler, P., Hennrich, M., Monz, T., Martin-Delgado, M. A., and Blatt, R., *Science* **345**, 302 (2014).
- Nowack, K., *Electrical Control, Read-out and Initialization of Single Electron Spins*, Ph.D. thesis, Delft University of Technology (2009).
- Nowack, K. C., Koppens, F. H. L., Nazarov, Y. V., and Vandersypen, L. M. K., *Science* **318**, 1430 (2007).
- Nowack, K. C., Shafiei, M., Laforest, M., Prawiroatmodjo, G. E. D. K., Schreiber, L. R., Reichl, C., Wegscheider, W., and Vandersypen, L. M. K., *Science* **333**, 1269 (2011).
- Nowak, M. P., Szafran, B., and Peeters, F. M., *Physical Review B* **86**, 125428 (2012).
- Obata, T., Pioro-Ladrière, M., Tokura, Y., Shin, Y.-S., Kubo, T., Yoshida, K., Taniyama, T., and Tarucha, S., *Physical Review B* **81**, 81.085317 (2010).
- Oliver, W. D., Yu, Y., Lee, J. C., Berggren, K. K., Levitov, L. S., and Orlando, T. P., *Science* **310**, 1653 (2005).
- Ono, K., Austing, D. G., Tokura, Y., and Tarucha, S., *Science* **297**, 1313 (2002).
- Oosterkamp, T. H., Fujisawa, T., van der Wiel, W. G., Ishibashi, K., Hijman, R. V., Tarucha, S., and Kouwenhoven, L. P., *Nature* **395**, 873 (1998).
- Oosterkamp, T. H., Kouwenhoven, L. P., Koolen, A. E. A., van der Vaart, N. C., and Harman, C. J. P. M., *Physica Scripta* **T69**, 98 (1997).
- Osika, E. N., Mrenca, A., and Szafran, B., *Physical Review B* **90**, 125302 (2014).
- Pei, F., Laird, E. A., Steele, G. A., and Kouwenhoven, L. P., *Nature nanotechnology* **7**, 630 (2012).
- Petersson, K. D., McFaul, L. W., Schroer, M. D., Jung, M., Taylor, J. M., Houck, A. A., and Petta, J. R., *Nature* **490**, 380 (2012).
- Petersson, K. D., Petta, J. R., Lu, H., and Gossard, A. C., *Physical Review Letters* **105**, 246804 (2010).
- Petta, J. R., Johnson, A. C., Marcus, C. M., Hanson, M. P., and Gossard, A. C., *Physical Review Letters* **93**, 186802 (2004).
- Petta, J. R., Johnson, A. C., Taylor, J. M., Laird, E. A., Yacoby, A., Lukin, M. D., Marcus, C. M., Hanson, M. P., and Gossard, A. C., *Science* **309**, 2180 (2005).
- Pingenot, J., Pryor, C. E., and Flatté, M. E., *Physical Review B* **84**, 195403 (2011).

- Pioro-Ladrière, M., Obata, T., Tokura, Y., Shin, Y.-S., Kubo, T., Yoshida, K., Taniyama, T., and Tarucha, S., [Nature Physics](#) **4**, 776 (2008a).
- Pioro-Ladrière, M., Obata, T., Tokura, Y., Shin, Y.-S., Kubo, T., Yoshida, K., Taniyama, T., and Tarucha, S., [Progress of Theoretical Physics Supplement](#) **176**, 322 (2008b).
- Pioro-Ladrière, M., Tokura, Y., Obata, T., Kubo, T., and Tarucha, S., [Applied Physics Letters](#) **90**, 024105 (2007).
- Pla, J. J., Tan, K. Y., Dehollain, J. P., Lim, W. H., Morton, J. J. L., Jamieson, D. N., Dzurak, A. S., and Morello, A., [Nature](#) **489**, 541 (2012).
- Pla, J. J., Tan, K. Y., Dehollain, J. P., Lim, W. H., Morton, J. J. L., Zwanenburg, F. A., Jamieson, D. N., Dzurak, A. S., and Morello, A., [Nature](#) **496**, 334 (2013).
- Poletto, S., Gambetta, J. M., Merkel, S. T., Smolin, J. A., Chow, J. M., Córcoles, A. D., Keefe, G. A., Rothwell, M. B., Rozen, J. R., Abraham, D. W., Rigetti, C., and Steffen, M., [Physical Review Letters](#) **109**, 240505 (2012).
- Prance, J. R., Shi, Z., Simmons, C. B., Savage, D. E., Lagally, M. G., Schreiber, L. R., Vandersypen, L. M. K., Friesen, M., Joynt, R., Coppersmith, S. N., and Eriksson, M. A., [Physical Review Letters](#) **108**, 046808 (2012).
- Prati, E., Latempa, R., and Fanciulli, M., [Physical Review B](#) **80**, 165331 (2009).
- Rahman, R., Lansbergen, G. P., Park, S. H., Verduijn, J., Klimeck, G., Rogge, S., and Hollenberg, L. C. L., [Physical Review B](#) **80**, 165314 (2009).
- Rančić, M. J. and Burkard, G., [Physical Review B](#) **93**, 205433 (2016).
- Rashba, E. I., [Physical Review B](#) **84**, 241305 (2011).
- Reinhard, F., Shi, F., Zhao, N., Rempp, F., Naydenov, B., Meijer, J., Hall, L. T., Hollenberg, L., Du, J., Liu, R.-B., and Wrachtrup, J., [Physical Review Letters](#) **108**, 200402 (2012).
- Roberts, M. M., Klein, L. J., Savage, D. E., Slinker, K. A., Friesen, M., Celler, G., Eriksson, M. A., and Lagally, M. G., [Nature Materials](#) **5**, 388 (2006).
- Rohling, N. and Burkard, G., [New Journal of Physics](#) **14**, 083008 (2012).
- Romhányi, J., Burkard, G., and Pályi, A., [Physical Review B](#) **92**, 054422 (2015).
- Sakurai, J., *Modern Quantum Mechanics*, revised ed ed. (Addison Wesley, 1993).
- Samkharadze, N., Bruno, A., Scarlino, P., Zheng, G., DiVincenzo, D. P., DiCarlo, L., and Vandersypen, L. M. K., (2015), [arXiv:1511.01760](#).
- Saraiva, A. L., Koiller, B., and Friesen, M., [Physical Review B](#) **82**, 245314 (2010).
- Scarlino, P., *Spin and valley physics in a Si/SiGe quantum dot*, Ph.D. thesis, Delft University of Technology (2016).

- Scarlino, P., Kawakami, E., Stano, P., Shafiei, M., Reichl, C., Wegscheider, W., and Vandersypen, L. M. K., [Physical Review Letters](#) **113**, 256802 (2014).
- Schäffler, F., [Semiconductor Science and Technology](#) **12**, 1515 (1997).
- Schreiber, L., Braakman, F., Meunier, T., Calado, V., Danon, J., Taylor, J., Wegscheider, W., and Vandersypen, L., [Nature Communications](#) **2**, 556 (2011).
- Schweiger, A. and Jeschke, G., *Principles of Pulse Electron Paramagnetic Resonance* (Oxford Univ Pr on Demand, 2001).
- Shafiei, M., *Electrical Manipulation and Detection of Single Electron Spins in Quantum Dots*, Ph.D. thesis, Delft University of Technology (2013).
- Shafiei, M., Nowack, K. C., Reichl, C., Wegscheider, W., and Vandersypen, L. M. K., [Physical Review Letters](#) **110**, 107601 (2013).
- Shang, R., Li, H.-O., Cao, G., Xiao, M., Tu, T., Jiang, H., Guo, G.-C., and Guo, G.-P., [Applied Physics Letters](#) **103**, 162109 (2013).
- Shen, Y. R., [Nature](#) **337**, 519 (1989).
- Shevchenko, S., Ashhab, S., and Nori, F., [Physics Reports](#) **492**, 1 (2010).
- Shevchenko, S. N., Omelyanchouk, A. N., and Il'ichev, E., [Low Temperature Physics](#) **38**, 283 (2012).
- Shi, Z., Simmons, C. B., Prance, J. R., Gamble, J. K., Koh, T. S., Shim, Y.-P., Hu, X., Savage, D. E., Lagally, M. G., Eriksson, M. A., Friesen, M., and Coppersmith, S. N., [Physical Review Letters](#) **108**, 140503 (2012).
- Shi, Z., Simmons, C. B., Ward, D. R., Prance, J. R., Mohr, R. T., Koh, T. S., Gamble, J. K., Wu, X., Savage, D. E., Lagally, M. G., Friesen, M., Coppersmith, S. N., and Eriksson, M. A., [Physical Review B](#) **88**, 075416 (2013).
- Shor, P. W., [Physical Review A](#) **52**, R2493 (1995).
- Shor, P. W., [SIAM Journal on Computing](#) **26**, 1484 (1997).
- Shulman, M. D., Dial, O. E., Harvey, S. P., Bluhm, H., Umansky, V., and Yacoby, A., [Science](#) **336**, 202 (2012).
- Simmons, C., Koh, T., Shaji, N., Thalakulam, M., Klein, L., Qin, H., Luo, H., Savage, D., Lagally, M., Rimberg, a., Joynt, R., Blick, R., Friesen, M., Coppersmith, S., and Eriksson, M., [Physical Review B](#) **82**, 245312 (2010).
- Simmons, C., Prance, J., Van Bael, B., Koh, T., Shi, Z., Savage, D., Lagally, M., Joynt, R., Friesen, M., Coppersmith, S., and Eriksson, M., [Physical Review Letters](#) **106** (2011a), [10.1103/PhysRevLett.106.156804](#).

- Simmons, C. B., Thalakulam, M., Shaji, N., Klein, L. J., Qin, H., Blick, R. H., Savage, D. E., Lagally, M. G., Coppersmith, S. N., and Eriksson, M. A., *Applied Physics Letters* **91**, 213103 (2007).
- Simmons, S., Brown, R. M., Riemann, H., Abrosimov, N. V., Becker, P., Pohl, H.-j., Thewalt, M. L. W., Itoh, K. M., and Morton, J. J. L., *Nature* **470**, 69 (2011b), [arXiv:1010.0107](https://arxiv.org/abs/1010.0107).
- Slichter, C. P., *Principles of Magnetic Resonance*, Springer Series in Solid-State Sciences, Vol. 1 (Springer Berlin Heidelberg, Berlin, Heidelberg, 1990).
- Smolin, J. A., Smith, G., and Vargo, A., *Nature* **499**, 163 (2013).
- Soare, A., Ball, H., Hayes, D., Sastrawan, J., Jarratt, M. C., McLoughlin, J. J., Zhen, X., Green, T. J., and Biercuk, M. J., *Nature Physics* **10**, 825 (2014).
- de Sousa, R., *Electron Spin Resonance and Related Phenomena in Low-Dimensional Structures*, edited by M. Fanciulli (Springer Berlin Heidelberg, Berlin, Heidelberg, 2009) Chap. Electron spin as a spectrometer of nuclear spin noise and other fluctuations, pp. 183–220.
- de Sousa, R. and Das Sarma, S., *Physical Review B* **68**, 115322 (2003).
- Souza, A. M., Álvarez, G. A., and Suter, D., *Physical Review A* **85**, 032306 (2012).
- Srinivasa, V., Nowack, K. C., Shafei, M., Vandersypen, L. M. K., and Taylor, J. M., *Physical Review Letters* **110**, 196803 (2013).
- Stafford, C. A. and Wingreen, N. S., *Physical Review Letters* **76**, 1916 (1996).
- Steane, A. M., (2004), [arXiv:quant-ph/0412165](https://arxiv.org/abs/quant-ph/0412165).
- Stehlik, J., Dovzhenko, Y., Petta, J. R., Johansson, J. R., Nori, F., Lu, H., and Gossard, A. C., *Physical Review B* **86**, 121303 (2012).
- Stehlik, J., Schroer, M. D., Maialle, M. Z., Degani, M. H., and Petta, J. R., *Physical Review Letters* **112**, 227601 (2014).
- Stoof, T. H. and Nazarov, Y. V., *Physical Review B* **53**, 1050 (1996).
- Strauch, F. W., Dutta, S. K., Paik, H., Palomaki, T. A., Mitra, K., Cooper, B. K., Lewis, R. M., Anderson, J. R., Dragt, A. J., Lobb, C. J., and Wellstood, F. C., *IEEE Transactions on Applied Superconductivity* **17**, 105 (2007).
- Stufler, S., Machnikowski, P., Ester, P., Bichler, M., Axt, V. M., Kuhn, T., and Zrenner, A., *Physical Review B* **73**, 125304 (2006).
- Széchenyi, G. and Pályi, A., *Physical Review B* **89**, 115409 (2014).
- Tahan, C. and Joynt, R., *Physical Review B* **89**, 075302 (2014).
- Takahashi, M., Bartlett, S. D., and Doherty, A. C., *Physical Review A* **88**, 022120 (2013).

- Takakura, T., Pioro-Ladrière, M., Obata, T., Shin, Y.-S., Brunner, R., Yoshida, K., Taniyama, T., and Tarucha, S., [Applied Physics Letters](#) **97**, 212104 (2010).
- Takeda, K., private communication (2015).
- Takeda, K., Kamioka, J., Otsuka, T., Yoneda, J., Nakajima, T., Delbecq, M. R., Amaha, S., Allison, G., Kodera, T., Oda, S., and Tarucha, S., (2016), [arXiv:1602.07833](#) .
- Tarucha, S., Austing, D., Honda, T., van der Hage RJ,, and Kouwenhoven, L., [Physical Review Letters](#) **77**, 3613 (1996).
- Thalineaau, R., Hermelin, S., Wieck, A. D., Bauerle, C., Saminadayar, L., and Meunier, T., [Applied Physics Letters](#) **101**, 103102 (2012).
- Tokura, Y., Kubo, T., and Munro, W. J., (2013), [arXiv:1308.0071](#) .
- Tokura, Y., van der Wiel, W. G., Obata, T., and Tarucha, S., [Physical Review Letters](#) **96**, 047202 (2006).
- Tosi, G., Mohiyaddin, F. A., Tenberg, S. B., Rahman, R., Klimeck, G., and Morello, A., (2015), [arXiv:1509.08538](#) .
- Trifunovic, L., Dial, O., Trif, M., Wootton, J. R., Abebe, R., Yacoby, A., and Loss, D., [Physical Review X](#) **2**, 011006 (2012).
- Trifunovic, L., Pedrocchi, F. L., and Loss, D., [Physical Review X](#) **3**, 041023 (2013).
- Truitt, J. L., Slinker, K. A., Lewis, K. L. M., Savage, D. E., Tahan, C., Klein, L. J., Chu, J. O., Mooney, P. M., Tyryshkin, A. M., Weide, D. W., Joynt, R., Coppersmith, S. N., Friesen, M., and Eriksson, M. A., [Electron Spin Resonance and Related Phenomena in Low-Dimensional Structures](#), edited by M. Fanciulli (Springer Berlin Heidelberg, Berlin, Heidelberg, 2009) Chap. Si/SiGe Quantum Devices, Quantum Wells, and Electron-Spin Coherence, pp. 101–127.
- Tyryshkin, A. M., Lyon, S. A., Astashkin, A. V., and Raitsimring, A. M., [Physical Review B](#) **68**, 193207 (2003).
- Tyryshkin, A. M., Lyon, S. A., Jantsch, W., and Schäffler, F., [Physical Review Letters](#) **94**, 126802 (2005).
- Tyryshkin, A. M., Tojo, S., Morton, J. J. L., Riemann, H., Abrosimov, N. V., Becker, P., Pohl, H.-J., Schenkel, T., Thewalt, M. L. W., Itoh, K. M., and Lyon, S. a., [Nature Materials](#) **11**, 18 (2011), [arXiv:1105.3772](#) .
- Tyryshkin, A. M., Tojo, S., Morton, J. J. L., Riemann, H., Abrosimov, N. V., Becker, P., Pohl, H.-J., Schenkel, T., Thewalt, M. L. W., Itoh, K. M., and Lyon, S. A., [Nature materials](#) **11**, 143 (2012).
- Uhrig, G. S., [Physical Review Letters](#) **98**, 100504 (2007).
- Van Meter, R. and Horsman, C., [Communications of the ACM](#) **56**, 84 (2013).

- Vandersypen, L., *Experimental Quantum Computation with Nuclear Spins in Liquid Solution*, Ph.D. thesis, Stanford University (2001).
- Vandersypen, L. M., Steffen, M., Breyta, G., Yannoni, C. S., Sherwood, M. H., and Chuang, I. L., [Nature](#) **414**, 883 (2001).
- Vandersypen, L. M. K. and Chuang, I. L., [Reviews of Modern Physics](#) **76**, 1037 (2005).
- Vandersypen, L. M. K., Elzerman, J. M., Schouten, R. N., Willems van Beveren, L. H., Hanson, R., and Kouwenhoven, L. P., [Applied Physics Letters](#) **85**, 4394 (2004).
- Veldhorst, M., Hwang, J. C. C., Yang, C. H., Leenstra, A. W., de Ronde, B., Dehollain, J. P., Muhonen, J. T., Hudson, F. E., Itoh, K. M., Morello, A., and Dzurak, A. S., [Nature nanotechnology](#) **9**, 981 (2014).
- Veldhorst, M., Ruskov, R., Yang, C. H., Hwang, J. C. C., Hudson, F. E., Flatté, M. E., Tahan, C., Itoh, K. M., Morello, A., and Dzurak, A. S., [Physical Review B](#) **92**, 201401 (2015a).
- Veldhorst, M., Yang, C. H., Hwang, J. C. C., Huang, W., Dehollain, J. P., Muhonen, J. T., Simmons, S., Laucht, A., Hudson, F. E., Itoh, K. M., Morello, A., and Dzurak, A. S., [Nature](#) **526**, 410 (2015b).
- Viola, L., Lloyd, S., and Knill, E., [Physical Review Letters](#) **83**, 4888 (1999).
- Wallraff, A., Duty, T., Lukashenko, A., and Ustinov, A. V., [Physical Review Letters](#) **90**, 037003 (2003).
- Walvoort, F., *Fabrication and characterization of double quantum dots in an undoped Si-SiGe heterostructure*, Master's thesis, Delft University of Technology (2014).
- Wang, D. S., Fowler, A. G., and Hollenberg, L. C. L., [Physical Review A](#) **83**, 020302 (2011).
- Wang, Z.-H., Zhang, W., Tyryshkin, A. M., Lyon, S. A., Ager, J. W., Haller, E. E., and Dobrovitski, V. V., [Physical Review B](#) **85**, 085206 (2012).
- Warburton, R. J., [Nature Materials](#) **12**, 483 (2013).
- Ward, D. R., Kim, D., Savage, D. E., Lagally, M. G., Foote, R. H., Friesen, M., Coppersmith, S. N., and Eriksson, M. A., (2016), [arXiv:1604.07956](#).
- Ward, D. R., Savage, D. E., Lagally, M. G., Coppersmith, S. N., and Eriksson, M. A., [Applied Physics Letters](#) **102**, 213107 (2013).
- van Wees, B. J., van Houten, H., Beenakker, C. W. J., Williamson, J. G., Kouwenhoven, L. P., van der Marel, D., and Foxon, C. T., [Physical Review Letters](#) **60**, 848 (1988).
- van der Wiel, W., Fujisawa, T., Oosterkamp, T., and Kouwenhoven, L., [Physica B: Condensed Matter](#) **272**, 31 (1999).
- van der Wiel, W. G., De Franceschi, S., Elzerman, J. M., Fujisawa, T., Tarucha, S., and Kouwenhoven, L. P., [Reviews of Modern Physics](#) **75**, 1 (2002).

- Wilamowski, Z., Jantsch, W., Malissa, H., and Rössler, U., [Physical Review B](#) **66**, 195315 (2002).
- Wilson, C. M., Duty, T., Persson, F., Sandberg, M., Johansson, G., and Delsing, P., [Physical Review Letters](#) **98**, 257003 (2007).
- Winkler, R., *Spin–Orbit Coupling Effects in Two-Dimensional Electron and Hole Systems*, Springer Tracts in Modern Physics, Vol. 191 (Springer Berlin Heidelberg, Berlin, Heidelberg, 2003).
- Witzel, W. M. and Das Sarma, S., [Physical Review B](#) **74**, 035322 (2006).
- Wu, X., Ward, D. R., Prance, J. R., Kim, D., Gamble, J. K., Mohr, R. T., Shi, Z., Savage, D. E., Lagally, M. G., Friesen, M., Coppersmith, S. N., and Eriksson, M. A., [Proceedings of the National Academy of Sciences of the United States of America](#) **111**, 11938 (2014).
- Xiang, Z.-L., Ashhab, S., You, J. Q., and Nori, F., [Reviews of Modern Physics](#) **85**, 623 (2013).
- Xu, C., Zipfel, W., Shear, J. B., Williams, R. M., and Webb, W. W., [Proceedings of the National Academy of Sciences](#) **93**, 10763 (1996).
- Yang, C. H., Rossi, A., Ruskov, R., Lai, N. S., Mohiyaddin, F. A., Lee, S., Tahan, C., Klimeck, G., Morello, A., and Dzurak, A. S., [Nature communications](#) **4**, 2069 (2013).
- Yang, W. and Liu, R.-B., [Physical Review B](#) **79**, 115320 (2009).
- Yoneda, J., Otsuka, T., Nakajima, T., Takakura, T., Obata, T., Pioro-Ladrière, M., Lu, H., Palmstrøm, C. J., and Gossard, A. C. and Tarucha, S., [Physical Review Letters](#) **113**, 267601 (2014).
- Yoneda, J., Otsuka, T., Takakura, T., Pioro-Ladrière, M., Brunner, R., Lu, H., Nakajima, T., Obata, T., Noiri, A., Palmstrøm, C. J., Gossard, A. C., and Tarucha, S., [Applied Physics Express](#) **8**, 084401 (2015).
- Zajac, D. M., Hazard, T. M., Mi, X., Wang, K., and Petta, J. R., [Applied Physics Letters](#) **106**, 223507 (2015).
- Zalka, C., (2006), [arXiv:quant-ph/0601097](#) .
- Zener, C., [Proceedings of the Royal Society A: Mathematical, Physical and Engineering Sciences](#) **137**, 696 (1932).
- Zhang, W., Konstantinidis, N., Al-Hassanieh, K. A., and Dobrovitski, V. V., [Journal of Physics: Condensed Matter](#) **19**, 083202 (2007).
- Zimmerman, N. M., Yang, C.-H., Lai, N. S., Lim, W. H., and Dzurak, A. S., (2014).
- Zwanenburg, F. A., Dzurak, A. S., Morello, A., Simmons, M. Y., Hollenberg, L. C. L., Klimeck, G., Rogge, S., Coppersmith, S. N., and Eriksson, M. A., [Reviews of Modern Physics](#) **85**, 961 (2013).

ACKNOWLEDGMENTS

The first acknowledgment goes to Lieven. Lieven, it was the happiest day in my life when I received the offer for the Ph.D. position from you. I believed that you would be the best Ph.D. supervisor I could find in the world and now I know that I was totally right. Thank you for always supporting me whenever and whatever situation I was in. Thanks for always letting me take rest when I needed. I have always respected your courage to admit mistakes and change your mind after listening to other people's opinions. Thank you for letting me write the thesis taking as much time as I needed without putting a rush on me.

Enormous special thanks go to Pasquale. Pasquale, you have been an unofficial promoter of the Si quantum dots project during the past 4 years. When I arrived in Delft, you were working on a Si project alone. Now you know how many people are working on Si qubits in Delft. It is one of the most precious and wonderful things in my life to meet you. Despite all difficult and unfortunate things I encountered in Delft, I cannot regret my decision to come here when I remember this point. I will never be able to thank you enough. You taught me really a lot of things from the physics to unwritten rules in QT, or in (European) life. Almost everything I know about the physics in quantum dots is what I first learned from you. Without you, my Ph.D. would be much harder. I don't even want to imagine that. There also was a lot of fun in the adventure in Silicon with you. You always have wonderful experimental ideas and a big enthusiasm of pursuing experimental physics. You once told me that you will become an electron and then you will get inside the fridge, arrive on the position of the sample and get inside the dot as the last electron and then you will change your spin state as I manipulate. That was sweet, but we are happy that we achieved the experiments without losing you as one of electrons. There are many good memories shared with you. It was always fun to work with you. Thank you for always listening to me. Thank you for always being beside me. Thank you for always supporting me. Thank you so much for showing your wonderful hometown. "Salento, lu sule, lu mare, lu ientu." I cannot thank you too much. I wish you a lot of good luck in Zürich. My dream is to one day visit you in your own lab and I am sure that that day will come in not far future.

"Thibaut, thank you for joining in the SiGe qubits project. Your deep understanding of physics and good insight on what is going in the lab are really amazing. I have always been impressed by your talent. I am sure that you will make astonishing physics happen using Si/SiGe qubits." The above message to you had been written before you passed away. Now I should like to rephrase it a little bit. You are the only person who I have ever met that I thought might be worth being called a genius. I write this here not sentimentally but being driven by a sense of duty. Sadly you cannot make this kind of impression on people directly by yourself anymore and happily I am one of the lucky people who have worked with you very closely. I have thought many times, when you were still alive, if such a talented person like you cannot get a position in the academic

world, there must be something wrong with the academic world. I wanted to see you go through to a successful and wealthy life. It is regrettable and I am sorry. Thank you a lot for sharing your time and discussing many things with me. Even though you are not here anymore, you left us many precious things.

Floris, thank you for always coming to B059 and F006, having nice chats and giving valuable advice. Thank you for teaching me how to operate the wet fridge. Thank you for always answering both my silly and serious questions. Thank you for always cheering us up in order to motivate us on the research.

Tom, thank you for reading this thesis very carefully and patiently and giving me useful feedback. I am very happy to see the two-qubit gate happening before I leave Delft. The number of results that you have achieved within less than one year is amazing. I am sure that I will enjoy reading the papers on the further results that you will achieve in the future as well. Zubin, it was a short time but it was fun to work with you! Thank you for the translation of the summary of this thesis.

Lars, if I didn't find your announcement to recruit a master student, I wouldn't have known that the Si project was starting and I wouldn't have come to Delft. The weekly Skype meetings with you during my early stage of Ph.D. was precious to the two 1st year Ph.D. students. Thank you for teaching me how to turn on the magnet power, how to write LabView and Python codes, valley physics, and photon-assisted tunneling. By listing here what I learned from you, I cannot believe that I have never worked with you on site.

Tim, I always admire your effective working style. I respect your communication skill to accomplish your profit and others' profit at the same time. This may be the most important trait to be creative and productive which one might want to get and it is difficult to get.

Mohammad, when I joined QT, there were you, Pasquale and me working in B059. Thank you for always helping young Ph.D. students. I didn't even know how to turn on AWG. Your knowledge on microwave components was invaluable and we were able to skip all the problems we would encounter without your assistance. Thank you for patiently telling me how to understand measurement and analysis programs. To be honest, your Matlab codes and Python codes seem to me as if they are written in the language C. Thank you for helping us measuring T1 in GaAs.

Pierre, thank you for creating the driver for pulses created by AWG. It would be a nightmare to program complicated pulses without your driver. Ferdy, it was so nice to have you in the group. Thank you for making the micromagnets program readable to everyone. Toivo, thank you for asking everyone for going to lunch time by time. Takafumi, thank you for our secret chats in Japanese! Nodar, thank you for making a new wind blow in the team. Your project is the key to the realization of a quantum computer. Udit, thank you for making fun of me about tomato juice. Yes, I really like it! Jelmer, thank you for measuring the DQD Si/SiGe quantum dot sample with me in the dry fridge. All the best with SiMOS! Giordano, Gouji, JP, Delphine, Gabriel, Lareine, Nima, Diego, it was a short time to work with you but I was happy to work with all of you. All the best.

Acknowledgments also go to our colleagues in Wisconsin. Mark, thank you for always keeping our collaboration powerful. It is so nice that you are now in Delft! Max and Don, thank you for growing nice substrate. Jon and Dan, thank you for fabricating such nice

devices. Without your work, none of the results in this thesis would exist. Mark and Sue, thank you so much for your patience in guiding us through the rigorous theoretical explanations to explain our data.

Now I change location a bit inside the US. Rajib and Rifat, thank you so much for providing the nice theory to fit our data and taking time to explain how it works. Slava, thank you for always giving easy-to-understand explanations. I learned a lot from you.

I would also like to thank our local theorist Michael. Thank you so much for applying your deep knowledge on spin-orbit now to Si.

Next, I move to the other Qutech PIs to thank them. Leo K, thank you for offering me your sympathetic comments just after Thibaut's leave. Your comments were reassuring and encouraging especially because Lieven was away at that time. Thank you. Ronald, thank you for reading our paper carefully. Leo DC, thank you for visiting F006 for the air conditioning during the summer and showing me papers to be read for quantum process tomography and randomized benchmarking. Stephanie, thank you for listening to me when I was not OK. I would like to discuss on randomized benchmarking with you after I am done with this thesis.

Next, I go to the technicians' room. Jelle, thank you for always helping with the fridge. Your help was enormous. We couldn't have been able to change the Dewar, move the wet fridge or install a new dry fridge without you. Remco, thank you for liquefying He. Thank you for listening to all our complains about cryogenic stuff and offering nice solutions. Mark, thank you so much for helping us to survive many weekends without electricity. Bram, we had depended on the history book of QT which exists in your mind. I miss your whistle.

Raymond S., like all the other Ph.D. students, I learned enormous things from you. I think the core of QT is you. Thanks a lot. I respect not only your knowledge but also your patience to explain it to people. Raymond V. and Marijn, thank you a lot for all the FPGAs. The last chapters of this thesis couldn't exist without you. Rogier, thank you so much for PCBs. Ruth, thank you so much for high-frequency components. Jack, thank you so much for batteries and always making fancy electronics. Olaf, thank you for your insightful inputs on cryogenic systems.

Oxford technicians, Phil, Mark, Ricardo, despite all the problems which Triton has given, I would like to thank you for all your efforts to try to fix problems. I suffered a lot with the installation of Tritons, but I enjoyed working with you and I learned a lot from you when you were on site.

Kun and Vincent, thank you so much for taking your time to listen to my story. Stephan, thank you for making tasty lasagna. It was so delicious that I cannot believe that it was the first time you made it. Julia, I really appreciate that you helped me a lot when I was in a most horrible condition. It is terrifying to imagine that you were not next to me when I received the bad news. I really missed having fun with you during one week in San Antonio but I am happy that I enjoyed one week in Baltimore with you! Anaïs, thank you for listening to my story and making us brownies. It was very precious and tasty. Maja, thank you for sharing your knowledge on the Oxford dry fridges. I enjoyed our chats at the Mexican place.

Yuki-san, thank you for always supporting me in many aspects. Thank you so much for all the Japanese cuisine you cooked for me. Like many of QT people, I also owe thanks

for your constant encouragement. Marja, thank you for helping me out so many times. Without your help, I would have been an illegal immigrant or adrift in the streets. Tessel, thank you for checking and correcting this thesis.

Acknowledgments also go to our new colleagues from EWI. Jeroen, Fabio, Edoardo, Masoud, it was a nice opportunity to work with you. I also learned a lot from you. It was admirable how fast you learned quantum information. Alice, Miki-kun, Ishihara-sensei, the scalability of qubits must depend on your technology. Good luck with the multiplexer!

I would also like to thank the people I met at conferences, although I should first thank Lieven for letting me have these opportunities. Thank you for the valuable discussions on our experiments and their experiments or theories. The last 5 years have been a very fruitful period for Si quantum computing and I was lucky for being in this field in this period to see the dynamic development. I was able to have useful discussions with many excellent researchers outside of TU Delft. Menno, you gave us very useful inputs when we met at the conference and it is so nice that you are now in Delft. You always have brilliant ideas, you understand things super fast, and it is sometimes difficult for me to catch you up during the conversation. Good luck with building up your own lab!

I would especially like to thank Dr. Negoro and Dr. Tokura for inviting me to their workshop. It was a very good opportunity to see young Japanese scientists working on quantum computer. I was able to realize how naive I had been not to follow the theoretical parts of the progress in quantum computer. I hope you will continue this workshop regularly. I would like to thank Dr. Semba for inviting me to the JSAP annual meeting. I always admired your high productivity and thank you for letting me to visit your lab.

In some sense, obtaining a Ph.D. is the culmination of many years of study. I had the privilege of learning from and being supervised by excellent people even before coming to Delft. Prof. Kohei Itoh, thank you for supporting me to reach this Ph.D. position. I am very happy to see that the collaboration between Lieven and you on ^{28}Si has started and I hope that it will work out well. John and Stephanie, thank you for teaching me pulsed-ESR and introducing the field. Paula and Massimo, thank you for teaching me fundamental quantum mechanics. What I learned from you were very useful on the course of my Ph.D.

I would like to thank the Nakajima foundation not only for their financial support but also for their kind considerations. It was really a nice opportunity to see the director and other members of the foundations together with other scholarship recipients. Thank you for accepting a half year prolongation.

Last but not least, I would like to thank my family and friends in Japan.

CURRICULUM VITAE

Erika Kawakami

- February 5, 1986 Born in Osaka, Japan.
- 1998 – 2004 Shibuya Makuhari high school, Chiba, Japan
- 2005 – 2009 BSc in Applied Physics
Keio University, Japan.
- 2007 – 2009 Engineering degree in General Engineering (double degree program)
École Centrale de Marseille, France.
- 2009 – 2011 Master of engineering in Applied Physics
Keio University, Japan,
under supervision of prof. dr. Kohei M. Itoh.
*"Suppressing the Decoherence of Phosphorus Electron Spins in Silicon
Using Pulsed Electron Paramagnetic Resonance"*.
- 2011 – 2016 PhD research
Delft University of Technology, The Netherlands,
under supervision of prof. dr. ir. L. M. K. Vandersypen.
"Characterization of an Electron Spin Qubit in a Si/SiGe quantum dot".

LIST OF PUBLICATIONS

1. *Coherent storage of photoexcited triplet states using ^{29}Si nuclear spins in silicon*
W. Akhtar, V. Filidou, T. Sekiguchi, E. Kawakami, T. Itahashi, L. Vlasenko, J. J. L. Morton, K. M. Itoh
[Phys. Rev. Lett. **108**, 097601 \(2012\).](#)
2. *Excitation of a Si/SiGe quantum dot using an on-chip microwave antenna*
E. Kawakami, P. Scarlino, L. R. Schreiber, J. R. Prance, D. E. Savage, M. G. Lagally, M. A. Eriksson, L. M. K. Vandersypen
[Appl. Phys. Lett. **103**, 132410 \(2013\).](#)
3. *Electrical control of a long-lived spin qubit in a Si/SiGe quantum dot*
E. Kawakami*, P. Scarlino*, D. R. Ward, F. R. Braakman, D. E. Savage, M. G. Lagally, Mark Friesen, S. N. Coppersmith, M. A. Eriksson, L. M. K. Vandersypen
[Nature Nanotechnology **9**, 666–670 \(2014\).](#)
4. *Spin relaxation anisotropy in a GaAs quantum dot*
P. Scarlino, E. Kawakami, P. Stano, M. Shafiei, C. Reichl, W. Wegscheider, L. M. K. Vandersypen
[Phys. Rev. Lett. **113**, 256802 \(2014\).](#)
5. *Second Harmonic Coherent Driving of a Spin Qubit in a Si/SiGe Quantum Dot*
P. Scarlino, E. Kawakami, D. R. Ward, D. E. Savage, M. G. Lagally, Mark Friesen, S. N. Coppersmith, M. A. Eriksson, L. M. K. Vandersypen
[Phys. Rev. Lett. **115**, 106802 \(2015\).](#)
6. *EDSR detection of dressed orbital states in a quantum dot*
P. Scarlino, E. Kawakami, T. Jullien, D. R. Ward, D. E. Savage, M. G. Lagally, Mark Friesen, S. N. Coppersmith, M. A. Eriksson, L. M. K. Vandersypen
submitted to Phys. Rev. X.
7. *Gate fidelity and coherence of an electron spin in a Si/SiGe quantum dot with micromagnet*
E. Kawakami, T. Jullien, P. Scarlino, D. R. Ward, D. E. Savage, M. G. Lagally, V. V. Dobrovitski, Mark Friesen, S. N. Coppersmith, M. A. Eriksson, L. M. K. Vandersypen
[accepted for publication in Proceedings of the National Academy of Sciences, arXiv:1602.08334.](#)
8. *Valley dependent g-factor anisotropy in Silicon quantum dots*
R. Ferdous, P. Scarlino, E. Kawakami, M. Novak, D. E. Savage, M. G. Lagally, Mark Friesen, S. N. Coppersmith, M. A. Eriksson, L. M. K. Vandersypen, R. Rahman
in preparation.